University of Alberta

A Magnetotelluric Investigation of the Arabia – Eurasia Collision in Eastern Anatolia

by

Erşan Türkoğlu

A thesis submitted to the Faculty of Graduate Studies and Research
in partial fulfillment of the requirements for the degree of Doctor of Philosophy in
Geophysics

Department of Physics

Edmonton, Alberta
Spring 2009

ABSTRACT

Eastern Anatolia is the location of a young continent – continent collision between the Arabian and Eurasian plates in Eastern Turkey. The first long-period magnetotelluric (MT) data were collected in eastern Anatolia in 2005 as part of this thesis. These MT data have been used to image the electrical resistivity of the crust and upper mantle as well as the continental boundaries. Two and three-dimensional inversion algorithms were used to obtain resistivity models of the study area.

The MT inversion models indicate that the Anatolian Block is characterized by a low-resistivity (10-30 Ωm) fluid-rich lower crust underlain by relatively normal upper mantle structure. The Anatolian Plateau has a lower crust that contains pockets of very low resistivity (2-5 Ωm) that may indicate local accumulations of melt. These pockets require at least 5-14% of partial melt to account for the observed bulk resistivities. The lower crust is underlain by an upper mantle with an anomalously low resistivity that can be accounted for by an asthenosphere containing ~2% percent partial melt. The presence of fluids along with high temperatures may weaken the crust and mantle sufficiently to permit lateral flow, and may also allow a decoupling of the upper and lower portions of the lithosphere. South of the Bitlis Suture Zone, the depth of the lithosphere-asthenosphere boundary on the Arabian foreland was found to be around 110 km from constrained MT inversions. The average resistivity of the Arabian lithosphere is 100-300 Ωm which is one order of

magnitude higher than the Anatolian Plateau. A fault zone conductor observed beneath the East Anatolian Fault at Hazar Lake correlates with a band of low seismicity and may represent a weak segment of the fault that is creeping. The thickness of the Erzincan Basin was found to be 3±0.25 km with a slight (0.25 km) increase towards the western part of the basin. The lithospheric structure of the Anatolian Plateau is similar to that of the northern Tibetan Plateau, with zones of inferred elevated fluid content. However, low resistivity in the Anatolian crust is found in isolated pockets, rather than the widespread regions observed in Tibet.

ACKNOWLEDGEMENTS

My special thanks to Prof. Martyn Unsworth for providing me with the opportunity to work on an interesting research topic. I also appreciated his guidance, encouragement and experience throughout the course of this thesis, spending extensive time in the field during data collection, and always being available to discuss processing and interpretation of the data.

This project was made possible by the extensive support of Prof. İlyas Çağlar of Istanbul Technical University (ITU). I particularly wish to thank Prof. Tuncay Taymaz of Istanbul Technical University who made me aware of the Ph.D. position at the University of Alberta (UA).

Volkan Tuncer and Ümit Avşar are greatly appreciated for their friendship and efforts during the fieldwork and thereafter. ITU geophysics students Ahmet Şener and Tunç Demir are thanked for their cheer in the field. Dr. Bülent Tank of Boğaziçi University is also thanked for assistance during data collection in the Erzincan Basin. Dr. Wolfgang Soyer and Ahmet Ökeler are thanked for their encouragement and discussions on various problems of the MT data processing. I thank Edward Bertrand for proofreading this thesis. Cheers to friends who I enjoyed being a colleague of in the same department. The friendship of non-academic friends, particularly Celadet Aytek, was necessary to complete this thesis.

I would like to thank Prof. Mehmet Keskin and Prof. Eric Sandvol for reviewing part of this thesis used for a publication in *Geology*.

Initial results of this thesis were presented at the AGU 2005 fall meeting in San Francisco, USA. Partial support was provided by a travel award from the Institute for Geophysical

Research at UA. In addition, the organizing committee of the 18th EMIW in Barcelona, Spain is thanked for a travel award where parts of this research were also presented.

Phoenix Geophysics is thanked for an instrument loan and technical support. Shaded topography maps were generated using the GMT software of Paul Wessel and Walter H. F. Smith (1991). Prof. Alan Jones and Gary McNeice are thanked for providing their tensor decomposition program. Dr. Weerachai Siripunvaraporn is thanked for providing the 3-D inversion code. Numerical and Statistical Servers at the University of Alberta were used for extensive computations required for the 3-D inversions.

This research was financially supported by NSERC and Alberta Ingenuity Fund grants to Prof. Martyn Unsworth and Scientific Council of Turkey (TUBİTAK, project 105Y022) funds to Prof. İlyas Çağlar.

I am grateful to many Turkish government and military officials for their hospitality, providing accommodation and logistics. I appreciate local residents of eastern Turkey for helping in many ways to accomplish the fieldwork.

Finally, many thanks to my family for their patience and invaluable support during my long lasting Ph.D. adventure in a distant country.

At the end, I have to say that I admire my wife Eylem's encouragement and endurance throughout the course of my Ph.D. study. She is the biggest fan of this project and deserves a big thank you for assuring proper installation of the MT instruments and excellent public relations with the local people in the field.

TABLE OF CONTENTS

SYMBOLS AND ABBREVIATIONS

AB	Anatolian Block
BNS	Banggong-Nuijang Suture
BPM	Bitlis Pötürge Massif
BSZ	Bitlis Suture Zone
CLVZ	crustal low velocity zone
CMT	Central Moment Tensor
DSF	Dead Sea Fault
EAAC	Eastern Anatolia Accretionary Complex
EAF	East Anatolian Fault
EAP	East Anatolian Plateau
EAP	Eastern Anatolian Plateau
EB	Erzincan basin
ETME	Eastern Turkey Magnetotelluric Experiment
ETSE	Eastern Turkey Seismic Experiment
FZC	fault zone conductor
GHS	Great Himalaya Suture
GPS	Global Positioning Systems
HSL	Hashin-Strikman lower bound
INDEPTH	International Deep Profiling of Tibet and Himalaya
ITS	Indus-Tsangpo Suture
JRS	Jinsha River Suture
KF	Kunlun Fault
KTJ	Karlıova Triple Junction
LAB	Lithosphere-Asthenosphere Boundary

LC	Lesser Caucasus
Ma	Million years
MBLM	Modified brick layer model
MTJ	Maraş Triple Junction
NAF	North Anatolian Fault
NEAF	North East Anatolian Fault
Nem	Nemrut
Süp	Süphan
Ağ	Ağrı
Ten	Tendürek
OF	Ovacık fault
QB	Qaidam Basin
RP	Rhodope-Pontide
KOERI	Kandilli Observatory and Earthquake Research Institute Boğaziçi Üniversitesi, Kandilli Rasathanesi ve Deprem Araştırma Enstitüsü, Ulusal Deprem İzleme Merkezi

π	3.14159265
$A_{R,I}$	amplitude of the induction vectors
ρ_a	apparent resistivity (Ω m)
η	Bahr skew
η_f	density of free electric charges (C/m^3)
$\phi_{R,I}$	direction of the induction vector
$\mathbf{C}$	distortion tensor
σ	electric conductivity (S/m)
ε	electric permittivity
ε_0	electric permittivity of free space ($8.85x10^{-12}$ F/m)
Ω	electrical resistance (Ohm)
f	frequency (Hz)
α	geoelectric strike angle

μ	magnetic permeability
μ_0	magnetic permeability of free space ($1.2566x10^{-6}$ H/m)
T_{zx}, T_{zy}	magnetic transfer functions – tipper
Σ	measure of departure from 1-D
δ	MT skin depth
ϕ	phase (degree)
ρ	resistivity (Ω m)
ρ_f	resistivity of the pore fluid (Ω m)
R_α	rotation matrix
κ	Swift's skew
x', y'	rotated Cartesian coordinates
Z_{TE}, Z_{TM}	TE and TM impedances
H_x, H_y, H_z	elements of electric field
E_x, E_y, E_z	elements of magnetic field
Z_{xx}, Z_{xy}, Z_{yx}, Z_{yy}	elements of impedance tensor
1-D	one dimensional
2-D	two-dimensional
3-D	three-dimensional
A	electric current (Ampére)
B	magnetic flux in Tesla
C	electric charge (Coulomb)
C	Weidelt transfer function
D	electric displacement (C/m^2)
E	electric field (V/m)
EM	Electromagnetic
g,**T**, **S** and **A**	components of distortion tensor
H	magnetic field (A/m)
J	conduction current density (A/m^2)

m	Archie's Law exponent
mGal	mili Gal – unit of gravity
MPa	Mega Pascal – unit of pressure
M_s	surface wave magnitude
MT	Magnetotellurics
MTA	General Directorate of Mineral Research and Exploration
M_w	moment magnitude
mW/m^2	mili watts per meter square – unit of heat flow
NIMS	Narod Intelligent Magnetotelluric Systems
NLCG	Nonlinear conjugate gradients algorithm
nT	nano Tesla – unit of magnetic field
P-waves	Primary earthquake waves
S-waves	Secondary earthquake waves
Pg	Crustal guided P wave
Lg	Crustal guided S wave
Pn	Upper mantle guided P wave
Sn	Upper mantle guided S wave
SKS	Outer core refracted S waves
S	electrical conductance (Siemens)
R	electric resistance (ohm)
r.m.s.	root mean square
RhoXY, RhoYX	apparent resistivity in field coordinates (Ω m)
T	Period (s)
TE	transverse electric
TM	transverse magnetic
x, y, z	Cartesian coordinates ($x \equiv north, y \equiv east, z \equiv depth$)
XY, YX	field coordinates
Z	impedance tensor
α	horizontal roughness parameter
τ	regularization parameter
ω	angular frequency ($2\pi f$)

TABLE CAPTIONS

FIGURE CAPTIONS

1 INTRODUCTION

The Magnetotelluric (MT) method has been primarily used to image the deep electrical resistivity structure of the Earth in the last three decades. The use of natural magnetic field variations makes this method practically applicable to any location on the Earth. However, some limitations apply towards the poles at very long periods. Prior to the development of the MT method the only means to extract direct information on the physical state of the crust and upper mantle was earthquake seismology. The combined analysis of the electrical resistivity and seismic velocity allows comprehensive interpretation of both data sets.

The MT method was independently discovered by Tikhonov (1950) and Cagniard (1953). MT is different from the other electromagnetic (EM) methods, in which the ground is induced using electrical or electromagnetic sources. MT samples a volume of the medium and the penetration depth depends on the period of the EM wave used and the conductivity of the subsurface. A high sampling rate is used for mineral, geothermal and hydrocarbon exploration while longer recordings with a reduced sampling rate are used for regional tectonic studies.

The MT method is very powerful at detecting enhanced conductivity in the crust due to aqueous fluids, metallic minerals, interconnected graphite films and partial melt. Supplementary data such as gravity, heat flow and seismic velocities are necessary in most cases to distinguish the source of the conductivity. For example, a region with high seismic velocities, low heat flow and high electrical conductivity is likely due to a small fraction of brines, metallic minerals or interconnected graphite films in the crust depending on the geology and tectonics of the region. Low seismic velocities, particularly very low shear wave velocity or the complete absence of shear waves with enhanced conductivity are likely due to partial melting. Brines have lower electrical resistivity (0.01 Ωm) than melt

(0.1-0.3 Ωm); thus a 0.1-1% fraction of pore fluid, depending on the pore geometry, can reduce the bulk resistivity of the medium up to three orders of magnitude (e.g. from 1000 Ωm to 1 Ωm). Such low porosity will not be detected as a significant reduction in seismic velocities.

Defining the source of conductance is critical for understanding the upper and mid crustal conductivity anomalies observed worldwide. In active tectonic regions, lower crustal conductors are usually associated with low temperature (~650° C) wet partial melting. The melting temperature of dry crustal material is above 1000° C. However, free fluids transported into the lower crust by tectonism or dehydration of amphibole-bearing rocks at 650-700° C (Vanyan and Gliko, 1999) could initiate partial melting at lower crustal temperatures. On the other hand, free water in stable regions is petrologically not viable. Deep continental crust in stable regions behaves as a sink rather than source of water as retrograde metamorphism absorbs water into hydrated mineral assemblages (Yardley and Valley, 1997).

MT data can directly determine the thickness of the lithosphere by identifying the lithosphere-asthenosphere boundary (LAB), which is associated with a decrease in electrical resistivity. The lithospheric mantle typically has a resistivity 10^2–10^4 Ωm (Xu et al., 2000), and two factors cause a decrease in electrical resistivity with increasing temperature. The first occurs below the melting point as thermal activation allows electrons and ions to move more easily through the mineral lattice. The second factor occurs as partial melting begins and permits ions to easily move through the melt and allow electric current to flow. Most crustal and upper mantle rocks form partial melts with the melt well interconnected at low melt fractions owing to a low dihedral (wetting) angle. Laboratory experiments by Schilling et al., (1997) and Partzsch et al., (2000) showed that 2% partial melting occurs in typical mantle rocks at 1030° C and that the resistivity of the molten rock at melt fractions above 3% is almost independent of the resistivity of the solid phase (Partzsch et al., 2000).

In this thesis, the first long-period magnetotelluric data collected in eastern Anatolia are presented. In eastern Anatolia, Arabia-Eurasia continental convergence is occurring. MT data were collected between 38.5° E and 43° E longitudes and 37° N and 41.5° N latitudes

in 2005. The goal is to determine the geodynamic processes at work in eastern Anatolia and to provide new insights on the initial stages of continental convergence.

The theoretical concepts and practical application steps of the MT method are described in chapter 2. Terminology and data processing steps are also introduced in this chapter.

The location and geological setting of the study area are described in detail in chapter 3. Previous geological and geophysical data as well as recent geological reviews and geophysical observations such as the Eastern Turkey Seismic Experiment are also included. Previously suggested geodynamic models for the ongoing continental collision in eastern Anatolia are discussed with respect to recently available geochemistry, geology, gravity, magnetic and seismic data.

The data acquisition and preliminary interpretation of the MT data are given in chapter 4. This includes, planning and data collection stages of this project, MT instrumentation, robust statistical processing of the collected time series data, dimensionality and directionality analysis and the first quantitative and qualitative interpretations of the data in terms of geoelectrical strike direction and induction vectors. Dimensional properties defined in this chapter are used to determine the robust features in the inversion models.

Two-dimensional and three-dimensional inversions were performed to quantitatively convert the observed apparent resistivity-period curves into resistivity-depth sections in chapter 5. Principles of the Nonlinear Conjugate Gradient (NLCG) 2-D inversion (Rodi and Mackie, 2001) and the WSINV3DMT (Siripunvaraporn et al., 2005b) algorithm used for 3-D inversions are discussed. The sensitivity of the MT data to various inversion model features is investigated through constrained inversions and by using a range of inversion parameters. Input data preparation and visualization of the 3-D inversion models were performed using MATLAB[1]-based programs (M3DET and S3DET) developed as part of this thesis. M3DET was generated using MATLAB's graphical user interface and it can independently generate 3-D mesh models for inversion and can be used to import

[1] MATLAB is a language of technical programming developed by Mathworks.

Winglink[2] 3-D mesh models. S3DET is used to plot 3-D inversion results and export response data into standard electronic data interchange (EDI) format for further analysis. S3DET also exports final inversion models in standard Winglink format.

Chapter 6 is devoted to detailed analysis of the MT data in the Erzincan Basin and on the North Anatolian and East Anatolian Faults. The goal is to determine the basin thickness and the geometry as well as imaging the fault zones with higher accuracy. A fault zone conductor imaged on the East Anatolian Fault is compared to the San Andreas Fault zone conductor. A quantitative estimate of the fluid content at the fault zone is also given.

The MT resistivity images obtained for eastern Anatolia are associated with the known tectonic elements and compared to available geological and geophysical data along with quantitative and qualitative interpretations in Chapter 7. The source of the lower crustal and upper mantle low resistivity zones in eastern Anatolia is evaluated. Previously suggested geodynamic models are reconsidered with respect to MT resistivity images of the deep subsurface. Results are compared to the India – Eurasia continent-continent collision zone.

Finally the major findings of this thesis are summarized and future perspective and thoughts are included in chapter 8. This thesis is completed with an appendix showing the inversion response and the observed apparent resistivity curves.

---

[2] Winglink is commercial software for multi disciplinary geophysical data processing and interpretation developed by Geosystem.

2 THEORY OF MAGNETOTELLURICS

2.1 Principles of magnetotellurics

2.1.1 Introduction to method

Magnetotellurics (MT) is a passive electromagnetic exploration method that uses temporal fluctuations of the Earth's electromagnetic (EM) field to remotely sense the electrical properties of the subsurface. These naturally occurring electromagnetic fields induce electric currents in the Earth. Measurement of time variations of the electric and magnetic fields at the surface of the Earth allow variations of electrical resistivity with depth and horizontal location to be determined. The EM signals can be classified into two groups depending on their frequency, or the reciprocal quantity, termed the period. At frequencies greater than 1 Hz, signals are generated by worldwide lightning activity. Signals at frequencies below 1 Hz are induced by the interactions between the solar wind and the Earth's magnetic field. The depth to which the EM signals propagate is inversely related to their frequency (Vozoff, 1991). The MT exploration method was independently discovered by Tikhonov (1950) and Cagniard (1953). The analysis of Cagniard (1953) assumed a planar wave in the mathematical development. Shortly thereafter, a debate occurred regarding the validity of the MT method since it was suggested that the EM waves could not be assumed planar at the Earth's surface (Wait, 1954, Price 1962). It was later shown that the plane wave assumption is valid for periods less than 10^5 s (Madden and Nelson 1964), and the MT method was established as a useful exploration method.

Since the development of MT, numerous improvements have been made and the method is now generally considered to be a reliable exploration tool. Detailed descriptions of MT can be found in textbooks devoted to electromagnetic methods in geophysics (Kaufman and Keller, 1981; Berdichevsky and Zhdavov, 1984; Vozoff, 1991; Zhdanov and Keller, 1994).

Simpson and Bahr (2005) present an introduction and overview of the MT method as well as a description of the theory and application principles.

2.1.2 Maxwell's equations

The propagation of electromagnetic fields in the atmosphere and Earth is governed by Maxwell's equations:

$$\nabla \times \mathbf{E} = -\frac{\partial \mathbf{B}}{\partial t} \tag{2.1}$$

$$\nabla \times \mathbf{H} = \mathbf{J} + \frac{\partial \mathbf{D}}{\partial t} \tag{2.2}$$

$$\nabla \cdot \mathbf{B} = 0 \tag{2.3}$$

$$\nabla \cdot \mathbf{D} = \eta_f \tag{2.4}$$

where **E** is the electric field (in V/m), **B** is the magnetic flux density (in T), **H** is the magnetic intensity (in A/m), **D** is the electric displacement (in C/m^2), $\mathbf{J}$ is the conduction current density (in A/m^2) and η_f is the density of free electric charges (in C/m^3) . Note that eq. 2.1 is a statement of Faraday's Law and eq. 2.2 is a statement of Ampère's Law. For a linear isotropic material three constitutive relationships are defined as:

$$\mathbf{B} = \mu \mathbf{H} \tag{2.5}$$

$$\mathbf{D} = \varepsilon \mathbf{E} \tag{2.6}$$

$$\mathbf{J} = \sigma \mathbf{E} \tag{2.7}$$

where ε is the electric permittivity and μ is the magnetic permeability of the medium. According to Ohm's Law, electric current density **J** can be defined by eq. 2.7, where σ is the electrical conductivity (in S/m) which is the inverse of the resistivity ρ (in Ωm).

Faraday's Law (eq. 2.1), defines that the induced electric field (**E**) is proportional to the rate of change of the magnetic flux in a closed loop. For example moving a conductor through a magnetic field produces a voltage that is proportional to the speed of movement. Similarly, Ampere's Law (eq. 2.2) states that a magnetic field is produced around any closed loop of electric current. The magnitude of the magnetic field is directly proportional to the total current flow.

$$\nabla \times \mathbf{H} = \mathbf{J} + \varepsilon \frac{\partial \mathbf{E}}{\partial t}. \tag{2.8}$$

Using eq. 2.7 and assuming that there are no free charges in the Earth, eq. 2.4 can be simplified to:

$$\nabla \cdot \mathbf{E} = 0. \tag{2.9}$$

Taking the curl of the eq. 2.1,

$$\nabla \times \left(\nabla \times \mathbf{E}\right) = -\nabla \times \left(\frac{\partial \mathbf{B}}{\partial t}\right). \tag{2.10}$$

The vector identity (eq. 2.11)

$$\nabla \times (\nabla \times \mathbf{E}) = \nabla \cdot (\nabla \cdot \mathbf{E}) - \nabla^2 \mathbf{E} \tag{2.11}$$

can be used to show that

$$\nabla \cdot \left(\nabla \cdot \mathbf{E}\right) - \nabla^2 \mathbf{E} = -\nabla \times \left(\frac{\partial \mathbf{B}}{\partial t}\right). \tag{2.12}$$

Assuming that $\nabla \cdot \mathbf{E} = 0$ then it can be shown that

$$\nabla^2 \mathbf{E} = \mu_0 \sigma \frac{\partial \mathbf{E}}{\partial t} + \mu_o \varepsilon \frac{\partial^2 \mathbf{E}}{\partial^2 t}. \tag{2.13}$$

If the EM fields are assumed to have harmonic time dependence ($e^{-i\omega t}$) with frequency ω then in the air where σ = 0, eq. 2.13 can be rewritten as:

$$\nabla^2 \mathbf{E} + \omega^2 \mu_0 \varepsilon \mathbf{E} = 0 \,. \tag{2.14}$$

Thus in the air the EM signals travel as a wave, since the conduction current can be ignored due to the extremely high electrical resistivity of the air (~$10^9\,\Omega$m) compared to ground resistivity (10^{-1}-10^5 Ωm). Due to a large contrast in resistivity at the Earth-air interface, most of the incident EM wave is reflected at the surface. Only a small fraction of the signal penetrates into the relatively conductive Earth where the EM fields travel by diffusion, not as a wave. At frequencies lower than 100 kHz, displacement currents can be neglected as they will be very small compared to the conduction currents ($\omega^2 \mu_0 \varepsilon << \omega \mu_0 \sigma$). Therefore, EM signal propagation in the Earth can be considered a diffusion process. Further, variations in the electric permittivity and magnetic permeability of rocks are negligible compared to variations in electrical resistivity (Zhdanov and Keller, 1994). Therefore, free space values of ε and μ are assumed to be constant within the earth ($\varepsilon = \varepsilon_0 = 8.85\,x10^{-12}$ F/m and $\mu = \mu_0 = 1.2566\,x10^{-6}$ H/m). Thus it can be shown that the electric field in the Earth is given by a diffusion equation:

$$\nabla^2 \mathbf{E} = i\omega \mu_0 \sigma \mathbf{E} \,. \tag{2.15}$$

It can also be shown that the magnetic field satisfies a similar diffusion equation:

$$\nabla^2 \mathbf{B} = i\omega \mu_0 \sigma \mathbf{B} \,. \tag{2.16}$$

Eqs. 2.15 and 2.16 are termed the Helmholtz equations and describe quasi-stationary electromagnetic diffusion in terms of electric and magnetic fields, respectively.

2.1.3 Penetration depth and impedance

Consider a plane EM wave that propagates vertically with wavefronts parallel to the Earth's surface. The plane wave has an angular frequency ω and penetrates a homogeneous isotropic planar Earth of finite electrical conductivity σ and magnetic permeability, μ . The angular frequency is defined as $\omega = 2\pi f$, where f is the frequency in Hertz. The electric field is polarized in the x direction and the magnetic field is polarized

in the *y* direction (Figure 2-1). Since it is a plane wave, the derivatives of E_x with respect *x* and *y* will be zero and eq. 2.15 simplifies to:

$$\frac{\partial^2 E_x(z)}{\partial z^2} + i\omega\mu\sigma E_x(z) = 0\,. \tag{2.17}$$

A general solution to eq. 2.15 can be found of the form:

$$E = Ae^{kz}\,. \tag{2.18}$$

Substituting into 2.17 gives

$$Ak^2 e^{kz} + i\omega\mu\sigma Ae^{kz} = 0\,. \tag{2.19}$$

Equation 2.19 is satisfied when A=0 or $k^2 = -i\omega\mu\sigma$. Using the second solution and noting that there are positive and negative square roots, the solution can be written as:

$$E_x(z) = E_1 e^{-kz} + E_2 e^{+kz}\,, \tag{2.20}$$

where E_1 and E_2 are constants and *k* is the wave number. The first boundary condition requires that $E_x(z)$must remain bounded as *z* tends to infinity, which requires that $E_2 = 0.$

Eq. 2.20 can be written as:

$$E_x(z) = E_1 e^{-kz} \tag{2.21}$$

$$E_x(z) = E_1 e^{-(1-i)\sqrt{\frac{\omega\mu\sigma}{2}}z}\,. \tag{2.22}$$

A second boundary condition must be imposed that the value of $E_x(z=0)$ is defined as E_1. The penetration depth in MT is defined as the depth at which the amplitude of the

wave is reduced to e^{-1} of its amplitude at the surface of the Earth. Therefore, from the magnitude of eq. 2.22, the MT skin depth δ can be defined as:

$$\delta = \sqrt{\frac{2}{\omega \mu_0 \sigma}} . \tag{2.23}$$

A more practical expression of the skin depth is:

$$\delta \approx 503\sqrt{\rho T} \text{ (in m)}, \tag{2.24}$$

where *T* is the period of the wave. The inverse of eq. 2.23 is referred to as the Schmucker – Weidelt transfer function (*C*) (Weidelt, 1972; Schmucker, 1973).

$$C = \frac{1}{k} \tag{2.25}$$

Using eq. 2.1 and 2.22 we can derive the following equations:

$$\frac{\partial E_x}{\partial z} = -kE_x \tag{2.26}$$

,

$$\frac{\partial B_y}{\partial t} = -i\omega B_y = -kE_x . \tag{2.27}$$

Therefore, the transfer function can be defined from the observed orthogonal electric and magnetic field components (E_x and B_y) at a given angular frequency ω as:

$$C = \frac{1}{k} = -\frac{E_x}{i\omega B_y} . \tag{2.28}$$

Using eq. 2.28 and the definition of *k*, the resistivity of a homogenous half-space becomes:

$$\rho = \frac{1}{\sigma} = \frac{1}{|k|^2}\mu_0\omega = |C|^2 \mu_0 \omega . \tag{2.29}$$

The frequency domain ratio of orthogonal electric and magnetic fields is commonly called the *electromagnetic impedance (Z)*:

$$Z = \frac{E_x}{H_y}. \tag{2.30}$$

The impedance is also referred to as a transfer function, since it relates the observed electric and magnetic fields to the resistivity of the Earth. Note that ω and μ_0 are independent of the resistivity of the medium. Combining eqs. 2.28, 2.29 and 2.30, the resistivity of a homogenous and isotropic medium can be calculated from observed electric and magnetic fields as:

$$\rho = \frac{1}{\mu_0 \omega}\left|Z\right|^2 = \frac{T}{5}\left|\frac{E_x}{B_y}\right|^2, \tag{2.31}$$

where ρ is the resistivity of the medium in Ωm . Note that *Z* is a complex number and its argument defines the phase difference between the electric and magnetic fields:

$$\phi = \arg(Z). \tag{2.32}$$

For a homogenous isotropic half-space, the real and imaginary components of *Z* have equal magnitude; therefore, the phase is 45°.

2.1.4 Apparent resistivity over a multilayered Earth

Apparent resistivity is a widely used parameter in MT exploration and represents the volume average of resistivity in a heterogeneous Earth. The initial interpretation of MT data often considers the variation of apparent resistivity with frequency. Note that a decrease in the frequency of an EM signal causes an increase in the penetration depth. Thus, a plot of apparent resistivity as a function of frequency gives a qualitative impression of how the true resistivity varies with depth. MT data analysis seeks a quantitative method to convert frequency domain apparent resistivity data into true resistivity as a function of

depth (and horizontal position) using an automated inversion scheme. More details on the inversion of MT data are given in chapter 5.

In the previous section, it was shown how the resistivity of a homogeneous half-space can be determined from observations of surface electric and magnetic fields. However, the resistivity structure of the Earth is rarely so simple and a more general case must be considered to include variations with depth.

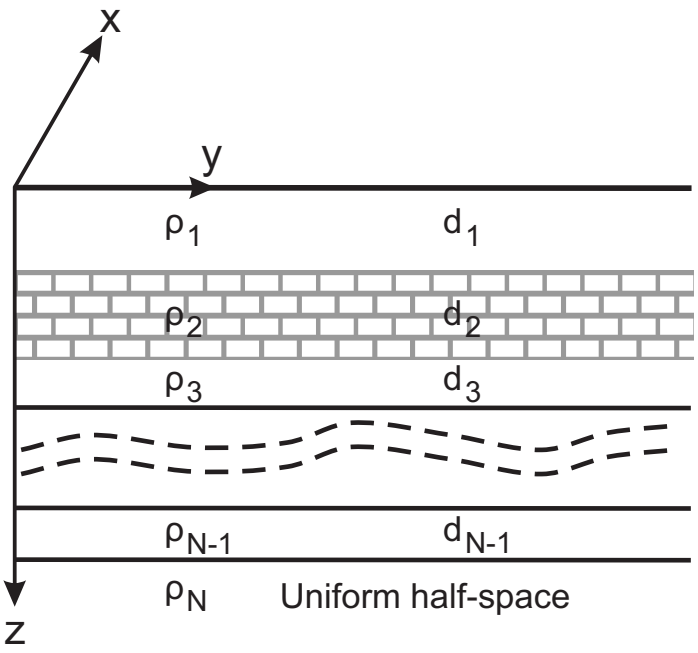

Figure 2-1. An N-layered Earth resistivity model.

The transfer function $C(\omega)$ for a uniform, stratified Earth can recursively be calculated from the top of the lowermost layer to the surface using Wait's recursion formula (Wait 1954, 1970) as:

$$C_n(z_{n-1}) = \frac{1}{k_n} \frac{k_n C_{n+1}(z_n) + \tanh(k_n d_n)}{1 + k_n C_{n+1}(z_n) \tanh(k_n d_n)} \tag{2.33}$$

where,

$$C_N = \frac{1}{k_N} \tag{2.34}$$

and

$$k_n = (1-i)\sqrt{\frac{\omega\mu_0\sigma_n}{2}}\,. \tag{2.35}$$

The transfer function for a homogenous half-space is given by eq. 2.31. According to Wait's recursion formula (eq. 2.34), the transfer function of the n^{th} layer is calculated using the transfer function of the n+1th layer. Therefore, eq. 2.33 is recursively solved starting from the lowermost layer, which is a homogeneous half-space.

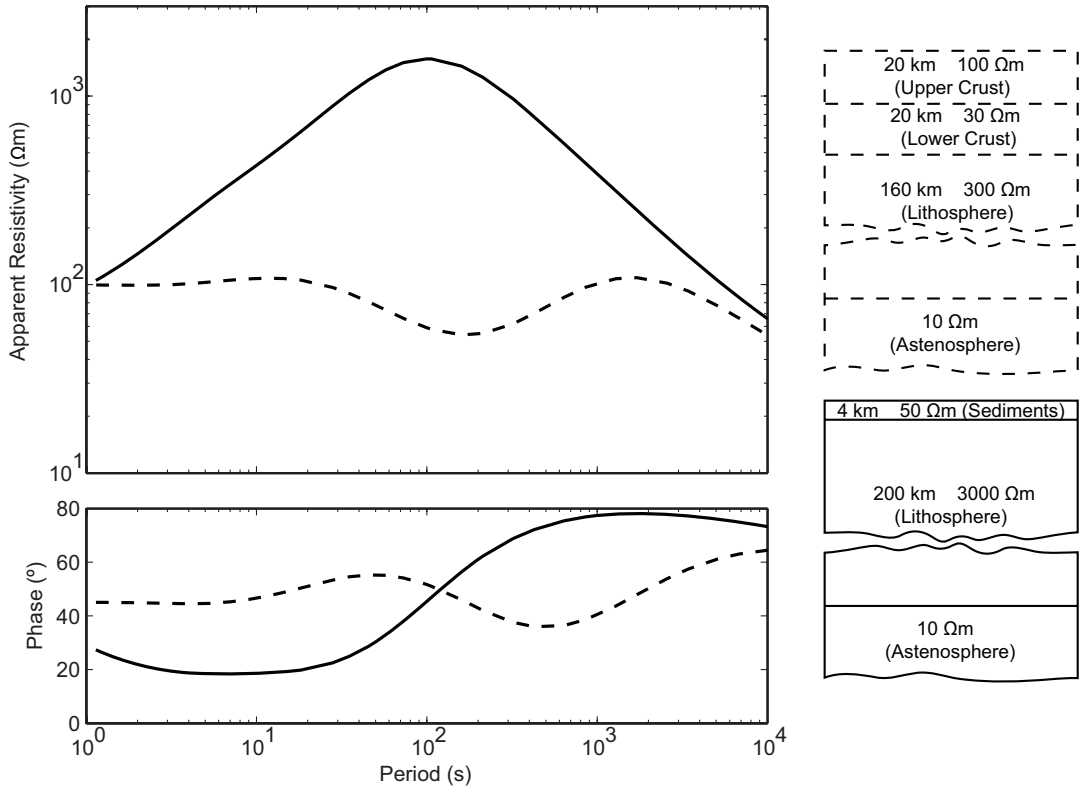

Figure 2-2. Synthetic one dimensional curves for typical stable continental regions (solid) and tectonically active regions (dashed). The model resistivities used for stable continental regions are from Boerner et al. (2000) and Türkoğlu et al. (2009), and for active regions from this study.

Eq. 2.31 yields the true resistivity of a homogeneous half-space. In contrast, the recursively calculated transfer functions in eq. 2.33 include resistivity variations across interfaces. Thus, the calculated apparent resistivity represents an average value of an equivalent

homogenous half-space. In this case, the resistivity ρ in eq. 2.31 is replaced by the apparent resistivity ρ_a (eq. 2.36).

$$\rho_a(\omega) = \frac{T}{5}\left|\frac{E_x(\omega)}{B_y(\omega)}\right|^2 . \tag{2.36}$$

Figure 2-2 shows synthetic apparent resistivity curves produced for typical stable and active tectonic settings. As the period increases the deeper parts of the subsurface are sampled. If the resistivity is constant with respect to depth the apparent resistivity is constant with respect to period and the phase remains at 45° (dashed curve in Figure 2-2). The phase is less than 45° if resistivity increases with depth and is greater than 45° if resistivity decreases with depth. Thus the phase is more sensitive to changes in resistivity with depth than the apparent resistivity.

2.1.5 Magnetotellurics over a 2-D resistivity model

A 1-D resistivity model is a useful approximation that allows the MT method to be understood (Figure 2-2). However, this type of 1-D analysis is rarely applicable to actual MT data because the Earth's subsurface rarely consists of horizontally layered strata. Therefore, it is necessary to consider EM signal propagation in a two-dimensional Earth.

Maxwell's equations have six components (E_x, E_y, E_z, B_x, B_y and B_z) and in general, a full solution is required. However, over a 2-D Earth, Maxwell's equations simplify and can be separated into the two independent subsets listed in eq. 2.37 where interactions between electric and magnetic fields are always orthogonal:

$$\left.\begin{aligned} \frac{\partial E_x}{\partial y} &= \frac{\partial B_z}{\partial t} = i\omega B_z \\ \frac{\partial E_x}{\partial z} &= \frac{\partial B_y}{\partial t} = -i\omega B_y \\ \frac{\partial B_x}{\partial y} - \frac{\partial B_y}{\partial z} &= \mu\sigma E_x \end{aligned}\right\}\text{TE Mode} \qquad \left.\begin{aligned} \frac{\partial B_x}{\partial y} &= \mu_0\sigma E_z \\ -\frac{\partial B_x}{\partial z} &= \mu_0\sigma E_y \\ \frac{\partial E_z}{\partial y} - \frac{\partial E_y}{\partial z} &= i\omega B_x \end{aligned}\right\}\text{TM Mode} \tag{2.37}$$

These sets of equations are referred to as the *Transverse Electric* (TE) and *Transverse Magnetic* (TM) modes (Figure 2-3).

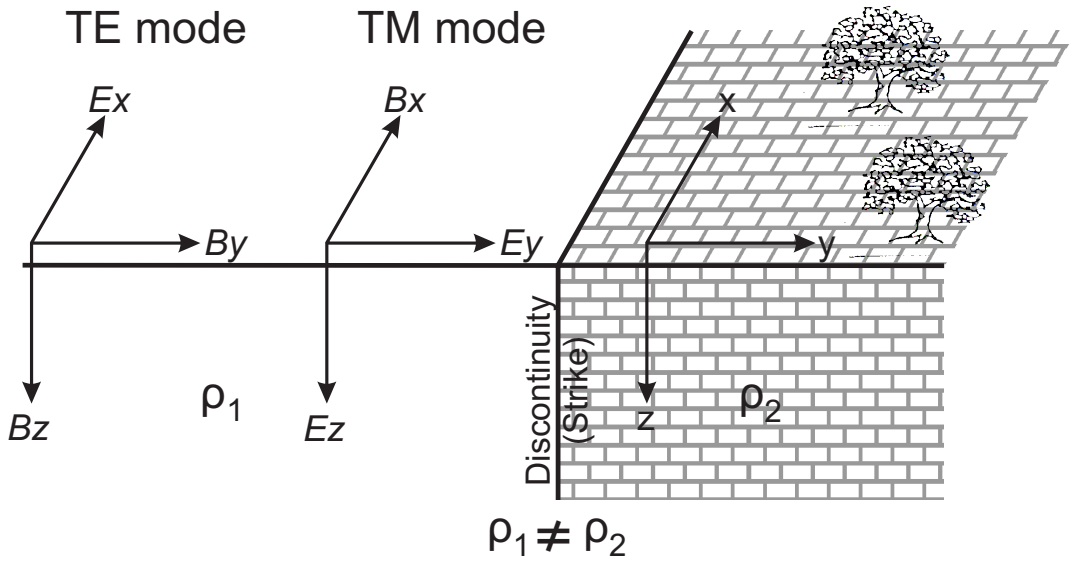

Figure 2-3. Basic 2-D resistivity model consisting of two quarter-spaces. The structure is invariant along strike (x-direction) and the EM fields can be decomposed into two modes. (1) the electric field parallel to strike induces magnetic fields perpendicular to strike and in the vertical plane (TE mode). (2) magnetic fields parallel to the strike only induce electric fields perpendicular to strike and in the vertical plane (TM mode). TE and TM stands for *Transverse Electric* and *Transverse Magnetic,* respectively.

Conservation of electric charge requires electric currents be continuous normal to a boundary. In the quarter-space model in Figure 2-3, conservation of current density across the vertical boundary is required and gives:

$$j_y = \frac{E_y}{\rho} \tag{2.38}$$

Thus, from Ohm's Law, a discontinuity in resistivity causes a discontinuity in E_y which leads to a discontinuous TM mode apparent resistivity (Figure 2-4). This boundary effect gives the TM mode more sensitivity to lateral resistivity changes than the TE mode. However, the TE mode has an associated vertical magnetic field which gives enhanced sensitivity to conductive features in the subsurface. Figure 2-4 shows the synthetic MT responses for a simple 2-D model. Note that the TE mode curves vary smoothly across the

boundary while the TM mode curves are discontinuous. Furthermore, the TE mode apparent resistivity curves are more sensitive to the conductive part of the model.

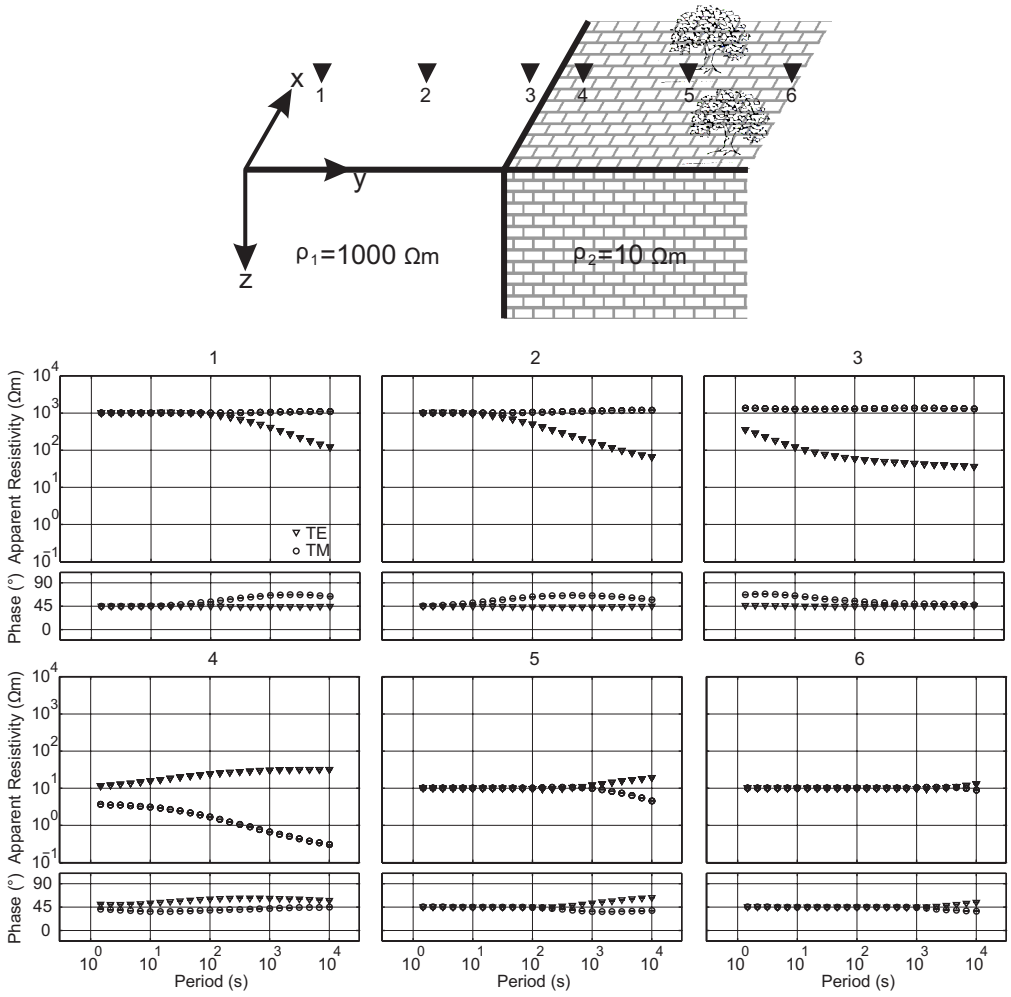

Figure 2-4. MT responses of the TE and TM modes for a quarter-space model. The TE mode apparent resistivity curves gradually increase from site to site towards the resistive space. The TM mode resistivity curves significantly change across the boundary.

2.1.6 Induction vectors

The magnetotelluric method uses the relationship of the horizontal, mutually orthogonal electric and magnetic fields to image subsurface resistivity. The ratio of the orthogonal electric and magnetic field components is called the impedance. In a two-dimensional Earth model, non-zero vertical magnetic fields are generated in the TE mode. In the simple

example shown in Figure 2-5, these vertical magnetic fields reverse direction above a conductor and are thus sensitive to horizontal changes in resistivity structure. The concept of magnetic transfer functions (also called induction vectors) was independently discovered by Parkinson (1962) and Wiese (1962) and is expressed as follows:

$$B_z(\omega) = T_{zx}(\omega)B_x + T_{zy}(\omega)B_y(\omega), \tag{2.39}$$

where T_{zx} and T_{zy} are the complex magnetic transfer functions that relate the vertical and horizontal magnetic fields.

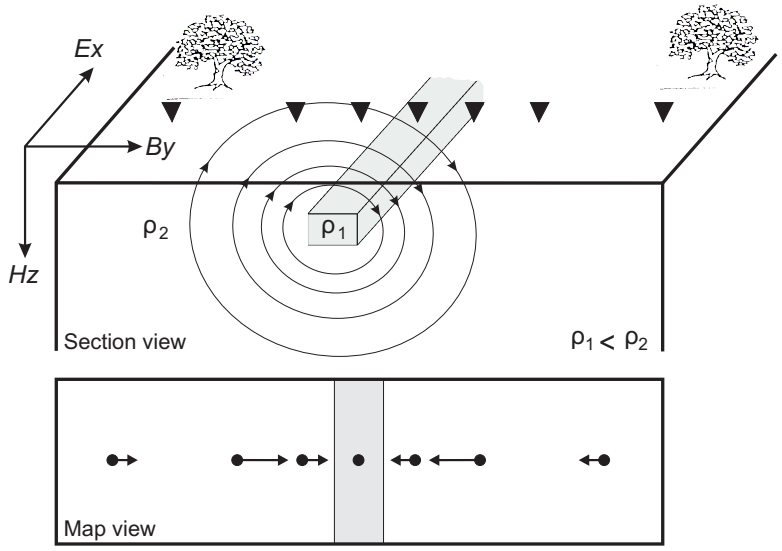

Figure 2-5. Behavior of induction vectors over a 2-D resistivity model. The amplitude of the induction vectors are zero directly above the conductor. As the distance away from the conductor increases, the amplitude of the vectors initially increases, then tends to zero at distances larger than the skin depth of the EM signal.

Induction vectors are a useful way of graphically displaying the magnetic transfer functions on a map. As the vertical magnetic fields are produced by lateral resistivity changes, the induction vectors can be used to delineate zones of high conductivity. The amplitude of the real and imaginary parts of the induction vector $A_{R,I}$ and direction of the vector $\phi_{R,I}$ are given by:

$$A_{R,I} = \sqrt{\mathrm{Re,Im}(T_{zx})^2 + \mathrm{Re,Im}(T_{zy})^2}, \tag{2.40}$$

$$\phi_{R,I} = \arctan \frac{\text{Re, Im}(T_{zy})}{\text{Re, Im}(T_{zx})}. \tag{2.41}$$

An important characteristic of the induction vectors is that they are independent of the electromagnetic impedances derived from the electric and magnetic field measurements. Thus, they carry independent information on the geoelectric structure of the subsurface. This is important because they are not affected by small shallow inhomogeneities (galvanic distortions). The real part of the induction vectors point to conductive features in the Parkinson convention and their magnitude is proportional to the intensities of the anomalous current concentrations (Jones and Price, 1970). For a 2-D isotropic medium, the real and imaginary components of the induction vectors are either parallel or anti-parallel to each other and orthogonal to the geoelectric strike direction.

2.2 Impedance tensor and spatial dimensionality

In the general case, the horizontal electric and magnetic field components (E_x, E_y, B_x and B_y) can be related to one another through the impedance tensor. In the frequency domain, the impedance tensor **Z** is defined as:

$$\mathbf{E}(\omega) = \mathbf{Z}(\omega)\mathbf{B}(\omega). \tag{2.42}$$

In Cartesian coordinates, where x denotes magnetic north and y magnetic east, this tensor can be written using matrix notation as:

$$\begin{pmatrix} E_x \\ E_y \end{pmatrix} = \begin{pmatrix} Z_{xx} & Z_{xy} \\ Z_{yx} & Z_{yy} \end{pmatrix} \begin{pmatrix} B_x \\ B_y \end{pmatrix}. \tag{2.43}$$

The impedance tensor **Z** contains information about the geoelectric dimensionality and directionality of the subsurface.

2.2.1 Impedance tensor for a 1-D Earth

In the 1-D case, electrical resistivity varies only with depth. Thus the measured impedance will not depend on the azimuth of the MT measurements and the vertical magnetic fields will be zero. Maxwell's equations show that a changing magnetic field induces an orthogonal electric field. Thus it is required that the diagonal components of the impedance tensor in eq. 2.42 are zero and eq. 2.43 can be written as:

$$\begin{pmatrix} E_x \\ E_y \end{pmatrix} = \begin{pmatrix} 0 & Z_{xy} \\ -Z_{xy} & 0 \end{pmatrix} \begin{pmatrix} B_x \\ B_y \end{pmatrix} \tag{2.44}$$

Note that the off-diagonal components are equal in magnitude, but have opposite sign.

2.2.2 Impedance tensor for a 2-D Earth

In the 2-D case, electrical resistivity varies in only one horizontal direction (y) and with depth (Figure 2-6). In general the measured impedance tensor will vary with the azimuth of the electric and magnetic field measurements (Simpson and Bahr, 2005).

If the measurement direction is aligned with the geoelectric strike, the diagonal components of the impedance tensor will be zero and the tensor becomes:

$$\mathbf{Z} = \begin{pmatrix} 0 & Z_{TE} \\ Z_{TM} & 0 \end{pmatrix} \tag{2.45}$$

where Z_{TE} and Z_{TM} are the impedances for the TE and TM modes, respectively. These MT impedances are not equal, and yield different values of apparent resistivity and phase for each mode. It rarely occurs that MT instruments are exactly aligned with the geoelectric strike, since this is not known prior to the survey (Figure 2-6). Therefore, the measured impedance tensor will generally have four non-zero components.

The observed impedance tensor $\mathbf{Z}$ is usually rotated mathematically to a defined geoelectric strike direction (α) using the rotation matrix R_α. The rotated impedance tensor $\mathbf{Z}'$ in the rotated coordinate frame (x', y' and z) can be written as:

$$\mathbf{Z}'(\omega) = R_\alpha \mathbf{Z}(\omega) R_\alpha^T, \tag{2.46}$$

where

$$R_\alpha = \begin{pmatrix} \cos\alpha & \sin\alpha \\ -\sin\alpha & \cos\alpha \end{pmatrix} \tag{2.47}$$

is the rotation matrix. Note that the superscript *T* denotes the transpose of the matrix.

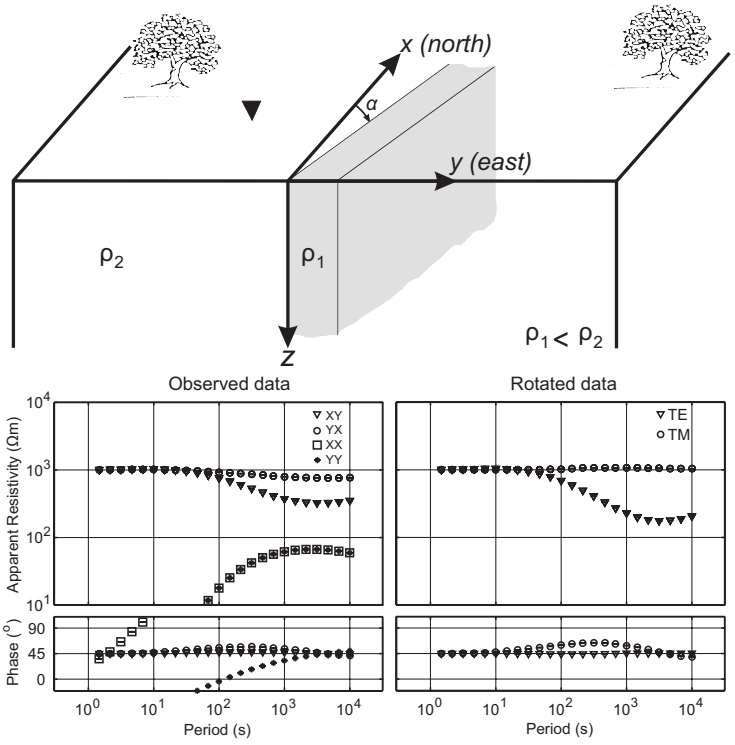

Figure 2-6. Simple 2-D Earth model composed of an infinitely long conductive dike with a geoelectric strike angle (α =30º) from magnetic north. The lower panels show synthetic MT data that would be observed at the measurement location (black triangle). MT data are shown in field coordinates (left) and after rotation to the geoelectric strike direction (right). The off-diagonal components (XY and YX) are labeled as TE and TM modes in the right panel.

It can be seen that determination of the geoelectric strike angle α is important. This angle can be determined from the impedance tensor using the methods described in section 2.3. However, it should be noted that the geoelectric strike direction obtained from the MT impedance tensor contains a 90° ambiguity, since rotation through 90° only changes the location of the principal impedances within the tensor. Therefore, correct determination of the TE and TM modes can only be made after defining the geoelectric strike direction.

2.2.3 Impedance tensor for a 3-D Earth

Real MT data are never exactly 2-D. Even if a well constrained strike direction is computed, rotation of the impedance tensor can result in non-zero diagonal elements. Deviation from ideal 2-D behavior occurs when the subsurface is 3-D, or when the MT data are distorted by near surface structure or contain noise. For a 3-D Earth, the conductivity can vary in three directions and there is no single rotation angle that will reduce the diagonal elements of the impedance tensor to zero.

2.3 Geoelectric strike and distortions

Determination of the geoelectric strike direction and dimensionality is an important step in MT data analysis because the choice of modeling strategy is based on the dimensionality. 1-D and 2-D inversions are widely available and relatively simple to apply to MT data. However, full 3-D MT data analysis is computationally challenging and few forward and inverse algorithms are publicly available. Therefore, the conventional strategy for MT data interpretation relies heavily on 2-D inversions. In this situation, dimensionality analysis is used to measure the validity of 2-D resistivity models obtained by inversion. It can be shown that the inversion of 3-D MT data with a 2-D algorithm can be acceptable in some cases where the bulk of the MT data are 2-D (Wannamaker, 1999; Park and Mackie 2000; Ledo, 2005).

2.3.1 Galvanic distortion

The measured MT impedance depends on subsurface structures with a range of spatial scales. Low frequency (long-period) MT data sample regional structures and are generated

by EM induction within the Earth. However, very small-scale[3] structures can influence the impedances through non-inductive (galvanic) effects. The directionality and dimensionality of MT data reflect both these effects. Inductive distortions are frequency dependant and can be classified as a complex tensor having amplitude and phase. In contrast, non-inductive distortions, commonly termed galvanic effects, can be described by a real distortion tensor and only affect the magnitude of the MT impedance data (Bahr, 1988; Jiracek, 1990; Chave and Smith, 1994; Smith, 1997; McNeice and Jones, 2001). Galvanic effects occur when there are multi-dimensional heterogeneities close to the Earth's surface with dimensions and depths much less than the skin depth of the electromagnetic waves. For galvanic effects, the amplitude change in the resulting apparent resistivity is frequency (period) independent. Therefore, a shift of the apparent resistivity curve occurs over the whole period range. The shape of the curve and the phase curve remains unchanged. This shift is known as a static shift and is most pronounced in resistive environments where small-scale conductivity anomalies have large effects on the electric fields.

Static shifts need to be accounted for, or corrected, because the un-shifted apparent resistivity curves can produce un-realistic resistivity models in MT inversion (Simpson and Bahr, 2005). Various methods of removing static shifts have been suggested in recent years and are discussed below. Spatial filtering using closely spaced MT stations was proposed as a method to correct for static shifts. However, this approach requires collection of additional MT data beyond that required for target exploration, significantly increasing the survey cost (Torres-Verdin and Bostick, 1992). For shallow MT exploration studies, time domain electromagnetic (TEM) or direct current resistivity (DC) measurements are one of the most practical ways to correct the static shifts. However, this approach requires the acquisition of extra data (Stenberg et al., 1988; Simpson and Warner, 1998; Yılmaz and Özel, 2008). Magnetic transfer functions are not affected by galvanic distortion and can be used to estimate the regional 2-D resistivity distribution of the Earth (Utada and Munekane, 2000). For long-period MT data ($T > 10^4$ s), apparent resistivity curves can be shifted to match global apparent resistivity values computed from geomagnetic observatory

[3] Small-scale is a relative term that indicates that the body is smaller than the penetration depth of the electromagnetic fields.

data with the assumption that a sharp resistivity decrease occurs at the mid-mantle transition zone (Simpson, 2002). However this method is rarely practical due to the requirements of very long period MT data. An alternative method involves simultaneous inversion of model resistivities and static shift coefficients in an iterative inversion scheme (de Groot-Hedlin, 1991; Rodi and Mackie, 2001; Ogawa and Uchida, 1993). In this method, determination of smoothing parameters and limits on the variations of the static shifts at each iteration are important. These parameters can be adjusted to achieve the best results for a given dataset. All static shift corrections in this thesis have been estimated using an iterative correction scheme.

2.3.2 Swift's dimensionality parameters

Dimensionality and directional information can be extracted from the impedance tensor using several methods. For noise free MT data observed on a perfectly 2-D subsurface, the diagonal components of the impedance tensor ($\mathbf{Z}'$) in eq. 2.43 are zero when rotated to the regional strike angle. In real data, deviations from the ideal 2-D situation requires a search for the best strike angle that minimizes the diagonal elements (Z_{xx} and Z_{yy}), or maximizes the off-diagonal (Z_{xy} and Z_{yx}) elements of the impedance tensor (Swift, 1967). This angle is called the Swift strike, α_S. Minimizing the diagonal components or maximizing the off-diagonal components of the impedance tensor does not always give the same regional strike angle. Therefore, a measure of how accurately the MT impedance tensor satisfies the Swift criteria is required. This quantity is known as the Swift skew $\kappa = (Z_{xx} + Z_{yy})/(Z_{xy} - Z_{yx})$ and a value less than 0.3 can indicate 2-D behavior (Swift, 1967). However, this criterion can provide misleading results when the impedance tensor is distorted or contains high levels of noise.

2.3.3 Bahr's dimensionality parameters

Bahr (1991) suggested a new method of deriving the regional geoelectric strike direction from MT data and proposed three rotationally invariant parameters to classify the dimensionality and distortion. The Bahr model assumes that the measured impedance tensor is the product of small 3-D inhomogeneities over a 1-D or 2-D regional Earth

structure. Therefore, the goal is to determine the geoelectric strike direction of the regional structure free of disturbances from the 3-D inhomogeneities. The regional geoelectric strike found using the Bahr model is referred to as the phase sensitive strike α_B. Analogous to the Swift approach, the Bahr model makes use of several quantities to characterize the dimensionality. η is the phase sensitive skew, μ is a normalized measure of the phase difference between components of the impedance tensor and Σ is a measure of departures from one dimensionality and can exceed 1 in the presence of galvanic distortion. A threshold value of η >0.3 is considered a strong indication of 3-D data. However, the opposite is not true; η <0.3 does not necessarily imply 2-D. Therefore, other information such as the variation of induction vectors and regional strike angles along the profile and in frequency should be inspected (Bahr, 1988 and 1991; Simpson and Bahr, 2005).

2.3.4 Groom-Bailey decomposition

The main goals of dimensionality and directional analysis are to find a regional 2-D geoelectric strike direction and ultimately recover the undistorted regional impedance tensor. A range of different decomposition techniques have been proposed (Groom and Bailey, 1989; Chave and Smith 1994). These decomposition methods assume the regional geoelectric structure is 2-D after the removal of galvanic distortions caused by small-scale, near-surface heterogeneities. The basic model for the decomposition method can be mathematically expressed as:

$$\mathbf{Z}_{observed} = \mathbf{RCZ}_{2D}\mathbf{R}^T \tag{2.48}$$

where $\mathbf{Z}_{2D}$ is the regional 2-D impedance tensor and $\mathbf{C}$ is a 2x2 telluric distortion tensor. Groom and Bailey (1989) proposed a tensor decomposition method (GB decomposition) based on the parameterization of the telluric distortion tensor as a product of four effects as follows:

$$\mathbf{C} = g\mathbf{TSA} \tag{2.49}$$

where g is a real scale factor named site gain and **T**, **S** and **A** represent the real twist, shear and anisotropy matrices, respectively. Not all components of **C** can be determined. While it

can be shown that the twist and shear matrices can be determined, the site gain and anisotropy terms cannot. The site gain and anisotropy terms influence the impedance amplitudes and can be considered part of the static shifts (Jones, 1988). Thus, g and **A** have no effect on the determination of the geoelectric strike angle. McNeice and Jones (2001) extended Groom-Bailey decomposition to consider multiple sites and frequencies in a single calculation. This method uses a statistical approach to iteratively determine the optimal geoelectric strike direction over a range of periods and/or stations.

Tensor decomposition methods can be applied as hypothesis tests of the preferred 2-D regional geoelectric subsurface in addition to removing effects caused by near surface inhomogeneities. If the subsurface is 2-D, after decomposition the r.m.s misfit between the observed and calculated impedance tensor should be small. If using single site decomposition, small r.m.s misfit values may be obtained at the expense of different strike angles computed for each period, which invalidates assumptions made in section 2.2.2.

2.4 Modeling magnetotelluric data

Modeling is the final step of MT data analysis. A model of the subsurface resistivity is sought that reproduces the observed MT data to within a given statistical tolerance. Modeling of MT data can use trial-and-error forward modeling or an automated inversion scheme.

Many forward modeling algorithms use finite element and finite difference numerical solutions for an isotropic conductivity model in 1-D, 2-D or 3-D (Wannamaker et al., 1987; Mackie et al., 1993). Pek and Verner (1997) have developed a 2-D finite difference code for modeling electrically anisotropic media.

Inversion methods generally use a linearization of the problem around a starting model and iteratively update the model based on defined parameters (e.g. smoothing, number of layers, scale factors). A fundamental concern arising from the inversion of any sparsely sampled dataset is that of non-uniqueness. In MT, this problem was illustrated by Parker (1980) who showed that the lowest possible r.m.s. misfit (best fit) for a 1-D MT dataset could be achieved with a model that comprised a series of infinitesimally thin sheets of

finite conductance (delta functions) embedded in a perfectly insulating half-space. Clearly such a model is physically unrealistic. Practical, regularized inversion schemes for MT data are widely used and designed to constrain both model roughness and the fit to the observed MT data (Tikhonov and Arsenin, 1977; Constable et al., 1987; Siripunvaraporn and Egbert, 2000; Rodi and Mackie, 2001). Early 1-D MT inversion algorithms were based on linearized inversion for a limited number of layers (Jupp and Vozoff, 1975; Constable et al., 1987; Smith and Booker, 1991; Parker and Booker, 1996). It is now clear that 1-D interpretation of MT data is rarely applicable and 2-D MT inversion has become the standard approach. The most commonly used algorithms for the solution of the inverse problem use non-linear least squares methods beginning from a starting model with subsequent iterations required to be spatially smooth (de Groot-Hedlin and Constable 1990; Uchida, 1993). Approximate methods for faster solutions were proposed by Smith and Booker (1991) and Oldenburg et al. (1993). Siripunvaraporn and Egbert (2000) used a data-space direct minimization of a regularized penalty function. Rodi and Mackie (2001) developed a widely used inversion scheme that uses conjugate gradients to compute model updates.

A number of 3-D inversion algorithms have been developed for MT data (Mackie and Madden, 1993; Zhdanov and Hursan, 2000; Newman and Alumbaugh, 1997; Sasaki, 2001; Farquharson et al., 2002). These algorithms require large amounts of computer memory and time and can be difficult to use. Three-dimensional MT inversion has been used commercially for the last decade. Recently, Siripunvaraporn et al., (2005b) released a 3-D inversion algorithm to the academic community and this algorithm has been used in this thesis. This inversion code is based on a data space approach that significantly reduces the amount of computer time required compared to model space approaches.

2.4.1 Nonlinear conjugate gradients algorithm (NLCG)

The 2-D inversion code developed by Rodi and Mackie (2001) was used in this study for 2-D inversion of the magnetotelluric (impedance tensor) and vertical magnetic transfer functions (induction vectors). The MT inversion problem is non-unique (i.e. multiple models can be obtained from the same MT data depending on the inversion algorithm and the parameters used). Based on the fact that EM signals sample average values over a

volume, the final subsurface images obtained from MT data should be smooth. Therefore, a regularization parameter was introduced by Tikhonov and Arsenin (1977). There are several approaches in the literature that minimize the objective function and maintain as smooth a model as possible. The nonlinear conjugate gradients algorithm of Rodi and Mackie (2001) was used to invert MT data in this thesis. More information about inversion codes and practical aspects of MT inversion can be found in chapter 5.

2.5 Summary

The MT method allows the resistivity of the subsurface to be imaged using measurements of the electric and magnetic fields at the surface of the earth. In the following chapters, this method will be used in a study of the crustal and upper mantle structure in eastern Anatolia.

3 GEOLOGY AND TECTONICS

3.1 Introduction

The Cenozoic tectonics of Anatolia and the Eastern Mediterranean has been dominated by the closure of the Tethys Ocean and the subsequent collision of the Arabian and Eurasian plates. The final closure of the Tethys Ocean occurred around 13 Ma (Şengör et al., 2003) and led to the formation of the Iranian-East Anatolian plateau (Figure 3-1). This is the second largest orogenic plateau in the Alpine-Himalayan mountain belt and has a mean elevation of 2 km (Şengör and Kidd, 1979; Dewey et al., 1986). A number of studies of the Tibetan Plateau have taken place in the last two decades and led to an improved understanding of the process of continent-continent collision (Beaumont et al., 2001; Owens et al., 1997; Nelson et al., 1996; Tapponier et al., 2001; Unsworth et al., 2005). Understanding the formation mechanism of the Iranian-East Anatolian plateau has the potential to give a broader perspective on this topic since this collision is at an earlier stage of temporal evolution than the Tibetan Plateau.

The ongoing convergence between Arabia and Eurasia makes eastern Anatolia one of the most tectonically active regions on Earth. The neotectonic regime of Anatolia has been dominated by the continuing northward motions of the African and Arabian plates with respect to Eurasian plate. These began in the Middle to Late Miocene and resulted in the closure of the Neo-Tethys Ocean and subsequent westward extrusion of the Anatolian block along the North and East Anatolian fault zones (McKenzie, 1972; Dewey and Şengör, 1979; Şengör and Yılmaz, 1981; Jackson and McKenzie, 1984). Active underthrusting occurs along the Bitlis Suture Zone (BSZ) on the south side of the 2 km high plateau. The Anatolian block moves westward along the North Anatolian Fault (NAF) and the East Anatolian Fault (EAF) with minimal fault-normal convergence (Reilinger et

al., 2006). East of the Karlıova Triple Junction (KTJ), convergence is mainly accommodated through crustal thickening (Şengör and Yılmaz, 1981).

3.2 Active tectonics

The present day deformation of Anatolia is dominated by the convergence of the Arabian and Eurasian plates (see reviews by Barka and Reilinger, 1997 and McClusky et al., 2003). Eastern Anatolia experiences convergence over a region that extends from the Caucasus in the north to the Bitlis Suture Zone (BSZ) in the south, and the Anatolian block is forced westward. A second area of active deformation occurs in western Anatolia and the Aegean.

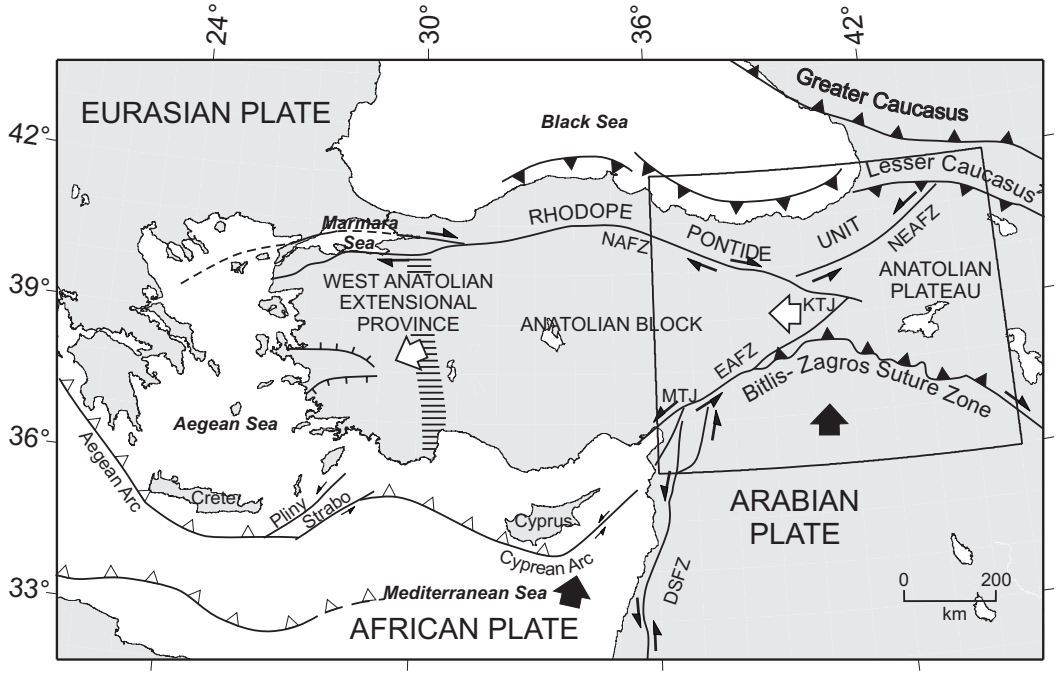

Figure 3-1. Simplified tectonic map of Turkey and surroundings (modified from Şengör et al., 1985; Barka, 1992). Rectangular box indicates the study area of this thesis. NAFZ: North Anatolian Fault Zone. NEAFZ: North East Anatolian Fault Zone. EAFZ: East Anatolian Fault Zone. DSFZ: Dead Sea Fault Zone. KTJ: Karlıova Triple Junction. MTJ: Maraş Triple Junction.

The northward subduction of the African plate beneath Western Anatolia and the Aegean Sea causes extension of the overlying continental crust. Forces generated by trench rollback and southward migration at the Aegean arc contribute to the westward motion of the Anatolian block along large-scale strike slip fault systems (Reilinger et al., 2006).

Convergence of the African/Arabian and Eurasian plates was initially accommodated by shortening and thickening of the Arabian continental margin after the Middle to Late Eocene (Hempton, 1985). This convergence regime was changed by rifting in the Red Sea in the Late Oligocene and Early Miocene (20-25 Ma). This rifting increased the northward velocity of the Arabian Plate relative to Africa and led to the first phase of motion on the Dead Sea Transform Fault (Hempton, 1987). An increase in the northward velocity of the Arabian plate compared to Africa in the Early Pliocene increased the convergence rate of the Arabian and Eurasian plates and led to the development of the North and East Anatolian faults (Bozkurt, 2001; Koçyiğit et al., 2001). The development of these fault systems provided the mechanism for the tectonic escape of the Anatolian block towards the Aegean arc (Burke and Şengör, 1986). In the model of Hempton (1987) the increase in velocity coincided with a second phase of motion on the Dead Sea Fault and the onset of sea-floor spreading in the Red Sea. However, cause and effect in this statement is unclear and could be vice versa.

3.2.1 North Anatolian Fault

The North Anatolian Fault (NAF) is a major right-lateral transform fault that accommodates motion between the Eurasian Plate and the Anatolian block (Figure 3-1). It was first recognized by Ketin (1948) and is one of the largest strike slip faults on Earth. It starts at Karlıova in Eastern Turkey and extends through the Marmara Sea to the Gulf of Saros in the Northern Aegean. The NAF is located some 100 km to the south of the Black Sea coast for a large part of its 1200 km length. GPS (Global Positioning Systems) data show that the North Anatolian Fault presently moves right-laterally at 24 ±1 mm/yr with slight compression in the easternmost segment and extension in the Marmara Sea and Northern Aegean (McClusky et al., 2003). The total offset is around 75-85 km in the east (around Erzincan and Karlıova) based on offsets of geological and drainage systems (Seymen, 1975; Westaway, 1994; Armijo et al., 1999; Bozkurt, 2001). Şengör et al. (2005) compiled all available offset data and their own observations along the NAF using geological and geomorphologic markers. These offset data revealed a gradual decrease in the cumulative offset towards the west as the fault becomes younger. The total offset is 75-85 km around Erzincan, 40 km in central Anatolia and 4 km in the Marmara Sea where the fault is youngest (200 ka) (Le Pichon et al., 2001).

Linear extrapolation of the present day GPS-derived slip rates would produce the observed 75-85 km displacement in just 3.5 Ma which is geologically unlikely because it is known that basins formed by the NAF in the east have an age of 11-13 Ma (Şengör et al., 2005). Şengör et al., (2005) computed the cumulative displacement as a function of time using the depositional ages of basins on the NAF. This showed that the slip rate increased with time from the Tortonian (~11 Ma) to the Pliocene (~2 Ma). At this time, the NAF had accumulated a total offset of 45 km. Subsequent displacement occurred at a roughly constant rate of 24 ±1 mm/yr. It should be noted that geological and geodetic estimates of fault zone velocity can give different values. Discrepancy can occur because geologic estimates average over many earthquake cycles, while geodetic measurement gives a snapshot of one point in the earthquake cycle.

The NAF has been characterized by a sequence of major earthquakes that have migrated from east to west (Egeran and Lahn, 1944; Ketin and Rösli, 1953). This sequence began with the 1939 Erzincan earthquake (Canıtez and Üçer, 1967) and these events are summarized by Şengör et al., (2005). Stein et al. (1997) modeled this earthquake sequence and showed that many earthquakes could be attributed to the increase in stress caused by the previous earthquake, including the August 17, 1999, Kocaeli earthquake (Barka, 1999). This stress modeling also predicts that the 1999 event has resulted in an increased chance of a major event on the segment of the NAF in the Marmara Sea (King et al., 2001; Parsons et al., 2000; Le Pichon et al., 2003). Historical earthquakes from the 11^{th} to 16^{th} centuries also show century-long westward migrations of earthquake sequences but the timing is poorly constrained (Şengör et al., 2005). A longer earthquake sequence with westward motion was observed between the 16^{th} and 19^{th} centuries and may have terminated in a large earthquake at the western end of the North Anatolian Fault in 1766 (Altınok et al., 2003).

Does the North Anatolian Fault extend beyond the Karlıova Triple Junction? Recent geophysical studies have defined a continuous band of seismicity east of the KTJ and extending towards Lake Van. This trend is coincident with the eastward projection of the mapped section of the NAF (Turkelli et al., 2003). This finding supports the idea of Talebian and Jackson (2002) that the NAF and the Main Recent Fault in northwestern Iran

form a nearly continuous band of right-lateral shear on the boundary of the Arabian and Eurasian plates.

At the western end of the NAF, a zone of deformation with right lateral shear continues across the northern Aegean and Greek mainland to the Hellenic subduction zone (Dewey and Şengör, 1979; McKenzie and Jackson, 1983; Le Pichon et al., 1993). Şengör et al., (2005) suggest that this western extension of the NAF should be regarded as a shear zone that narrows to the east through strain localization. It consists of shear-related basins that become younger from east to west (late Miocene age to Pleistocene).

3.2.2 East Anatolian Fault

The East Anatolian Fault (EAF) is a left-lateral transform fault that accommodates the relative motion between the Arabian Plate and the Anatolian Block (Figure 3-1). The EAF was first mentioned by Ketin (1948) who suggested that Anatolia was moving westward and this required another strike slip fault to accommodate the relative motion between Arabia and Anatolia. The presence of a fault zone between Karlıova and Hazar Lake was first reported by Allen (1969) and the fault was better defined after the 1971 Bingöl earthquake (Arpat and Şaroğlu, 1972; Seymen and Aydın, 1972; McKenzie, 1972). Arpat and Şaroğlu (1972) used air photos and topographic maps as well as the 1971 Bingöl earthquake to determine the location and extension of the EAF. McKenzie (1976) also used satellite photographs and confirmed the location and the strike direction to be 60° NE.

The East Anatolian Fault starts at the Maraş triple junction where it intersects with the Dead Sea Fault (DSF) and extends 600 km NE until it reaches KTJ, where it joins the NAF. Geological studies show an average of 22 km total slip on this fault (Arpat and Şaroğlu, 1972; Şaroğlu et al., 1992). In a more detailed study, Westaway (1994) divided this fault into two parts. The first part is from the KTJ to northeast of Hazar Lake (see Figure 6-3 for locations). The second is from Hazar Lake to the DSF and exhibits 35 km of left-lateral slip (Westaway, 1994).

Geodetic studies using GPS data show that the current slip rate is 9 ±1 mm/yr with a component of extension on the eastern segment of the fault (McClusky et al., 2000). This rate is faster than the 4-7 mm/yr slip rate defined by matching related geological features

across the fault zone (e.g. Arpat and Şaroğlu, 1972; Dewey et al., 1986). This contradiction is similar to that observed on the NAF and is likely due to a variable slip rate in time depending on the earthquake cycles as mentioned above.

The date at which the EAF initiated is poorly constrained. It was once suggested to have started around the late Miocene or early Pliocene (~5 Ma) (e.g. Şengör et al., 1985; Dewey et al., 1986; Hempton, 1987). An alternative view suggests a later origin in the late Pliocene (~2 Ma) based on the offset of late Pliocene-age volcanic rocks (Şaroğlu et al., 1992; Westaway and Arger, 2001). This earlier date is consistent with the 9 ±1 mm/yr slip rate required by the 24-33 km offset, determined from GPS measurements and geological markers (Westaway and Arger, 1996). Recent geological field observations by Yilmaz et al. (2006) also led to an estimate of at least a Pliocene (~5 Ma) age for the EAF.

It has long been accepted that the northward motion of the Arabian plate has been accommodated by (a) a combination of lithospheric deformation in eastern Anatolia, east of KTJ, and (b) by extrusion of the Anatolian Block along the North and East Anatolian Faults (Şengör et al., 1985). Recent GPS studies show a gradual westward increase in plate velocity along the EAF and NAF towards the Hellenic trench (McClusky et al., 2000). This observation is inconsistent with the extrusion of the Anatolian block as this requires fault normal convergence. It thus appears that the westward motion of the Anatolian block was initiated by north-south compression that pushed the Anatolian block west. However, the current behavior of the EAF is extension due to rollback along the Aegean Arc.

3.2.3 North East Anatolian Fault

The North East Anatolian Fault (NEAF) is a left-lateral (sinistral) strike-slip fault system (Tatar, 1978) which defines the northern boundary of eastward-escaping eastern Anatolia towards the Caucasus (Barka and Gülen, 1989). The NEAF was formed in the early Pliocene at a similar time to the North Anatolian and East Anatolian faults (Barka and Gülen, 1989; Bozkurt, 2001; Koçyiğit et al., 2001). This fault extends from the Erzincan Basin in the west to the Great Caucasus in the east, with a NNE strike direction. It moves at 1.8 to 2.5 cm/yr slip rate (Philip et al., 1989). The crest of the Great Caucasus is offset by 90 km across the NEAF, where it was originally called the Borjomi-Kazbeg fault by

Philip et al., (1989). The seismic activity of this fault decreases from east to west (Philip et al., 1989). It has also been suggested that the NEAF could be a system of echelon faults rather then a single linear form (Fuenzalida et al., 1997).

3.3 Basement Geology

The basement of the study area (Figure 3-2) is composed of crustal blocks (terranes) that were accreted to each other during the late Cretaceous to Early Tertiary. These continental fragments exhibit a varied geological history and their accretion to Eurasia has formed the complex geology of eastern Anatolia. These accreted terranes are separated by ophiolite belts and accretionary complexes (Şengör, 1990). The paleotectonic structures of the East Anatolian High Plateau can be divided into five major tectonic units.

The Rhodope-Pontide Fragment defines the northernmost part of the study area (Figure 3-2). The metamorphic basement of this unit is characterized by relatively heterogeneous granulite rocks (Topuz et al., 2004) of Albian to Oligocene age (Şengör, 1990). Above the basement is a thick, south facing volcano-sedimentary sequence (Yilmaz et al., 1997).

The Northwest Iranian Fragment is masked by collision-related volcanic units in eastern Anatolia. It is exposed in western Armenia and composed of a heterogeneous sequence of rhyolite, perlite, pumice and rarely obsidian (Karapetian et al., 2001).

The Eastern Anatolia Accretionary Complex (EAAC) is a 150-180 km wide belt (Figure 3-2) that extends roughly east-west (Keskin et al., 2006) in eastern Turkey. This unit is believed to be the remnants of a large accretionary complex formed by the north-dipping subduction of Tethyan lithosphere under the Eurasia between the Late Cretaceous and Oligocene. The EAAC consists of Late Cretaceous ophiolitic melange and mainly north-dipping Paleocene to Late Oligocene flysch sequences, incorporated into ophiolitic melange. The flysch becomes younger from north to south and gradually shallower from the Cretaceous to the Oligocene (Şengör, et al., 2003) as expected for an accretionary complex formed on a north-dipping subduction zone. Thus, the EAAC does have a lithospheric root since it is supported and underlain by a subducting slab (Şengör et al., 2003; Keskin, 2003; Al-Lazki et al., 2004).

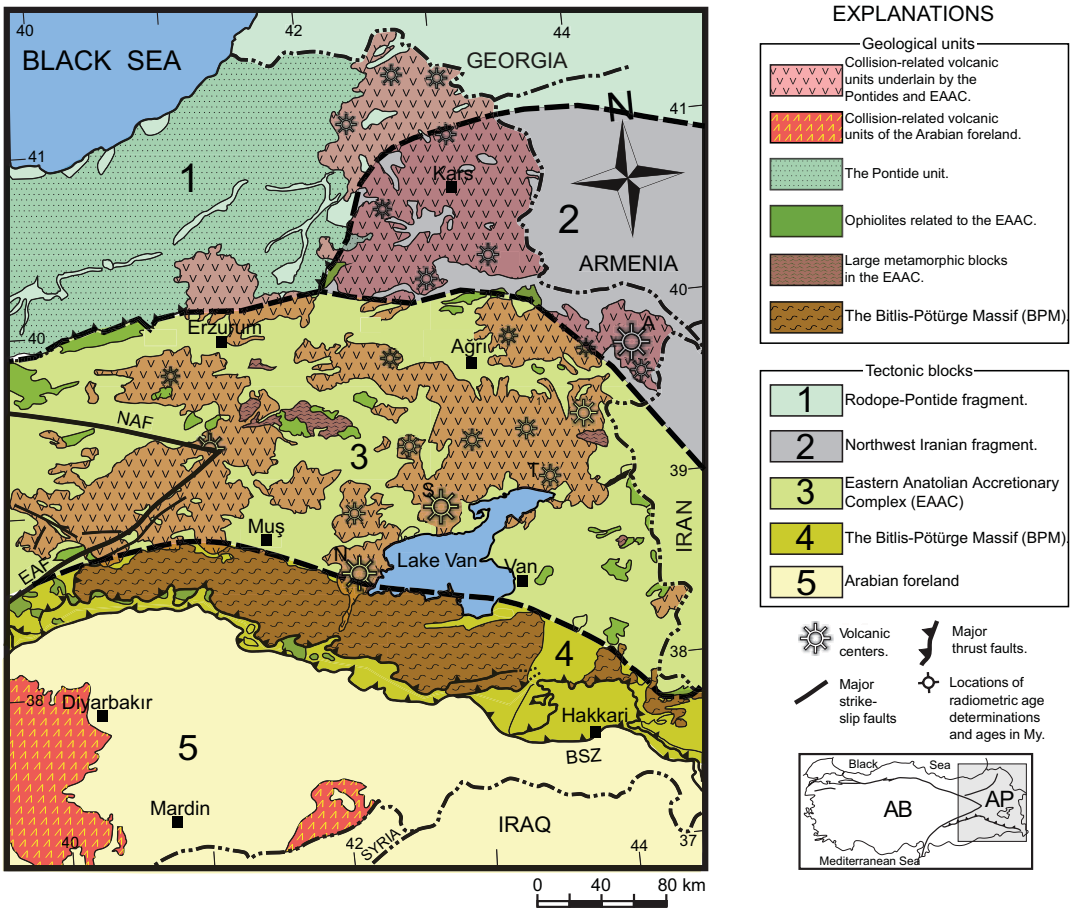

Figure 3-2. Map showing tectonic units and major tectonic blocks in the study area. The borders are modified from Şengör et al., (2003). The figure and explanations are modified from Keskin (2007). AB: Anatolian Block; AP: Anatolian Plateau.

The Bitlis-Pötürge Massif (Figure 3-2) was formed by the collision of the easternmost extremity of Menderes-Taurus block with the northern margin of the Arabian Foreland in the Early Eocene (~50 Ma) (Görür et al., 1984). It consists of series of highly deformed metamorphic massifs that are allochthonous, with late Cretaceous and mid Eocene melange complexes (Şengör et al., 2003).

The Arabian Foreland (Figure 3-2) is the southern extremity of the study area. The Southern Arabian Plate was formed by the accretion of a number of island arcs and microplates to northeast Africa during the Late Precambrian (Beydoun, 1991). Suture zones between different tectonic blocks in the Arabian Plate represent Proterozoic weakness zones (e.g. Stoeser and Camp, 1985; Barazangi et al., 1993; Al-Damegh et al.,

2004). As part of the Arabian Plate, the Arabian Foreland continues its northward motion with minimal internal deformation and forms the most stable tectonic unit in the study area and the most electrically resistive unit as shown later in this thesis.

Shallow marine deposits of Oligocene and Middle Miocene age partly overlie these five main tectonic structures. Furthermore, collision-related subaerial volcanic units of Neogene and Quaternary cover two-thirds of the area, masking a large portion of the main tectonic features and marine deposits (Keskin, 2007). Volcanic units are the oldest in the northeast exhibiting a calc-alkaline subduction signature (Keskin et al., 1998, Pearce et al., 1990). Volcanism becomes younger to the south and the composition changes to an intraplate signature (Keskin, 2007). Volcanos in the Erzurum-Kars Plateau and Ağrı (Ararat) exhibit a subduction signature while Nemrut and Tendürek volcanos (Figure 3-2) are mildly alkaline, and Süphan shows transitional characteristic (Keskin et al., 1998, Pearce et al., 1990). The most recent and most mafic volcanic rocks are found in the Arabian foreland, where basalts of Karacadağ volcano are widespread (Figure 3-2). The lavas are 1.9–0.1 Ma in age and exhibit a mantle origin (Pearce et al., 1990; Notsu et al., 1995).

3.4 Regional geophysical background

3.4.1 Heat flow

Heat flow data provide important information about the subsurface temperature. A compilation of heat flow data collected in Turkey is given by Tezcan, (1979) and Tezcan and Turgay (1987). Obtaining reliable heat flow data requires that the measured data are corrected for localized volcanic activity, the amount of sedimentary cover, mantle heat flow and crustal heat production. The corrected heat flow data should be validated by an alternative technique. One method of verification uses geochemical data and relies on the fact that as meteoric waters percolate through the upper crust, the interactions between the water and the rocks change the chemical composition of the water. Soluble components are leached from silicate minerals and the concentration of these ions in pore fluid is dependent on the temperature (Fournier and Rowe, 1977). Heat flow values calculated from conventional geothermal gradients are very similar to the silica data (Koçak 1989, İlkışık et al., 1995). The mean value of heat flow for Western Anatolia is very high, 107 mW/m^2 for

the silica data, and 97 mW/m^2 for the conventional heat flow data and 50-60% above the global average (İlkışık et al., 1995). Eastern Anatolia also has high heat flow (Koçyiğit et al., 2001). Heat flow in eastern Anatolia shows an increase from 50 mW/m^2 in the Arabian foreland to values of 80-90 mW/m^2 in the Anatolian Plateau (Figure 3-3).

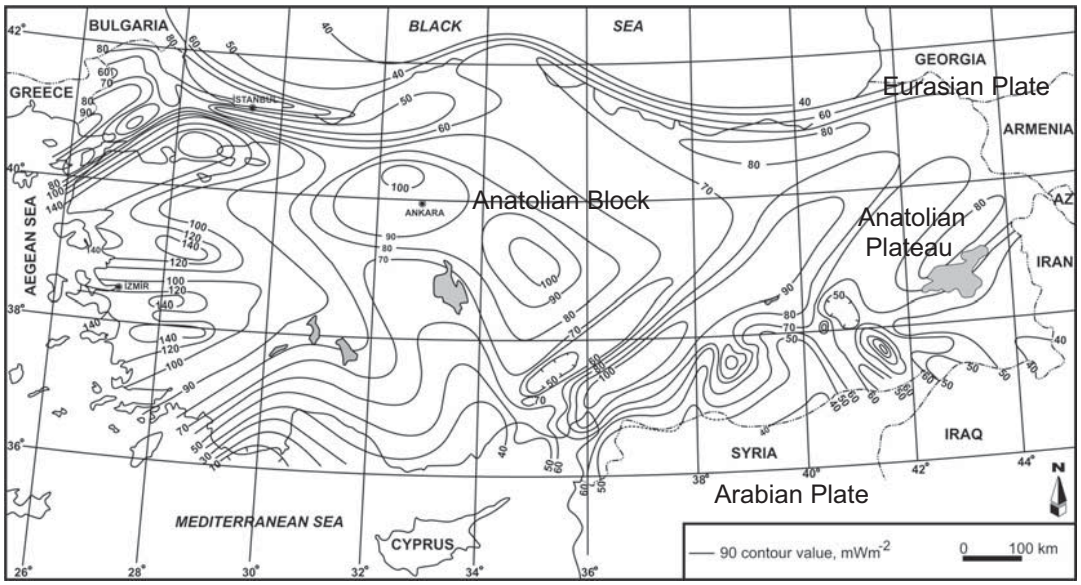

Figure 3-3. Heat flow distribution map of Turkey (from Tezcan 1995).

Eastern Anatolia was the location of subduction of the Tethys Ocean. Thus, it is useful to compare this location with other backarc regions. Hyndman et al., (2005) summarized the heat flow distribution of eight major subduction zones. Current and recent backarc heat flow values are in the range 70-85 mW/m^2 while forearc heat flow averages 40 mW/m^2. They also noted that there is a 1.5-2.5% and 3.5-5% reduction in Pn and Sn seismic wave velocities respectively in the backarc regions compared to global averages. High heat flow in backarc regions is related to shallow asthenosphere convection that is caused by water from the subducting slab that lowers the viscosity of the mantle wedge. Backarc and subsequent orogenic belt temperatures may be high enough for lower crust detachment that can (a) decouple complex surface tectonics from the uppermost mantle and (b) permit lower crustal flow (Hyndman et al., 2005). This statement is applicable to eastern Anatolia since this region was once a backarc region during the previous episode of subduction. Low tomographic seismic velocities and high heat flow values are observed north of the BSZ. Keskin (2007) estimated that 15,000 km^3 of extrusive volcanic rocks were erupted in

eastern Anatolia and suggested that this volume is a small fraction of the total melt generated beneath the region.

3.4.2 Magnetic data

Aeromagnetic data were acquired in eastern Anatolia by the General Directorate of Mineral Research and Exploration (MTA) of Turkey (Ateş et al., 1999; Aydın et al., 2005) and are shown in Figure 3-4. Magnetic data are commonly used for mapping the distribution of magnetized rocks, basin depth and variations in the Curie depth. Short wavelength anomalies are associated with shallow features and long wavelength anomalies are associated with deeper magnetic sources. The long spatial wavelength magnetic anomaly observed in the south of the study area (Figure 3-4) is either due to weakly magnetic material or from a deep source (Ateş et al., 1999). The short spatial wavelength magnetic anomalies near Van, Erzincan, east of Sivas and the northeast part of the study area are associated with outcrops of volcanic and ophiolitic rocks (Bektaş et al., 2007). Magnetic anomalies on the Anatolian Plateau appear to correlate with the location of highly magnetic volcanic rocks at the surface (Bektaş et al., 2007). Two thirds of the Anatolian Plateau is covered by collision-related volcanic units (Figure 3-2). These volcanic units correlate with the locations of the most anomalous area on the aeromagnetic map (Figure 3-4).

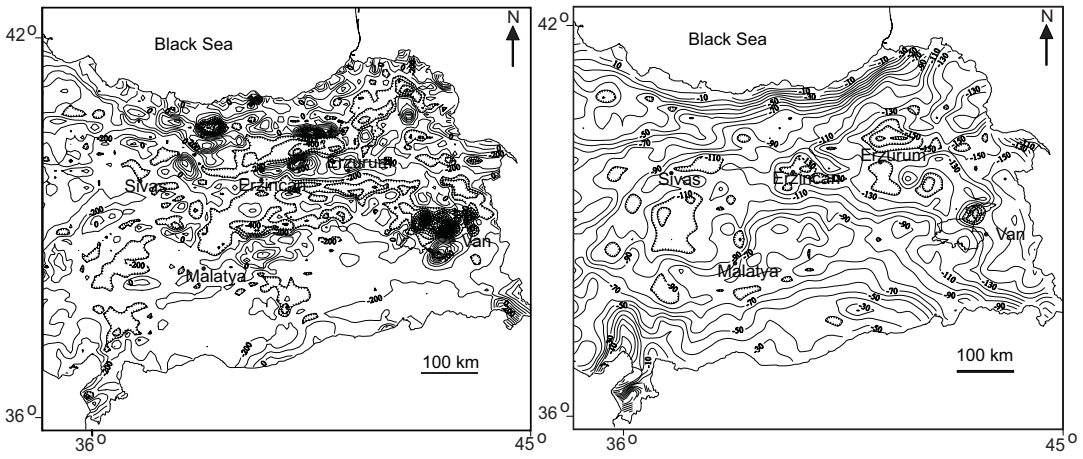

Figure 3-4. Residual total field aeromagnetic anomaly map of eastern Anatolia (left). Bouguer anomaly map of eastern Anatolia (right). Lows are hachured (from Bektaş et al., 2007). Contour intervals are 100 nT and 10 mGal for aeromagnetic and gravity maps respectively.

Crustal rocks lose their ferromagnetic characteristics at the Curie temperature (approximately 580° C) which typically occurs in the depth range 10 to 70 km for active and stable tectonic regions respectively (Negi et al., 1987). The Curie depth depends primarily on the temperature and secondarily on the rock composition (Hunt et al., 1995). A shallow Curie depth indicates regions of high crustal temperatures (Bhattacharyya and Leu, 1975; Connard et al., 1983; Tanaka et al., 1999) and thinner lithosphere (Negi et al., 1987).

A Curie depth map of Turkey was first published by Karat and Aydın, (2004). The more detailed compilation by Aydın et al., (2005) showed some very shallow depths that were biased by the topography and highly magnetic rocks. To eliminate these biases, Bektaş et al., (2007) low-pass filtered the aeromagnetic data and found Curie depths in the range 13-20 km throughout eastern Anatolia (Figure 3-5). Joint interpretation of surface heat flow and magnetically inferred Curie depths in the crust are useful in the exploration of geothermal energy, tectonic strength of the lithosphere and the understanding of tectonic features.

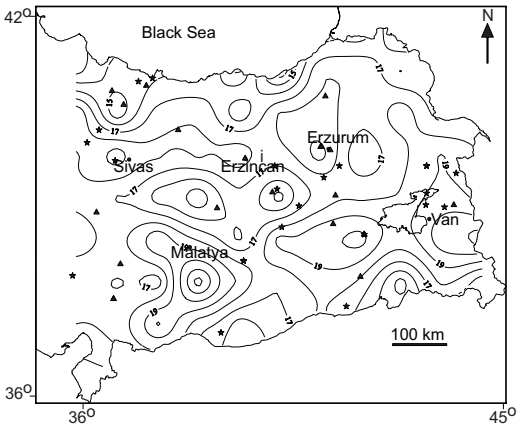

Figure 3-5. Map of Curie depth for eastern Anatolia estimated from low-pass filtered residual magnetic anomaly data. Contour interval is 1 km. Hot springs with temperatures greater and less than 45° C are shown with stars and triangles respectively (Bektaş et al., 2007).

3.4.3 Gravity data

A Bouguer gravity map of Turkey was also prepared by the MTA with a 2-5 km station spacing (Ateş et al., 1999). Gravity data must be corrected for a number of factors,

including elevation, before it can be interpreted in terms of subsurface density. The Bouguer anomaly accounts for these factors and should indicate variations in subsurface density. Most of eastern Anatolia is characterized by a negative Bouguer anomaly (Figure 3-4). Some regions of the 2 km high eastern Anatolian Plateau have a Bouguer anomaly below -150 mGal which indicates lower than average densities in the crust and upper mantle. This could be the result of a thickened crust or lower densities in crust and/or mantle (e.g. Shin et al., 2007; Tesha et al., 1997; Gupta et al., 2003; Braitenberg et al., 2000). Some early geodynamic models of eastern Anatolia assumed that the gravity low implied that significant crustal thickening had occurred (Şengör, 1980; Dewey et al., 1986) in a manner similar to Tibetan Plateau. Based on isostasic compensation, Şengör (1980) estimated that a 55 km thick crust was needed in eastern Anatolian Plateau to support the 2 km of observed topography. Recent gravity and seismic studies have refined this view with crustal thicknesses of 38-40 km in the Arabian Plate and 46-50 km beneath the Anatolian Plateau (Zor et al., 2003; Angus et al., 2006; Pamukçu et al., 2007; Gök et al., 2007; Ozacar et al., 2008). The fact that the crust is thinner than predicted by isostasy shows that the Anatolian Plateau is slightly undercompensated. Therefore, the Anatolian Plateau must be partially supported by mechanisms other than a low density crustal root. This could include buoyancy forces from a low density (hot) upper mantle or dynamic effects such as mantle upwelling or flexure of the Arabian Plate.

3.4.3 Seismicity

Eastern Anatolia is seismically very active with numerous earthquakes each year. Earthquake hypocenter locations were previously not well defined owing to a limited network of recording stations with an average spacing of 100 km. (http://www.koeri.boun.edu.tr/sismo/default.htm). The recent Eastern Turkey Seismic Experiment (ETSE) seismic array significantly improved the station coverage in the region (Sandvol et al., 2003a). ETSE operated a 29 broadband station PASSCAL network that was deployed across the NAF, EAF and the BSZ with 50 km average spacing between stations (Figure 3-6). A total of 1165 local seismic events were recorded between October 1999 and August 2001 (Turkelli et al., 2003).

The majority of earthquakes occurred in the 20-30 km depth range on the EAF and in the range 0-10 km on the NAF. Therefore, the seismogenic depth of the EAF appears to be significantly greater than for the NAF. No earthquakes were observed at depths greater than 35 km during this study, indicating an aseismic lower crust and upper mantle. A continuous band of earthquakes southeast of Karlıova was interpreted as a possible extension of the NAF towards Lake Van and was also interpreted as a possible continuation of the Main Recent Fault in northwest Iran (Turkelli et al., 2003; Talebian and Jackson, 2002).

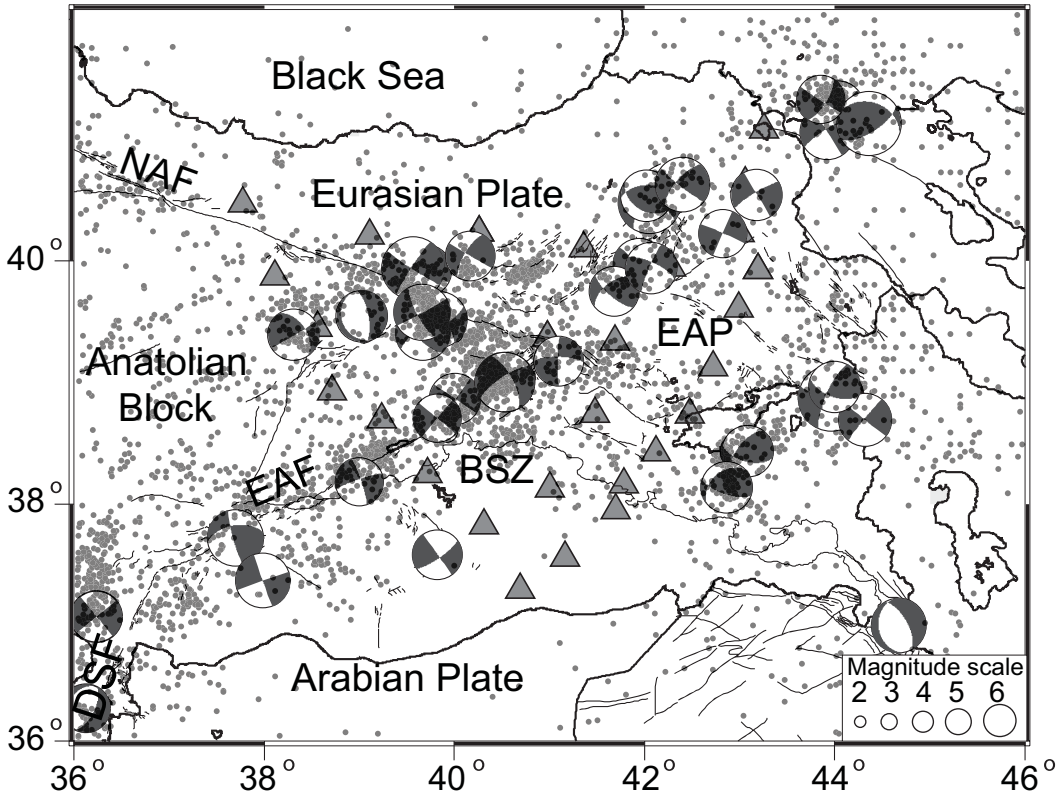

Figure 3-6. Map showing the locations of broadband seismic stations (solid triangles) deployed during the Eastern Turkey Seismic Experiment (Sandvol et al., 2003a). Fault plane solutions are taken from the Harvard CMT catalogue (from Örgülü et al., 2003). Labels indicate North Anatolian Fault (NAF), East Anatolian Fault (EAF), Bitlis Suture Zone (BSZ), East Anatolian Plateau (EAP), and Dead Sea Fault (DSF). Gray dots are earthquake epicenters (between 1960-2004 from KOERI, Turkelli et al. (2003) and Kaypak and Eyidoğan (2005)).

3.4.4 Seismic velocity structure

Some of the most important constraints on lithospheric structure come from studies of seismic velocity. Unfortunately, no regional-scale active-source seismic data are available in eastern Anatolia and all shallow seismic reflection data remain in the private domain. Therefore knowledge of the deeper seismic velocity structure of the area relies on earthquake seismology. Knowledge of the seismic velocity structure beneath eastern Anatolia was greatly improved by the ETSE. Data collected during ETSE were processed in a number of different ways outlined in the following 4 sections.

3.4.4.1 Upper mantle P-waves and S-waves

Studies of refracted P-waves traveling in the upper mantle (Pn) in the study area were described by Al-Lazki et al. (2004). The ETSE Pn velocity map (Figure 3-6) shows a number of large-scale zones with relatively low Pn velocity (<8 km/s) underlying most of the continental regions of the study area except the eastern Arabian Plate. Small-scale zones of very low Pn (<7.8 km/s) velocity anomalies underlie Syria, Lesser Caucasus, Central Anatolia and the northern Aegean (Figure 3-7). Note that the resolution test described by Al-Lazki et al., (2003) showed that the data are capable of resolving the velocity structure beneath the Anatolian Plateau and eastern Mediterranean while the resolution is lower on the Arabian Plate, around the Black Sea and Caspian Sea. Lattice preferred orientation of the upper mantle due to plastic deformation (e.g. Karato, 1998) causes seismic anisotropy. Therefore, Pn velocity shows azimuthal variations. Anisotropy was included in tomographic inversions of the ETSE Pn data (Al-Lazki et al., 2004).

The Sn phase comprises shear waves that follow a similar path to Pn. They are especially sensitive to the presence of fluids present in the uppermost mantle (also called the mantle lid). Strong attenuation of these waves is generally attributed to partial melt in the upper mantle. Sn attenuation tomography for the ETSE dataset used the Sn efficiencies from Gök et al. (2000) where the amplitude of Sn was compared to the other regional waves (primarily Pg and Lg) and classified into three groups: efficient, inefficient, or not observed, depending on the amplitude of the Sn arrivals. Figure 3-8 includes data from Gök et al. (2000), Sandvol et al. (2001) and ETSE (Sandvol et al., 2003a).

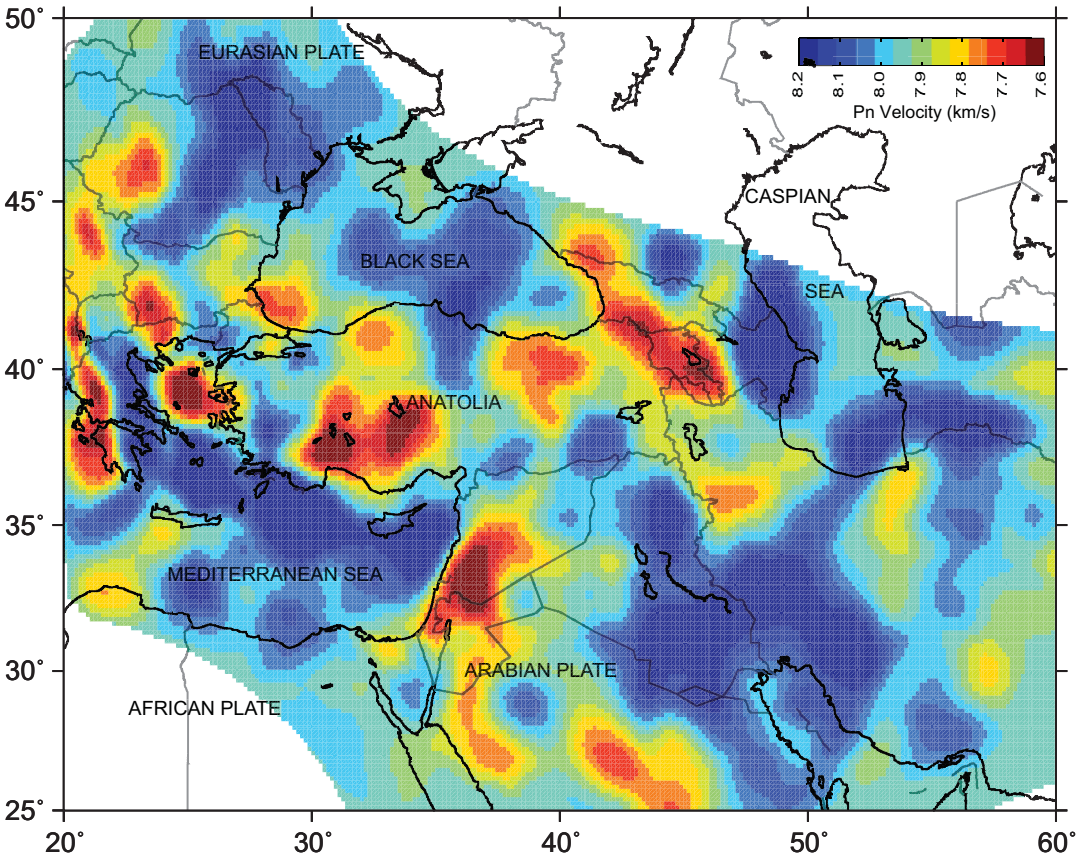

Figure 3-7. Map of Pn tomography including anisotropy (Al-Lazki et al., 2004).

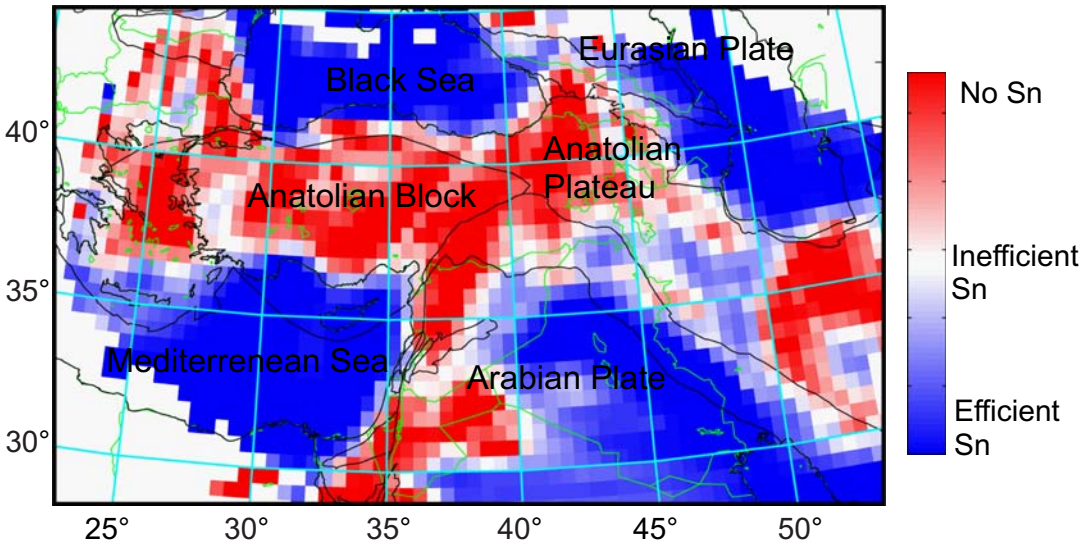

Figure 3-8. Map showing Sn efficiency tomography in the Middle East (Gök et al., 2003).

Blockage of Sn waves in central Anatolia, eastern Anatolia and west of Caucasus implies that S-waves do not travel in the upper mantle in this region. This blockage implies an upper mantle that is unusually hot, perhaps containing a few percent partial melt. This explanation is supported by the coincidence of this region with a number of Holocene volcanoes (Gök et al., 2003). Pn velocity is also very slow (<7.6 km/s) in this region (Al-Lazki et al., 2004). The BSZ is a sharp boundary between regions with efficient and very inefficient Sn propagation in eastern Anatolia. This contrast was interpreted as an indication of fundamental differences in the rheology of the upper mantle across the BSZ as well as a lack of strong mantle lithosphere beneath the eastern Anatolian Plateau (Gök et al., 2003).

A similar attenuation study in the Arabian Plate and the surrounding regions using Lg attenuations (Al-Damegh et al., 2004) showed similar results to that obtained from Sn attenuation. Lg is a crustal guided wave that is weakened or blocked by rapid changes in the crustal thickness (Bostock and Kennet, 1990).

3.4.4.2 Receiver functions

Seismic P and S-waves recorded during the ETSE project were also used to infer the crustal and upper mantle structure from receiver functions (Zor et al., 2003; Angus et al., 2006). Receiver functions are computed from ground motion at a seismic station as a teleseismic signal arrives. The waveform is normalized with respect to the incident P-wave and examined for converted phases generated at subsurface layers (both P and S-waves). In eastern Anatolia, the receiver functions show that the crust thickens from 40-42 km south of the BSZ to 50 km north of the EAAC (Figure 3-9). At the stations marked by black squares in Figure 3-9, the receiver functions exhibit crustal low velocity zones in the depth range 15-25 km. Overall, there is no significant crustal thickening determined from P-wave receiver functions across the Bitlis Suture Zone (Zor et al., 2003). As mentioned previously, this observation supports the hypothesis that the Anatolian Plateau is isostasically under-compensated (Şengör, 1980; Dewey et al., 1986; Şengör et al., 2003).

P-wave receiver function analysis can be complicated by the presence of multiple reflections. This problem can sometimes be overcome by studying S-wave receiver

functions that are generated when an incident S-wave is converted to P-waves at sub-surface interfaces (Li et al., 2004). The S-wave receiver function analysis of the ETSE data by Angus et al., (2006) gave similar results to those derived from P-wave receiver functions (Zor et al., 2003). This analysis confirmed an average crustal thickness of 45 km in eastern Anatolia with thickening from west to east and south to north (see Figure 3-9 for exact locations and values).

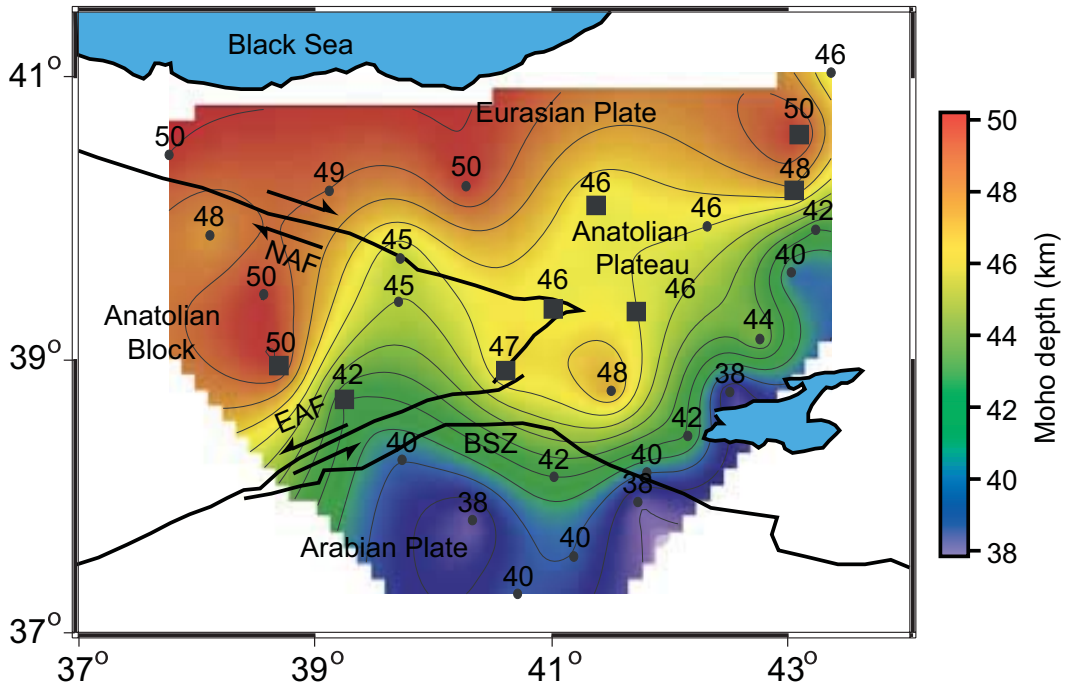

Figure 3-9. Map of Moho depth calculated from S-wave receiver functions (figure modified from Zor et al., 2003). Black squares indicate stations which may have a low velocity layer in the crust. Red lines indicate the major tectonic boundaries.

The crustal low velocity zones imaged with S-wave receiver functions are broadly coincident with the locations of the Quaternary volcanic centres. The crustal low velocities in these zones were interpreted as an indication of localized pockets of partial melt in the middle crust (Angus et al., 2006). A crustal discontinuity was also detected at a depth of 10 km and was interpreted as the boundary between crystalline basement and the thick volcano-sedimentary successions above it (Angus et al., 2006). The receiver functions also detected the lithosphere-asthenosphere boundary (LAB) at a depth of 70 km below the eastern Anatolian Plateau. Beneath the Arabian shield and the Iranian block the LAB was

detected at a depth of roughly 100-125 km (Angus et al., 2006). Lithospheric thickness is generally around 50 km in the oceanic regions but averages 150-200 km in the continents (see Priestley and McKenzie (2006) for global coverage).

3.4.4.3 Anisotropy from shear wave splitting

Passive earthquake recording such as the ETSE can also be used to study anisotropy in the upper mantle, and sometimes the crust. Teleseismic phases such as SKS and SKKS can be polarized as they travel through the upper mantle prior to reaching the seismic recording stations. The amount of the anisotropy is proportional the time delay between the two orthogonal phases of the S-waves. Sandvol et al., (2003b) showed that the fast polarization directions in eastern Anatolia are uniformly oriented in a NE-SW direction with no indication of rapid changes across the main tectonic units (Sandvol et al., 2003b). Observed delay times increase up to 2 seconds in the northern part of eastern Anatolia (Figure 3-10). The shear wave splitting fast directions were interpreted as the result of flow of the asthenospheric mantle in NE-SW direction. Figure 3-10 shows the comparison of S-wave splitting and GPS velocity vectors.

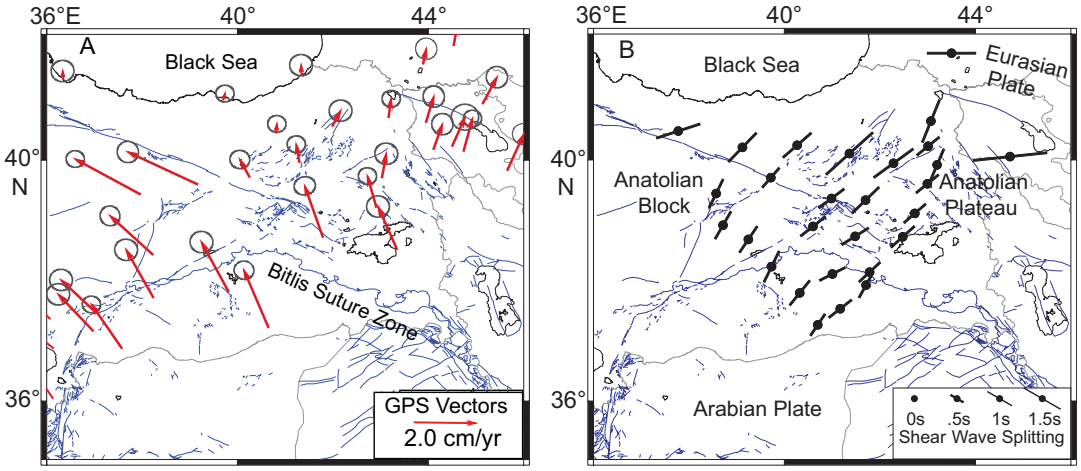

Figure 3-10. (A) GPS velocity vectors in eastern Anatolia in a frame of reference relative to Eurasia (McClusky et al., 2000). (B) Map showing averaged fast directions and delay times from SKS and SKKS shear wave splitting measurements taken from Eastern Turkey Seismic Experiment (Sandvol et al., 2003b). Shear wave splitting directions are consistently showing NE direction that can be explained by an absolute velocity in a northeast direction. Figure modified from Barazangi et al. (2006).

There appears to be a correlation between larger delay times and regions with low Pn velocities. Generally, north of the NAF, KTJ and EAAC are characterized by low Pn and larger delay times. This observation also partly coincides with GPS data where the lowest motion correlates with low Pn velocity and larger delay times (Figure 3-10). This correlation promotes increased mantle deformation and mechanically weak lithosphere. This could be caused by motion of the plate relative to the upper mantle and the creation of texture that is aligned with the plate motion generating anisotropic fabric in the upper mantle parallel to the absolute plate motion (Sandvol et al., 2003b).

3.4.4.4 Surface wave analysis

Surface waves (Love and Rayleigh) are dispersive and as the period increases they are sensitive to seismic velocity at greater depths. This information can be jointly used with the receiver function analysis to constrain the velocity-depth trade-off (Julià et al., 2002). Joint inversion of surface waves and receiver functions for eastern Anatolia improved the results of Gök et al. (2003) and provided similar results for the variation of the Moho depth (Gök et al., 2007). The Anatolian Block, west of KTJ and eastern Anatolian Plateau, were found to have average crustal thicknesses of 40-45 km and 48 km, respectively (Gök et al., 2007). Surface waves can also determine S-wave velocities and the lower values beneath the Anatolian Plateau were interpreted as requiring 2-3% partial melt to reduce the S-wave velocity by 15 percent (Gök et al., 2007).

3.4.5 Geodetic data

Global Positioning System (GPS) measurements from 1988 to 2005 were used to derive a velocity map (Figure 3-11) of the study area (Figure 3-11Reilinger et al., 2006). The first order feature observed from the GPS velocity map is the rapid motion (20-30 mm/yr) of the Arabian Peninsula, Iran, Aegean and the Anatolia. In contrast the Somalian, Eurasian and Nubian plates are moving slowly relative to each other (Reilinger et al., 2006). The rapidly moving plates are involved with a counterclockwise rotation relative to Eurasia. The velocity increases toward the Hellenic trench system because of the trench roll-back in the Aegean arc (Reilinger et al., 2006).

The plate velocity relative to Eurasia increases from 17.8 ± 1.1 mm/yr on the Arabian foreland to 20.6 ± 0.8 mm/yr in eastern and central Turkey, to 24.6 ± 1.0 mm/yr in western Turkey, and to 31.1 ± 0.9 mm/yr in the Aegean (Reilinger et al., 2006). This continuous increase in velocities toward the Aegean Arc and the absence of fault-normal convergence across the EAF is contrary to the idea of simple westward extrusion of the Anatolian Block (Şengör et al., 1985). It suggests that motion of the Anatolian Block is largely due to roll-back at the Aegean arc (Conrad and Lithgow-Bertelloni, 2004), and may be associated with crustal extension. Note the striking velocity change across the NAF and the eastward rotation of velocities around the eastern edge of the Black Sea. McClusky et al., (2000) interpreted these features as being a consequence of greater strength of the oceanic lithosphere underlying the Black Sea than the continental lithosphere to the south. Thus the Black Sea acts as a backstop that resists deformation and deflects the impinging continental lithosphere.

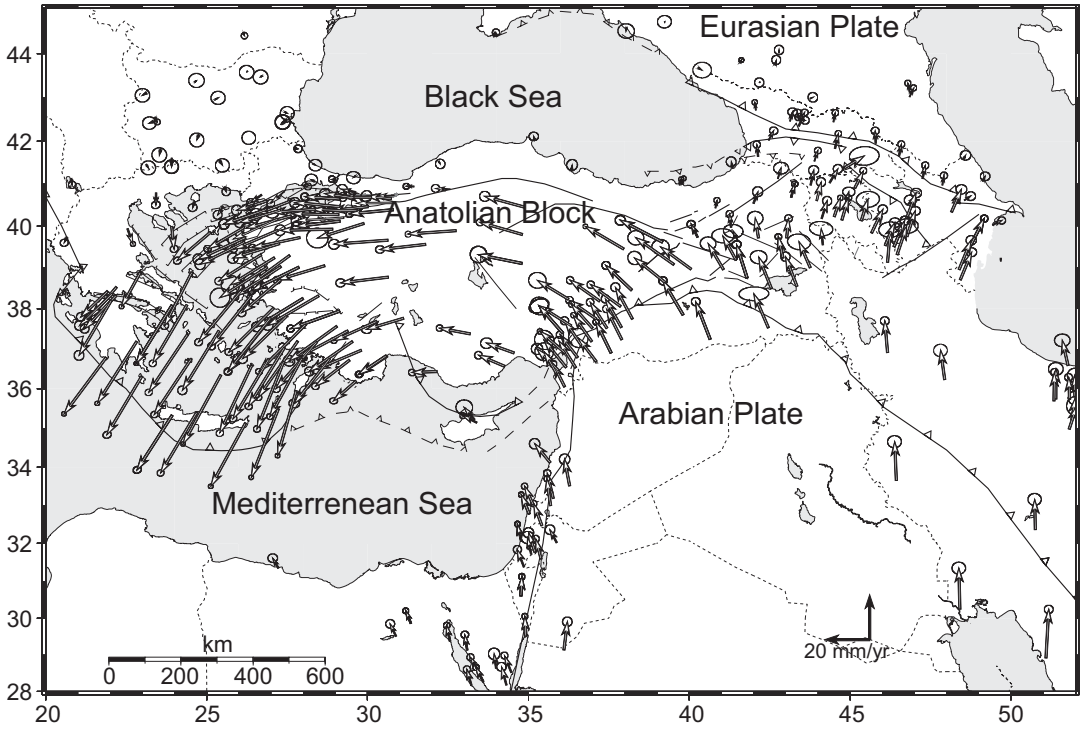

Figure 3-11. GPS velocities with respect to Eurasia. Ellipses represent uncertainties in the data and define 95% confidence limits (figure modified from Reilinger et al., 2006). GPS data from McClusky et al., (2000), Vernant et al., (2004) and Bendick et al., (2005).

3.5 Geodynamic Models

One of the goals of this study is to understand the mechanisms at work in continent-continent collisions using a synthesis of the available geological and geophysical information. A range of models have been proposed, but need to be critically compared with all geological and geophysical data. In this section, the various geodynamic models for eastern Anatolia are reviewed. The different mechanisms listed below are not mutually exclusive and it is likely that a combination of mechanisms is at work.

All geodynamic models for the Arabia – Eurasia continent-continent collision begin with subduction ceasing at approximately 11 Ma. (Şengör et al., 2003; Keskin, 2003). Continental crust can be temporarily subducted to depths in excess of 50 km (Leech et al., 2005). When exhumed this material forms ultra high pressure (UHP) rocks. However, continental crust is too buoyant to be permanently subducted so a different mode of deformation must have developed after the final closure of the Tethys Ocean. Various geodynamic models have been suggested and are summarized by Keskin (2007). The most important models are described below and summarized in Table 3.1 and Figure 3-12.

3.5.1 Tectonic escape

The northward motion of the Arabian Plate was suggested to be accommodated by tectonic escape along the large-scale strike-slip faults (McKenzie, 1972) (Figure 3-12-A). This model was based on observations of horizontal motion on the NAF and EAF. This process is clearly active today based on GPS velocities, fault plane solutions of earthquakes and geomorphic studies (Reilinger et al., 2006; Örgülü et al., 2003; Şengör et al., 2005). However, this process on its own cannot account for all observations of the Arabia – Eurasia collision. For example, this process does not explain the widespread volcanism and shallow asthenosphere found from recent seismic studies.

3.5.2 Lithospheric thickening

An alternative class of models for deformation in continent-continent collision zones was suggested for the Tibetan Plateau by Dewey and Burke (1973). Based on geological studies of exhumed mountain belts such as the Variscides, they proposed that continental crust was

thickened in the vertical direction by horizontal compression. A number of authors have suggested that a similar mechanism was responsible for crustal thickening of the Anatolian Plateau, which may be a younger analogue of the Tibetan Plateau (Şengör and Kidd, 1979; Dewey et al., 1986; Barazangi, 1989). The thickening model is supported by negative Bouguer anomalies that could be accounted for by thickening of low density crustal rocks. This model explains the elevated high plateau and suggests that lavas were erupted through north-south aligned cracks. If the crust and mantle remain connected, then this style of deformation could also thicken the entire lithosphere (Keskin, 2007).

Recent geophysical studies do not entirely support this model. Seismic and MT studies have shown that the mantle lithosphere is either completely absent or very thin beneath a large portion of eastern Anatolia (Gök et al., 2003; Al-Lazki et al., 2003; Piromallo and Morelli, 2003; Maggi and Priestly, 2005; Al-Damegh et al., 2004; Angus et al., 2006; Türkoğlu et al., 2008). An upper mantle with weak rheology and a shallow, hot, partially molten layer beneath the crust or very thin (20-30 km) lithosphere is contrary to the predictions of simple lithospheric thickening. Additionally, Şengör et al., (1980) showed that a 55 km thick crust is needed to isostasically compensate the 2 km elevation of the plateau. The receiver function analysis (Zor et al., 2003; Angus et al., 2006) showed that crustal thickness averages 45 km throughout the region. Other mechanisms are thus needed to explain the ~2 km elevation of the Anatolian Plateau. This could include dynamic topography effects or low density in the upper mantle caused by thermal expansion.

3.5.3 Lithospheric delamination

Delamination can occur when a region of the lithosphere is thickened and becomes mechanically unstable (Houseman et al., 1981; Houseman and England, 1986). This occurs because the surface layer becomes colder and denser than the underlying hot asthenosphere. Therefore, this layer could be convectively replaced by the asthenosphere (Figure 3-12-D). This localized upper mantle convection could promote widespread melting and large-scale volcanism (Elkins-Tanton, 2004). Pearce et al., (1990) studied the geochemistry of lavas in eastern Anatolia and suggested that a major delamination event had occurred in eastern Anatolia at 6 Ma. Delamination can broadly explain a number of key features in the structure and evolution of eastern Anatolia.

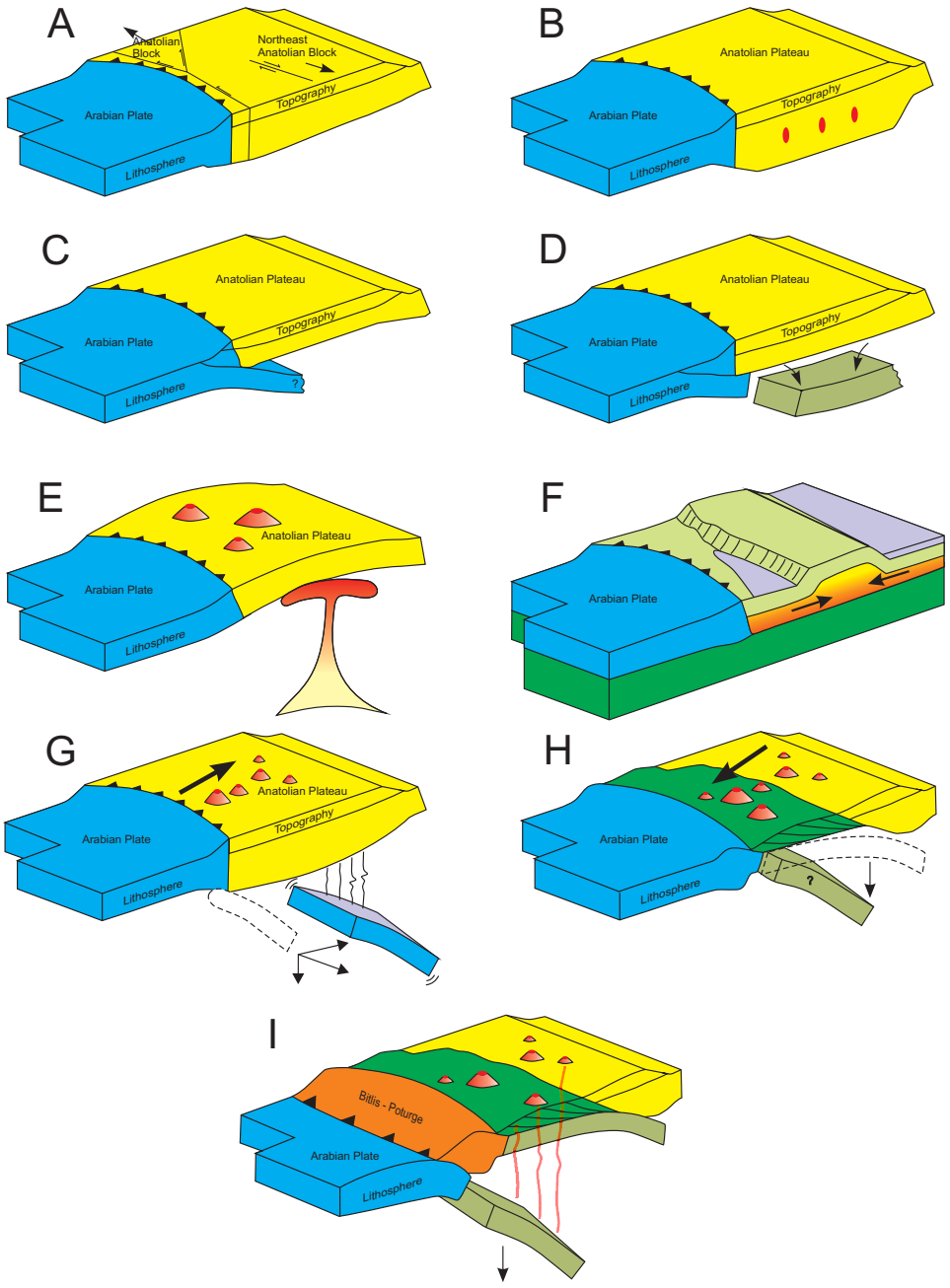

Figure 3-12. Cartoon illustrations of geodynamic models, proposed for the Arabia – Eurasia collision in eastern Anatolia. (A) Tectonic escape (McKenzie, 1972). (B) Lithospheric thickening (Dewey et al., 1986). (C) Continued continental subduction (Rotstein and Kafka, 1982). (D) Delamination (Pearce et al., 1990). (E) Mantle plume (Ershov and Nikishin, 2004). (F) Inflow of the lower crust (Mitchell and Westaway, 1999). (G) Detachment and northward movement of the slab (Innocenti et al., 1982a,b). (H) Slab steepening and break-off beneath the subduction accretionary complex (Şengör et al., 2003; Keskin, 2003). (I) Modified slab break-off (Barazangi et al., 2006).

It was previously noted that seismic and gravity data show that the eastern Anatolian Plateau is isostasically undercompensated. Only buoyancy cannot support the 2 km high plateau, an additional process is needed. Delamination could do this with dynamic support from rising hot material from the asthenosphere. Additional support for delamination comes from the variable geochemistry of lavas found in eastern Anatolia (Pearce et al., 1990; Keskin et al., 1998). The lavas require both enriched mantle with subduction signature (calc-alkaline) and intraplate (alkaline) sources (Pearce et al., 1990). The delamination model is also consistent with a high velocity body imaged around 500 km depth beneath eastern Anatolia and has been interpreted as the broken off slab (Piromallo and Morelli, 2003; Maggi and Priestly, 2005).

However, a number of important observations are not entirely consistent with a simple delamination event. These include:

- The absence of continental lithosphere beneath a large accretionary complex.

- Systematic spatial variation of lava chemistry from north to south (Keskin et al., 1998). Volcanic centers in northeast Anatolia exhibit a calc-alkaline subduction signature while the composition changes gradually to mildly alkaline to alkaline around the Bitlis Pötürge Massif and Arabian Plate (Pearce et al., 1990; Keskin et al., 1998).

- Radiometric dating also shows a systematic temporal trend in the character of the volcanism. Eruptions started in the north then migrated to south in time (Pearce et al., 1990; Ercan et al., 1990; Keskin et al., 1998).

Therefore, the geometry of the delamination process may have changed from north to south. The delamination model involves thickening and subsequent detachment of the lithosphere because of the density contrast between the lithosphere and asthenosphere. A single delamination event predicts that the whole thickened lithosphere detached at the same time and systematic temporal and spatial variations in volcanism would not be expected. If delamination occurred by opening a mantle wedge, a more complex pattern of volcanism might be expected. The systematic chemical and age distribution of volcanic centres in Anatolia give reasonable agreement with this prediction (Keskin, 2003).

A recent reexamination of the available geophysical and geological data by Şengör et al. (2003) and Keskin (2003) suggested that eastern Anatolia is a remnant of a large subduction accretionary prism. Accretionary prisms do not have their own lithosphere, but are generated and supported by an underlying subducting slab. Spatial and temporal variation of lava chemistry (see section 3.3) requires both subduction and subsequent invasion of asthenosphere in the upper mantle rather than thermal lithospheric detachment. Therefore, a modified delamination model may be required to explain the volcano chronology and chemistry data.

3.5.4 Mantle plume in eastern Anatolia

The correlation of the topography and pattern of volcanoes in eastern Anatolia and Armenia was cited as evidence for a localized mantle plume by Ershov and Nikishin (2004). According to their model, mantle flow from the African superplume flowed north along a lithospheric channel and caused the uplift of eastern Anatolia (Figure 3-12-E). Şengör et al., (2003) compared topographic profiles of the Ethiopian High Plateau and the Anatolian Plateau and concluded that both features could have been formed by upwelling asthenosphere (Şengör et al., 2003). In this scenario, eastern Anatolia represents a domal mantle plume modified by tectonic processes. This class of model predicts that extension and normal faulting should be observed throughout the plateau. However, strike-slip faulting and thrust faulting are widely observed in eastern Anatolia (Örgülü et al., 2003) showing that the pattern of faulting is inconsistent with this model. This plume model predicts similar lava compositions, with similar melting depths, across the whole of eastern Anatolia, and this is not observed (see section 3.3). In terms of temporal patterns in volcanism, the plume model predicts that the youngest volcanos should be in the centre of the plateau, with older ones at the edges. This is not observed in the field where a north-to-south progression is observed.

3.5.5 Inflow of lower crust

Mitchell and Westaway, (1999) proposed an alternative model for the formation of the high mountain ranges and plateaus such as the Greater Caucasus, Lesser Caucasus and Armenian high plateaus. Their model is based on the observation that the uplift rate of the

Caucasus is too great to be the result of the collision tectonics alone (Figure 3-12-F). They proposed that the inflow of the ductile lower crust was driven by sedimentation in adjacent basins (Mitchell and Westaway, 1999). This model is similar to that proposed for crustal flow beneath the Southern and Eastern parts of the Tibetan Plateau (Beaumont et al., 2001; Clark and Royden, 2000). However, the proposed crustal flow direction for Tibet is in the opposite direction to that proposed for the Caucasus by Mitchell and Westaway, (1999). Beaumont et al., (2001) showed that gravitational forces cause extrusion with flow away from the high plateau. In contrast, the model of Mitchell and Westaway, (1999) inflow of lower crust model suggest crustal flow towards high mountains. This model may represent the ongoing conditions in eastern Anatolia but cannot satisfy the aforementioned recent geophysical and geological findings.

3.5.6 Subduction

Some studies suggest that subduction of the Arabian Plate continues at the present time (Rotstein and Kafka, 1982). However continued, or renewed, continental subduction of the Arabian Plate beneath eastern Anatolia (Figure 3-12-C) is not a viable model. P-wave tomography (Piromallo and Morelli, 2003) and surface waveform tomography studies (Maggi and Priestly, 2005) showed evidence that the subducting slab has broken off from the continental lithosphere of the Arabian Plate. The lack of subcrustal earthquakes supports this view (Turkelli et al., 2003).

3.5.7 Northward moving slab break-off

Another geodynamic process that could have contributed to the formation of the Anatolian Plateau is the occurrence of slab break-off. This process could have occurred following closure of the Tethys Ocean. Low density continental crust cannot be easily subducted owing to buoyancy forces. However the descending slab continues to sink and this can result in slab break-off. Support for this process was presented by Innocenti et al., (1982a,b) who suggested that there was geochronological evidence for a northward migration of the andesitic volcanic front. This variation could be explained by a slab detachment process where the slab moved northward as it sank into the asthenosphere (Figure 3-12-G). This model appears to be incorrect since more detailed geochronology

studies by Keskin (1998) revealed that the volcanism started in the north at 11 Ma and migrated southward.

3.5.8 Slab steepening and break-off

In a more complex scenario, it has been suggested that slab steepening and slab break-off may have been triggered by the development of a large accretionary complex that loaded the subduction zone (Figure 3-12-H). Şengör et al., (2003) argued that the Eastern Anatolian Accretionary Complex can be regarded as a remnant of a large accretionary prism between the Pontides and the Bitlis-Pötürge Massif that accumulated on the northward subducting oceanic lithosphere. Accretionary complexes overlie oceanic crust and therefore do not have their own lithospheric root. They are formed and supported by subducting oceanic slabs (Figure 3-12-H). Therefore, in this model, a large portion of eastern Anatolia has never had a continental lithosphere. Seismic tomography results indicate no evidence for a mantle lid of the lithosphere; therefore the underlying subducting slab must have sunk into the asthenosphere, possibly prior to the uplift of the region at 11-13 Ma (Şengör et al., 2003; Keskin, 2003). In this model, volcanism initiated in the north with a distinct calc-alkaline subduction signature at 11 Ma (Keskin, 2003). Slab break-off was probably completed at ~8 Ma (Şengör et al., 2003) and widespread volcanism started in the whole region causing the volcanic front to migrate southward as composition changed from a subduction to an intraplate alkaline signature (Keskin et al., 2003).

3.5.9 Modified slab break-off

An alternative model involving slab break-off with two northward subducting slabs was recently proposed by Barazangi et al. (2006). According to this model, the EAAC is underlain by the subducting oceanic lithosphere that is attached to the Bitlis Pötürge Massif (BPM) and EAAC crust. The second subduction and the slab break-off occurred beneath the BPM at 11 Ma causing widespread volcanism in the eastern Anatolian Plateau (Figure 3-12-I), and resulting in domal uplift of the region (Barazangi et al., 2006). This model was criticized by Keskin (2007) who suggested that slab-break off beneath the BPM would produce a vast amount of young volcanism in this region and this is not observed.

Geophysical support for slab break-off and delamination models comes from recent seismic tomography and surface wave studies that show a detached slab imaged beneath eastern Anatolia (Maggi and Priestly, 2005; Piromallo and Morelli, 2003) at a depth of around 500 km. The slab is imaged as 2% positive velocity anomaly in tomographic P-wave depth sections. Slab steepening and slab break-off models predicts similar temporal and compositional variations of the lava chemistry as observed (see section 3.3) and also agree with the seismic velocity structure of the upper mantle. Water released from the sinking slab and increased temperature due to asthenospheric invasion can promote widespread melting which subsequently reduces seismic velocity. Therefore, the rise of hot material from the asthenosphere can be accounted for by low upper mantle Pn velocity and blockage of Sn waves.

3.6 Tectonic history

The geological and geophysical data presented in this chapter allow the evolution of Arabia – Eurasia collision to be constrained. The Neo-Tethys Ocean was subducted beneath the southern margin of Eurasia and was completely consumed during the late Paleocene along the Pontide arc (Şengör and Yılmaz 1981; Bozkurt and Mittwede 2001). At this time the southern part of the Neo-Tethys Ocean, attached to the Arabian plate, continued its northward subduction at the Bitlis arc through the middle Miocene (~15 Ma) (Yilmaz, 1993; Barazangi et al., 2006). The contact between the Arabian and Eurasian continents along the Bitlis Pötürge Massif (BPM) occurred between the late Eocene and Oligocene (Şengör et al., 2003). During the period between late Oligocene (~25 Ma) and middle Miocene (~15 Ma), the Eastern Anatolian Accretionary Complex (EAAC) was shortened and thickened over the oceanic lithospheric slab. When the EAAC thickened to a normal crustal thickness, subduction began to terminate. The slab may have steepened at this time and eventually detached from the EAAC around 10–11 Ma, due to the buoyancy contrast between the slab and the BPM (Keskin, 2003). Slab break-off opened an asthenospheric mantle wedge (also called a slab window) around the Pontides. This wedge gradually widened and allowed the asthenospheric invasion from north to south (Şengör et al., 2003).

Subsequently, a major episode of widespread volcanism affected most of the eastern Anatolian region starting at about 11 Ma (Keskin, 2003). Meanwhile, a large portion of the

collisional belt was uplifted to an elevation of 1.5-2 km forming the Anatolian plateau (Figure 3-13). Even though the age of uplift is not precisely defined, the change from marine to terrestrial sedimentation that occurred during or soon after the Serravalian (12 Ma) (Şengör et al., 1985; Gelati, 1975) provides evidence for the age of the uplift.

Soon after the cessation of subduction beneath eastern Anatolia, a drastic change occurred in the regional tectonics. Thrusting and NNW trending compression changed to strike slip faulting and extension in the Anatolian block between late and middle Miocene (Şengör et al., 1985). This change occurred later in the East Anatolian high plateau between Late Miocene and Early Pliocene (Bozkurt, 2001; Koçyiğit et al., 2001). Slab break-off was probably complete by 8 Ma when post-collisional volcanism became widespread in the eastern Anatolia high plateau and moved southward (Keskin et al, 1998). Therefore, the termination of subduction of the Neo-Tethys Ocean underneath eastern Anatolia and consequently slab break-off started a new era of strike slip movements of the plates with little or no intraplate deformation across Anatolia. The relative movements of the each block along the fault zones in Anatolia and surroundings are discussed in detail by McClusky et al (2000), McClusky et al (2003), Vernant et al (2004) and Reilinger et al (2006).

Geological evidence shows that the primary mechanism that has accommodated the northward motion of the Arabian plate was crustal shortening in Eastern Turkey until the Late Miocene and Pliocene (~5 Ma) (Şengör and Yilmaz, 1981). At 3-5 Ma, this changed and westward extrusion of the Anatolian Block began to be a significant factor (Reilinger et al., 2006). With the development of the NAF and its eastward extension into the Lesser Caucasus and Iran, shortening south of the Greater Caucasus ceased and was replaced by lateral escape of coherent lithospheric blocks with shortening being concentrated along the Greater Caucasus and Zagros thrusts (Reilinger et al., 2006). Westward motion of Anatolia coupled to subduction in the Aegean led to widespread extension in the Aegean (Armijo et al., 1996). The NAF propagated across the north Aegean and decoupled the Aegean from Eurasia. This allowed the central and southern Aegean and the Peloponnese to move trenchward with little or no internal deformation.

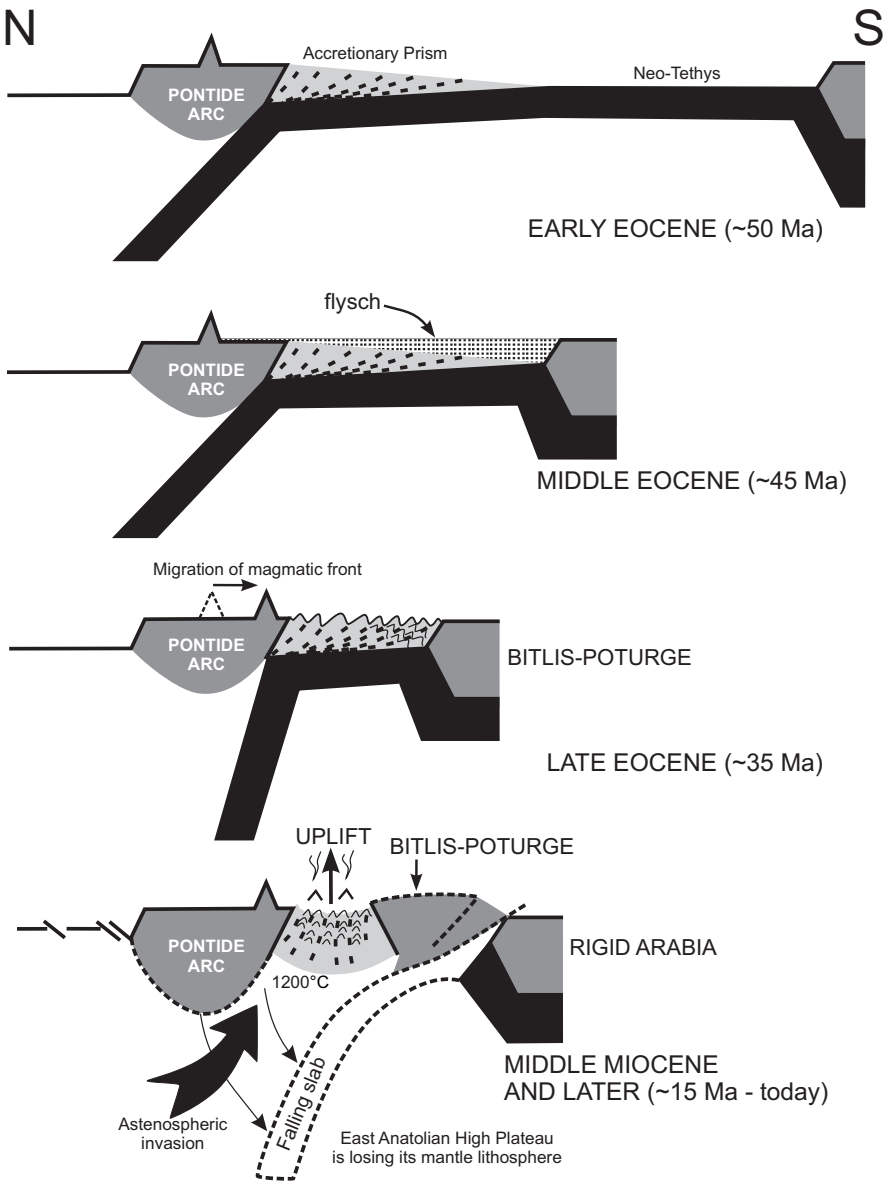

Figure 3-13. Illustration of the tectonic evolution of eastern Anatolia (figure from Şengör et al., 2003).

3.7 Summary

Based on the available geological and geophysical data, tectonic escape (A), crustal and lithospheric thickening (B), ongoing subduction (C), and inflow of lower crust (F) models cannot individually account for the geological and geophysical observations. However these processes clearly occur, and in combination with others may be important in the

Arabia – Eurasia collision. Delamination of the lithosphere (D) can account for many of the observations but fails to account for details of the spatial and temporal variation of volcanic rocks in eastern Anatolia. Models with a mantle plume (E), slab break-off (G) and northward motion of the subducting slab fail to account for important aspects of the lava chemistry and radiometric dating of the volcanos. Models with slab steepening (H) and break-off of the subducting slab (I) beneath the eastern Anatolian Accretionary Complex are the preferred form for the past and ongoing deformation. However, as mentioned above, a combination of these processes is occurring today and has done so during the earlier stages of the Arabia – Eurasia collision.

The observed geological and geophysical features and their compatibility with the suggested geodynamic models are summarized in Table 3.1. It can be seen that some tectonic process provide a better explanation for some observations but no single model can explain all the observations. Therefore, a combination of these tectonic models/processes is likely to have occurred during the Arabia – Eurasia collision. This began with subduction during the initial phases of collision and crustal thickening, delamination and/or slab break-off became important at a later date. These events were potentially followed by asthenospheric flow and escape along the large-scale strike slip faults.

Many aspects of the present day structure and temporal evolution of the Arabia – Eurasia collision zone are poorly understood. For example, a high velocity body imaged around 500 km depth beneath the plateau was interpreted as the broken off slab (Piromallo and Morelli, 2003; Maggi and Priestly, 2005) but this could also be the delaminating mantle lid of the lithosphere. On the other hand, spatial variation of this high velocity body at 500 km and relatively small parts hanging above it need more detailed studies in this region. The northernmost extension of the Arabian Plate and possible underthrusting beneath eastern Anatolia are poorly understood. More geochemistry and dating of the lavas are also required for a better understanding of the spatial variation of the magmatic front. Additional seismic data (active seismic reflection and refraction) are needed to image lateral variation of the Moho in the study area.

Table 3-1. Summary of the geodynamic models suggested for the Arabia – Eurasia continent-continent collision zone. See Figure 3-12 for explanations of the models referred in this table. The last row shows what kind of models could be justified by MT data.

Observation / **Model**	Low Gravity anomaly	High heat flow	Elevation	Low Pn & High Sn attenuation	Crustal thickness (RF)	Transform & reverse faulting	Shallow seismogenic depth	Widespread Volcanism	Spatial and temporal variation of volcanism	Lava chemistry	MT
A-escape	×	×	×	×	✓	✓	✓	?	×	×	N/A
B-thickening	✓	✓	✓	×	×	×	N/A	?	×	×	✓
C-subduction	✓	✓	✓	×	✓	?	×	✓	×	×	✓
D-delamination	✓	✓	✓	✓	✓	?	✓	✓	?	✓	✓
E-mantle plume	✓	✓	✓	✓	✓	×	×	✓	×	×	✓
F-inflow of lower crust	✓	✓	✓	✓	×	×	N/A	✓	×	×	✓
G-broken slab moves northward	✓	✓	✓	×	×	×	N/A	✓	×	✓	N/A
H-slab steepening and break-off	✓	✓	✓	✓	✓	?	N/A	✓	✓	✓	?
I-Modified slab break-off	✓	✓	✓	✓	✓	?	N/A	✓	×	✓	?

Deep probing long-period magnetotelluric (MT) data provide a valuable addition to previous studies. They are essential to distinguish between a strong, thick crust and lithosphere and the weak rheology suggested recently. The velocity of seismic waves is sensitive to the rheology and fluid content of the upper mantle. Partial melting in the upper mantle and lower crust can cause a 6-7% reduction in seismic velocity. In contrast, this amount of melting can reduce the resistivity by two orders of magnitude (Schilling et al., 1997). These resistivity values can be detected with MT studies and the electrical resistivity information about the subsurface can be linked to the percentage of partial melting and viscosity (Unsworth et al., 2005).

This thesis describes the first long-period magnetotelluric data collected in eastern Anatolia with the aim of imaging the subsurface resistivity distribution to reveal the geodynamic processes at work in this continental convergence zone.

4 DATA ACQUISITION AND PROCESSING

4.1 Introduction

This chapter describes the planning, data collection and processing stages of the 2005 Eastern Turkey Magnetotelluric Experiment (ETME). The instrumentation and data acquisition parameters are briefly introduced. The time series analysis is described, along with the dimensionality and directionality analysis of the magnetotelluric (MT) data.

4.2 Planning and data acquisition

The Eastern Turkey Magnetotelluric Experiment was primarily designed to collect long-period MT data that would define the resistivity structure of the crust and upper mantle beneath eastern Anatolia. Broad-band MT data were also collected in some areas to fill gaps on the profiles and to permit detailed resolution of smaller-scale structures within major fault zones. At the time the experiment was planned in 2003, very few geophysical data were available to constrain crustal and lithospheric structure in eastern Anatolia. No deep-sounding (long-period) MT data were available, and these data are essential to study lithospheric structure below 30 km depth. The 2005 project was mainly focused on regional tectonics with the goal of understanding the mechanism of a continent-continent collision. Profiles were selected to cross the major tectonic features which include the Bitlis Suture Zone (BSZ), the East Anatolian Fault (EAF), the North Anatolian Fault (NAF) and North East Anatolian Fault (NEAF). The profiles were chosen to be perpendicular to the major fault zones and plate boundaries. Deviations from this ideal layout were a consequence of both road access and security issues.

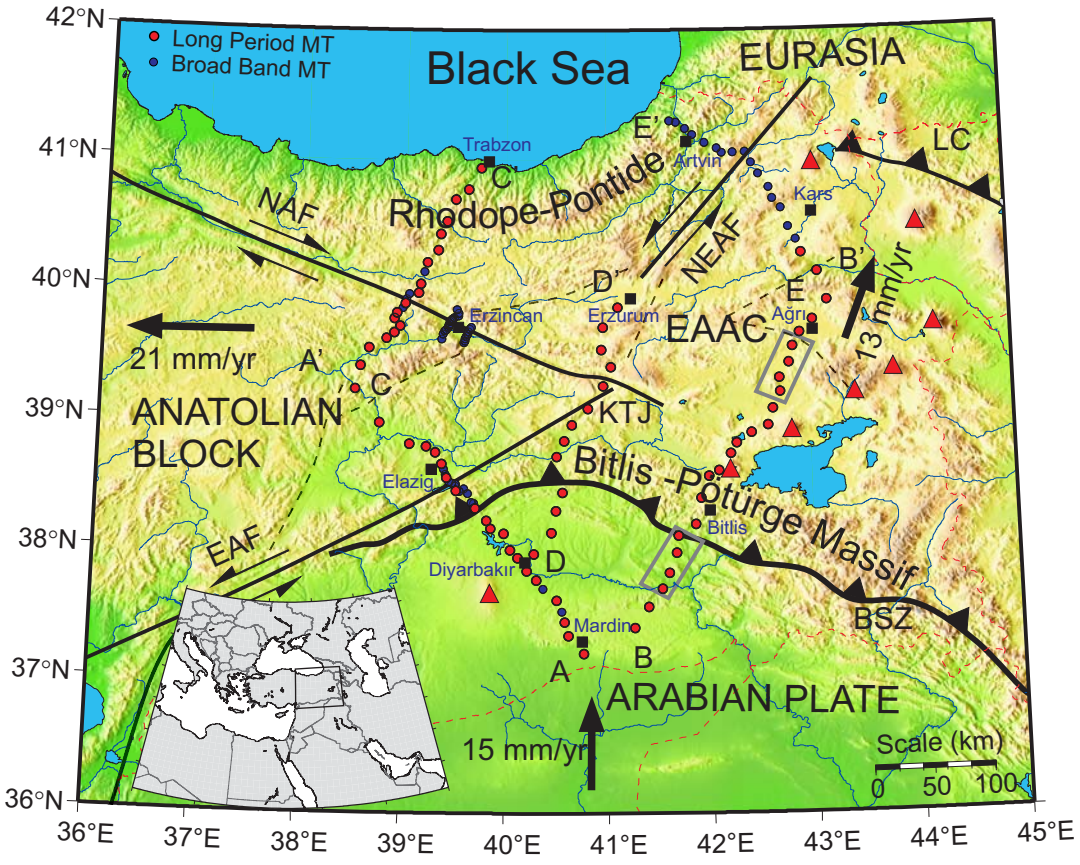

Figure 4-1. Map showing 2005 magnetotelluric stations and major tectonic features of the study area. Red and blue dots represent long-period and broad-band MT stations respectively. Red triangles and black rectangles show volcanoes and important cities respectively. Plate motions are taken from Reilinger et al., (2006). BSZ: Bitlis Suture Zone; KTJ: Karlıova Triple Junction; NAF: North Anatolian Fault; EAF: East Anatolian Fault; LC: Lesser Caucasus; EAAC: Eastern Anatolia Accretionary Complex.

Locations of the MT stations were chosen to avoid cultural noise and other possible disturbances such as curious children, tractors, livestock and military activity. Wind and strong sunlight are also two other factors that can severely effect data quality and instrument safety. To address these issues, electric field wires were either buried or stabilized on the ground. MT instruments were placed in boxes and buried 40-50 cm underground to avoid exposing them to temperatures in excess of 80° C. Two or three MT stations were deployed per day. Several MT instruments were relocated after a few days of recording because of unacceptable noise levels in the time series data.

4.2.1 A-profile

The first long-period MT station of the survey was deployed near Diyarbakir on May 12 2005. A total of 15 stations were subsequently deployed on the A-profile between Mardin and Elazığ (Figure 4-1). The average station spacing was 10 km and data were recorded for 30 days. Each station was visited weekly for maintenance and data-download. The data were processed at the site to confirm that the instrument was working correctly and recording useful data. Three MT sites collected very high quality data in just 10-15 days and were redeployed at different sites along this profile. In total 18 long-period magnetotelluric stations were obtained on the A-profile. Broad-band MT data were also collected at three locations to fill gaps between the long-period stations on the Arabian Plate (Figure 4-1). In addition, 10 broad-band stations were deployed across the BSZ and EAF. These extra stations provided improved spatial coverage across the BSZ and EAF. These broad-band MT stations typically recorded 1-3 days of data. Smooth MT transfer functions were obtained from the broad-band MT stations in the period range 0.01-2000 s and a remote reference station was operated at all times to remove bias from magnetic field noise.

4.2.2 B-profile

The second profile extended from Mardin to Kars and comprised 24 long-period MT stations. This profile crosses the BSZ and the northern stations are located on the Anatolian Plateau where numerous Neogene and Quaternary volcanoes are distributed and where two thirds of the surface is covered with volcanic rocks. The southern stations were placed on the Arabian foreland. This profile was intended to determine if there was a significant difference in the geoelectric structure of these regions. The first 15 MT stations were deployed north of the BSZ in June 2005 and only one station was redeployed. The remaining 9 MT stations south of the BSZ on this profile were deployed in October 2005 when temperatures in the Arabian foreland were moderate. MT data quality was excellent and comparable to that recorded on the A-profile.

4.2.3 E-profile

While long-period MT data recording was in progress on the northern part of the B-profile, 16 broad-band MT stations were deployed on the E-profile between Kars and Artvin. This

profile crosses the NEAF. The northwestern stations on this profile were located on the Eurasian Plate while the southeastern and central stations were located on the Anatolian Plateau. The MT data quality on the E-profile was lower than on the A-profile because most of the MT stations were close to electric power lines in villages. Sites were placed in these non-ideal locations because of the rugged terrain and limited road access.

4.2.4 C-profile

The C-profile extended from north of Elazığ to Trabzon and crosses the main branch of the North Anatolian fault (NAF) at right angles. Data were recorded at 18 long-period stations in August and September 2005. Three stations were redeployed after they completed data collection early. Stations north of the NAF were located on the Eurasian Plate while southern stations were on the Anatolian Block. The northernmost three stations were close to the Black Sea and this caused some strong 3-D induction effects in the MT data. This resulted in low data quality caused by very weak electric field amplitudes in the direction parallel to the coastline. Overall, the MT data quality on the C-profile was comparable to that on the A-profile except for the three sites close to the Black Sea coast.

4.2.5 F and G profiles

Characterization of the major faults in eastern Anatolia is important in terms of earthquake hazards. In addition, knowledge of the local structure of the Erzincan basin is needed for calculation of seismic amplification after a major earthquake. There have been two large earthquakes in (M_s=7.8) 1939 and (M_s=6.8) 1992 around Erzincan. To address questions relevant to earthquake hazards, some detailed studies were undertaken. Four broad-band MT stations were deployed on the C-profile to give more detailed images of the NAF. Two profiles were collected in the Erzincan Basin (F-profile with 16 stations and G-profile with 8 stations). Chapter 6 is devoted to processing of the MT data collected on the F and G profiles.

4.2.6 D-profile

The final month of field work (October 2005) was used to extend the B-profile onto the Arabian Plate and to collect a central profile. The D-profile had 12 stations and extends from Diyarbakır to the Karlıova Triple Junction and crosses the BSZ (Figure 4-1). Two

more stations were added on A-profile around Diyarbakır during these measurements. All stations collected high quality time series data.

Table 4-1. Summary of MT data acquisition in the summer of 2005 in eastern Turkey. LP and BB stand for long-period and broad-band respectively.

Profile	A	B-(north)	E	C	F	G	B-(south)	D	TOTAL
Start date	12-May	20-June	4-July	19-Aug.	29-Aug.	10-Sep.	27-Sep.	3-Oct.	174 days
End date	17-June	23-July	23-July	23-Sep.	9-Sep.	14-Sep.	1-Nov.	1-Nov	
L.P. stations	20	16	-	18	-	-	8	12	74 LP
B.B. stations	13	-	16	4	16	8	-	-	57 BB

The MT data collection took 174 fieldwork days and 4 weeks of pre-field preparation. Magnetotelluric data were recorded at a total of 133 stations. All the long-period MT stations were successful while two broad-band stations on E-profile could not be used for interpretation due to instrument-related problems. Therefore, 74 long-period and 57 broad-band stations were used for transfer function estimation. Table 4.1 summarizes the MT data acquisition.

4.3 Magnetotelluric instrumentation

4.3.1 Broad-band MT system

The V5-2000 Magnetotelluric system of Phoenix Geophysics was used for broad-band MT data collection (Figure 4-2). The University of Alberta owns two of these instruments which record both electric and magnetic field data. An additional instrument that record just electric fields was loaned by Phoenix Geophysics for the duration of the survey. These instruments are synchronized by time signals broadcast by the Global Positioning Satellites (GPS) and use a 24 bit analog-to-digital converter to give a wide dynamic range.

Figure 4-2. Phoenix V5-2000 MT system. From left to right; five non-polarizing electrodes, 3 induction coil cables, 3 MTC-50 induction coils, battery, recording unit, GPS antenna, case for the unit. Picture used courtesy of Phoenix Geophysics.

Non-polarizing electrodes were used to measure the electric field in two orthogonal directions, usually magnetic north-south and east-west. A non-polarizing electrode consists of a porous porcelain base that is sealed on the top and the sides. It has a metallic conductor immersed in a saturated solution (electrolyte) of a salt to avoid unwanted voltages generated by direct contact of the metal with the soil. This electrolyte acts as a liquid connection between the wire and the soil. Contact with the ground is accomplished by infiltration of the solution through the porous base. The electrodes are typically placed 100 m apart to give a measurable signal which must be much higher than noise levels. Most of the electric field noise comes from the electrodes and the most practical way to increase the signal-to-noise ratio is using larger dipole lengths. The broad-band MT system measures magnetic field variations with three orthogonal induction coils that measure the temporal changes in the magnetic field through the voltage induced in a solenoid (coil). Collection of high quality MT data requires that the coils are mechanically stabilized, and this usually requires burial. The wind causes noise through vibration of the induction coils which induces voltages in the coil that are unrelated to the MT signals. The MTC-50 induction coils used in this study give data in the frequency range 384-0.000018 Hz. The power required to run the MT system is provided by a 12 V battery. These units use a compact flash card to store the data. Details of data recording and bands can be found at http://www.phoenix-geophysics.com/products/receivers/mtu/?

4.3.2 Long-period magnetotelluric systems

The NIMS (**N**arod **I**ntelligent **M**agnetotelluric **S**ystems) instruments were used for long-period MT data collection. Electric field measurements were made using the same non-polarizing electrodes and wires as for the broad-band MT systems. However variations of Earth's magnetic field are measured with a three component fluxgate magnetometer. The fluxgate sensors must be precisely oriented to detect variations in the three components of the Earth's magnetic field. Details of the operation of the fluxgate magnetometer can be found in Russell and Narod, (1994).

The NIMS instruments sample the electric and magnetic fields at 8 Hz. Data are recorded on a compact flash card and GPS synchronization used for accurate timing. The NIMS systems used in this study give data in the period range 1-20,000 s. There are several technical and practical differences between the broad-band and long-period MT systems:

The power needed to run the NIMS instrument is 10 times less than the power needed for the V5-2000 system.

Figure 4-3. The NIMS MT system. From left to right; three component fluxgate magnetometer, sensor cable, GPS antenna and the data logger contained in the gray plastic case. Palmtop computer is used to control the data logger.

Induction coils can be used to obtain long-period MT data if a long time series is recorded. However, the fluxgate magnetometers cannot be used for high frequency MT data collection due to their higher noise levels in this frequency band.

The total weight of the V5-2000 system is about 50 kg while the whole NIMS systems weigh only about half this. This makes NIMS deployment easier if vehicle access is not possible or if difficult digging conditions are encountered.

4.4 Magnetotelluric time series analysis

Figure 4-4 shows approximately one hour of simultaneous NIMS time series data at three MT stations on the A-profile near Elazığ. These time variations contain information about both the magnetosphere and the resistivity of the Earth beneath the recording station. Data processing is needed to extract information about the resistivity structure of the Earth from the time series. The conversion of these data into frequency domain estimates of apparent resistivity and phase is known as time series processing. Horizontal magnetic field variations are generally small because the source is far away from the Earth's surface. However the horizontal electric fields and the vertical magnetic field depend on the resistivity of the Earth and show larger variations from site to site (Figure 4-4).

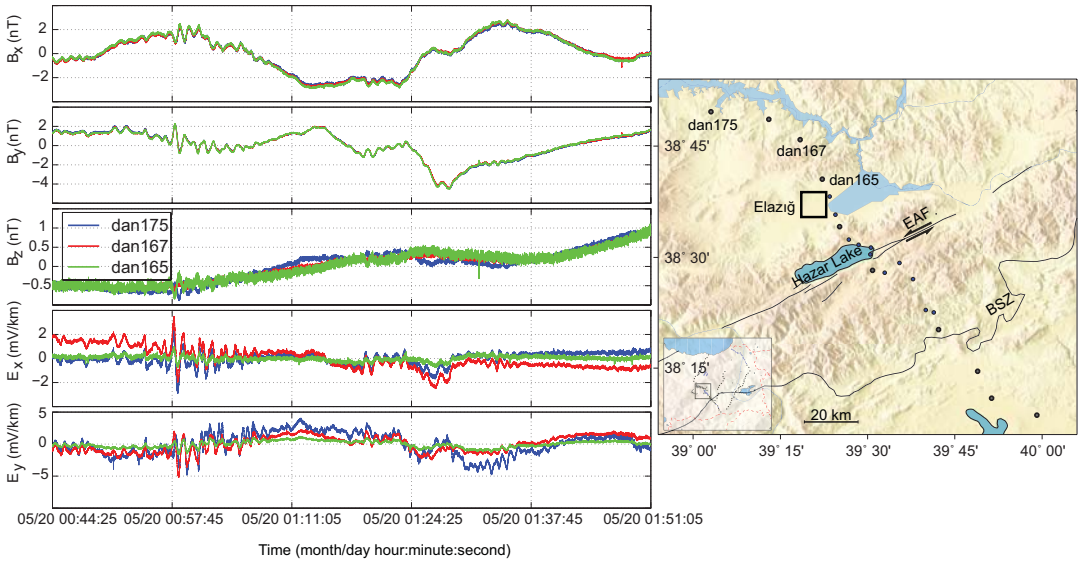

Figure 4-4. Time variations in the magnetic and electric field at three locations around Elazığ. Note that the horizontal magnetic fields are very similar, while the electric field data show significant variations from site to site.

4.4.1 Principles of MT data reduction

Time series processing requires that the time series are converted into frequency domain estimates of impedance and other transfer functions. This typically involves estimating a

small number of impedance values (10-100) from a time series containing more than a million data points. The transfer function estimates are inexact due to noise in the measured electric and magnetic field data. If it is assumed that the external source fields are spatially uniform and the noise can be considered Gaussian, a linear least squares method can be used to estimate transfer functions. This process is described by Sims et al., (1971) who showed that a number of equations can be derived for the Z_{xy} component of the impedance tensor. One formulation can be written as:

$$Z_{xy} = \frac{\langle H_x H_x^* \rangle \langle E_x H_y^* \rangle - \langle H_x H_y^* \rangle \langle E_x H_x^* \rangle}{\langle H_x H_x^* \rangle \langle H_y H_y^* \rangle - \langle H_x H_y^* \rangle \langle H_y H_x^* \rangle} \tag{4.1}$$

or alternatively,

$$Z_{xy} = \frac{\langle H_x E_x^* \rangle \langle E_x E_y^* \rangle - \langle H_x E_y^* \rangle \langle E_x E_x^* \rangle}{\langle H_x E_x^* \rangle \langle H_y E_y^* \rangle - \langle H_x E_y^* \rangle \langle H_y E_x^* \rangle} \tag{4.2}$$

where * denotes complex conjugate. Other estimates are possible but it can be shown that they are numerically unstable in certain circumstances. The autopower of the electric and magnetic fields should be uncorrelated as well as the cross power of the parallel electric and magnetic fields. Thus eq. 4.1 reduces to:

$$Z_{xy} = \frac{\langle E_x H_y^* \rangle}{\langle H_y H_y^* \rangle} \tag{4.3}$$

Eqs. 4.1, 4.2 and 4.3 are in the frequency domain and $\langle\rangle$ denotes the stacked average of many estimates around the frequency ω . The estimated value of Z_{xy} is sensitive to noise in the electric and magnetic fields. For example, in 4.3, if the measured H_y contains noise, then,

$$H_{y\,obs.} = H_y + H_{y\,noise} \tag{4.4}$$

$$\langle H_{y\,obs.} H_{y\,obs.}^* \rangle = \langle H_y H_y^* \rangle + \langle H_{y\,noise} H_{y\,noise}^* \rangle \tag{4.5}$$

Thus, noise is amplified and estimates of Z_{xy} will be downward biased. To mitigate this bias, an alternative approach is to use eq. 4.2. Again it can be shown that:

$$Z_{xy} = \frac{\langle E_x E_x^* \rangle}{\langle H_y E_x^* \rangle} \tag{4.6}$$

This estimate will be susceptible to noise in the electric field E_x that will cause the estimate for Z_{xy} to be too large (upward biased) (Swift, 1967; Sims et al., 1971). One method to reduce the effects of bias is to compute the weighted average of the upward and downward biased estimates (Jones, 1977). A better way is to use the remote reference method (Gamble et al., 1979). This method involves deploying additional sensors at a remote, preferably electromagnetically quiet, location. Magnetic remote reference is favored over electric, because magnetic fields are homogeneous in the vicinity of lateral inhomogeneities and less contaminated by noise than the electric field. Therefore, multiplying eq. 4.1 through 4.3 by the conjugates of the remote fields eliminates uncorrelated noise between the sites; correlated noise that is present in both sites cannot be removed by this method.

Application of remote reference processing led to a major improvement in the quality of MT data. However, the simplistic processing strategy can fail if the MT data contain non-Gaussian noise. Egbert and Booker (1986) showed that this problem could be overcome through the application of robust statistics. Robust processing systematically adjusts the weighting of each estimate to account for departures from a Gaussian distribution (Chave et al., 1987; Chave and Thomson, 1989). Egbert (1997) developed a multiple-station magnetotelluric data processing algorithm using multivariate statistical methods to identify and remove coherent and incoherent noise.

4.4.2 MT data processing

The robust multiple-station MT data processing software of Egbert (1997) was applied to all the MT time-series data collected in eastern Anatolia. The time series data were visually inspected and compared to neighboring stations in order to identify data segments containing noise. These could have been caused by electrode problems, broken telluric wires or instrument failure. These bad segments were excluded from further processing. The selected data segments were pre-whitened within a decimation scheme using an adaptive, autoregressive filter described by Egbert and Booker (1986). The data were then Fourier transformed and both local and remote estimates of the impedance computed. Finally, components of the MT impedance tensor and two magnetic transfer functions were

calculated for logarithmically spaced frequencies using the statistically robust method of Egbert and Booker (1986).

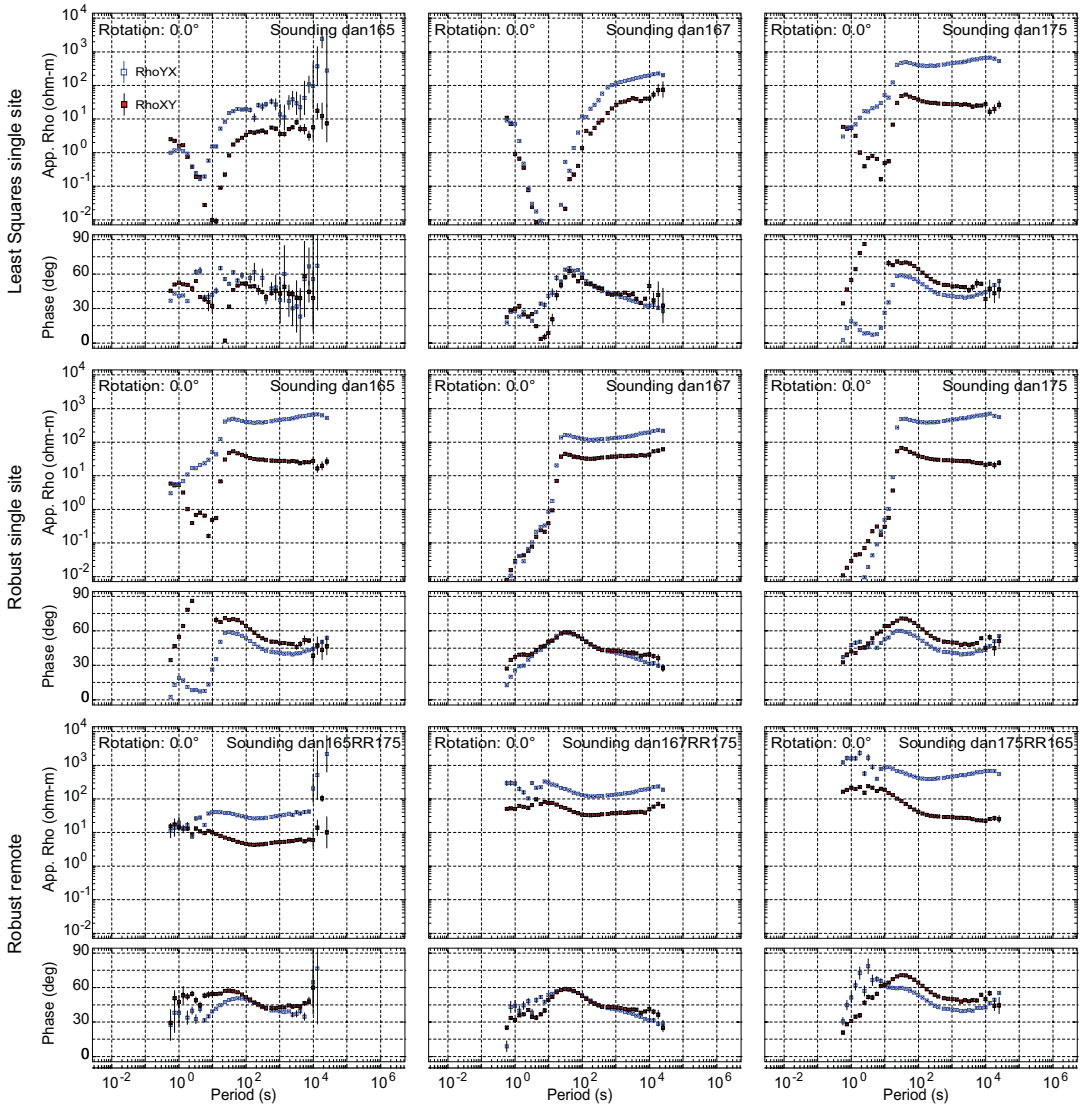

Figure 4-5. Local least squares (first row), local robust (second row) and remote robust (third row) processing of three MT stations around Elazığ (see Figure 4-4 for station locations).

The results of this data processing are shown in Figure 4-5. The XY notation defines the impedance estimated from E_x and H_y, and YX denotes the impedance computed from E_y and H_x. The signal period increases to the right, corresponds to an increasing depth of penetration in the Earth. MT measurements were made in magnetic coordinates where X denotes local magnetic north and Y denotes magnetic east (see details in Chapter 2).

Figure 4-4 shows similar MT data quality at all three stations. The horizontal magnetic fields were quite similar at all sites, while the electric field amplitudes show more site-to-site variation. Electric fields at station dan165 are 5-10 times lower than the other two stations (Figure 4-4) which reduces the signal-to-noise ratio at this site. Furthermore, this station shows a strong downward bias due to noise in the high frequency magnetic fields. Simple least-squares estimation failed while the robust method succeeded and gave a smooth curve for this station. Downward bias at short periods (T<20 s) caused by random noise in the magnetic data is successfully removed by using a remote reference station (Gamble et.al., 1979). Another reason for noisy estimates for periods around 10 s in Figure 4-5 is the presence of low signal strength in the so-called MT dead band (Garcia and Jones, 2008).

4.5 Dimensionality and directionality

Once the MT impedance tensor has been estimated, the next stage of data analysis is to determine the dimensionality and directionality of the tensors. Dimensionality analysis is used to determine if the data require a 1-D, 2-D or 3-D interpretation. Directional features of the MT data are also closely linked to dimensionality. For example, acute angles between geoelectric strike and induction vector directions and varying directions in period are generally indications of a 2-D or 3-D subsurface. Furthermore, the real parts of the induction vectors are expected to be orthogonal to the geoelectric strike directions in the 2-D scenario. This relationship will not be observed in a 3-D geoelectric environment. Directionality analysis is required to determine the geoelectric strike direction that is used in 2-D inverse modeling.

4.5.1 Dimensionality analysis

The dimensionality of the MT impedance tensor at a given frequency can be quantified from the skew values (Swift, 1967; Bahr, 1991) defined in Chapter 2. A skew value $\eta > 0.3$ generally implies the MT data are three-dimensional. However lower skew value are not considered an adequate indication that the data can be considered 2-D (Simpson and Bahr, 2005). Bahr and Swift skew values were computed for the eastern Anatolia data and gave similar results (Figure 4-6)

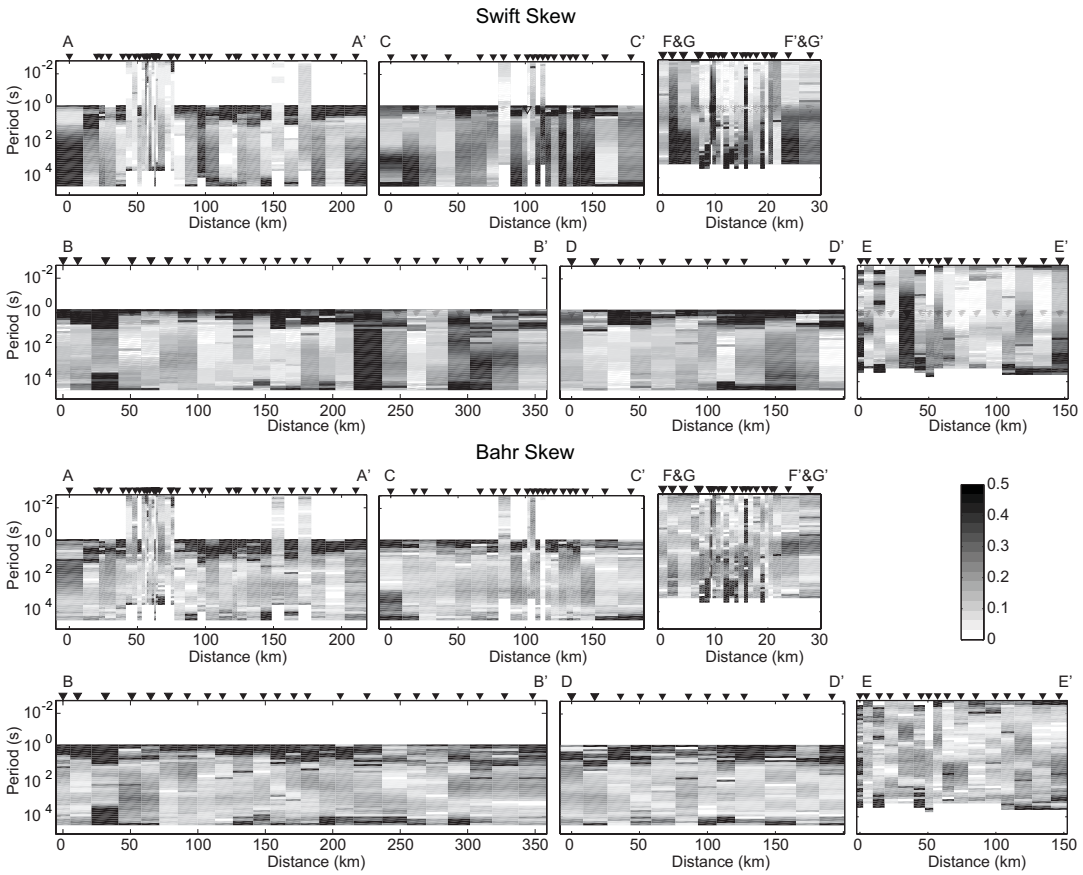

Figure 4-6. Swift skew (top two rows) and Bahr skew (bottom two rows). Stations grouped into profiles and divided into west and east. The A, C, F and G-profiles shows skew values well above the threshold value while the B, D and E profiles are mostly below the threshold. The F and G-profiles are projected onto one profile and the horizontal scale is 4 times exaggerated compared to the other profiles.

Overall, both skew values are similar at short periods but some differences occur at long periods (Figure 4-6). Most skew values at periods less than 10 s are below 0.2. Note that at periods less than 10 s for long-period NIMS data are biased. At periods longer than 10 s, the Bahr skew lies between 0.05 and 0.25 while many sites have Swift skew values >0.3. Individual profiles were then examined to see which MT stations exhibit 3-D behavior.

Virtually all the skew values for the period range 10^{1}-10^{4} s are below 0.25 for the B and D-profiles and below 0.3 for the E-profile (10^{-2}-10^{3} s). On the other hand, a number of data points are greater than 0.3 on the A, C, F and G-profiles. These higher values indicate that data on these profiles require special attention when applying 2-D inversion. This information does not mean that the other profiles are necessarily 2-D. A more rigorous way

to investigate the dimensionality is through tensor decomposition which is described below.

4.5.2 Directionality analysis

Geoelectric strike and induction vector analysis are used for directionality analysis. As mentioned in Chapter 2 there are several approaches that can be used to determine the geoelectric strike direction of the MT impedance tensor. The most widely used methods include analysis of the induction vectors and tensor decomposition (Groom and Bailey, 1989; McNeice and Jones, 2001).

Tensor decomposition was applied to the MT data using the algorithm of McNeice and Jones (2001) for the period bands shown in Figure 4-7. The central periods of these bands are 10, 100, 500 and 2000 s which correspond to penetration depths of 5 km, 16 km, 35 km and 70 km for a 10 Ωm half-space, respectively. Induction vectors can also indicate the geoelectric strike direction and are plotted for these same period bands in Figure 4-7. Geoelectric strike directions for the B, D and E-profiles do not change as the signal period increases from 10 s up to 2000 s (Figure 4-7) and this is an important indication that the MT data on these profiles can be considered 2-D. This result is consistent with the relatively low skew values observed for these profiles.

Stations on the Arabian Plate show a clockwise rotation in strike direction as the period increases. This rotation is visible at ~2000 s as strike arrows become roughly parallel to the boundary between the Anatolian Plateau and Arabian Plate east of 40.5° E (Figure 4-7). Note that the induction vectors and strike directions are not orthogonal at short periods on the A-profile. This indicates divergence from ideal 2-D behaviour.

Strike directions for the western profiles (A, C, F and G-profiles) are deviated from the direction of the surface fault ruptures. The strike of the NAF around C-profile, and in the Erzincan Basin (F and G-profiles) profiles is approximately 110°-125° NE and ~135° NE respectively. However, geoelectric strike directions were found to be between 80° and 110° NE on the C-profile and 60° and 80° NE on the F and G-profiles (Figure 4-8). A similar difference was also observed on A-profile where the strike of NAF and the calculated geoelectric strike differ by 10°-20° from each other.

The difference is less pronounced at periods of 10-100 s on the C-profile. It is likely that the long-period strike directions for the A and C-profiles are affected by major structural changes across the BSZ as well as strike-slip faults (NAF and EAF). Therefore, strike directions on these profiles are only close to being parallel to the NAF and EAF at short periods. The anomalous strike directions around Erzincan could be a consequence of localized 3-D geoelectric structure, either due to the Erzincan Basin or 3-D regional effects.

Short period (~10 s) induction vectors show no consistent direction across the entire survey area, but do reveal some important local structure (Figure 4-7). The three northern stations on the C-profile point towards the Black Sea. This behaviour is as expected since sea water has a low resistivity (0.3 Ωm, Parkinson, 1962). A similar behavior was expected for stations on E-profile but was not observed, implying another strong conductor is present to the southeast of the coastal sites on the E-profile. This inferred conductor must have a larger inductive effect than the Black Sea. Short period induction vectors (~10 s) also point towards the NAF and EAF on the A and C-profiles. Some 50 km south of the Bitlis Suture Zone another lateral discontinuity is defined by the induction vectors (Figure 4-7).

At intermediate periods (100-2000 s) smooth site-to-site variations in induction vector magnitude and direction are observed. The effect of the Black Sea dominates the induction vector direction at coastal stations up to a period of 100 s and then decreases at periods longer than 500 s. The amplitude of the induction vectors at stations located north of the BSZ decreases significantly at periods longer than 10 s implying that lateral conductivity variations north of the BSZ are smaller than within the Arabian Plate.

Long-period induction vectors on the D and B-profiles point north, indicating that a major conductor must be located under the Northern Anatolian Plateau. Stations on the A-profile point north-northeast and stations on the C-profile point nearly due east. The E-profile shows that the long-period induction vectors reverse direction around Kars and indicate the location of a major conductor at this location. The lengths of the induction vectors are also relatively small on the B and D-profiles north of the BSZ. Overall, the amplitude and direction of mid to long-period induction vectors implies that the region bounded by the Rhodope Pontide Unit in the north and BSZ in the south has relatively low resistivity.

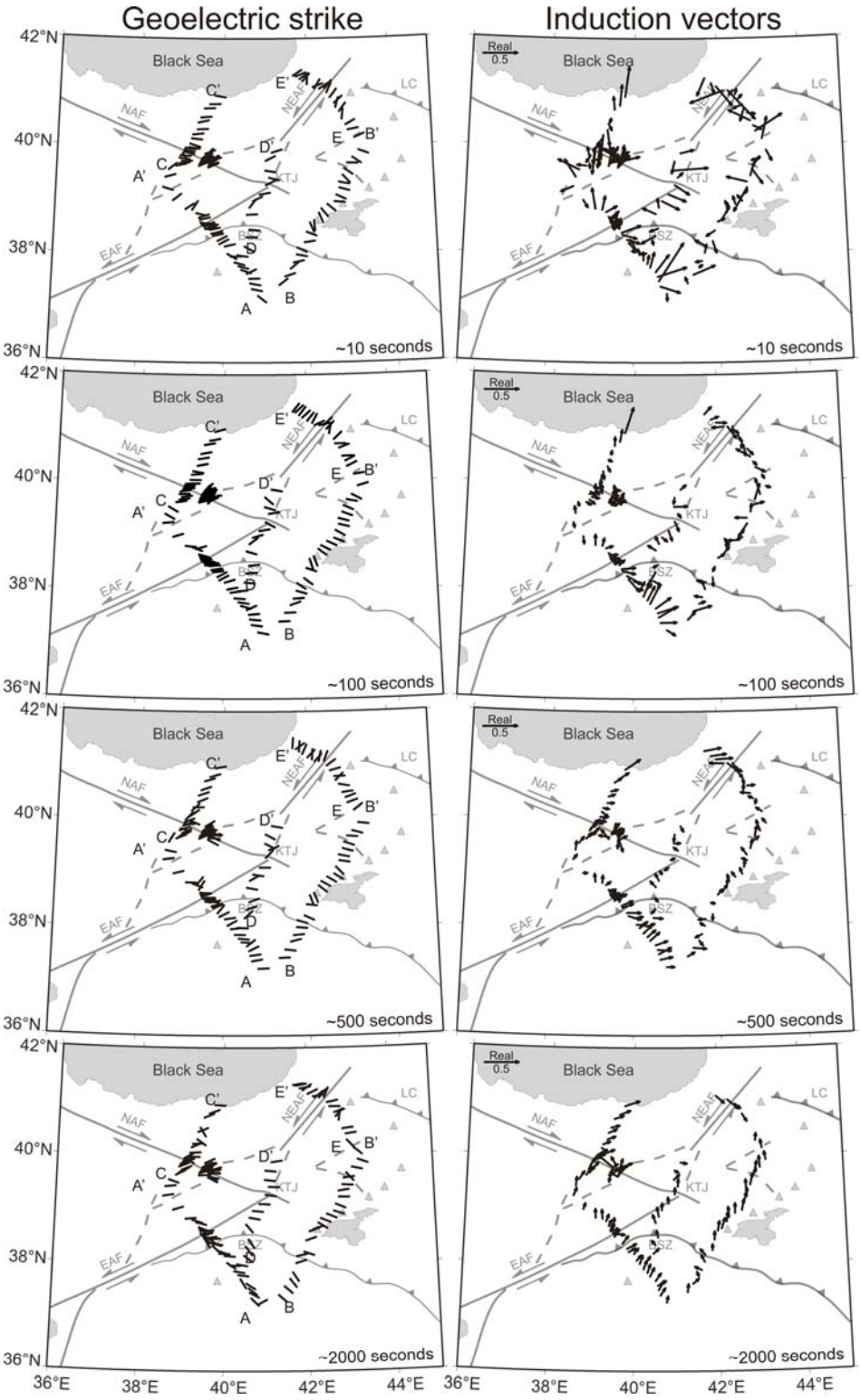

Figure 4-7. Maps showing geoelectric strike directions (left column) and induction vectors (right column). The strike was calculated with the multi-frequency, single station tensor decomposition (McNeice and Jones, 2001). The real part of the Parkinson induction vectors are plotted for the same period ranges.

As stated in chapter 2, the geoelectric strike direction computed with tensor decomposition has an inherent 90° ambiguity. Therefore, one could consider that the geoelectric strike directions on the central part of the C-profile and most of the A-profile could be northwest-southeast oriented. In this case, A-profile induction vectors would be roughly orthogonal with the geoelectric strike direction which makes this profile consistent with a 2-D assumption. Also, the clockwise rotation of the long-period strike directions on the A-profile, particularly for stations on the Arabian plate, must be counterclockwise. This rotation would be consistent with the counterclockwise rotation of the induction vectors from east to northeast (Figure 4-7). This observation is important and could be interpreted as existence of another shallower local conductive anomaly with strike direction perpendicular to the strike of BSZ and EAF.

4.5.3 Summary of dimensionality and directionality analysis

The dimensionality and directionality of the MT data are summarized in Figure 4-8. Note that the Bahr strike and tensor decomposition methods give similar results while the Swift strike is different from these two methods. Only the A, B, C, D and E-profiles are described in detail in this chapter. More information on the F and G profiles are described in Chapter 6.

A geoelectric strike direction of 85° NE is a reasonable assumption for the A and C-profiles. However, the relatively large skew values and oblique alignment of induction vectors implies that the geoelectric structure of these profiles is partially 3-D (Figure 4-8). The nearly parallel alignment of real and imaginary induction vectors on the C-profile implies that a 2-D interpretation of this profile may be valid (Figure 4-8). However, this is not observed on the A-profile. The large skew values and period-dependent strike direction at long periods implies that care is needed when applying 2-D inversion to data collected on the A and C-profiles.

The B, D and E profiles generally exhibit lower skew values and less period-dependent variability of the geoelectric strike than on the A and C-profiles. The preferred strike directions for the B, D and E-profiles were found to be 105°, 90° and 45° NE. These alignments are essentially parallel to the BSZ on the B and D-profiles and parallel to the NEAF for the E-profile. In addition, the geoelectric strike directions are mostly aligned perpendicular to the direction of the induction vectors (Figure 4-7). Antiparallel alignment

of the real and imaginary parts of the induction vectors are more pronounced on the B and E-profiles. In summary, data on the B, D and E-profiles appear to be the most 2-D in the study area.

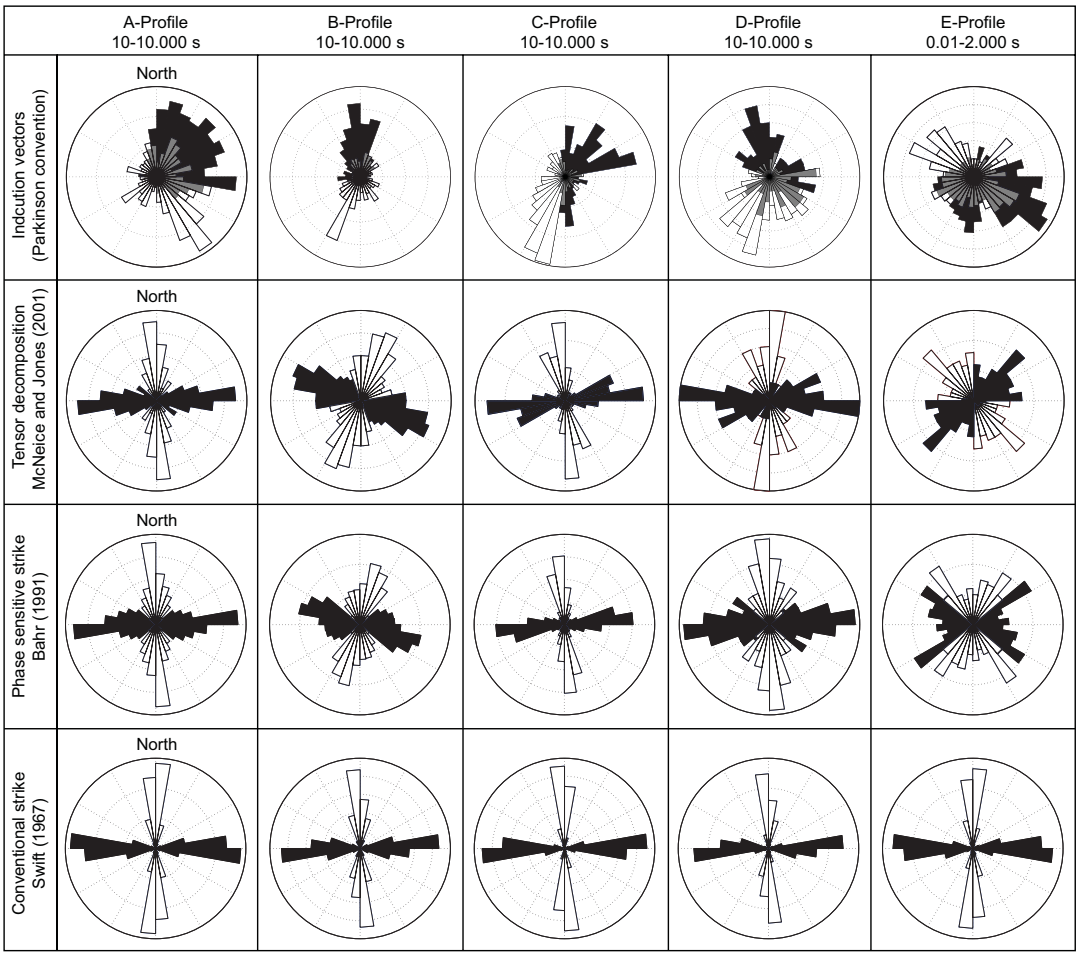

Figure 4-8. Summary of geoelectric strike and induction vector analysis. Each column represents a profile and each row is for a different analysis method. All calculations were made for a period range of 10^1-10^4 s except for the E-profile where only broad-band data were available.

5 INVERSION AND MODELING OF THE MAGNETOTELLURIC DATA

5.1 Introduction

The most important step in magnetotelluric (MT) data analysis is to convert the frequency domain impedance data into a resistivity model as function of true depth. This conversion can be accomplished by (a) forward modeling or (b) inversion. Forward modeling uses trial and error fitting of the measured MT data by systematically changing the resistivity model. Inversion is an automated procedure that iteratively updates the resistivity model so that it fits the MT data in a statistical sense. The nonlinear relationship between the MT data and the resistivity model is generally simplified by linearizing the problem relative to a starting model.

A number of 2-D and 3-D inversion and forward modeling codes are available to the academic MT community and were described in Chapter 2. In this chapter, the application of the non-linear conjugate gradient (NLCG) inversion algorithm of Rodi and Mackie (2001) to the eastern Anatolia MT dataset is described. The MT inverse problem is inherently non-unique, and thus considerable effort is required to validate the preferred resistivity models and determine how well they are constrained by the measured MT data. Furthermore, the 3-D inversion algorithm WSINV3DMT by Siripunvaraporn et al. (2005a) was also used to invert the full MT impedance tensor data where applicable.

5.2 Two-dimensional (2-D) inversion of the eastern Anatolia MT data

Real MT data always include some 3-D induction effects. If these 3-D effects are small then a 2-D inversion approach can be valid. Thus prior to inversion, it is very important that the dimensionality of the MT dataset is investigated. In Chapter 4 some widely used

methods of investigating the dimensionality were described and it was shown that most of the MT data collected in eastern Anatolia could be considered 2-D.

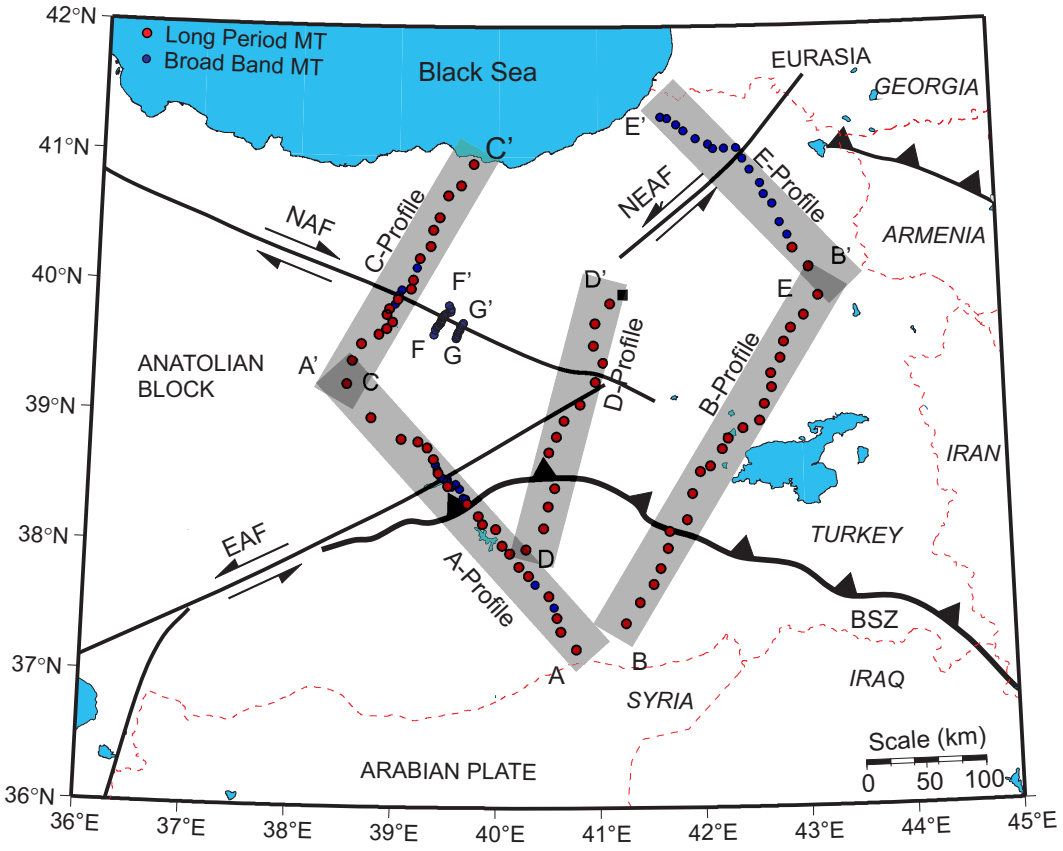

Figure 5-1. Magnetotelluric station locations and profiles in the study area. NAF = North Anatolian Fault; EAF = East Anatolian Fault; BSZ = Bitlis Suture Zone; NEAF = North East Anatolian Fault. Red and blue dots represent long-period and broad-band magnetotelluric stations.

Two-dimensional MT inversions were applied to the seven profiles shown in Figure 5-1. The MT stations were grouped into profiles and the impedance tensors were rotated mathematically to the geoelectric strike directions calculated in chapter 4. The stations were then projected on to a straight line perpendicular to the strike direction. Note that this projection can cause the total length of the profile to be less than on the map shown above. Electromagnetic (EM) energy propagates diffusively within the Earth (chapter 2) which is quite different from the situation in seismic exploration where seismic energy travels as a wave. The diffusive nature of the EM signals means that magnetotelluric exploration cannot sense discontinuities in resistivity structure, but is sensitive to resistivity gradients

and bulk structure. As a result, it is important that the 2-D inversion is not forced to generate a rough model with sharp spatial gradients. Overfitting the measured MT data will generate a rough model that likely contains artifacts that are not required by the measured data. Rather, the MT inversion should find a resistivity model that is as smooth as possible, while also fitting the MT data (Tikhonov and Arsenin, 1977).

5.2.1 Preferred 2-D inversion models

As mentioned above, inversion of MT data with a 2-D algorithm must be undertaken with caution in an environment that is potentially 3-D in terms of geoelectric structure. The mutual consistency of the individual 2-D inversions is a necessary, but not sufficient, step for justifying the use of a 2-D inversion. The dimensionality and directionality analysis should give additional evidence that a 2-D inversion is valid by showing that:

- The geoelectric strike direction is period independent and a similar strike direction is observed at all sites;
- The measured MT data can be fit to a distortion model with a small r.m.s misfit. See chapter 4 for discussion.

However, artifacts can occur in models generated by 2-D inversions, such as the low resistivity zone imaged beneath the northern end of C-profile in Figure 5-2 at a depth of 40 km. This could be the result of a 3-D effect caused by anisotropy or a strong current channeling effect combined with the coast effect in the MT data that is incorrectly interpreted by the 2-D inversion. On the other hand, a similar low resistivity anomaly at ~40 km depth was also imaged beneath the southern half of the A-profile (Figure 5-2). Both of these resistivity anomalies are suspicious in that neither could be identified directly from the real induction vectors (i.e. Parkinson (1959) convention induction vectors do not point towards these anomalies). Another reason for applying 3-D inversion is that 2-D inversions are based on the fact that the stations are aligned perpendicular to the strike direction. If this is not the case, then the impedance tensor is rotated to the strike direction and the stations are projected on a profile perpendicular to the strike direction. This theoretical requirement may result in artificial features in 2-D inversions due to shrinking

of the profiles. Maximum shrinking occurs on the A and C-profiles by some 15% of their actual lengths.

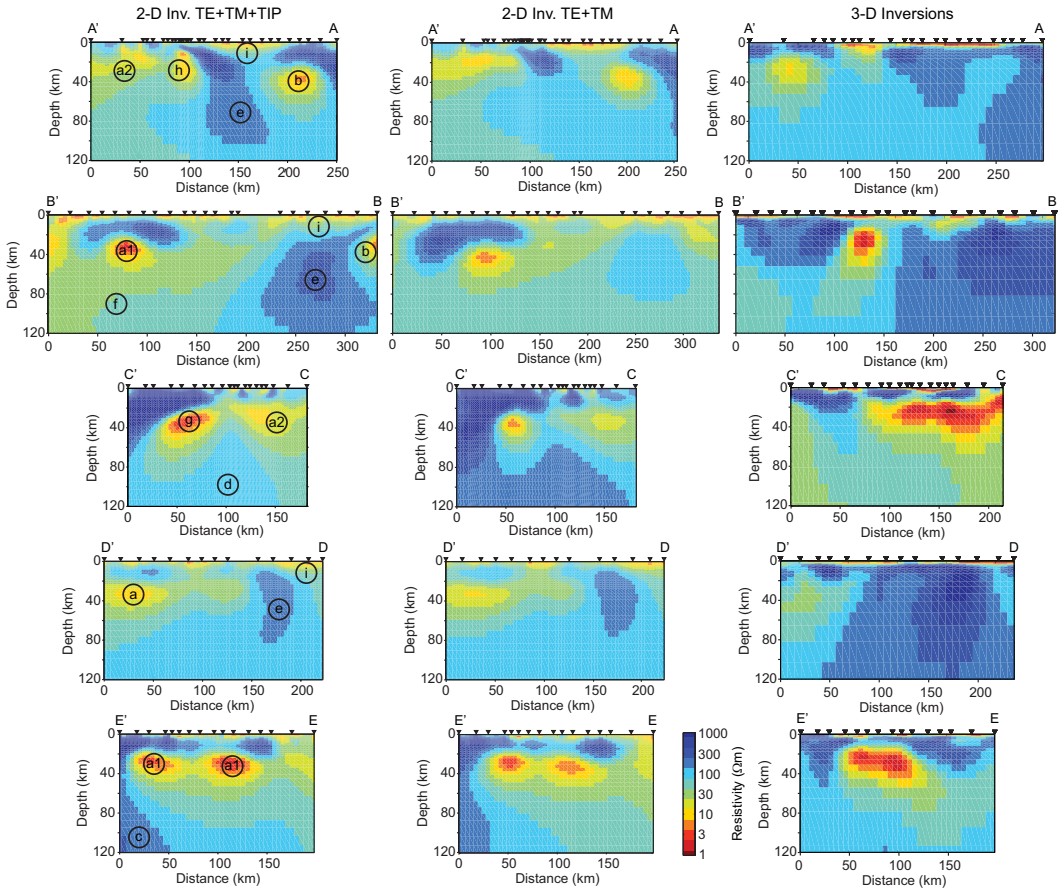

Figure 5-2. Preferred 2-D inversion models (left and middle columns) and vertical 2-D depth slices from the corresponding 3-D inversions. Note that the 2-D inversions used all the available MT stations and data points at every site and a fine mesh. However, some stations were eliminated in the 3-D inversion and the mesh was coarser than in the 2-D inversion. Error floor values of 20%, 5% and 0.02 were used for apparent resistivity, phase and tipper respectively in the 2-D inversions. Error floors of 10% and 20% were used for off-diagonal and diagonal components of the impedance tensor in the 3-D inversions. The regularization parameter tau (τ) and horizontal roughness parameter alpha (α) were set to 10 and 3 respectively. 3-D inversions do not include tipper data so 2-D inversions without tipper data are also shown in the middle column for comparison.

Figure 5-2 shows the preferred 2-D inversion models (left and middle columns) and 2-D slices along the profile obtained from 3-D inversions (right column) for direct comparison. The preferred 2-D inversion models were chosen after evaluating many 2-D inversions with a range of control parameters and starting models. These models used error floors of

20%, 5% and 0.02 for apparent resistivity, phase and tipper data respectively. Static shifts were estimated iteratively by the NLCG algorithm and a homogenous half-space of 100 Ωm was used as a starting model. The Black Sea was included in the starting model as a fixed feature for the inversion of the C and E-profiles. Each inversion was run for up to 200 iterations if not converged earlier. The regularization parameter tau (τ) and horizontal roughness parameter alpha (α) were set to 10 and 3 respectively. The effect of these parameters on final inversion models is further described in the following sections.

However, the real Earth contains features that have a sharp change in resistivity, such as faults, and the contacts between ore bodies and the host rock. Therefore, the user must examine the resolution by performing several inversions with various values of the inversion control parameters. Starting model or *a priori* information can be used to overcome the non-uniqueness. These include: geological information, ocean bathymetry, or other geophysical data such as seismic velocity models. τ=10 and α =3 was used for all the interpreted models in this thesis but α =1 was used for the fault zone studies in chapter 6.

5.2.2 Fit to measured MT data

The degree to which the measured MT data are reproduced by the predicted responses of the inversion model can be expressed numerically by the r.m.s. data misfit. The pseudosections in Figure 5-3 allow a graphical display of the fit at each station, and as a function of period. A satisfactory fit to the measured MT data was obtained for all profiles, including those shown in Figure 5-3. Blank parts on the observed data pseudosections indicate masked bad data points or the fact that data were not available at those periods.

Static shift coefficients were estimated by the inversion program and were in the range 0.1-10 (-1 to +1 in the log domain). Negative static shift values indicate that the curve needs to be shifted up and vice versa for positive values (see Figure 5-4 and Appendix-A). For example, if the observed curve is around 100 Ωm and the estimated static shift is -0.5 (in log domain) then the observed apparent resistivity data will be shifted to 316 Ωm.

Site-by-site misfit and static shift coefficients are shown in Figure 5-4. According to this figure, the inversion was able to fit the A, B and D-profiles very well with low r.m.s.

misfits for all of the stations. However, the data on the C and E-profiles were not equally well fit. The overall r.m.s. misfits are 1.69, 1.54, 2.08, 1.3 and 2.73 for the A, B, C, D and E-profiles respectively. The high r.m.s. misfit values are probably due to lower data quality on the E-profile and 3-D effects due to the effect of the Black Sea coast (discussed in chapter 4).

Static shift coefficients, r.m.s. misfits, and inversion response curves are plotted for every station in Appendix-A.

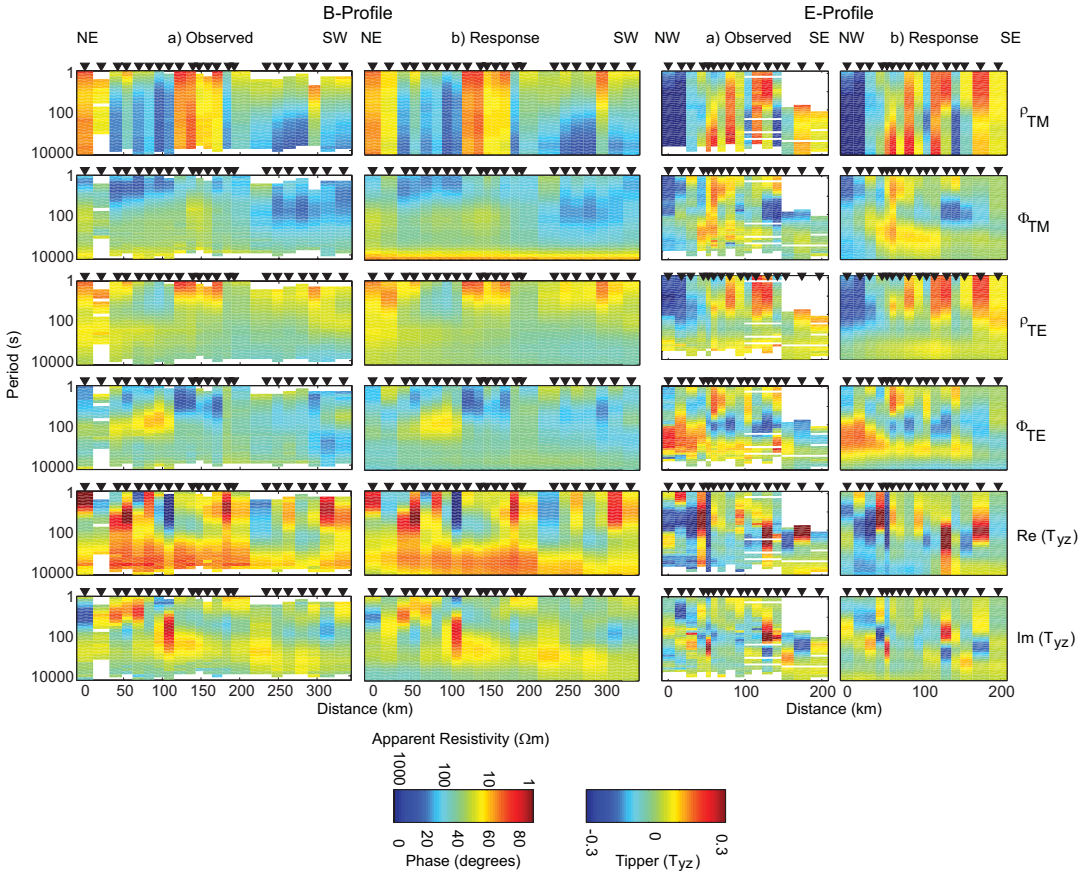

Figure 5-3. Pseudosections of the measured MT data on B (left) and E (right) profiles compared to model responses for the 2-D inversion using $\alpha = 3$ and $\tau = 10$. The top four rows show the apparent resistivity and phase for the TE and TM modes. The bottom two rows show the magnetic transfer functions also called the tipper (T_{yz}). Note that a satisfactory fit to the observed MT data is obtained for the whole period range.

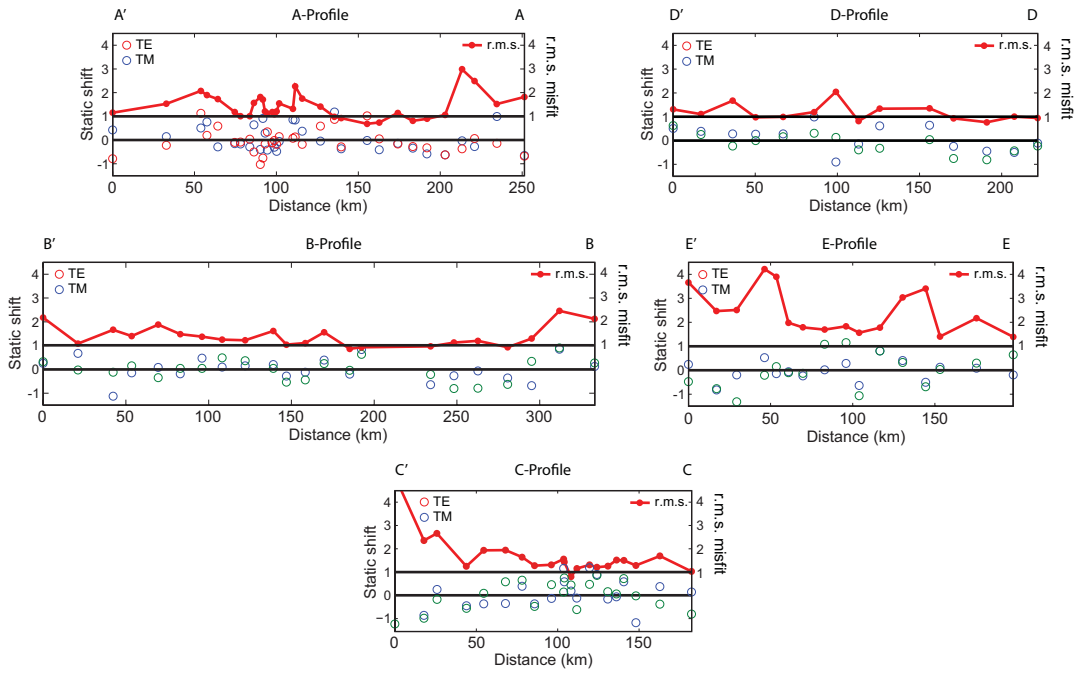

Figure 5-4. Statistical parameters for the 2-D MT inversions. Red dots show the r.m.s. misfit between the observed MT data and the response predicted by the inversion model. The blue and red circles indicate the static shift coefficients estimated by the inversion program. The overall model misfit for each profile is as follows: A=1.69, B=1.54, C=2.08, D=1.3 and E=2.73.

5.2.3 Robust features of the resistivity models

It is important to evaluate the resistivity models derived from the inversions to determine which features can be considered robust. These are features that will be generated by the inversion algorithm for a range of inversion control parameters and different subsets of the measured MT data. There are several factors that must be considered when applying a 2-D inversion to an MT dataset:

- Self-consistency of the resistivity models derived by inverting each data component individually (i.e. TE-mode, TM-mode and tipper)
- Dependence of the final resistivity model on the choice of starting model
- Dependence of the final resistivity model on the choice of model regularization used in the inversion (e.g. alpha and tau)

- Influence of static shift coefficients on the final resistivity model
- Influence of the error floor on the final resistivity model
- Coast effect.

Therefore, before choosing the preferred resistivity model, various inversions with different settings were considered.

5.2.3.1 Self-consistency of MT data components

The use of 2-D inversion is an approximation that must be applied to an MT dataset with caution. Tests must be applied to determine the validity of the 2-D analysis. In the situation of a 2-D Earth, it was shown in chapter 2 that the transverse electric (TE) mode and transverse magnetic (TM) mode data are sensitive to different aspects of the subsurface. In general, the TE mode is more sensitive to low resistivity features (conductors) while the TM mode is more sensitive to resistive features and along profile variations in resistivity. A third component of the data is the tipper which is part of the TE mode in a 2-D situation. Since it is not derived from electric fields (which can be distorted) it can be considered independent of the TE mode impedances.

When analyzing MT data with a 2-D approach, several facts can invalidate the approach. If the data are 3-D, or 2-D with anisotropy, then the 2-D inversion will not be able to recover the true subsurface model. The presence of 3-D resistivity or anisotropic structures can prevent the TE and TM mode data finding a consistent model (Boerner et al., 2000; Mareschal et al. 1995). Theoretically, electrical anisotropy is the combined response of small-scale electrical resistivity variations that are individually unresolvable by diffusive electromagnetic fields. An example of this kind of data is observed in Northern Alberta above an ancient subduction zone where interconnected graphite causes a significant drop in the TE mode resistivity curve while the TM mode does not detect any low resistivity anomaly (Boerner et al., 2000; Türkoğlu et al., 2009).

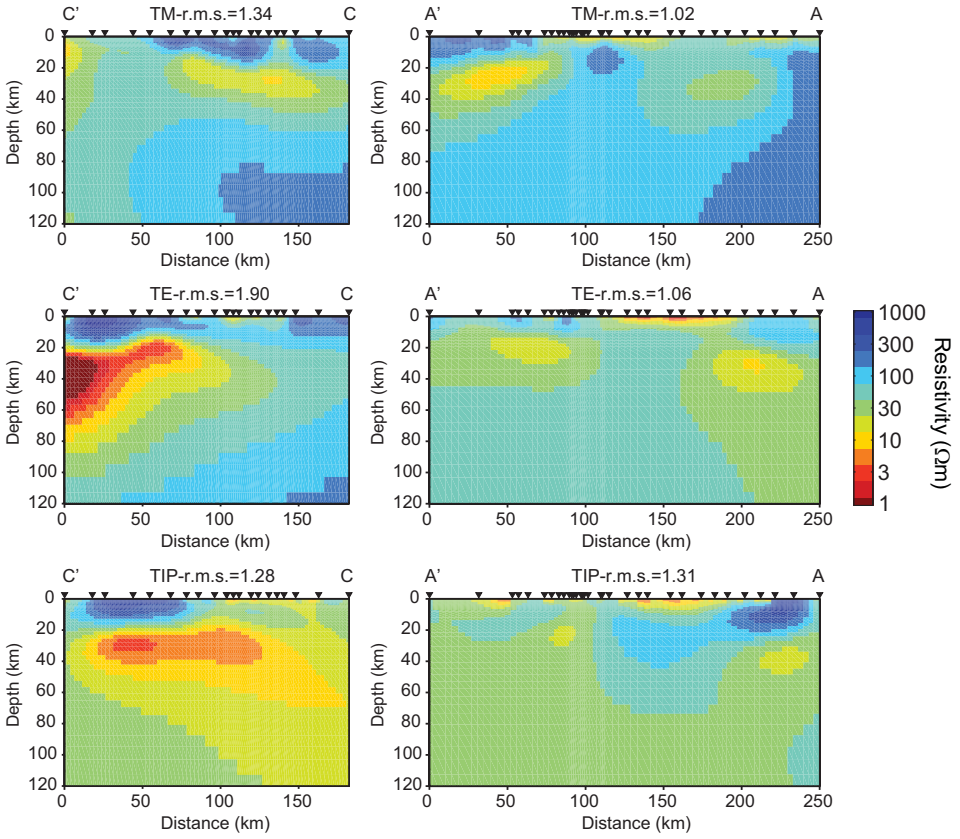

Figure 5-5. Inversion of single components of the MT data for the A-profile (left column) and C-profile (right column).

A first stage in validating the 2-D approach is to determine if each of the three data components can be inverted independently for a particular profile. Only if each component can be inverted separately can the joint inversion be considered. Figure 5-5 shows individual TE, TM and tipper inversions for the A and C-profiles, which are two of the most complicated MT profiles collected in eastern Anatolia. Each inversion used the same mesh and inversion control parameters. For the A-profile, the TM and TE inversions showed similar features. However, significant differences were observed between the TM and TE mode inversions on the C-profile, especially in the northernmost 70 km of the model and in the depth range 20-60 km. The TE inversion r.m.s. misfit was the highest (1.90) of all the profiles. Therefore, the TE component of the MT data were not fit very well on the C-profile compared to the other data components and profiles (Figure 5-5). It was shown in section 5.2.1 that joint 2-D and 3-D inversions produced similar resistivity models. However, 2-D inversions of the individual components were able to fit observed

data for the A, B, D and E-profiles while both components and 3-D inversion indicated that the northern half of the C-profile may not be equally modeled compared to other profiles.

5.2.3.2 Dependence on the initial model

Iterative inversion algorithms require a starting model for the algorithm to begin. In general, the starting model can be freely chosen and in the absence of geological information, a uniform half-space model is generally used. An appropriate half-space resistivity can be determined by finding the average resistivity of the individual MT sounding curves. Figure 5-6 shows stacked plots of the apparent resistivity curves (ρ_{xy} and ρ_{yx}) in geographical coordinates (e.g. not rotated to geoelectrical strike direction).

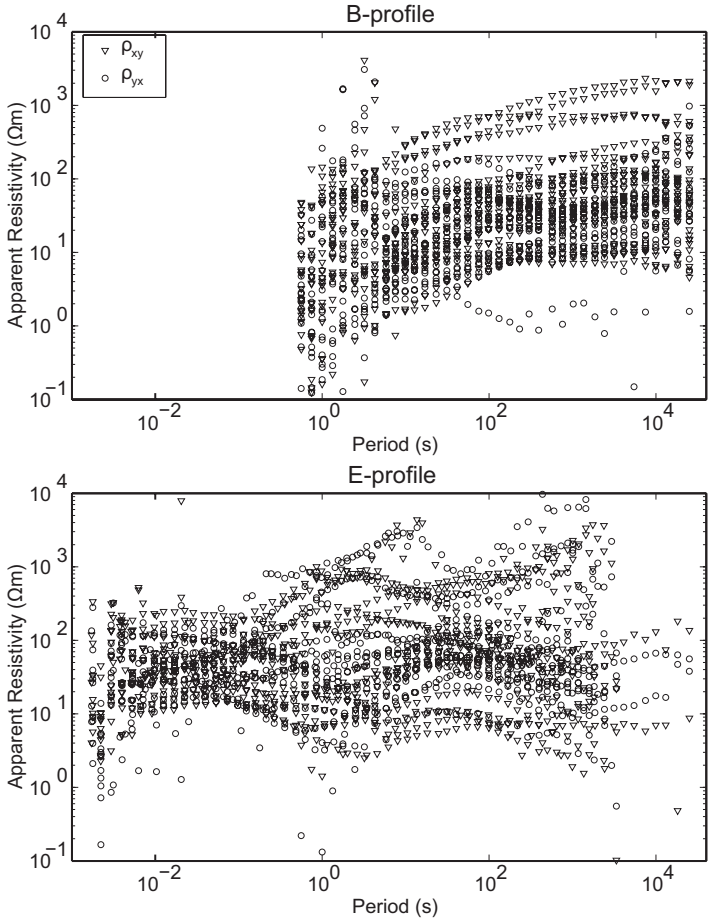

Figure 5-6. Stacked plots of apparent resistivity curves (ρ_{xy} and ρ_{yx}) for the B-profile (left) and E-profile (right). Note that the B-profile has only long-period MT data while the E-profile has both broad-band and long-period MT data.

According to Figure 5-6 the majority of the apparent resistivity values fall between 10 Ωm and 100 Ωm. Therefore, TE, TM and tipper data were jointly inverted for B and E-profiles using 10 Ωm, 100 Ωm and 1000 Ωm half-space resistivities as initial model to investigate whether final model features depend on the starting model (Figure 5-7).

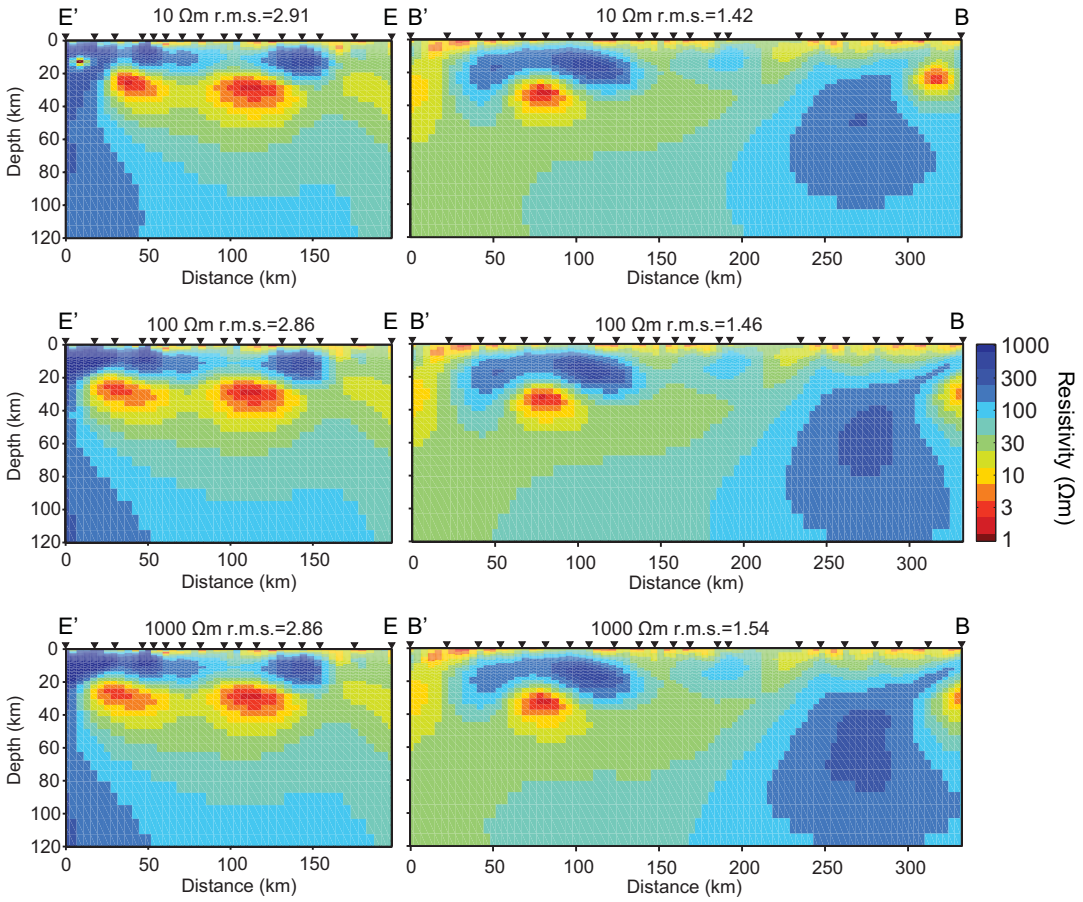

Figure 5-7. Influence of the starting model resistivity on the final inversion model for the B-profile (right) and E-profile (left). The same inversion parameters were used in all inversions for each profile. The first, second and third rows used starting model resistivities of 10 Ωm, 100 Ωm and 1000 Ωm respectively. Note that left side of the profiles indicates north or the direction closest to north.

Due to the diffusive nature of electromagnetic signal propagation in the Earth, MT resolves the conductance of the model features rather than the exact geometrical shapes of these structures. Therefore, starting the inversion with a lower resistivity half-space may cause the final model to have narrow bands of low resistivity pockets while a higher resistive half-space starting model may cause wider anomalies with higher resistivity. Overall, the

best resolved parameter is the conductance of the feature. In Figure 5-7 most model features do not depend on the initial model on both profiles. The difference between final model r.m.s. misfits was less than 0.1 for different starting models for both profiles. Minor differences between models were observed. All subsequent inversion models presented in this thesis were obtained using a 100 Ωm homogenous half-space as the starting model.

5.2.3.3 Effect of regularization

It is well known that the MT inverse problem is non-unique, which means that more than one resistivity model can be found that will fit a finite set of noisy MT data (Menke, 1989; Whittall and Oldenburg, 1992). Inversion algorithms such as the NLCG algorithm of Rodi and Mackie, (2001) generally use more model parameters than there are data points, which results in an under-determined set of equations. Solution of the inverse problem therefore requires additional constraints to be applied to the resistivity model. This is generally achieved with regularization that seeks a model that minimizes the misfit between the observed and predicted MT data and also keeps the model as spatially smooth as possible (Tikhonov and Arsenin, 1977). As mentioned in section 5.2, and in chapter 2, a regularized inversion reflects the diffusive nature of electromagnetic signal propagation in the Earth.

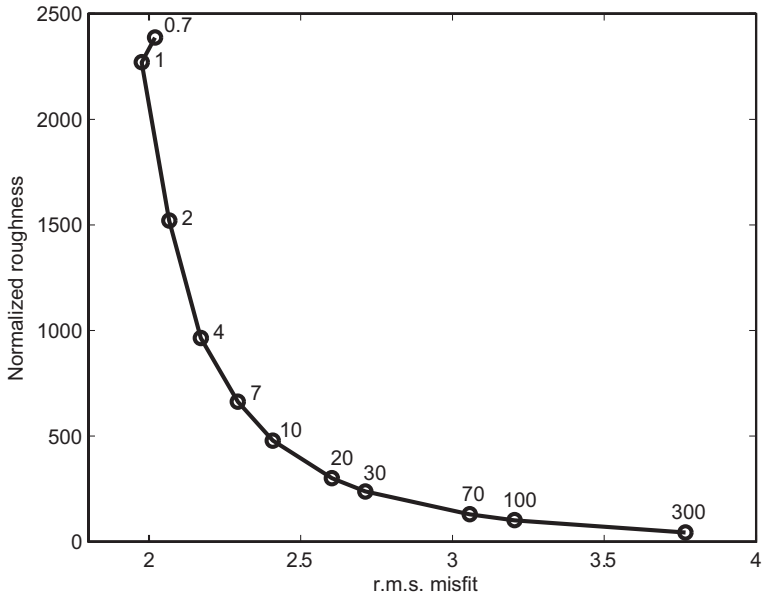

Figure 5-8. Resistivity model normalized roughness versus r.m.s. data misfit for a range of tau (τ) values for the F-profile.

In the NLCG6 inversion algorithm, the regularization parameter tau (τ) controls the overall smoothing of the model. As the value of τ increases, the model becomes smoother and the measured MT data are not fit as well. Figure 5-8 shows the trade-off between the data fit and model smoothness. The corner of the so called L-curve defines the optimum value of τ for a given MT data set and compromise between fitting the MT data and generating a smooth resistivity model. The L-curve test was applied to the F profile to determine the optimum τ value for the inversions. This test used a range of τ parameters from 0.7 to 300. Note that models that fit the MT data will have a low value of the r.m.s. misfit and are spatially rough. A compromise between these characteristics was obtained when $\tau = 10$ (i.e. the corner of L-curve in Figure 5-8).

Another way that the regularization in the NLCG algorithm can be controlled is to specify if the resistivity model is smooth in the horizontal or vertical directions. Horizontal smoothing is controlled by the parameter α. A combination of these two parameters (α and τ) was investigated. Three values of τ and two values of α were used (Figure 5-9). A 100 Ωm half-space was used as a starting model in all inversions. Error floors of 20%, 5% and 0.02 were used for apparent resistivity, phase and tipper data respectively. Figure 5-9 shows the six inversion models obtained for the B-profile. It is observed from the top two panels of Figure 5-9 that the large α value forces the inversion to produce horizontally smoother models in the case of smaller τ values. As the regularization parameter τ is increased, the effect of α is less pronounced but still present. It was noted that small values of tau ($\tau = 3$) allowed the inversion to find a resistivity model that fits the MT data with an r.m.s. data misfit values close to 1. However, these models contain some rough features such as the low resistivity pockets between the stations at shallow depths (0-10 km). Also two deeper low resistivity pockets are observed at both ends of the profile with smaller values of α and τ. These features are close to the ends of the profile and are not well constrained. On the other hand, selecting a large τ value ($\tau=30$) causes loss of information inherent in the data (Figure 5-9) so the measured MT data are not well fit.

The influence of α and τ on the inversion of MT data for the other profiles showed similar results. Overall, the same major features were visible in every resistivity model, although some features close to the end of the profiles were observed to depend on a particular selection of α and τ values. Therefore, based on Figure 5-8 and Figure 5-9 values of $\alpha= 3$

and τ= 10 were chosen as the preferred regularization parameters. The models shown in Figure 5-2 also used these parameters.

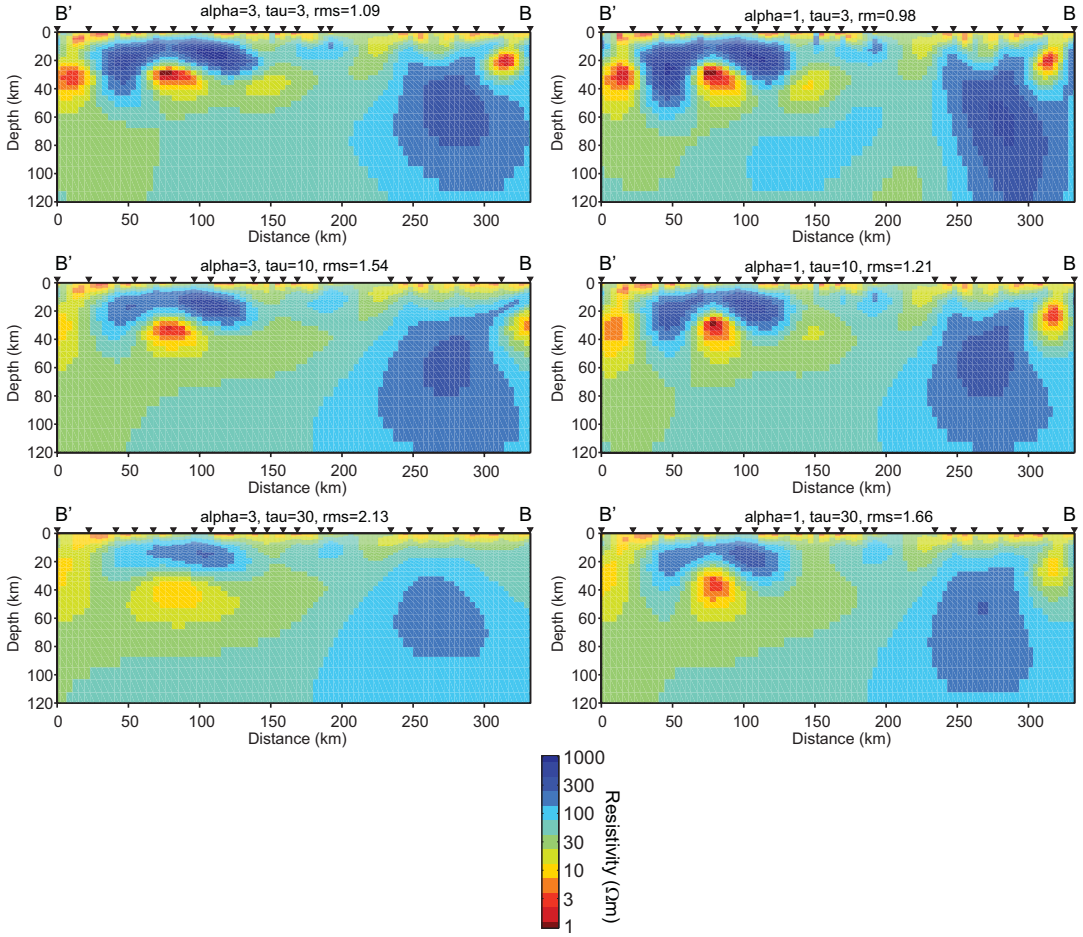

Figure 5-9. Influence of the regularization parameter (τ) and vertical to horizontal smoothness parameter (α) for the B-profile. α = [3, 10, 30] and τ = [1, 3].

5.2.3.4 Influence of static shift coefficients

As reviewed in chapter 2, static shifts in MT data are the frequency-independent offsets of the apparent resistivity curves. They are the result of small-scale, near-surface resistivity anomalies. The size of these anomalies is much less than the skin depth of the electromagnetic fields (Vozoff, 1991; Fischer et al., 1992). This vertical offset of the apparent resistivity curves can lead to incorrect estimates of layer depths. For example, if the apparent resistivities are shifted by a coefficient *s*, then the depths of layers will be

scaled by $\sqrt{s}$. Static shift coefficients can be estimated or removed by the methods summarized in chapter 2.

- Since phase data are not affected by static shift, the effects of statics shifts can be reduced by assigning larger error floors to the apparent resistivity data than to the phase data.

- Also it should be noted that vertical magnetic field transfer functions (tipper) are independent of galvanic distortions. Therefore, if a joint inversion scheme includes tipper the effects of static shift can be reduced.

- The preferred method is to allow the inversion algorithm to estimate the static shift coefficients. The coefficients are treated as additional parameters to be determined, in addition to the resistivity in each cell of the model. Some assumptions about the coefficients are made by the algorithm, and NLCG6 assumes that the statics must sum up to zero. Another issue to be considered is that there is an inherent trade-off between the static shift coefficients and resistivity structure.

The left panel in Figure 5-10 shows the resistivity model obtained when the static shift coefficients were not estimated by the inversion algorithm. The right panel shows the model when the static shift coefficients were estimated. It can be seen that the main features are the same in each resistivity model. However, the geometry of the vertical low resistivity body close to the EAF (~100 km distance) depends on the method used to estimate the static shift coefficients.

5.2.3.5 Influence of error floor

The normalized data misfit (r.m.s.) depends on the data errors assigned to each data point. Using data errors that are unrealistically small may cause the inversion to fit the MT data in a non-uniform way. Points with small errors will be better fit than those with large errors. A more uniform fit can be achieved by assigning an error floor for every data point. Larger error floor values make it easier to fit the MT data. Data errors are significantly lower than the assigned errors for the inversion. The influence of error floor on the final resistivity models was investigated using three different error floor values. Static shifts

were not estimated by the inversion algorithm for this test to isolate the effect of the choice of error floor.

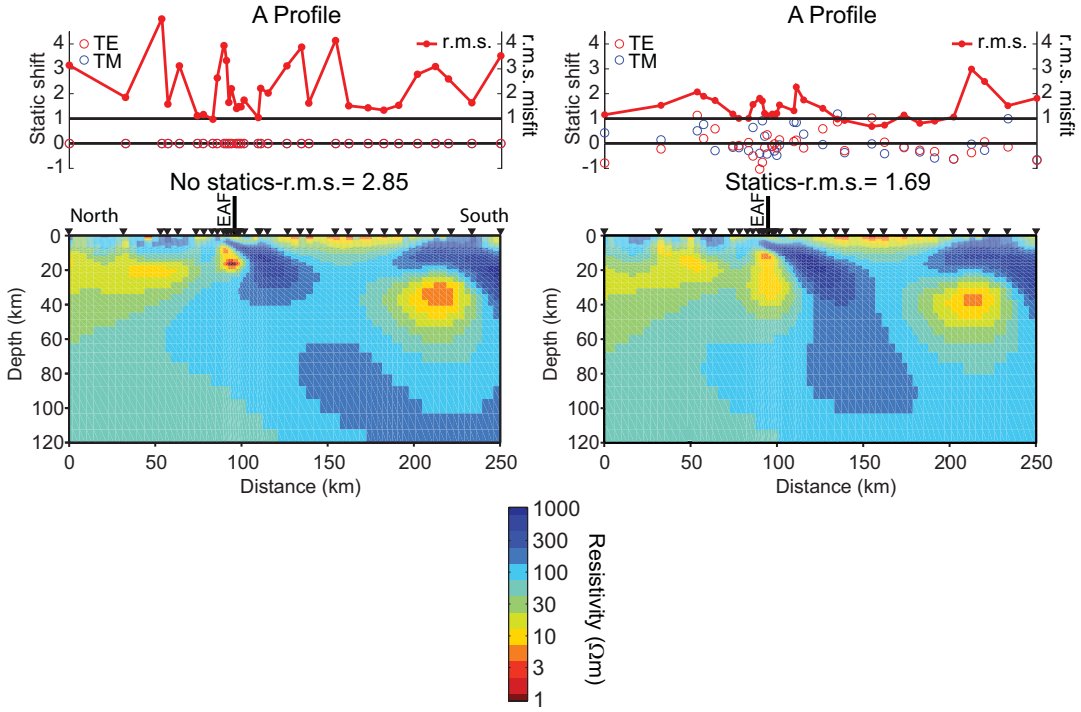

Figure 5-10. Influence of static shift in the 2-D inversion of the A-profile data. Each model is obtained by the joint inversion of the TE, TM and tipper data with error floors of 20%, 5% and 0.02 respectively. Note that the shape of the low resistivity anomaly underneath the EAF (East Anatolian Fault) depends on the method used for estimation of the static shift coefficients. Static shifts are plotted in the log domain, so that a value of 0 means no static shift.

The left panel in Figure 5-11 shows an inversion model with very low error floors (5%, 2% and 0.01). This model recovered some of the known features with very sharp boundaries. However, overall, the inversion was not able to fit the data (r.m.s. = 7.89) adequately. The middle model in Figure 5-11 used the default error floors (20%, 5% and 0.02), and produced a relatively smoother model. The r.m.s. misfit for this model is reduced but still high with a value of 2.85. The right panel model used high error floors for apparent resistivity (100%, 5% and 0.02). The final model r.m.s. was reduced to 1.73 which is very close to the r.m.s. misfit obtained by inversions that used static shift estimation (right panel in Figure 5-10). Furthermore, the final resistivity models obtained in the right panels in Figure 5-10 and Figure 5-11 also look very similar. Therefore, keeping the phase error

floor relatively low and including the tipper in the joint inversion can overcome the static shift problem in MT inversion.

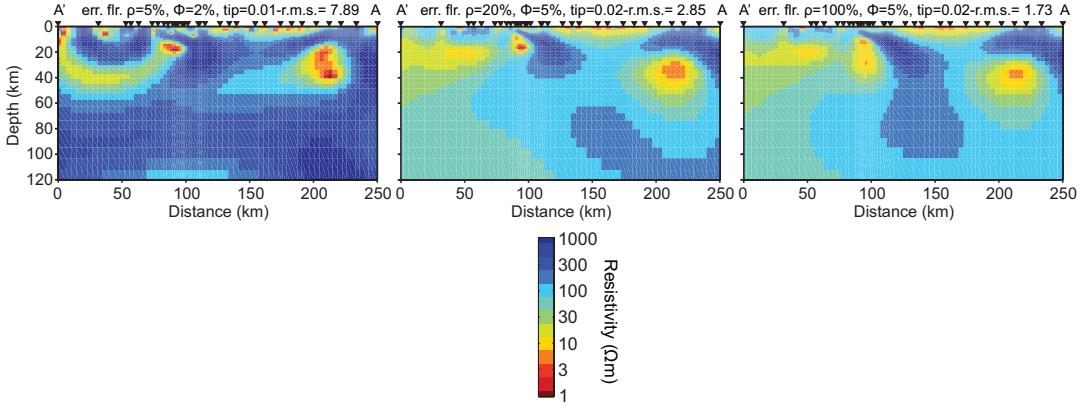

Figure 5-11. Influence of error floor values used in the 2-D inversion of the A-profile. Each model is obtained by TE, TM and tipper joint inversion. Error floors increase from left to right and r.m.s. misfit and model roughness reduces. Error floors as follows: left, 5%, 2% and 0.01; middle, 20%, 5% and 0.02; right, 100%, 5%, 0.02 for apparent resistivity, phase and tipper respectively.

Although the models in Figure 5-11 are generally quite similar, they fit the MT data in different ways. Figure 5-12 shows the observed MT data and inversion model response fit for the site at 0 km on the A-profile. This shows more than one order of magnitude split between the TE and TM mode apparent resistivities. On the left and middle columns the observed data remained constant throughout the inversion while the data on the right column shifted upwards and downwards from their observed levels. As stated before, the TE mode curves are subject to more galvanic distortions; TE data in Figure 5-12 are shifted (upwards) significantly more than the TM mode. The middle panel curves, where the error floor for resistivity is 100%, provided comparable r.m.s. misfit (1.35) to the static shift estimated inversion. Therefore, when the data are not strongly affected by the galvanic distortion, this method is applicable but in case of several orders of magnitude static shift, extensive error floors on the apparent resistivity are needed.

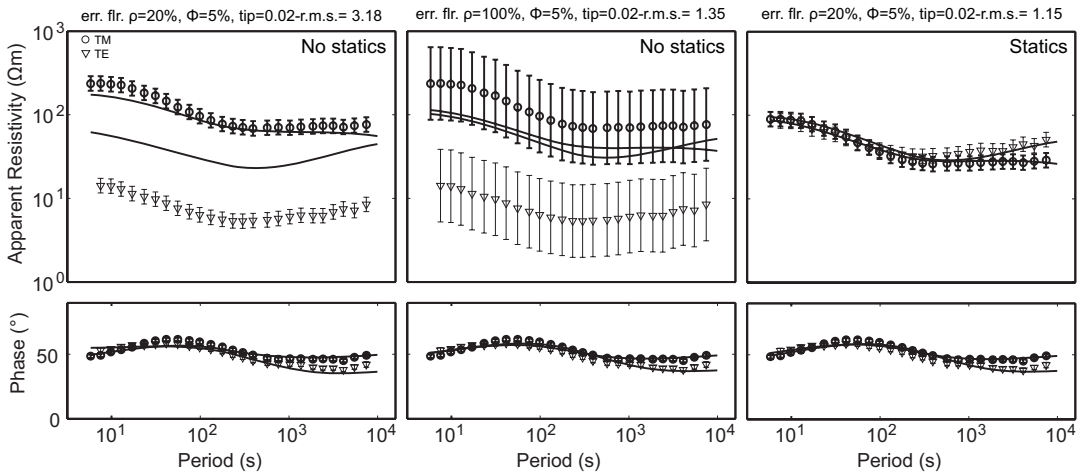

Figure 5-12. Observed MT data and inversion model response plotted together for the first site at 0 km on the A-profile. Triangles and squares represent the TE and TM data respectively while the solid lines are the model responses. The left panel used default error floors without static shifts being estimated. The middle panel used large error floors for resistivity (100%) without static shifts and the right panel used default error floor and static shifts.

5.2.3.6 Coast effect

Deep oceans are the largest conductors on the surface of the Earth and can have a significant influence on onshore MT data through the so-called coast effect (Parkinson, 1959). The resistivity of the seawater is many times smaller than the resistivity of the land. Both the magnetic transfer functions and MT impedances are affected by this sharp resistivity boundary. Parkinson (1959 and 1962) showed that horizontal projection of the ratios of the vertical to horizontal magnetic fields (induction vectors) will point towards the ocean. The ocean will also influence the MT impedance measured onshore. MT soundings are assumed to sample the average resistivity below the station but can be affected by structure at a lateral distance of 2-3 times the skin depth (Simpson and Bahr, 2005). Therefore, the so called *adjustment length* becomes very important for MT stations located hundreds of kilometers away from the ocean.

In eastern Anatolia, a coast effect might be expected from the presence of the 2 km deep Black Sea. However, salinity of the Black Sea is approximately 18-22 ppt salt, which is significantly lower than the global average 30-40 ppt salt (Boguslavsky et al., 2). The resistivity of sea water depends on the salinity and the temperature and can be estimated

using the equation of Block et al. (2001) as in the range 0.3-0.4 Ωm. The effect of the conductive seawater is to produce weak electric field amplitudes parallel to the coast, which causes a low apparent resistivity at long periods in the TE mode due to a decrease of onshore current concentrations. In contrast, the coast effect produces increased TM mode apparent resistivities. The coast effect at long periods can be observed hundreds of kilometers away from the coast at a distance that depends on the average resistivity of the continent.

A typical coast effect was observed on the C-profile where the induction vectors point towards the Black Sea at short periods (Figure 5-14). The extent of the coast effect on both induction vectors and apparent resistivity and phase curves was investigated for the C-profile. Figure 5-13 shows the 4 northernmost stations close to the Black Sea on the C-profile. The first station, dan396 is 7 km inland from the Black Sea. This station shows a large split between the two modes that could be due to static shifts. A coast effect is visible as a frequency-dependent split between the RhoXY and RhoYX curves occurring at all four stations shown in Figure 5-13. The second (dan392) and third (dan388) stations have phases exceeding 90° which cannot be explained by 1-D or 2-D resistivity models. In fact, these two MT stations are further from the coast and expected to be less influenced by the coast effect compared to dan396. Typical coast effects enhance the magnitude of the induction vectors and cause them to point towards the ocean. The coast effects also cause low phases and high apparent resistivities in the TM mode and high phases and low apparent resistivities in the TE-mode. However, the coast effect itself is a 2-D influence on the MT data. Therefore, phase angles must remain in the range 0° to 90°.

A simple 3-D resistivity model was used to investigate the coast effect of the Black Sea coast. The seawater resistivity was set to 0.3 Ωm and the land resistivity was assumed to be 1000 Ωm. The seawater resistivity value is the lower end of the possible values and was chosen to maximize the effect of the Black Sea. Dosso and Meng (1992) suggested that a coast effect occurs where the magnitude of the induction vector exceeds 0.2. Figure 5-15 shows the contour maps of the magnitude of the real induction vectors produced by the 3-D resistivity model described above. According to these maps and the definition given above, stations on the northern half of the C-profile should be strongly affected by the Black Sea. Only one station on the E-profile should be affected by the Black Sea. This conjecture is in

agreement with the observed data, although the induction vectors do not consistently point towards the ocean on the E-profile while they do on the C-profile (Figure 5-14).

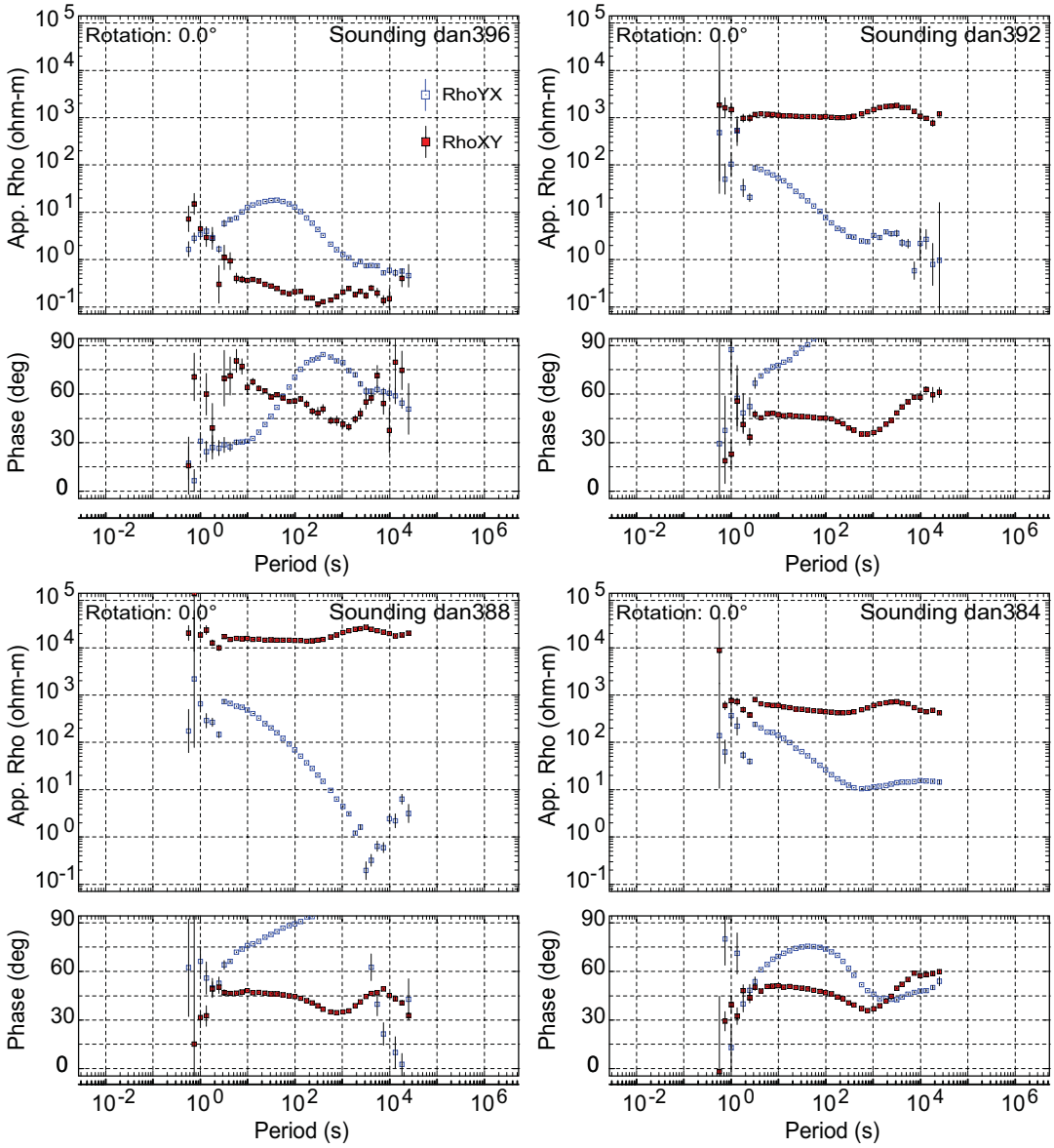

Figure 5-13. MT data at stations dan396, dan392, dan388 and dan384 close to the Black Sea coast on the C-profile. The rapid decrease of the XY apparent resistivity (RhoXY) is due to coast effect of the Black Sea.

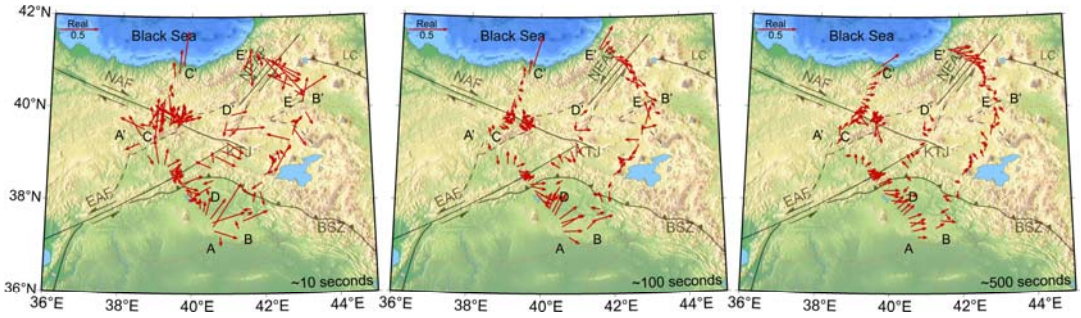

Figure 5-14. Maps showing the effect of the Black Sea on the direction and magnitude of the induction vectors. Vectors on the C-profile point towards to the deepest bathymetry at periods of 10 s and 100 s while the coast effect is weaker at periods longer than 500 s.

An ocean-land interface with a simple 2-D geometry is not capable of reproducing either the out of quadrant phases (>90°) or the steep decrease in the apparent resistivity curves at the northernmost MT stations on the C-profile (Figure 5-13). Therefore, a second conductor is necessary to produce these effects (Lazaeta and Haak, 2003). Including a low resistivity body (0.1 Ωm), almost parallel to the coast at depths between 20 km and 80 km produced phases >90° starting at a period of 100 s similar to that observed at stations dan392 and dan388 in Figure 5-13. This behaviour occurs for the particular case where the deep conductor is not parallel to the Black Sea coast, since 2-D resistivity models cannot produce phases >90°. Therefore, this situation invalidates the isotropic interpretation of these stations. A rotation of 45° of the real induction arrows between periods of 10-2000 s on the C-profile is another indicator of anisotropy (Heise and Pous, 2003).

In the first test the Black Sea was included as a fixed model parameter in the inversion (left panel in Figure 5-16). To investigate the overall effect of these distorted MT stations on the 2-D inversion, two additional tests were performed.

Test 1 – This model was compared to an inversion where the Black Sea was included in the starting model but the inversion was free to change all parts of the model (middle panel in Figure 5-16).

Test 2 – The 8 northernmost MT stations were excluded from the inversion (right panel in Figure 5-16).

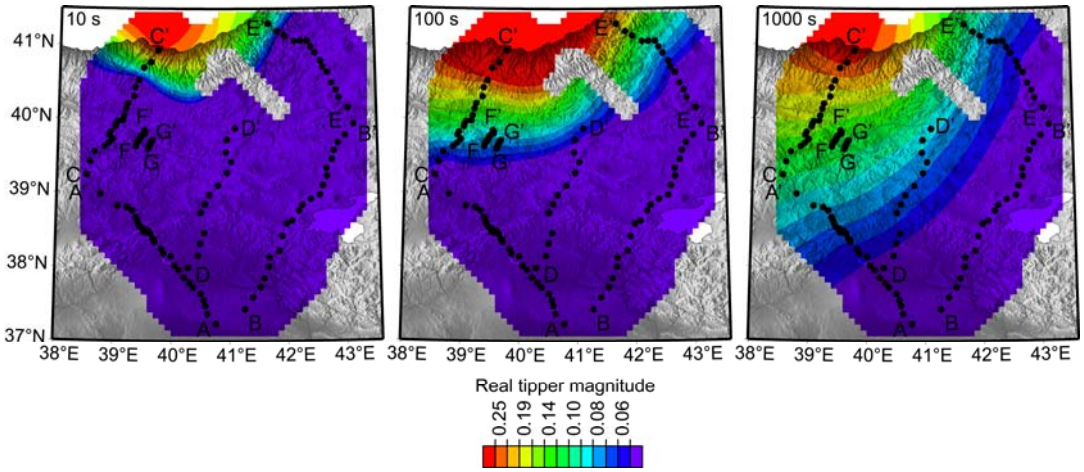

Figure 5-15. Maps showing the magnitude of the real induction vectors. Regions shaded red show a strong coast effect. At short periods (T = 10 s) the strong coast effect is limited to only one station close to the coast (left panel). At intermediate periods (T = 100 s), 6 stations remained in the high coast effect zone (i.e. real tipper magnitude >0.2). For long periods (T = 1000 s) coast effect is observed more than 100 km from the ocean but the magnitude is not as high on the induction vectors (right panel).

Overall, the main features of the resistivity model beneath the MT stations do not vary between the three models. However there are differences outside the area with station coverage. When the Black Sea is a fixed model parameter, the inversion places a highly resistive (~1000 Ωm) feature beneath the Black Sea, at the northern end of the C-profile. When the Black Sea is not fixed, the inversion places smooth structures including the ocean-land interface. This difference is due to the diffusive nature of the MT signals and the conditions imposed on the model by the regularized inversion.

Another test was applied to determine if the distorted MT stations have a significant effect on the model features. In this test, the Black Sea was set as a fixed model parameter in the inversion but the 8 northernmost stations from the coast were excluded (right panel in Figure 5-16). The same major resistivity structures were produced in this test, but the r.m.s. misfit was significantly lower than for the inversion of the full set of MT stations. This was also noticed for single mode inversions as the inversion algorithm could not adequately fit the TE mode data (Figure 5-5).

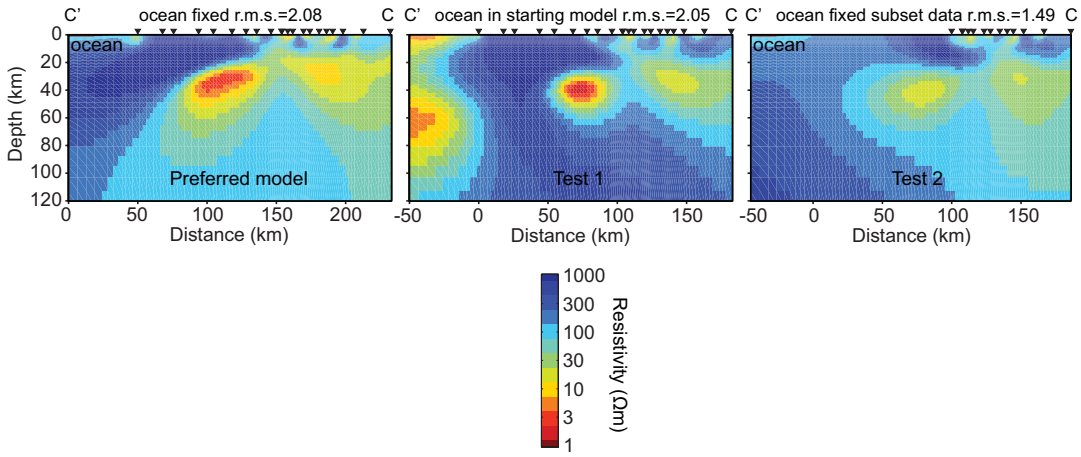

Figure 5-16. Influence of the coast effect on the 2-D inversion of the C-profile. The Black Sea is a fixed model feature and all the available MT data were used in the inversion shown in the left panel (Preferred model). Test 1 includes the Black Sea in the starting model but the inversion was free to change the boundary and resistivity of the seawater as the inversion proceeded. Test 2 used the Black Sea as a fixed model feature but the northernmost 8 stations from the coast were excluded.

5.3 Three-dimensional (3-D) inversion of eastern Anatolia MT data

To investigate whether the features observed in the 2-D inversions are robust, the Eastern Turkey MT data were also inverted using the three-dimensional WSINV3DMT algorithm of Siripunvaraporn et al. (2005b). A 3-D inversion of MT data is much more computationally demanding than a 2-D inversion in terms of computer time and memory requirements. This meant that the number of cells in the vertical and horizontal directions was significantly less in the 3-D inversion than the 2-D inversions previously described. A full 3-D inversion of the whole area with a subset of stations (77 out of 131) and 3-D inversions of individual 2-D-profiles is described in the following sections.

5.3.1 Three-dimensional (3-D) inversion of MT data set

Of the 131 MT stations collected in eastern Anatolia, 77 were chosen for a 3-D inversion that covered the entire study area. The mesh spacing used in the full 3-D inversion was 12 km in the horizontal directions. This spacing is much larger than the 2-4 km used in the 2-D inversions. The number of vertical mesh cells was 38 in the 3-D inversion compared to the 65-75 used in the 2-D inversions.

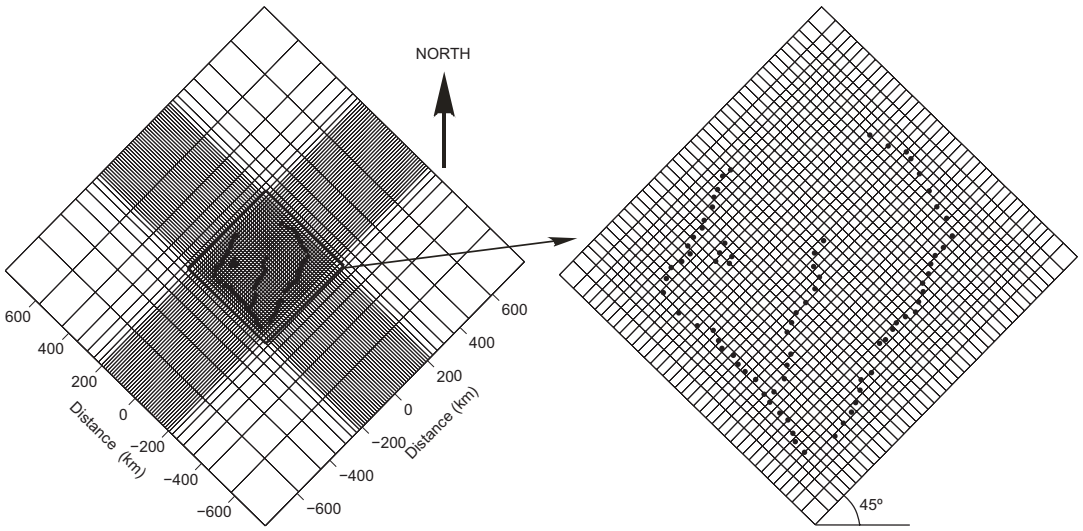

Figure 5-17. Finite difference mesh used for the 3-D inversion. The mesh is rotated 45 degrees to reduce the number of rows and columns by 16% compared to the unrotated mesh.

These factors made the 3-D inversion models appear blockier than those obtained from the 2-D inversions. It should also be noted that spatial distribution of the stations is far from ideal and there are large gaps within the study area where there are no MT stations.

To implement a 3-D inversion it was necessary to reduce the number of stations by selecting one from each group of stations in a particular area (77 out of 131). Figure 5-17 shows the finite difference mesh used for the inversion. The mesh was rotated 45° from geographic north and the number of rows and columns was reduced by 16% compared to the unrotated mesh. Furthermore, in the 2-D inversions, 8 periods per decade were used, but this is impractical in the 3-D inversion due to the large computer memory and time requirements.

Using the assumption that MT data are smoothly varying in both the spatial and frequency domain, just 4 samples per decade were used. The 3-D inversion used the full impedance tensor with an error floor of 10% for the off-diagonal elements of the impedance tensor (Z_{xy} and Z_{yx}) and 20% for the diagonal elements (Z_{xx} and Z_{yy}). The starting model was a 100 Ωm half-space to allow comparison with the 2-D inversions.

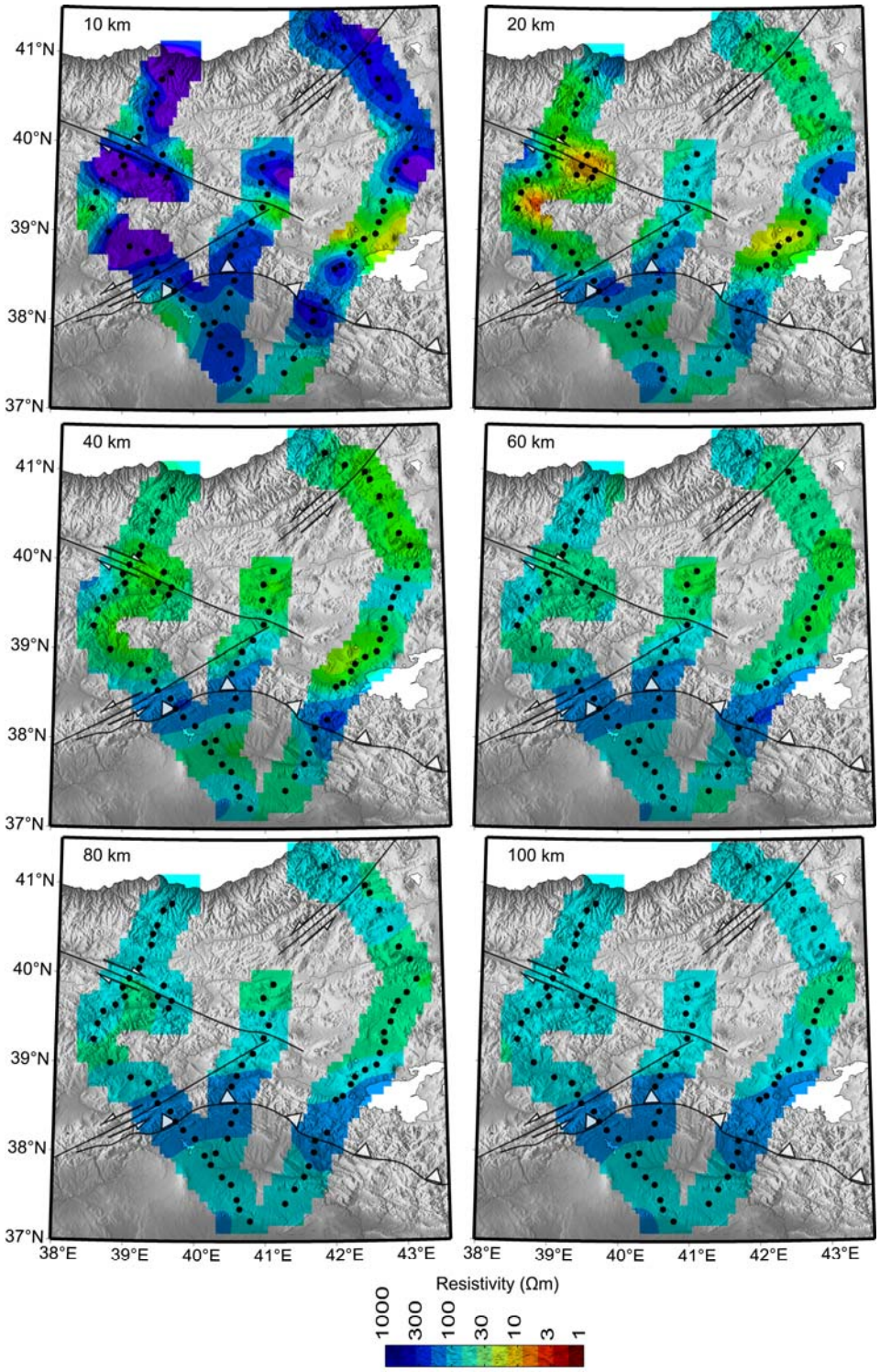

Figure 5-18. Depth slices from the full 3-D inversion model calculated from a subset of the MT data. Black dots show the locations of the MT stations used in the inversion.

5.3.2 Three-dimensional (3-D) inversion of individual MT profiles

A 3-D inversion of a single profile of MT data can be more reliable than a 2-D inversion of the same data if 3-D effects are present (Siripunvaraporn et al., 2005a). Inclusion of the off-diagonal elements of the impedance tensor provides information regarding the presence of off-profile structures (i.e. 3-D effects). When the MT data are rotated to the geoelectric strike direction, the diagonal components are expected to be zero in the ideal 2-D situation. However, this ideal situation is rarely the case in real MT data. Including the diagonal components of the impedance tensor and using a 3-D mesh allows better constraints on the resistivity model geometry. Including full impedance tensor data are particularly important for the case of an off-profile low resistivity zone close to the profile (Türkoğlu et al., 2009).

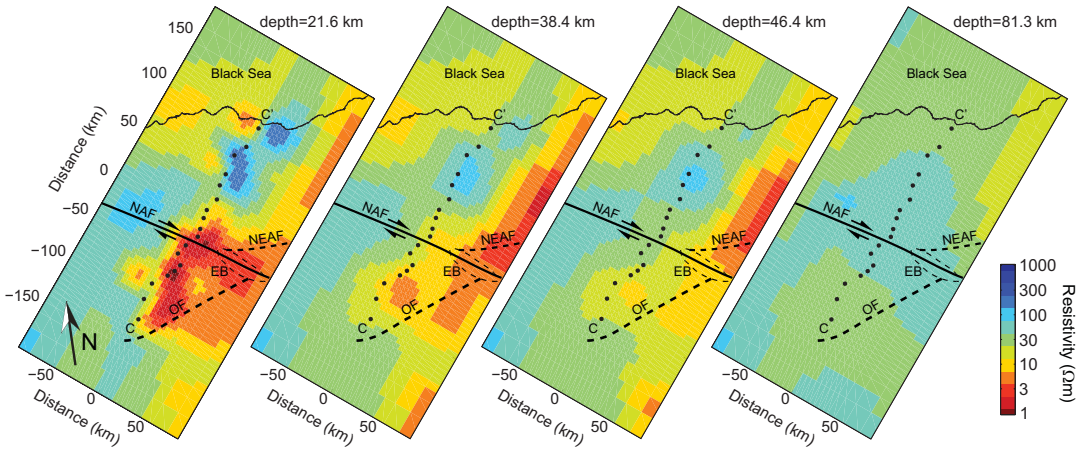

Figure 5-19. Depth slices from the 3-D inversion of the C-profile data. Coordinate frame (mesh) was rotated for 3-D inversion. Note the off-profile low resistivity anomaly on the right side of the profile around the Erzincan Basin (EB). Solid and dashed lines show the North Anatolian Fault (NAF), Ovacık Fault (OF) and North East Anatolian Fault (NEAF).

The 3-D inversions of individual profiles used a finer mesh than the 3-D inversion of the entire dataset. The horizontal mesh size was 7 km in each direction. This size can be compared with 12 km for the full 3-D inversion and 2-4 km for the 2-D inversions described in the previous sections. In the vertical direction, 30 depth slices were used. Four periods per decade were used giving a total of 13 periods between 10^1 and 10^4 s. Vertical sections were extracted from the 3-D inversion models and compared with the 2-D inversion results (Figure 5-2). The 2-D and 3-D inversion models for the B, D and E

profiles are generally similar. For the C-profile, the 2-D and 3-D models are somewhat different. A low resistivity anomaly at a depth of 40 km and at a distance of 70 km south from the Black Sea coast is observed in the 2-D inversion (Figure 5-2), but is not detected in the 3-D inversion (Figure 5-18).

Depth slices obtained from the 3-D inversion of the C-profile data revealed a low resistivity body located 50 km from the profile (Figure 5-19). The 3-D MT inversion provides off-profile information, but the spatial extension and the shape of this anomaly remains poorly constrained. Therefore, the isolated low resistivity body underneath the C-profile imaged by the 2-D inversions is probably a 3-D feature and is not necessarily underneath the profile. Note that the coordinate frame was rotated so the mesh lines are parallel and perpendicular to the profile direction. This rotation is necessary to save computation time through a reduction of the number of cells used in the mesh. Rotation also facilitates plotting vertical sections of the 3-D model for comparison with the 2-D inversions.

5.3.3 Constrained inversions and sensitivity analysis

The diffusive nature of electromagnetic (EM) energy propagation in the Earth does not allow the imaging of sharp boundaries. One way to investigate the sensitivity of a resistivity model to the field MT data is to use constrained inversions. In this approach, the locations of interfaces are defined from other geological and geophysical data. Figure 5-2 shows that the upper mantle beneath the Anatolian Plateau on the B-profile may have a low resistivity. However, a lower crustal conductor reduces the sensitivity of surface MT measurements. Thus, a constrained inversion approach was applied to this profile. The upper mantle resistivity beneath the Anatolian Plateau and Arabian Plate was fixed at four different resistivity values, 10 Ωm, 30 Ωm, 100 Ωm and 300 Ωm (Figure 5-20). Inversions used the same MT data, mesh and control parameters as the inversions in Figure 5-2, and only the crustal structure was allowed to change in these inversions. Results are shown in Figure 5-20.

Models 1 and 4 were only able to fit the observed MT data at the expense of generating new resistivity features in the lower crust that were not observed in the original inversion

models (Figure 5-2). The lowest r.m.s. misfit value was obtained in model 2 where the resistivity of the upper mantle north of the BSZ was fixed at 30 Ωm. The final r.m.s. values of each model from top left to bottom right are 2.1, 1.7, 2.0 and 2.1 respectively.

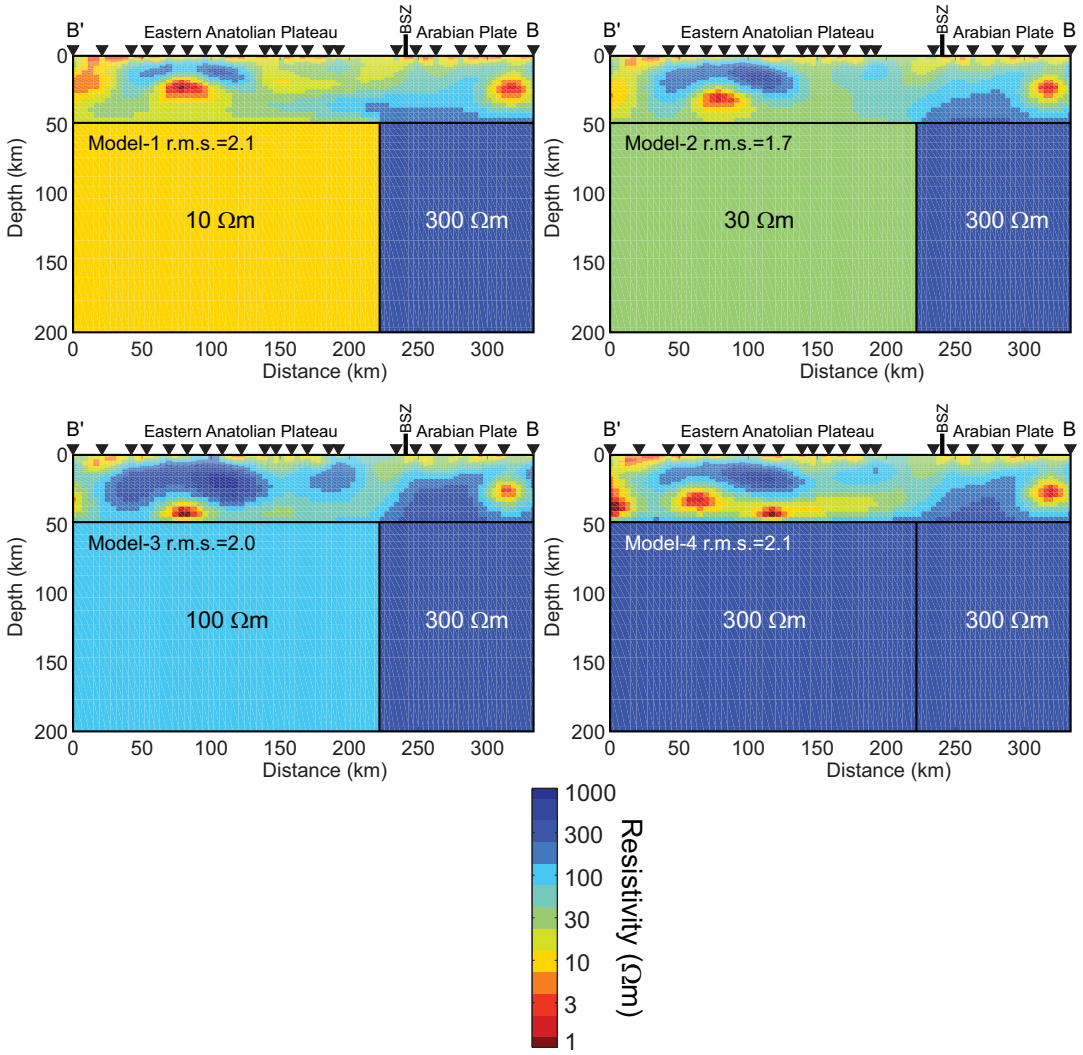

Figure 5-20. Sensitivity test to determine the resistivity of the upper mantle beneath eastern Anatolia on the B-profile. Four different resistivity models were generated and in each the resistivity of the upper mantle north of the Bitlis Suture Zone (BSZ) was fixed at values of 10, 30, 100 and 300 Ωm respectively. In the inversions the upper mantle resistivity was fixed for the Arabian Plate and eastern Anatolian Plateau.

5.4 Summary

This chapter presented the most important step of the MT data analysis, since further interpretation and geodynamic modeling depend on the resistivity models derived from the inversions. A single set of control parameters cannot be used for the inversion of every MT dataset. Therefore, sensitivity tests are needed to verify if resistivity features in the inversion models can be considered robust. The major features of these models are summarized below.

5.4.1 A-Profile

This profile detected a shallow (>5 km) low resistivity (~10 Ωm) top surface between model distances of 100 km and 200 km south of the BSZ. The resistivity and lateral extent of this feature is well constrained and it is observed in both the 2-D and 3-D inversions (Figure 5-2). This feature corresponds to the sedimentary basin on the Arabian Foreland.

There is a sharp sub-vertical resistivity boundary at 100 km distance. In the southern half of the model the deeper resistivity is around 100-300 Ωm (feature "e" in Figure 5-2) while the deeper resistivity in the northern part is lower (10-30 Ωm). This transition is also observed in the 3-D inversion, but the resistivity contrast is greatest in the 2-D inversion.

A vertical zone of low resistivity is observed at a distance of 100 km ("h" in Figure 5-2). This feature is produced by the inversion for a wide range of control parameters. However the use of static shift coefficients and error floor value caused some variations in the geometry of this feature.

Between distances of 0 km and 100 km there is a low resistivity layer at 20-40 km depth. This feature is observed in both 2-D and 3-D inversions and appears to be a robust feature ("a2" in Figure 5-2).

The low resistive body imaged at a distance of 200 km and depth of 40 km ("b" in Figure 5-2) is visible on 2-D inversions but there was no indication of such an anomaly from induction vectors. The 2-D inversions require this feature to fit the MT data. However, the 3-D inversion showed that this anomaly could be generated by smearing of the basin.

Therefore, this feature is robust but the geometry, location and resistivity of the anomaly remains poorly constrained and further data are needed for clarification.

5.4.2 B-Profile

A low resistivity (~10 Ωm) surface layer on the Arabian Plate was also imaged and is similar to that observed on the A-profile. However, this feature appears to be thicker than on the A-profile in the 2-D inversions, perhaps as thick as 20 km. This feature is only imaged to be a few kilometers thick by the 3-D inversions with reduced resistivity (Figure 5-2).

There is a sharp resistivity contrast at 200 km distance. To the south the deep resistivity is high (300 Ωm, "e" in Figure 5-2) while to the north the resistivity is lower (10-30 Ωm, "f" in Figure 5-2). This is a robust feature observed in all inversions and is supported by the 3-D inversions. However, the shape of the low resistivity pockets at distances of 50-100 km was imaged with a different geometry in 3-D ("a2" in Figure 5-2).

The isolated low resistivity feature around the southern end of the profile ("b" in Figure 5-2) imaged on some 2-D inversions depends on the MT components used and on the particular selection of the regularization parameter (Figure 5-9). Therefore, it is not a robust feature but spatial coincidence with the isolated low resistivity anomaly on A-profile ("b" in Figure 5-2) supports its existence.

5.4.3 C-Profile

Some stations on this profile were classified as 3-D because of anomalous phase angles that go out of quadrant. Between distances of 0 km and 75 km and depths of 0 to 40 km, a highly resistive zone was detected (>300 Ωm). Below this resistive feature is a low resistivity body ("g" in Figure 5-2). However, the 2-D inversion could not fit the observed MT data in this part of the profile. The 3-D inversions showed that this feature is needed to fit the data but it is not necessarily located underneath the profile (Figure 5-2 and Figure 5-19). The 3-D forward calculations also inferred that this anomaly could be due to a dyke-shaped low resistivity body, confined in a highly resistive host and subparallel to the coast.

Between distances of 75 km and 180 km, there is continuous band of low resistivity (10-30 Ωm) in the depth range 20 km to 40 km. This band of low resistivity is the most prominent feature on this profile and it is equally well detected by both the 2-D and 3-D inversions ("a2" in Figure 5-2).

Beneath feature a2 on the C-profile is more resistive (100-300 Ωm) upper mantle ("d" in Figure 5-2).

Vertical low resistivity channels between 100 km and 150 km distance extend from the surface down to the aforementioned 10-30 Ωm continuous band of low resistivity zone and these several vertical low resistivity channels are imaged as one wider channel in the 3-D inversions.

5.4.4 D-Profile

All the resistivity features on this profile are also observed on other profiles and explained above. These features do not depend on the particular inversion settings or on the MT component selection. The 3-D inversion models are similar, but the resistivity contrast is lower across the BSZ. A low resistivity layer was imaged from 0 km to 150 km ("a" in Figure 5-2). This feature is similar to that of observed on C and A-profiles.

5.4.5 E-Profile

The upper 20 km is a resistive feature and is broken up with low resistivity channels. Underneath this layer are very low resistivity pockets (2-5 Ωm, "a2" in Figure 5-2).

Overall the resistivity structure imaged on this profile does not depend on the particular selection of the 2-D inversion parameters. The 3-D inversion of E-profile produced a similar model to the 2-D inversion.

Below a depth of 40 km the resistivity increases, especially towards the Black Sea (Figure 5-2). However, this profile used mainly broad-band MT data which have limited penetration depth in this low resistivity environment. Therefore, the resistive basement is not as well resolved as on other MT profiles.

6 IMAGING OF THE NORTH AND EAST ANATOLIAN FAULTS

6.1 Introduction

The magnetotelluric (MT) data analysis presented in chapter 5 was focused on defining the regional, lithospheric scale structures in eastern Anatolia. Magnetotelluric data can also be used to study the tectonic processes at work on smaller spatial scales on active faults (Unsworth et al., 2004; Bedrosian et al., 2001-2004; Jones at al., 1992; Tank et al., 2005).

The seismic behavior of faults is believed to be controlled by spatial and temporal variations in fluid content (Byerlee, 1993; Sleep and Blanpied 1992). Over-pressured fluids in the fault-zone may trigger earthquakes through lowering the shear stress needed for failure (Sleep and Blanpied, 1992). A related observation is that the San Andreas Fault (SAF) appears to be inherently weak. The lack of a heat flow anomaly on the San Andreas Fault (Brune et al., 1969) suggests that the fault moves with a low effective coefficient of friction (μ <0.1-0.2) and moves at extremely low shear stress that averages 10-20 MPa (Zoback et al., 1987). More recent heat flow data from drilling at Parkfield, California also show absence of a frictional heat flow anomaly (Williams et al., 2004). These values are in contrast to laboratory studies of rock shear stress which are 5-10 orders of magnitude higher than SAF shear stress values (Byerlee, 1978; Sibson, 1974). Recent studies of the North Anatolian Fault also indicate very low friction coefficients ($0.05 \leq \mu \leq 0.2$) to account for the velocity model derived from GPS studies (Provost et al., 2003). These values are similar to those suggested for the SAF (Zoback et al., 1987; Mount and Suppe, 1987).

As outlined above, fault-zone fluids have been proposed as a way of lowering the in situ strength of major fault zones. Therefore, monitoring the fluid content at the fault zone is important for understanding the dynamics of the fault zone and earthquake cycle. MT is an

effective tool for investigating fault zones by mapping the resistivity distribution of the subsurface. Archie's Law (Archie, 1942) can be used to estimate the bulk resistivity of the fluid-saturated rock as a function of fluid conductivity and the porosity as follows:

$$\rho = \rho_f \Phi^{-m} \tag{6.1}$$

In eq. (6.1) ρ is the effective resistivity of the fluid saturated rock and ρ_f is the resistivity of the pore fluid. The porosity of the rock is Φ and m is the cementation factor that describes the spatial distribution of the fluid. A value of m=1 implies good interconnection with crack shaped pores while m=2 implies poorer interconnection with spherical shaped pores (see chapter 7 for more details on fluid conductivity). Note that the cementation factor contains information about permeability. Aqueous fluids contain dissolved ions and their resistivity decreases as the salinity increases (Block, 2001). Clay minerals are also capable of lowering the friction in a fault and modifying the seismic-tectonic behaviour (Hirono et al., 2008). Clay lowers the electrical resistivity of a fluid bearing rock through an electrical double layer that forms at the fluid-clay interface which allows ions to move more easily than in the fluid phase. However, it is difficult to distinguish between clay and aqueous fluids on the basis of resistivity values imaged with MT or other geophysical methods.

A number of MT surveys have been used to study the distribution of fluids within active fault zones (Unsworth et al., 2004; Bedrosian et al., 2001-2004; Jones at al., 1992; Tank et al., 2005). Studies of the San Andreas Fault in California revealed that some segments are characterized by a zone of low resistivity (fault-zone conductor or FZC). At Parkfield the SAF is in transition from creeping to locked and the FZC extends from the surface to a depth of 2-3 km (Unsworth et al., 1997). The conductor extends to mid-crustal depths at Hollister where the fault creeps at 10–15 mm/y (Burford and Harsh, 1980; Evans et al., 1981; Bedrosian et al., 2002). A small fault-zone conductor was observed on the locked Carrizo segment (Unsworth et al., 1999; Mackie et al., 1997). These observations suggest that there may be a correlation between the resistivity of the fault zone and its seismic behavior (i.e. locked or creeping). However, the source of the fluids is not completely understood. Earlier studies of Irwin and Barnes (1975) suggested that fluids emerged due to metamorphic reactions within the Franciscan formation in Central California could be

entering the SAF at mid-crustal depths and causing the creep in this area. Geochemical studies of springs and wells around the SAF indicate a meteoric origin for fault-zone fluids (Kharaka et al., 1999). Becken et al., (2008) suggested that the fault-zone conductor at SAF connects with a deeper upper mantle conductor which may infer a deep rooted fluid channel between the mantle and the crust.

The San Andreas Fault has been relatively well studied with magnetotellurics during the last decade and a number of detailed images of the fault zone have been published. However, the electrical structure of the North Anatolian Fault is not well understood. Tank et al., (2005) published the first detailed MT study on the western part of the NAF close to the surface rupture of the 1999 İzmit earthquake. This MT study on the western part of the NAF showed similarities with the SAF in terms of the conductivity structure. Earthquake hypocenters coincide with a resistive layer that is underlain by a highly conductive fluid-rich layer (Tank et al., 2005). This fluid-rich layer just below the seismogenic zone was interpreted as triggering earthquakes and responsible for postseismic creeping. The average station spacing for the study of the western part of the NAF was around 2 km, which is much larger than the few hundreds of meters in the MT study of the SAF (Bedrosian et al., 2004).

The North Anatolian Fault does not exhibit the same pattern of creeping and locked segments as the SAF. However, the NAF has been characterized by a sequence of major earthquakes that has migrated from east to west (Egeran and Lahn, 1944; Ketin and Rösli, 1953). Creeping behavior was observed on the western part of the NAF (Ambraseys, 1970; Aytun 1980). Çakır et al. (2005) used 10 years of Synthetic Aperture Radar Interferometry data and noticed that a region between the western end of the 1943 (M=7.6) and eastern end of the 1944 (M=7.3) earthquakes is creeping at 8 cm/y. However, no MT data are available elsewhere on the Anatolian Fault system. The first magnetotelluric data collected on the eastern part of the NAF and on the EAF are presented in this chapter. Results of these regions are also compared to data from the San Andreas Fault.

6.2 Seismic behavior of the North and East Anatolian Faults

6.2.1 North Anatolian Fault (NAF)

The tectonics of eastern Anatolia is dominated by the ongoing collision of the Eurasian and Arabian Plates. A significant amount of this deformation is accommodated by strike-slip motion on the North Anatolian and East Anatolian faults (Şengör et al., 1985). The North Anatolian Fault has been characterized by a westward propagating sequence of earthquakes that began with the (M_s=8.2) 1939 Erzincan earthquake (Parsons et al., 2000). The most recent earthquakes in this sequence occurred on the western part of the North Anatolian Fault in 1999. The August 17 1999 İzmit (M_w=7.4) and November 12 Düzce (M_w7.2) earthquakes ruptured 110-140 km and 40 km of the North Anatolian Fault, respectively, and caused 20000 fatalities (Armijo et al., 1999; Barka, 1999; Barka et al., 2000; Örgülü and Aktar, 2001; Fielding et al., 1999; Reilinger et al., 2000). Stress modeling of Stein et al. (1997) indicate that the 1999 events have resulted in an increased chance of a major event on the segment of the NAF in the Marmara Sea (King et al., 2001; Parsons et al., 2000; Le Pichon et al., 2003).

In terms of surface geomorphic expression, the North Anatolian Fault has formed a series of pull-apart basins which include, from west to east, the Gelibolu, Adapazarı, Pamukova, Kursunlu, Refahiye, and Erzincan basins (see Şengör et al., 2005 for complete list). The largest of these basins is the Erzincan basin that has formed at the junction of Ovacık Fault, North East Anatolian Fault and North Anatolian Fault.

In the last century, two destructive earthquakes have occurred around Erzincan (1939 and 1992). The devastating (M_s=8.2) 1939 earthquake (Barka and Kadinsky-Cade 1988) is estimated to have caused 40,000 fatalities within and around Erzincan (see Şengör et al., 2005).

The most recent of these destructive earthquakes occurred in the eastern part of the Erzincan basin (M_s =7.8) in 1992 (Barka et al., 1996; Eyidoğan et al., 1991; Fuenzalida et al., 1997; Grosser et al., 1998). The 1992 earthquake had a hypocentre at 10 km depth and caused serious damage and loss of life. Aftershocks were recorded for more than two months (Fuenzalida et al., 1997) and used for 1-D and 3-D basin modeling and revealed

ruptured parts of the fault (Kaypak and Eyidoğan, 2005; Aktar et al., 2004). It has been noted that following the largest aftershock (M_s =5.8) the events extended southeast rather than aligning parallel to the direction of the NAF towards the Karlıova Triple Junction (KTJ). This change was interpreted to be due to activity on the Pülümür Fault that is subparallel to the NAF (Fuenzalida et al., 1997; Aktar et al., 2004). Therefore, the zone between the Erzincan basin and the KTJ remains unruptured.

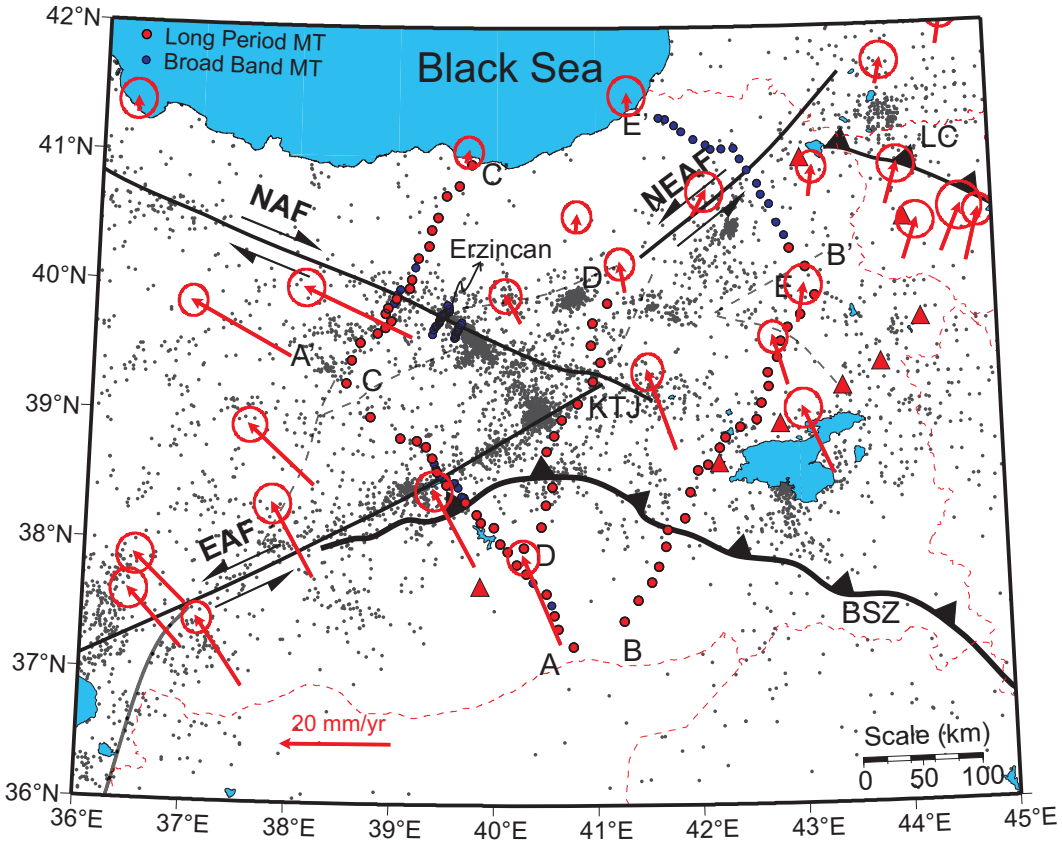

Figure 6-1. Tectonic setting of eastern Anatolia. GPS velocity vectors are relative to Eurasia (McClusky et al., 2000) and earthquake epicenters between 1960 and 2004 from KOERI, Turkelli et al. (2003) and Kaypak and Eyidoğan (2005). Red and blue dots show locations of the magnetotelluric stations used in this thesis. Red triangles show volcanic centers. NAF= North Anatolian Fault; EAF= East Anatolian Fault; NEAF= North East Anatolian Fault; BSZ= Bitlis Suture Zone; LC= Lesser Caucasus.

6.2.2 East Anatolian Fault (EAF)

In contrast to the high levels of seismic activity along the North Anatolian Fault, the East Anatolian Fault (EAF) has been characterized by low seismicity levels during the last

century (Jackson and McKenzie, 1988; Ambraseys and Jackson, 1998). However, the historical record clearly shows that major earthquakes have occurred on this fault (Ambraseys and Jackson, 1998; Nalbant et al., 2002). Continuous broad-band seismograph recordings between October 1999 and August 2001 showed that the East Anatolian Fault is more active than previously thought and the seismogenic zone may extend to greater depths than on the NAF (Turkelli et al., 2003). However, the total offset on this fault is around 22 km (Arpat and Şaroğlu, 1972; Şaroğlu et al., 1992), which is less than the 75-85 km observed on the NAF (Le Pichon et al., 2001).

Detailed MT imaging of the North Anatolian and East Anatolian Faults has the potential to provide new insight into the mode of deformation on these major strike-slip faults. It was also anticipated that a study of these faults would give a broader context to studies of the relationship between fluids and fault-zone seismotectonic behaviour observed at other active faults.

6.3 Magnetotelluric data

A subset of the magnetotelluric data presented in chapter 4 was used for detailed imaging of the North Anatolian and East Anatolian Faults. In chapter 5, the regional structure of eastern Anatolia was studied using deep-sounding (long-period) MT data. For shallower targets such as fault zones, higher frequencies with shorter skin depths are needed. Thus, the fault-zone studies emphasized the broadband MT data especially within the Erzincan Basin. These studies also used a smaller interstation spacing than in the regional studies.

In each study area, broad-band MT data were collected on profiles that were approximately perpendicular to the known surface trace of the major faults. On the NAF, the main profile (F-profile) crosses the fault close to Erzincan while the shorter G-profile is close to the eastern end of the basin (Figure 6-2). The third NAF profile is the N-profile which is a subset of the C-profile MT stations around Refahiye. This profile has 10 long-period and 3 broad-band MT stations.

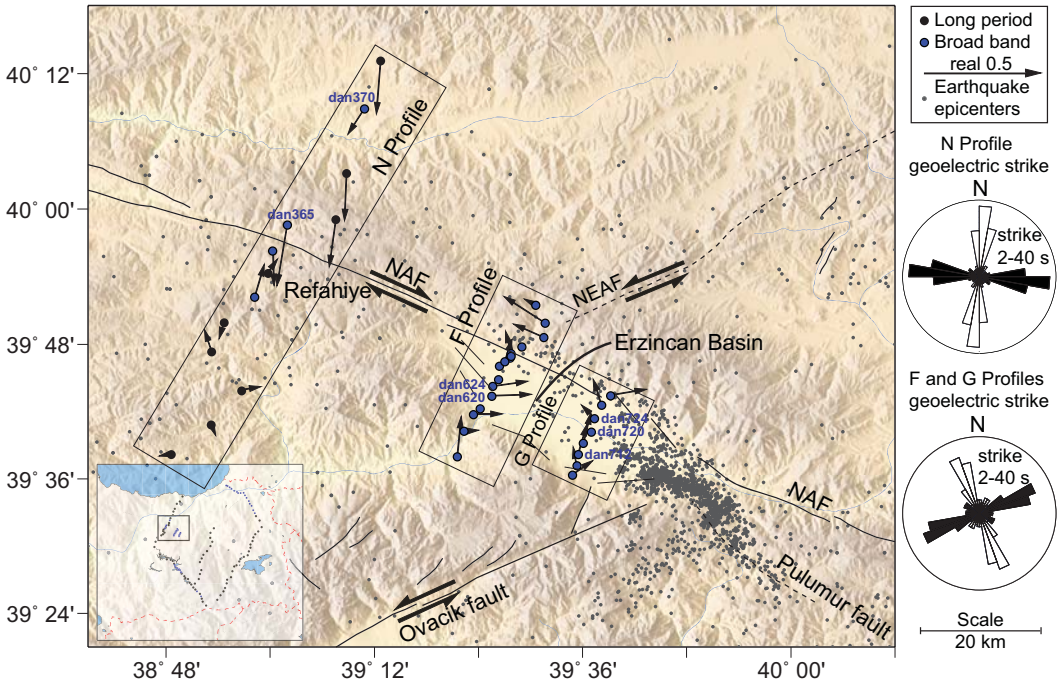

Figure 6-2. Magnetotelluric stations used for studies of the North Anatolian Fault within the Erzincan basin and around Refahiye. Black and blue circles show long-period and broad-band MT stations respectively while small gray dots represent earthquake epicenters from 1960-2004 KOERI, Turkelli et al. (2003) and Kaypak and Eyidoğan (2005). Black arrows show real induction vectors averaged over the period range 2-40 s. Rose diagrams show calculated geoelectric strike direction for the same period range as for the induction vectors. NAF= North Anatolian Fault; NEAF= North East Anatolian Fault.

A subset of the A-profile data across the EAF and BSZ around Hazar Lake was also used for detailed imaging of upper crustal structure (Figure 6-3). This profile was named the H-profile and consists of 10 long-period and 10 broad-band MT stations. In general, the station spacing is far from being adequate for detailed fault imaging. However, inversion of a subset of the MT data with a finer finite difference mesh and including all the available high frequency data (100-0.1 Hz) improves the final results.

MT data at most stations were of high quality, but two stations on the G-profile and four stations on the F-profile could not be used for further modeling due to high cultural noise around the city of Erzincan.

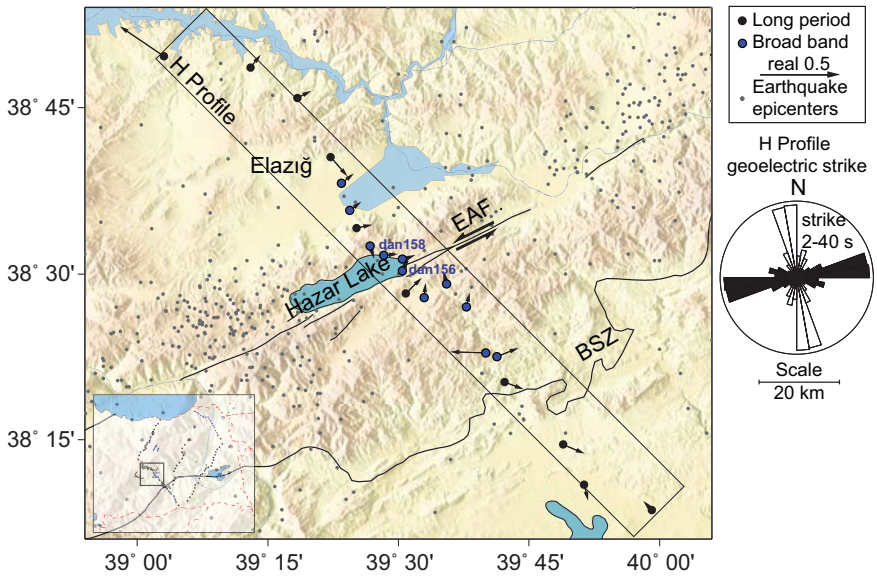

Figure 6-3. Magnetotelluric stations used for studies of the East Anatolian Fault around Hazar Lake. Black and blue circles show long-period and broad-band MT stations respectively while small gray dots represent earthquake epicenters from 1960-2004 KOERI, Turkelli et al. (2003) and Kaypak and Eyidoğan (2005). Black arrows show real induction vectors averaged over the period range 2-40 s. Rose diagrams show calculated geoelectric strike directions for the same period range as for the induction vectors. EAF= East Anatolian Fault; BSZ= Bitlis Suture Zone.

6.3.1 Dimensionality of the MT data

Dimensionality of the data is usually determined from the MT impedance skew by assigning a threshold value (see chapter 2 for details). However, a simple definition of the skew (Swift, 1967) is subject to bias when the data are affected by static shifts. Therefore, the modified phase sensitive skew (Bahr, 1991), which is insensitive to static shifts, is commonly used. On the other hand, the phase sensitive skew threshold is not statistically structured in terms of noise in the data. Marti et al. (2005) improved Bahr's phase sensitive skew and introduced the Bahr-Q method. However, when the data are of good quality, Bahr skew (Bahr, 1991) and Bahr-Q (Marti et al., 2005) methods work reasonably well and give corresponding results (Marti et al., 2005).

Bahr's dimensionality parameter skew is used to compare dimensionality features of the data in this chapter. Two-dimensional plots of the skew values are shown in Figure 6-4. In these plots, the horizontal axis shows the distance while the vertical axis corresponds to

signal period. Dimensionality analysis of the data on the A and C-profiles showed that 2-D inversion of both profiles is valid around the EAF and NAF (see chapter 4).

Overall, the N and H-profiles are characterized by relatively low skew values (<0.25) over the whole period range (<0.25). Isolated high skew values (>0.5) are observed at short periods (<10 s) for long-period MT stations and are due to noisy or biased data. These data were excluded from subsequent data analysis such as inversion. Three bands can be observed showing distinct skew values on the F and G-profiles:

- Band 1 – T= 0.005-10 s small skew values are observed (<0.1) indicating a one-dimensional subsurface on the F and G-profiles, especially in the middle of the profiles as expected for a 3km thick sedimentary basin (Aktar et al., 2004). This observation indicates that the basin depth does not change significantly between the two MT profiles.

- Band 2 – T= 10-100 s exhibits skew values close to 0.3. This implies subsurface resistivity structure that is two or three-dimensional in nature. Scattered data points with very high skew values are due to noisy data.

- Band 3 – T >100 s skew value reduces from 0.3 to 0.1. This implies that the electrical resistivity structure is complex for the upper crustal features within the Erzincan Basin and along the fault zones. The resistivity structure is more uniform for deeper sections.

6.3.2 Directionality of the MT data

The geoelectric strike direction is needed for subsequent MT data analysis. In chapter 4 it was demonstrated that the strike direction for the A and C-profiles at long periods was found to be subparallel to the surface traces of the EAF and NAF. In this chapter a more detailed data analysis was undertaken and the whole period range was grouped into 7 different period ranges to investigate the variations of the geoelectric strike direction with increasing period. Note that increasing period corresponds to an increasing depth of penetration into the Earth.

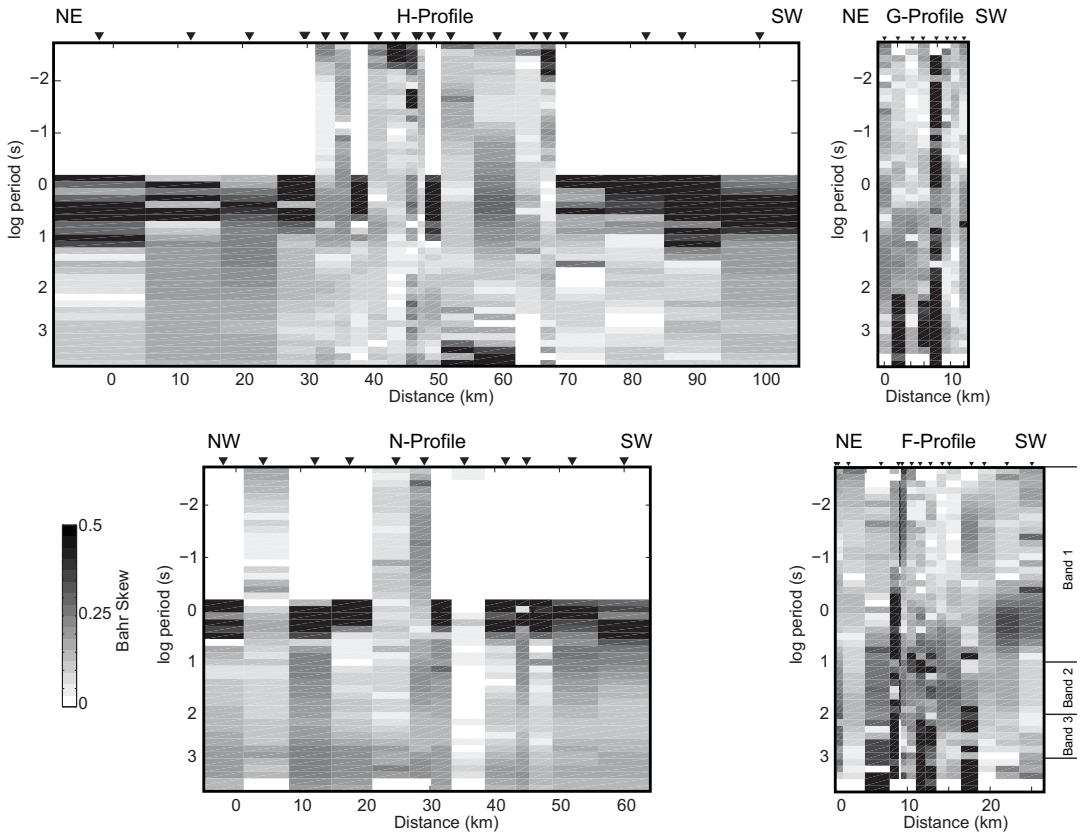

Figure 6-4. Bahr's phase sensitive skew (Bahr, 1991) for each profile investigated in this chapter. White space means that the data are not available at those particular periods. Skew values more than 0.3 indicate 3-D subsurface.

In chapter 4, it was shown that the geoelectric strike direction estimates from Groom-Bailey tensor decomposition (McNeice and Jones, 2001) and Bahr's phase sensitive (Bahr, 1991) methods give similar results. In this chapter Bahr's method is used for investigating the strike direction (see chapter 4 for details). Figure 6-5 shows these strike directions as rose diagrams. The N and H-profiles were analyzed individually while stations in the Erzincan Basin were analyzed as one group (ERZ in Figure 6-5).

No preferred geoelectric strike direction is observed in the first two period ranges (0.1-0.5 s and 0.5-2 s). Using the skin depth equation and maximum and minimum resistivity values inferred from the MT curves, an approximate depth of penetration of 2.2-7 km can be computed for these signals. Thus, the structure from the surface to these depths has no preferred strike direction.

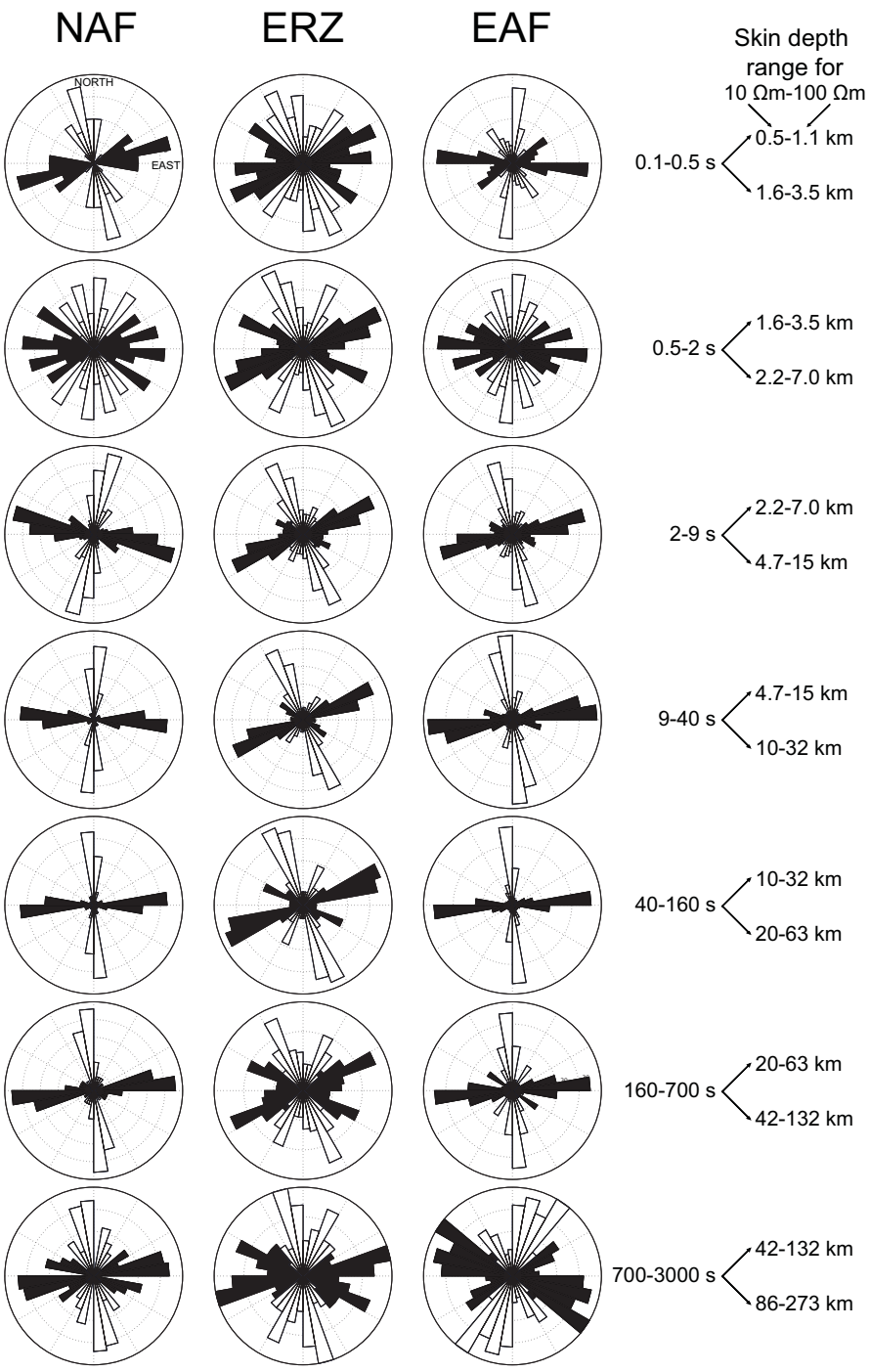

Figure 6-5. Bahr's phase sensitive strike (Bahr, 1991) direction for seven period bands. The skin depth equation was used to estimate the depth to which the MT signals penetrate in each period band. Rose diagrams represent histogram plots of the strike directions for all the stations. The first band (0.1-0.5 s) only used broad-band MT stations. Black and white histograms represent the 90° ambiguity in MT geoelectric strike direction.

The strike on the N-profile is well defined at 105° NE for the period range 2-40 s. This geoelectric strike direction is similar to the strike direction of the North Anatolian Fault defined from focal mechanism solutions of the large earthquakes (Barka and Eyidoğan, 1993; Grosser et al., 1998; Aktar et al., 2004) and mapping of the surface traces of the fault (Ketin, 1948; Şengör, 1979). MT signals with periods longer than 40 s show a well constrained strike direction of N85° E similar to that reported in chapter 4 for the C and A-profiles. A similar change in the geoelectric strike direction occurs on the H-profile (EAF in Figure 6-3) where a 75° NE strike direction is replaced by 85° NE at long periods (>40 s). This direction is also fairly close to the 65°-70° NE strike direction of the East Anatolian Fault. Surprisingly, almost no change with period in the geoelectric strike direction was observed for stations deployed in the Erzincan Basin. Furthermore, the calculated strike direction implies a significant difference from the known alignment of the NAF. The surface trace of the NAF in this region has a strike 115°-125° NE while the geoelectric strike direction of 150°-160° NE is observed for the periods between 2 s and 700 s. Note that MT strike direction has an inherent 90° ambiguity so stations within the Erzincan Basin could have a strike direction of 60°-70° NE.

The geoelectrical complexity of the Erzican basin could be due to interactions between North East Anatolian, North Anatolian, Ovacık and Pülümür faults around the Erzincan basin as well as the resistivity structure of the Erzincan basin itself. Periods of 700-3000 s correspond to signals penetrating to mid-crustal depths and the strike directions are somewhat scattered but remain parallel to the north-south continental convergence along the Bitlis Suture Zone.

For two-dimensional inversions, strike directions of 105° NE for the N-profile, 70° NE for stations within the basin and 75° NE for the H-profile were used.

6.3.3 Apparent resistivity curves

MT data were rotated to the geoelectric strike directions determined for each profile. Stations deployed within the Erzincan Basin and across the North Anatolian Fault showed similar apparent resistivity curves (Figure 6-6) for the whole period range (0.001-1000 s). These curves showed 3 distinct features:

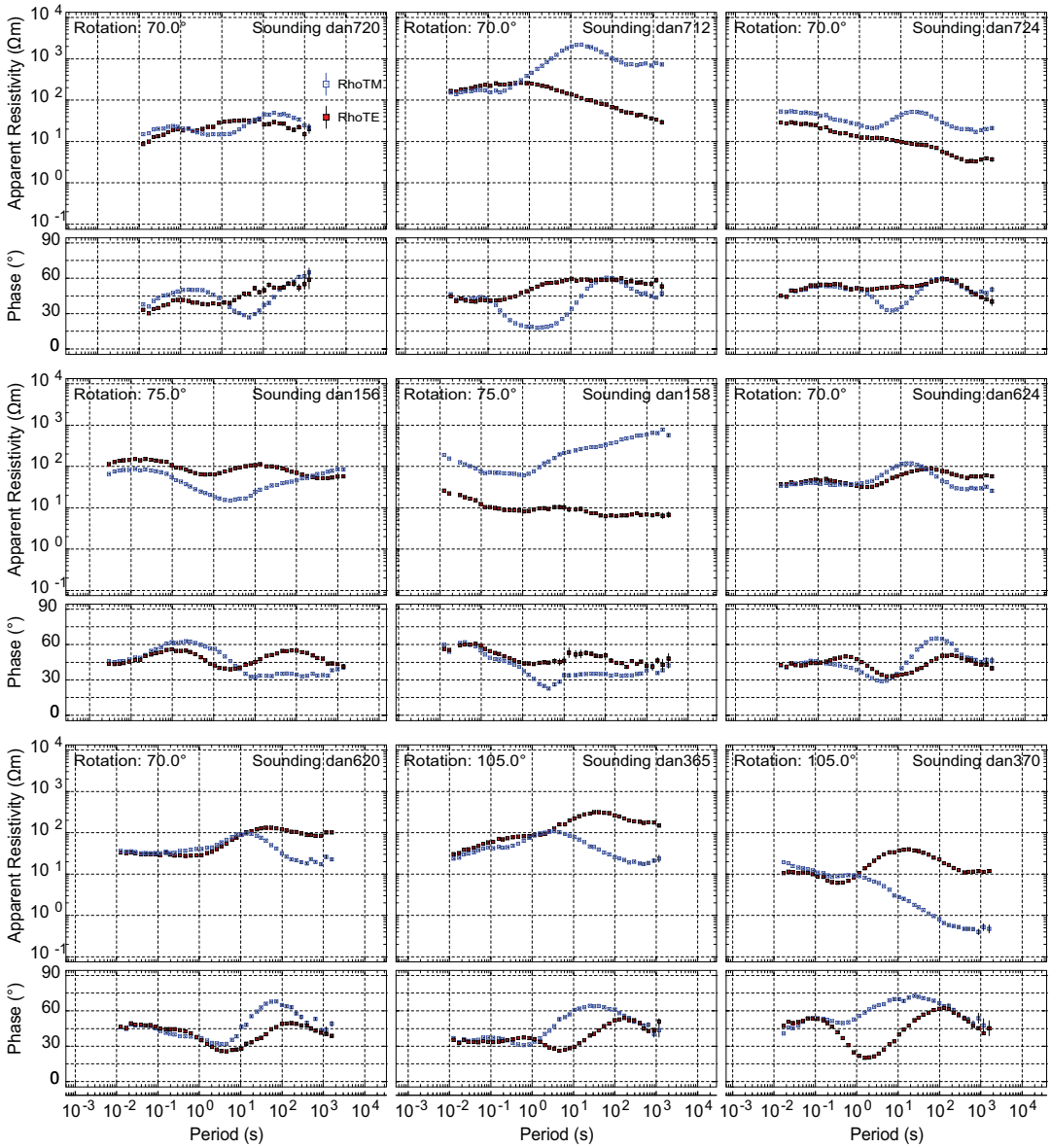

Figure 6-6. Apparent resistivity and phase curves for sample stations from F, G, N and H-profiles in geoelectric strike coordinates for each profile. See Figure 6-2 and Figure 6-3 for station locations.

- Nearly constant apparent resistivity in the period range from 0.01 s to 1 s for both TE and TM mode components. This implies that the resistivity structure is mostly constant vertically and horizontally.

- Increasing apparent resistivity in the period range 1-30 s.

- Decreasing apparent resistivity at periods longer than 30 s. This implies the presence of a low resistivity (conductive) layer at depth.

- However, apparent resistivity curves at MT stations within 10 km of the EAF demonstrate significantly different features (e.g. dan158 and dan156 in Figure 6-6). The shape of the curve implies a shallow low resistivity layer between the more resistive top and bottom layers.

6.4 Inversion of the MT data and resistivity models

The next stage of analysis was to determine appropriate resistivity models of the fault zones. As outlined above, the MT data appear to be relatively 2-D in nature. Thus, MT data at each station were rotated to the geoelectric strike direction (Figure 6-6). Stations were projected onto a profile normal to geoelectric strike, which causes the apparent length to be less than the true length shown on the map (Figure 6-2 and Figure 6-3). In the rotated coordinate frame, the TE (transverse electric) data are those with the electric field parallel to strike and the TM (transverse magnetic) mode has magnetic field parallel to the strike.

The inversion used the NLCG algorithm of Rodi and Mackie (2000) as described in chapter 5 and used both apparent resistivity and phase for the TE and TM modes, in addition to the vertical magnetic field transfer functions. Static shift coefficients were also estimated by the inversion. Cultural noise levels at 6 stations were very high and these stations were excluded from the data analysis. Thus, there are large gaps in the 2-D inversion model for the F and G-profiles. The starting model was a homogenous half-space with a resistivity of 100 Ωm. Error floors of 20% and 5% were assigned for apparent resistivity and phase data, respectively. Control parameters that were defined in chapter 5 were set to values of τ=10 and α=1. This choice of α favours sub-vertical features, which might be expected to occur in a fault zone.

6.4.1 Resistivity models of the Erzincan Basin

Inversion models for the F and G-profiles are shown in Figure 6-7. The inversions were able to fit the measured MT data with values of r.m.s data misfit of 2.42 for the F-profile

and 1.82 for the G-profile. These values are relatively high compared to the values of 1.4 for the N and H-profiles. The higher r.m.s. misfit is probably due to the relatively high noise level in Erzincan basin MT data, as well as using a 2-D inversion approach which disregards 3-D effects in the data. Due to sharp topographic changes and the highly conductive basement in the Erzincan basin, 3-D effects are more likely. Three prominent layers are observed in both models:

- A low resistivity surface layer with 20-30 Ωm resistivity extends to a depth of 3 km on the F-profile and 2 km on the G-profile (Figure 6-7). This layer is associated with low resistivity sediments in the Erzincan basin (Kaypak and Eyidoğan, 2005).

- A high resistivity layer (~1000 Ωm) was imaged in the centre of the basin. This feature becomes shallower towards the northern and southern margins of the basin. Therefore, this layer is associated with the upper crustal crystalline rocks and the mountain ranges around the basin.

- The third layer begins at a depth of 20 km with a resistivity of 20-30 Ωm. This feature was observed throughout the Anatolian Block and Anatolian Plateau at the same depth with the same resistivity values (see chapter 5 for more details).

One of the most significant features of the model is the vertical zone of low resistivity (~10 Ωm) that connects the lower crustal low resistivity to the surface. This feature coincides spatially with the surface trace of the NAF on the G-profile.

Figure 6-7 show the r.m.s misfit and static shift coefficients as well as two-dimensional electrical resistivity models obtained by inversion. These two profiles have higher r.m.s. misfits than all the other profiles investigated in this thesis (A, B, C, D, E, N and H). This indicates that the MT data were not fit as well as the other profiles. Note that the models in Figure 6-7 appear rougher.

Static shift coefficients in the Erzincan basin were mostly smaller than 1. Figure 6-8 shows the inversion response and the observed data for the F and G-profiles. It can be seen that the F-profile data show some sharp changes from site-to-site for both modes (TE and TM).

The TM mode pseudosection can exhibit rapid changes in apparent resistivity due to shallow subsurface resistivity variations. In contrast, sharp changes in the TE mode apparent resistivity data are generally due to static shifts and 3-D induction effects. The 2-D inversion was able to fit the general trend of the observed data for the whole period range. However, data at periods 1-100 s for stations located between 0 km and 10 km were not equally fit on the F-profile. This location corresponds to the surface rupture of the NAF in the Erzincan basin.

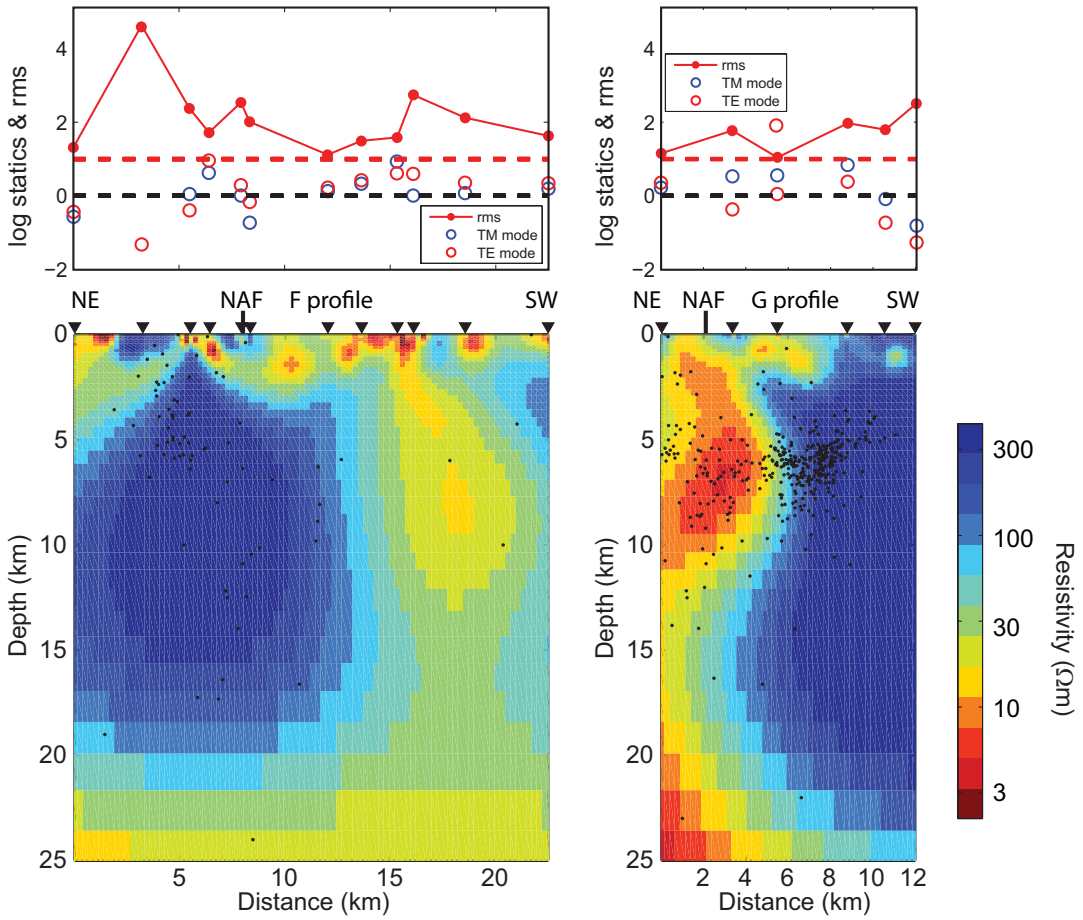

Figure 6-7. Two-dimensional electrical resistivity models for the F and G-profiles obtained by inversion of TE, TM and tipper data. Black dots show the earthquake hypocenters projected onto MT profiles (from 1960-2004 KOERI, Turkelli et al. (2003) and Kaypak and Eyidoğan (2005)). The width of the projection was 20 km. The r.m.s misfit for individual stations is plotted above the model, along with the static shift coefficients estimated by the inversion algorithm. Inversion parameters: both models used N70° E strike angle; 20%, 5%, 0.02 error floors for apparent resistivity, phase and tipper respectively; τ=10 and α=1.

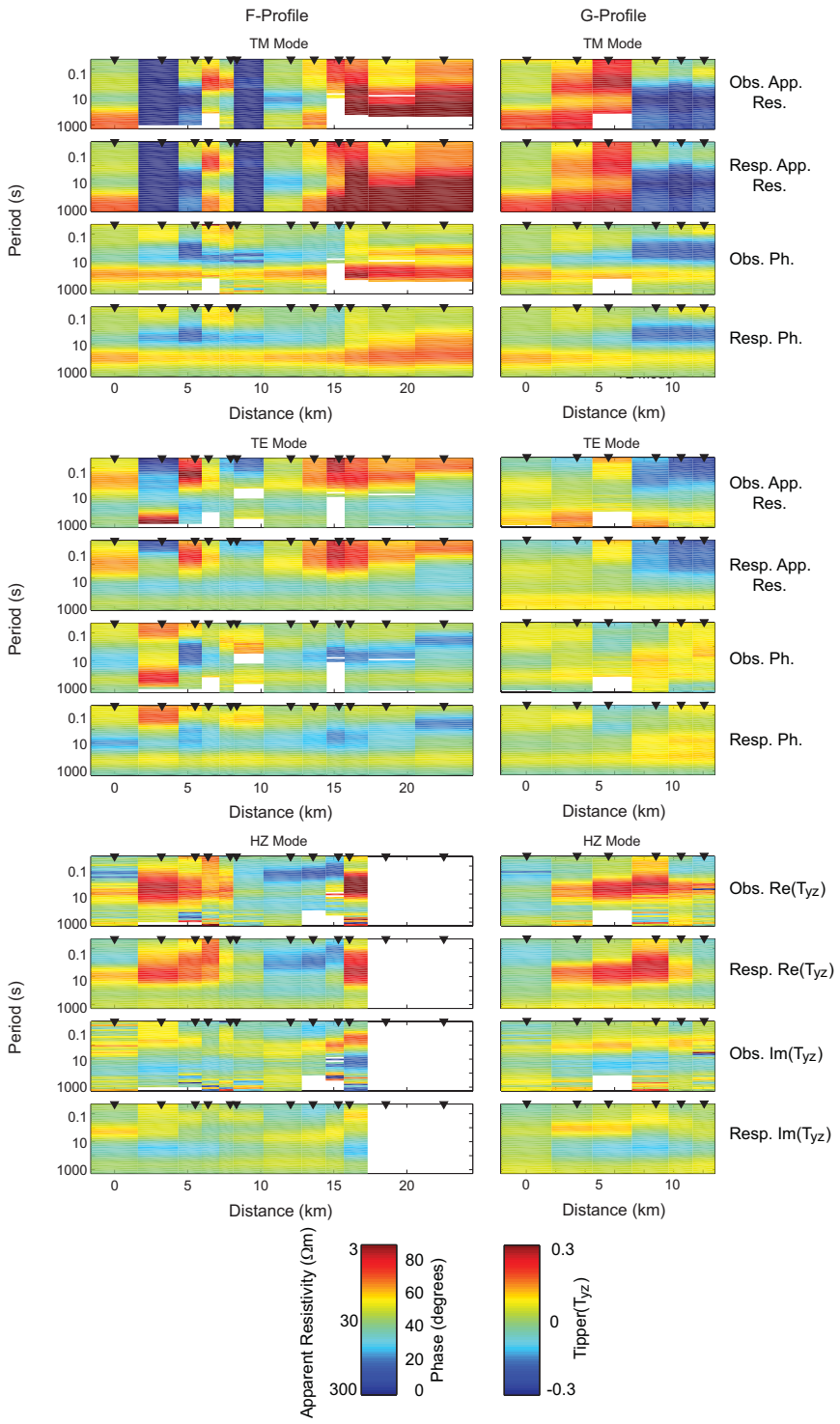

Figure 6-8. Pseudo section view of the observed and modeled apparent resistivity, phase and tipper data for the inversion models shown in Figure 6-7, for the F and G-profiles respectively. Two stations on the F-profile do not have tipper data.

6.4.2 Sensitivity test

The possibility of a vertical zone of low resistivity under the F and G-profiles (Figure 6-7) has important implications in terms of a fault-zone conductor which is similar to creeping segments of the SAF (Bedrosian et al., 2002). Therefore, the existence of this feature has to be justified by sensitivity analysis. Unfortunately, the profile lengths are short and station spacing is large in the Erzincan basin which limits the resolution of the MT data.

6.4.3 Effect of regularization

Using τ=10 was generally a good selection for inverting the eastern Anatolia MT data set. However, large station spacing (compared to shallow and detailed targets) particularly on the F-profile caused rough models when using τ=10. Therefore, the vertical channel of low resistivity could be an artifact of inversion due to smoothing. Three different values of τ (30, 10, 1) were used to invert the F-profile MT data and determine the effects of the regularization parameter. Reducing the regularization parameter τ from 10 to 1 decreased the r.m.s. misfit from 2.42 to 2.13, but resulted in even rougher and more unrealistic models (C in Figure 6-9). On the other hand, a larger smoothing parameter (τ=30) provided a smoother model and recovered similar features as shown in Figure 6-7. Therefore, presented models with τ=10 are the optimum ones that can be obtained from this data distribution and quality.

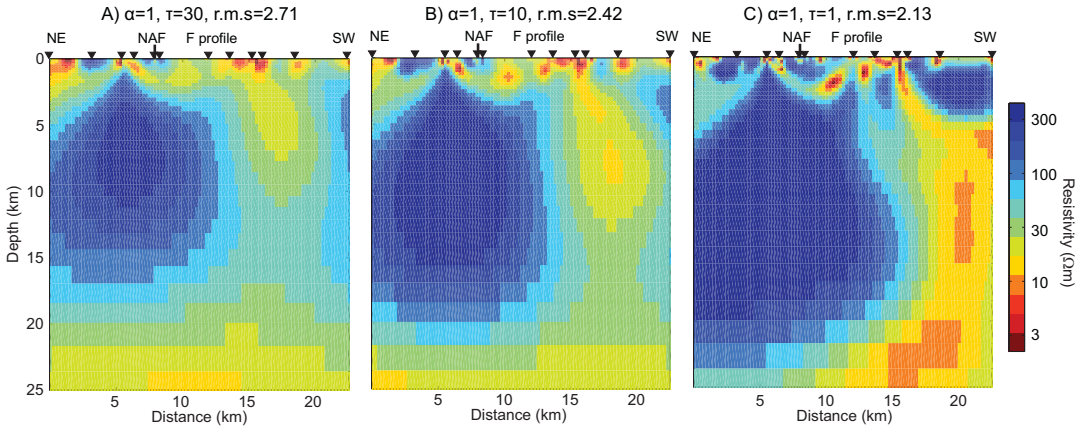

Figure 6-9. F-profile 2-D inversions for three values of τ (30, 10 and 1). Model C has the lowest r.m.s. misfit but is very rough compared to the A and B models. Model B is the preferred model.

6.4.4 Effect of geoelectric strike

It was shown in previous sections that geoelectric strike directions of the Erzincan basin MT data are frequency independent. Furthermore, the average geoelectric strike direction (70° NE) for the period range 2-40 s is not aligned with the surface strike of the NAF (115°-125° NE). Complexity of the Erzincan basin tipper data does not permit the 90° ambiguity of the MT data to be resolved. Therefore, a second set of inversions was implemented in which the geoelectric strike was assumed parallel to the fault strike (120° NE). The inversion models obtained with this strike direction give a better fit to the data and appear smoother than when the 70° NE strike was used. Final model r.m.s. misfit values reduced from 2.42 to 2.36 and from 1.82 to 1.58 for the F and G-profiles respectively.

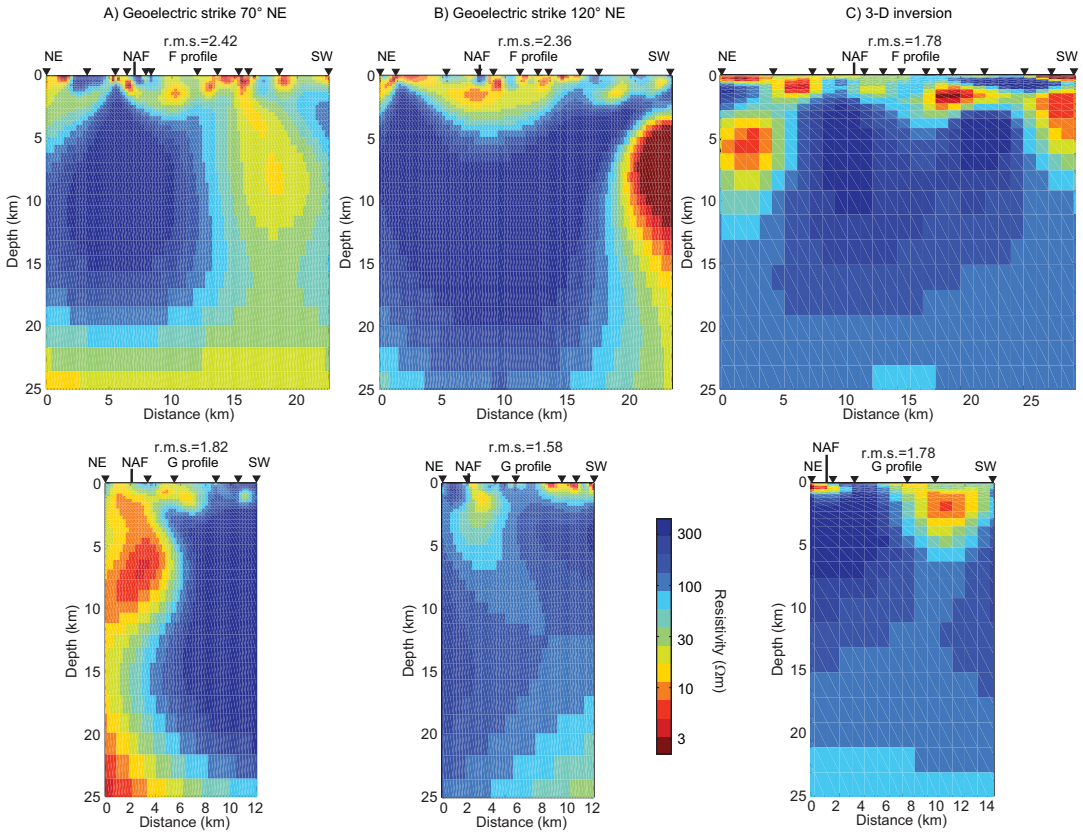

Figure 6-10. Models showing 2-D inversion results with different strike angles (A and B) and 3-D inversion result (C). A) strike= 70° NE; B) strike= 120° NE. Final model r.m.s. misfit values reduced from 2.42 to 2.36 and from 1.82 to 1.58 for the F and G-profiles respectively.

When the data were rotated to the direction of the fault strike, projected station spacing was more homogenous than when projected to the geoelectric strike direction as the MT stations was collected approximately perpendicular to the fault direction. The more homogenous station spacing could contribute to the models being smoother (Figure 6-10). Note that there is a significant difference between the locations of the vertical channel of low resistivity between the two approaches (Figure 6-7). Unfortunately, the available data quality and station spacing in the Erzincan Basin are not sufficient to yield a better estimation of the geometry and location of this anomaly. However, in both cases this zone is necessary to fit the observed data.

6.4.5 Thickness of the Erzincan basin

The depth of the Erzincan basin is an important parameter in models that predict the amount of shaking that would occur after a major earthquake. Sediments in the basin can cause resonance effects that amplify ground motion and increase damage (Olsen, 2000). The depth of the basin is also a necessary parameter for improving the 3-D earthquake relocation (Aktar et al., 2004; Kaypak and Eyidoğan, 2005). However, the depth of the basin is not well defined. Hempton and Dune (1984) used an empirical relationship of basin thickness and length and estimated 3 km for the sedimentary basin. S to P receiver function analysis of the 1992 Erzincan earthquake aftershocks used to determine the thickness of the basin and low velocity (<2 km/s) unconsolidated sediment thickness was found to be 0.65-2.1 km (Gaucher, 1993). Shear wave splitting studies detected anisotropy in the thick sedimentary layers and estimated 1-2 km for the thickness of the basin (Gamar and Bernard et al., 1997). Local earthquake tomography studies using aftershocks from the 1992 Erzincan earthquakes showed that the thickness of the low velocity (Vp <2 km/s) sediments in the basin could be as thick as 3 km (Aktar et al., 2004; Kaypak and Eyidoğan, 2005).

The two-dimensional MT inversions presented above are regularized (smoothed) and do not recover changes in subsurface resistivity such as the base of the Erzincan Basin. An alternative approach is to use layered 1-D inversions to estimate the basin thickness. Since the boundary between the low resistivity basin sediments and the upper crustal crystalline rocks is expected to be sharp, this approach could be useful in this situation.

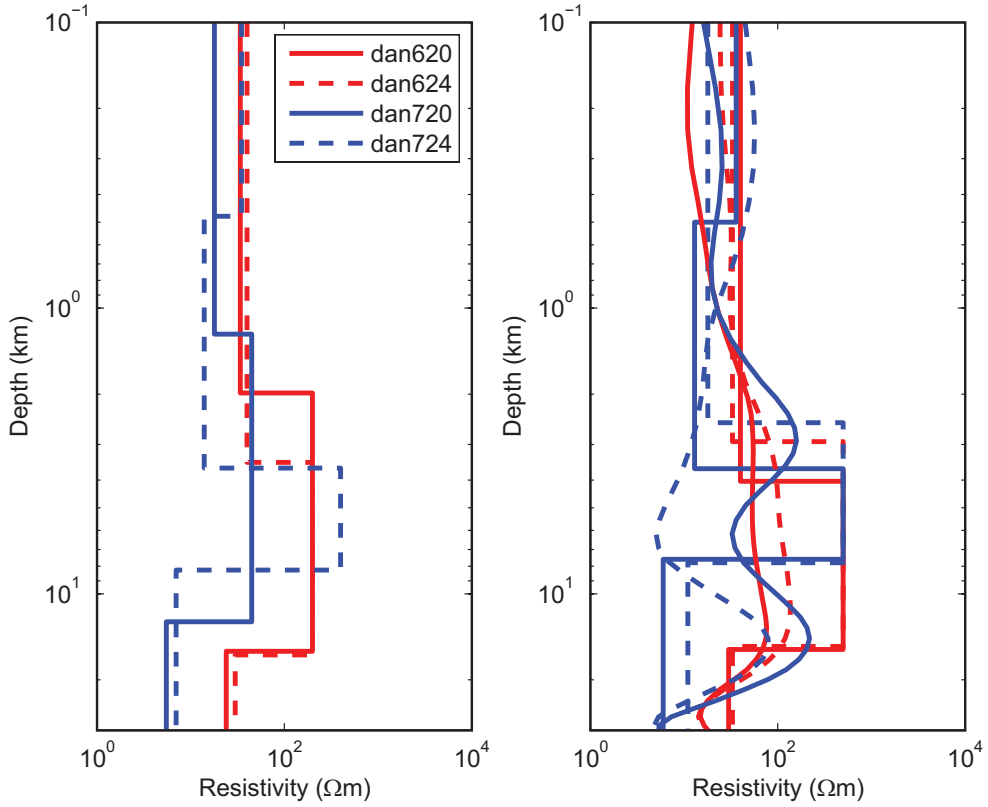

Figure 6-11. One-dimensional sharp layered inversion for central stations on the F and G-profiles. The left panel shows models obtained by unconstrained 1-D inversion. Models in the right panel were obtained by fixing the resistivity of the resistive layer to 500 Ωm. Straight lines and curves are 1-D and 2-D inversion results respectively.

The dimensionality analysis in section 6.3 indicated that the structure of the Erzincan Basin can be considered relatively 1-D near the surface. Thus, a simple one-dimensional inversion was used to determine the thickness of the Erzincan Basin at 4 stations. Two stations were chosen from the central F-profile (dan620 and dan624) and the other two stations were chosen from the central G-profile (dan720 and dan724). Initial inversions revealed the same 3-layer structure described above but the thickness of the basin varied significantly between closely spaced stations on both profiles. This variation is due to the non-uniqueness of the MT inverse problem and means that only the conductance (thickness of the layer multiplied by the conductivity of it) of a layer is well defined, and not the individual resistivity and thickness. A thick, less resistive layer will give exactly the same MT response as a more resistive and thicker layer (Parker, 1980). This problem is severe in the case of one-dimensional MT inversion and external constraints are generally used to fix

either the resistivity or the thickness of the layer. In this case the resistivity of the second zone that is a resistive layer between two conductors was fixed to 500 Ωm (Figure 6-11) with the assumption that the resistivity of the basement rock does not change significantly over such short distances. In this case, the 20-30 Ωm top layer that corresponds to the sedimentary fill of the Erzincan Basin was found to be at a depth of 3±0.25 km on both profiles with a slight increase (~0.25 km) in thickness underneath F-profile.

6.5 Inversion of magnetotelluric data on the North Anatolian Fault at Refahiye

A subset of the MT data on the C-profile close to the North Anatolian Fault (NAF) was reanalyzed with the goal of defining detailed fault zone structure (N-profile in Figure 6-2). All the MT stations were projected onto a profile perpendicular to the geoelectric strike directions determined in section 6.3.2. The inversions used a finer mesh than in the regional scale inversions described in chapter 5. All available high frequency MT data were included in the inversions to obtain detailed resistivity models. Identical inversion parameters were used as for the F and G-profiles shown in Figure 6-7.

The inversion model for the N-profile is shown in Figure 6-12 and has a data r.m.s. misfit value of 1.4. This value is statistically acceptable, in contrast to the inversions for the F and G-profiles in the Erzincan basin. This lower misfit is expected since the dimensionality analysis suggests the impedance tensor is relatively 2-D at this location. Static shift coefficients estimated by the inversion were less than 1. The final model is both vertically and horizontally smooth (Figure 6-12).

The inversion model for the N-profile is quite similar to those for the F-profile. A resistive block 15 km is located just south of the surface trace of the NAF is similar to that imaged at the northern end of F-profile. A narrow part of this block reaches the surface. Structure north of the NAF is highly resistive (>1000 Ωm). Beneath these resistive layers a low resistivity layer begins at a depth of ~20 km. The location, resistivity and the shape of this low resistivity channel beneath the NAF was also detected in 3-D inversions (Figure 5-2 in chapter 5). Therefore, this is a robust feature.

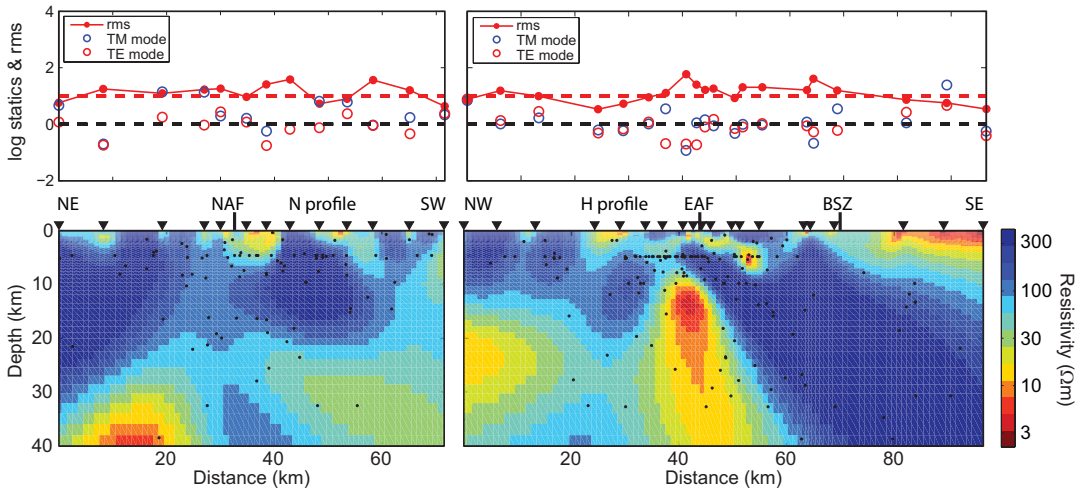

Figure 6-12. Two-dimensional electrical resistivity models for N and H-profiles obtained by inversion of the TE, TM and tipper data. Black dots show earthquake hypocenters projected onto the MT profiles (from 1960-2004 KOERI, Turkelli et al. (2003) and Kaypak and Eyidoğan (2005)). The width of the projection was 20 km. The r.m.s misfit for individual stations is plotted above the model, along with the static shift coefficients estimated by the inversion algorithm. Inversion parameters: N-profile model used 105° NE strike angle and H-profile model used 75° NE; 20%, 5%, 0.02 error floors for apparent resistivity, phase and tipper respectively; τ=10 and α=1.

6.6 Inversion of MT data on the East Anatolian Fault at Hazar Lake

A subset of the A-profile MT data was used for detailed imaging of the EAF. This profile (H-profile) crosses the Bitlis Suture Zone and the EAF. The inversion model for H-profile is shown in Figure 6-12. The final r.m.s. misfit value was 1.4. The magnitude of the r.m.s misfit and static shifts coefficients were similar to those obtained for the N-profile and the data were adequately fit. The inversion model for the H-profile reveals a number of significant features. The EAF represents the main boundary between the resistive block on the south and the lower resistivity crustal features to the north. The most prominent feature of this model is the vertical conductor located approximately beneath the EAF at 45 km distance and 10 km depth. A 3-D inversion of the A-profile also showed similar features as observed in this detailed study. However, the vertical conductor underneath the EAF was not as strong in the 3-D inversion models (Figure 5-2). This difference is probably due to the limited resolution in 3-D the inversions. Limited data and large mesh spacing were required to overcome the extensive computational time required for the 3-D inversions.

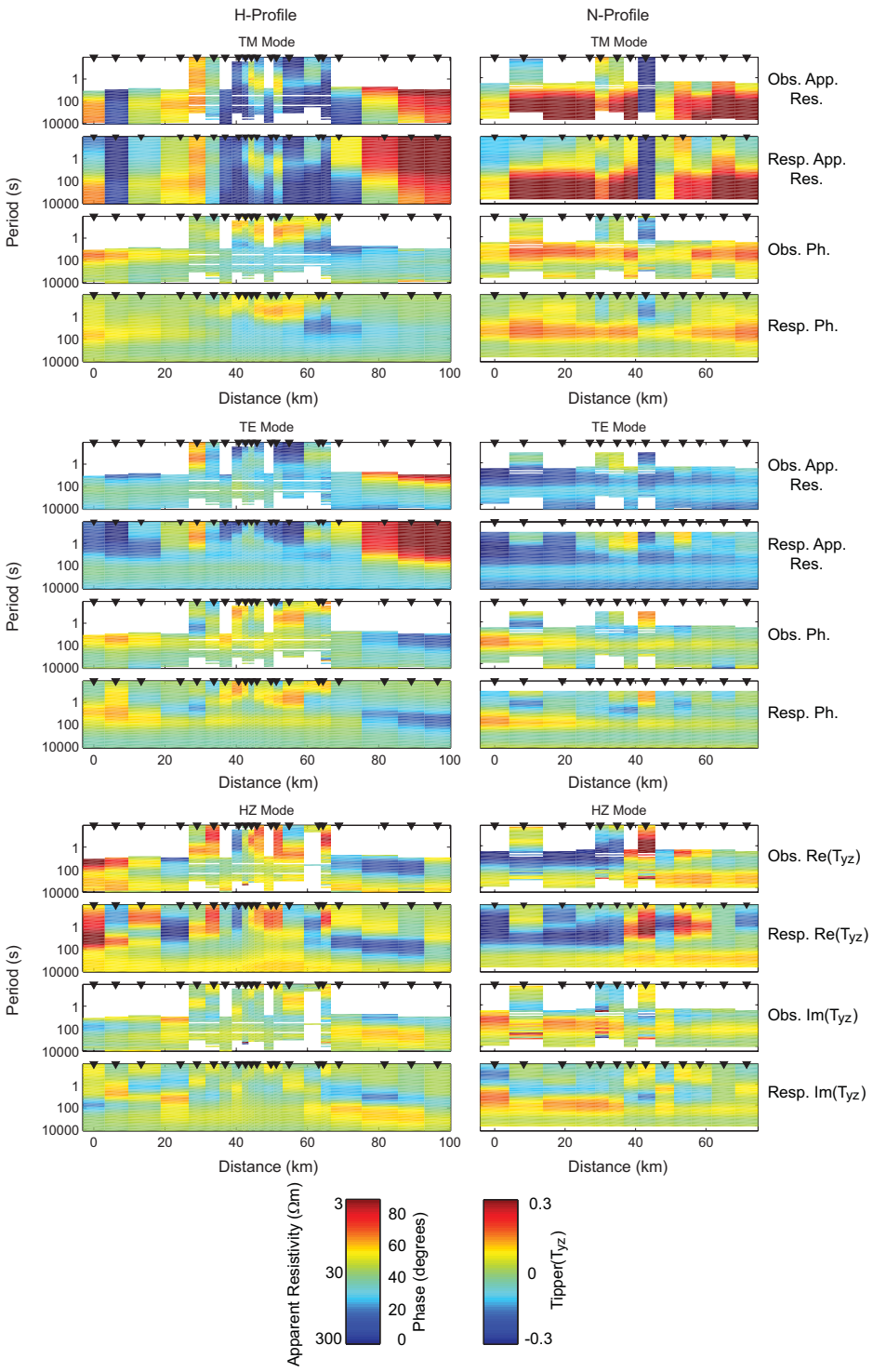

Figure 6-13. Pseudo section view of the observed and modeled apparent resistivity, phase and tipper data for the inversion models shown in Figure 6-12, for N and H-profiles respectively.

As introduced earlier in chapter 5 and in this chapter, the fit of the inversion response to the observed MT data should be examined to see if a uniform fit is obtained. Ideally a "white" fit is desired where all periods (frequencies) are fit equally well. If a particular range of periods are not well fit then the final inversion model may be misleading and larger error floor values may be needed to focus the inversion on a particular range of periods corresponding to structures of interest. Figure 6-12 shows that a satisfactory fit to the measured data was obtained for the entire period range used for inversion (0.01-10,000 s). Sharp lateral resistivity changes in the pseudo sections occur because computed static shifts have been applied to the apparent resistivities of the model response. In fact, the response data are laterally smoother than they appear in Figure 6-13. Comparing Figure 6-13 and Figure 6-8 indicates that N and H-profile 2-D inversions are capable of fitting the observed data while F and G-profile 2-D inversions are only partly well fit.

6.7 Interpretation

6.7.1 Erzincan Basin (F and G-profiles)

The thickness of the Erzincan basin is poorly known. The lack of seismic reflection and borehole data means that indirect methods must be used to determine the basin thickness. Inversion models obtained from MT data collected within the Erzincan Basin revealed a low resistivity surface top layer. This layer corresponds to the fluid and clay rich sedimentary basin of Erzincan. 1-D, 2-D and 3-D inversion of MT data in the basin showed that the thickness of the basin to be around 3±0.25 km. This depth is comparable to the 3 km estimate from earthquake tomography (Kaypak and Eyidoğan, 2005). However, current station spacing and distribution does not allow detailed imaging of the basin towards the edges.

6.7.2 Lower crustal conductor

A lower crustal low resistivity layer (10-30 Ωm) is observed at a depth of 20 km throughout eastern Anatolia. This zone spatially coincides with the eastern Anatolian Accretionary Complex, very low gravity anomaly (<-130 mGal) and low seismic velocity. Therefore, this zone likely indicates a weak rheology for the lower crust. The lower crustal

conductive layer appears to be connected to the NAF and EAF with a low resistivity vertical channel (Figure 6-7 and Figure 6-12). Lateral extent of the widespread lower crustal low resistivity zone is bounded by NAF, NEAF and BSZ in the study area. Detailed discussion on this feature is given in section 7.3.2.2.

6.7.3 Fault-zone conductor (FZC)

A vertical zone of low resistivity is imaged on both profiles (F and G) in the Erzincan Basin. This feature is required to fit the data. However, it is located close to the end of both the F and G-profiles where resolution of MT data is limited. Additionally, sparse station spacing does not allow further constraining properties of this feature. Furthermore, 2-D inversion of MT data is sensitive to a maximum depth that is shorter than the profile length. Therefore, 5-10 km depth of this vertical conductor target may not be correctly located, particularly on G-profile.

The NAF on the N-profile has a similar geoelectric structure to the F-profile in the Erzincan basin. However, the resistivity of this channel is not as low as in the Erzincan basin or on the H-profile (Figure 6-12). The NAF is located in a region where the MT inversion model indicates zones of lower resistivity from the surface down to a maximum depth of just 5 km. The NAF separates two resistive zones and is imaged as a 15 km wide zone of relatively low resistivity (100 Ωm). A feature comparable to the FZC on F and G-profiles was not detected. Furthermore, another zone of low resistivity is imaged north of the Fırat River.

The most prominent feature of the inversion model of the H-profile on the East Anatolian Fault (EAF) at Hazar Lake is the narrow vertical conductor located beneath the surface trace of the EAF (Figure 6-12). The low resistivity (~10 Ωm) and geometry of this feature is similar to that observed in the Erzincan Basin. Due to the non-uniqueness of MT inversion and limited resolution on the depth extent of the conductive anomalies, the amount of conductance (integrated conductivity) required to fit the MT data is preferred for comparison. The total conductance required by the MT data is around 4000 S for the EAF at Hazar Lake and around 1000 S for the NAF at Refahiye.

The top of the EAF fault conductor is well constrained by MT data and is at a depth of 10 km. If average resistivity above 10 km is around 100 Ωm (0.01 S/m) then 100 S of the observed conductance can be accounted for by the part above the conductor. Therefore, the NAF fault conductor requires a conductance of 3,900 S. This conductance can be explained in 2 ways.

- Firstly, assuming this feature extends throughout the crust, which is 40 km thick around this region (i.e. Zor et al., 2003); the resistivity of the EAF fault-zone conductor was calculated to be 7.6 Ωm.

- Second, if this feature extends only until the brittle-ductile transition zone which is 17-18 km in this area (Bektaş et. al., 2007), then the fault-zone conductor would have a resistivity of 4.5 Ωm.

Using Archie's Law (eq. 6.1) with fluid resistivity of 0.3 Ωm (saline fluid), 4-20% and 7-26% (m=1 for cracks and m=2 for spherical pores) porosities at the fault zone are required for the first and the second cases respectively. However, the expected pore geometry is aligned cracks in a fault environment which promotes interconnection at low porosities. Therefore, expected maximum porosity values are close to the first porosity values for each case. These values are comparable to 8.6% estimated for the San Andreas Fault at Parkfield (Unsworth et al., 1997).

Combined interpretation of magnetic, seismological and geologic data by Dolmaz et al., (2008) showed that a low seismic activity zone on the East Anatolian Fault coincides with a shallow curie depth (~14 km) and a high magnetic anomaly. They interpreted this area to have relatively thinner crust and higher local temperatures than the adjacent regions. Therefore, this part of the fault is behaving in a ductile way and allowing creep. The H-profile crosses the EAF at this low seismic activity zone (Figure 6-1). Therefore, the imaged fault-zone conductor beneath the H-profile (Figure 6-14) could be an indication of fluids, allowing the fault to creep. This fault-zone conductor is similar to the deep conductor imaged on the creeping segment of the SAF at Hollister (Bedrosian et al., 2004).

MT studies on the western part of the NAF revealed enhanced conductivity in the fault zone around İzmit (Tank et al., 2005). This anomaly started at a depth of 15 km and

extended down to the lower crust. This low resistivity (10-50 Ωm) anomaly was bounded by the northern and southern branches of the NAF and interpreted as a fluid-rich region, supplied at depth by partial melting. It was suggested that this layer could control seismicity and determine if the fault was locked or creeping (Tank et al, 2005). This part of the NAF can be considered as a rheologically weak fault where fluids allow creep which reduces the fault friction and in turn reduces the shear stress required for rupture. Creeping occurs at 8 mm/y rate around the İsmetpaşa region (Çakır et al., 2005) which is located ~150 km east of the study area of Tank et al., (2005).

In this study, the fault segment imaged on the N-profile does not show elevated conductivity. Furthermore, creeping was not reported previously. Therefore, the NAF could be a dry fault at this location. Regional stress studies are needed to determine if this dry segment overlaps with the seismically locked part of the NAF. On the other hand, induction vectors in Figure 6-2 show a cross-over south of the known surface rupture of the NAF. Therefore, the lower resistivity region from surface to 5 km depth and 5 km south of the marked location of the NAF could represent the fluid-rich branch of the NAF. However, large station spacing does not allow the resistivity and geometry of this feature to be investigated in detail (Figure 6-14).

Janssen et al., (1997) studied the geochemistry and geometry of various segments of the NAF around İznik, Düzce and Bolu. According to their results, east-west migrating earthquake cycles along the NAF are closely linked to spatial and temporal water flow within the fault zone. Therefore, the observed enhanced conductivity in the western part could be explained by this fluid migration model. However, trace element, isotopic data and fluid inclusion studies indicated that the source of the water at the fault zone is meteoric or intraformational (Janssen et al., 1997), rather than a lower crustal or mantle source suggested by Tank et al., (2005).

6.8 Conclusion

Detailed analysis of the MT data collected on the North and East Anatolian Faults was presented in this chapter. Profiles in the Erzincan basin provided an independent estimate for the thickness of the basin to be 3±0.25 km with a slight increase (~0.25 km) in

thickness towards the west. However, the basin shape towards the edges was not constrained due to limited data.

A vertical conductor from surface to lower crustal levels was imaged on both the F and G-profiles but neither the location nor the existence of this feature was verified by sensitivity analysis. To resolve this feature, a 3-D survey would be needed with additional MT data. This would require a grid of MT stations in the Erzincan basin as well as profiles that extend beyond the basin to the north and south. A zone of relatively low resistivity (100 Ωm) was observed beneath the NAF around Refahiye (N-profile). This resistivity value is almost an order of magnitude higher than those found underneath the western part of the fault (Tank et al., 2005). A vertical conductor was also observed beneath the H-profile on the EAF. This feature may imply that creep occurs on this segment of the EAF. Two other profiles crossing the EAF 100 km east and 100 km west of the H-profile where high seismic activity occurs are needed to clarify the argument that zones of high seismicity are dry and do not have a fault-zone conductor.

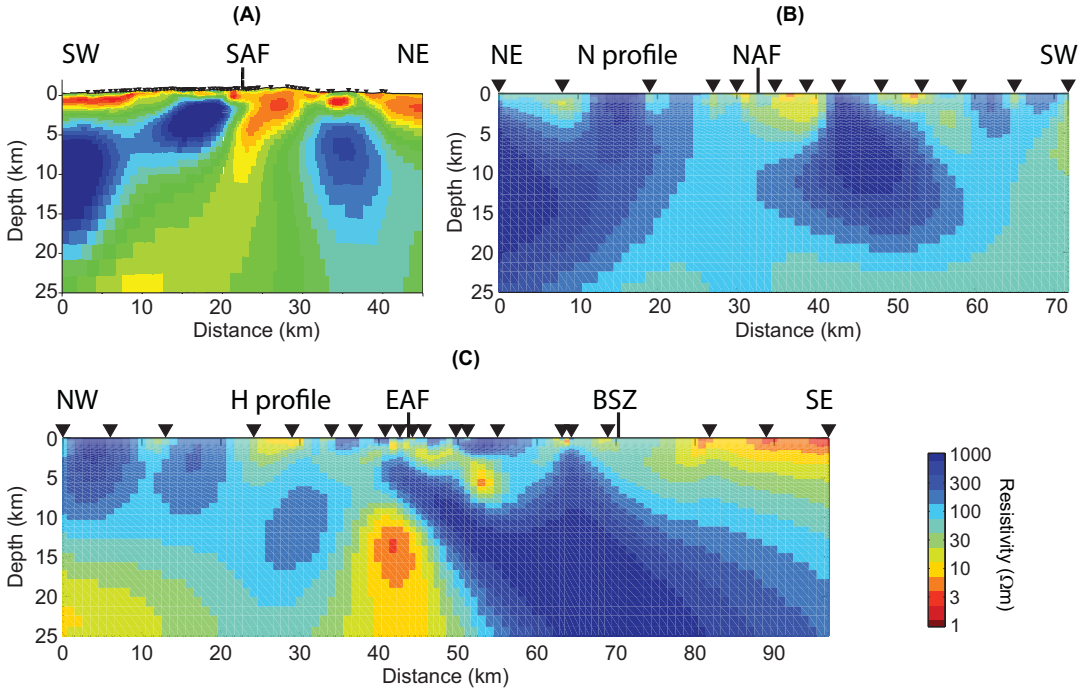

Figure 6-14. (A) MT profile across the San Andreas Fault (SAF) (figure from Becken et al., 2008); (B) N-profile across the North Anatolian Fault (NAF); (C) H-profile across the East Anatolian Fault (EAF). Station spacing is much larger in this study compared to the SAF.

Figure 6-14 shows a side-by-side comparison of the SAF (Becken et al., 2008), NAF and EAF magnetotelluric models. The models obtained in this thesis used wider station spacing than the SAF studies and this resulted in lower resolution. However, in both studies, ~10 km wide vertical conductors reaching lower crustal levels around the EAF and SAF are similar. As we do our observations within an earthquake cycle, creeping or locked segments of a fault system can be significantly different due to water flow in the fault before and after a large event. Therefore, repeated observations across the faults could be used for fault monitoring and risk assessment.

7 INTERPRETATION

This chapter describes the interpretation of the resistivity models obtained by 2-D and 3-D inversion of the eastern Anatolia MT dataset. The interpretation is focused on the regional scale features that characterize the collision zone, rather than smaller-scale structures associated with individual fault zones. The origin of low electrical resistivity in the crust and upper mantle is discussed. Previous geophysical and geological studies are used to reduce the ambiguity in the interpretation of the resistivity models and to determine which geodynamic processes are active.

7.1 Cause of low resistivity zones in crust and mantle

Zones with low resistivity are widely observed in the lower crust and upper mantle in many tectonic settings. The low resistivity has been attributed to a range of mechanisms including graphite films, sulphides, aqueous fluids or partial melt (Brown, 1994; Constable and Heinson, 1993; Jones, 1992; Yardley and Valley, 1997). Possible explanations for the low resistivities observed in eastern Anatolia are evaluated below.

7.1.1 Graphite films

Graphite has a very low electrical resistivity, typically 10^{-5} Ωm (Duba and Shankland, 1982) and when grain-boundary graphite films are interconnected over large distances they can account for a bulk resistivity of 1 Ωm with just 0.1% graphite content (Frost et al., 1989). Subducted metasediments are believed to be the source of the graphite. The North American Central Plain Anomaly (Camfield and Gough 1977) and Kiskatinaw Anomaly (Boerner et al., 2000; Türkoğlu et al., 2009) have been interpreted as ancient suture zones containing graphitic films that have remained interconnected in a stable tectonic setting.

Similar features have been reported from Namibia (Ritter et al. 2005), Fennoscandia (Rasmussen et al. 1987), the Iapetus suture zone (Rao et al. 2007; Tauber et al. 2003) and the Trans-Hudson orogen (Jones et al. 2005).

This type of graphitic conductor can probably be excluded as an explanation for the low resistivity in eastern Anatolia since interconnection of graphite is unlikely to be preserved in a high temperature, active tectonic regime (Li et al., 2003). Additionally, the low resistivity (10-30 Ωm) lower crustal layer is spatially widespread and extends across major tectonic features such as the NAF, EAF and NEAF (Figure 6-3) where interconnection of the graphite is unlikely to be preserved. It is possible that pockets of low resistivity zones on the B, C and E-profiles may be caused by graphitic conductors. However, these zones also exhibit unusually low seismic velocities and low resistivities. The presence of graphite films can explain the low resistivity, but not the low seismic velocity.

The presence of sulphides minerals is another possible explanation for the low resistivity of the upper mantle (Ducea and Park, 2000). Pure sulphides have electrical resistivities in the range of 10^{-2}-10^{-6} Ωm when found in discrete ore bodies. However, to lower the resistivity of a region in the upper mantle, they must be interconnected and this is not likely in an active tectonic regime over significant horizontal distances.

7.1.2 Fluids

Aqueous fluids or melt can also explain the low resistivity observed in the crust and mantle. Fluids present in the pore space can reduce the bulk electrical resistivity of a rock, as quantified by Archie's Law (Archie, 1942):

$$\rho = \rho_f \Phi^{-m} C^{-1} \tag{7.1}$$

In eq. 7.1 ρ is the bulk resistivity of the fluid saturated rock and ρ_f is the resistivity of the pore fluid. Archie's Law assumes that all electrical conduction occurs through the fluid, and therefore the resistivity of the rock grains does not appear in eq. 7.1. The porosity of the rock is Φ and m is the cementation factor that describes the geometry of the pore fluid distribution. A value of $m = 1$ implies good interconnection with crack shaped pores while

m = 2 implies poorer interconnection with spherical shaped pores. The scaling factor C used to account for the rapid geometrical change of the melt from 0.01% to 0.1% (ten Grotenhuis et al., 2005). Since the development of Archie's Law, other empirical formulae have been derived to relate the porosity, pore fluid resistivity and the bulk resistivity of the rock (Grant and West, 1965; Schmeling, 1986; Hashin and Strikman, 1962; Waff, 1974; Beekmans and Heyne, 1976; Schilling et al., 1997).

Archie's Law is still widely used and experimental studies are needed to determine the value of the cementation factor m. ten Grotenhuis et al. (2005) showed that olivine melts are well characterized by Archie's Law with C = 1.47 and m=1.3. Laboratory experiments showed that the transition from a network of triple junction tubes at grain interfaces to a network of grain-boundary melt layers occurs when the melt fraction increases from 0.01% to 0.1%. High values of m correspond to high values of dihedral angle while low values of m correspond to low values of dihedral angle. Laboratory experiments show that wetting of the grain boundaries can occur at melt fractions of 2-8% (Partzsch et al., 2000).

The Hashin-Strikman lower and upper bounds (Hashin and Strikman, 1962) correspond to the minimum and maximum bulk resistivity when the rock grains and the melt are connected in parallel and series respectively (eq. 7.2). The Hashin-Strikman Lower bound (ρ_{HSL}) and Archie's Law assume a two phase material to compute the bulk resistivity but disregard the fact that conduction through the mineral grains can occur at high temperature.

$$\rho_{HSL} = \rho_r + \frac{\Phi}{\frac{1}{\rho_f + \rho_r} + \frac{1-\Phi}{3\rho_r}} \tag{7.2}$$

The bulk resistivity of the partially molten rock at higher melt fractions is better described by the modified version of the Brick Layer Model (MBLM) of Beekmans and Heyne (1976) where conduction through both the mineral grains (ρ_r) and melt is considered ρ_f).

$$\rho_{MBLM} = \frac{\rho_f\left(\rho_f\left((1-\Phi)^{2/3}-1\right)-\rho_r(1-\Phi)^{2/3}\right)}{\rho_r\left((1-\Phi)-(1-\Phi)^{2/3}\right)+\rho_f\left((1-\Phi)^{2/3}-(1-\Phi)-1\right)} \tag{7.3}$$

As ρ_{MBLM} takes into account the change of the resistivity of the rock grains with increasing temperature, it may be more representative for higher melt fractions (Schilling et al., 1997).

7.2 Nature of fluids in the lower crust and upper mantle

7.2.1 Stable continental regions

Petrological studies show that the deep continental crust in stable regions is not a source of fluids. In fact this region absorbs water through retrograde metamorphic reactions that incorporate water into hydrated mineral assemblages (Yardley and Valley, 1997). Therefore, the presence of interconnected free water at lower crustal depths is not accepted by many petrologists. However, some studies of rock samples from deep boreholes (~12km) indicated the presence of brines (Kozlovsky, 1982; Borevsky et al., 1995) in the upper crust. When the brine is very conductive, only a low porosity (0.1%) is needed to account for the observed bulk resistivities (2-5 Ωm). Such low porosity cannot be detected by seismic velocity measurements (Vanyan et al., 2001). Fluid content is important because it controls the rheology of the lithosphere and in general stable regions are strong and dry while active regions have higher fluid content.

7.2.2 Tectonically active regions

There has been an ongoing debate regarding whether aqueous fluids, partial melt or a combination of both are the cause of low resistivity zones frequently observed in active tectonic regimes (Unsworth et al., 2005; Li et al., 2003; Marquis and Hyndman, 1992; Vanyan et al., 2001). Aqueous fluids at mid to lower crustal depths can be formed by dehydration of amphibole-bearing rocks at 650-700° C (Vanyan and Gliko, 1999), and meteoric waters circulating through the fault zones or by subduction of fluid saturated lithosphere. It has been shown that the water content of the backarc upper mantle controls the style of upper mantle convection (Hyndman et al., 2005).

The melting point of most rocks is dramatically lowered by the presence of water. Figure 7-1 shows conductivity measurements of wet (Lebedev and Khitarov, 1964) and dry

(Tyburczy and Waff, 1983) melting as compiled by Li et al. (2003). Wet partial melting of felsic rocks begins at 650° C and this temperature is generally reached at around 80 km in cratons and around 20 km within active mobile belts (Hyndman and Lewis, 1999; Chapman and Furlong, 1992). Mafic rocks begin melting slightly higher temperature. Assuming steady-state conductive heat transfer in the crust Chapman and Furlong (1992) predicted a heat flow of 90 mW/m^2 should be observed in such regions.

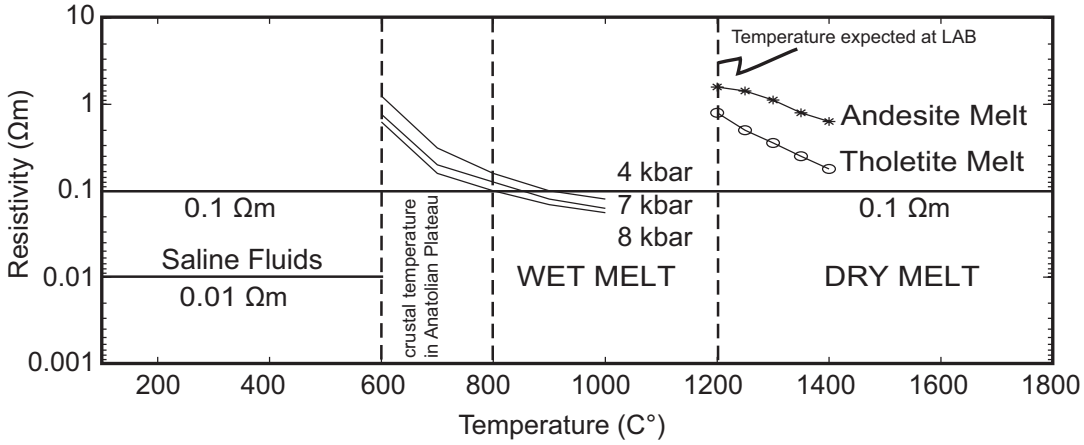

Figure 7-1. Electrical resistivity of saline fluids compared with wet (Lebedev and Khitarov, 1964) and dry (Tyburczy and Waff, 1983) partial melts (Figure modified after Li et al., 2003). LAB: Lithosphere-asthenosphere boundary.

Since eastern Anatolia is tectonically active, with a high heat flow (80-90 mW/m^2), it is possible that low resistivities are due to partial melts and aqueous fluids. The Curie depth in eastern Anatolia is 17-19 km and corresponds to a temperature of approximately 580° C. Assuming that the crust is hydrated then a few percent partial melt is expected to occur at mid and lower crustal depths in eastern Anatolia.

The resistivity data alone cannot determine the type of fluids and other geophysical methods (e.g. seismic velocities) are needed to distinguish the type of the fluids in the crust. Aqueous fluids may reduce the bulk resistivity by two orders of magnitude at very small (0.1%) fractions but this will likely have a small impact on the observed seismic velocities compared to few percent partial melt.

7.3 Interpretation of resistivity models

The first order variations in resistivity structure in eastern Anatolia can be observed from the apparent resistivity curves measured with the MT survey (Figure 7-2). MT stations on the Arabian Plate show an increase in apparent resistivity with increasing periods, while MT stations on the Anatolian Plateau show apparent resistivities that are constant, or which decrease with increasing period. This observation is quantified by the 2-D inversions presented in Chapter 5. Figure 7-2 shows resistivity-depth curves for MT stations on the north (Figure 7-2b) and on the south (Figure 7-2c) of the Bitlis Suture Zone (BSZ) obtained from 2-D inversions of the B-profile. According to this figure, the lower crust and upper mantle are more conductive beneath the Anatolian Plateau than the Arabian Plate.

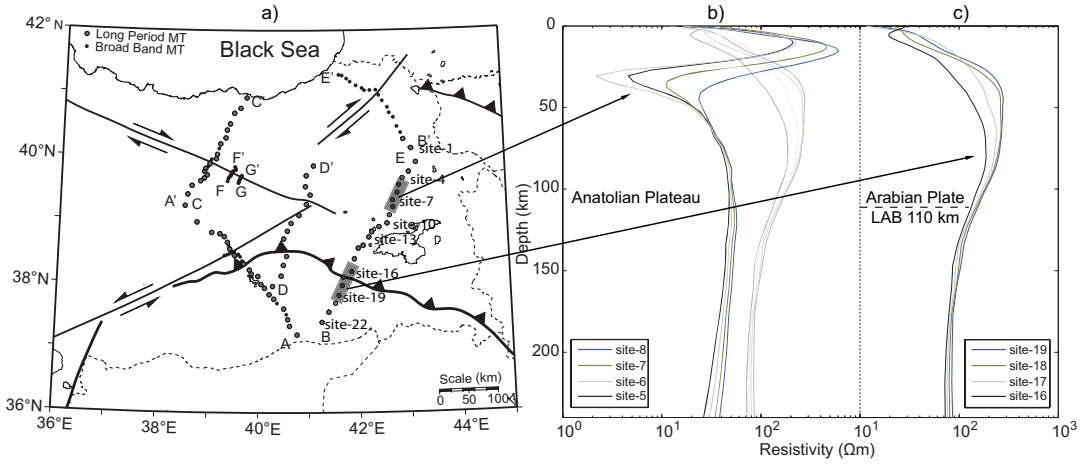

Figure 7-2. Resistivity-depth plots for selected MT stations on the B-profile obtained by 2-D inversions. Curves on the left are from the Anatolian Plateau (b), curves on the right are from the Arabian Plate (c). Lower crust and upper mantle has a lower resistivity beneath the Anatolian Plateau than the Arabian Plate. The dashed line shows the Lithosphere-asthenosphere boundary (LAB) of the Arabian Plate from constrained 2-D MT inversions.

The MT-derived resistivity models are displayed in Figure 7-3 along with available geological and geophysical data and explained in the following sections. The study area can be divided into three main parts based on the characteristics of the resistivity models shown in Figure 7-3. The boundaries of these regions correlate well with the margins of the tectonic blocks described in Chapter 3. The BSZ defines the boundary between the Arabian Plate (AP) and the Eastern Anatolian Accretionary Complex (EAAC). The Pontide Suture defines the boundary between the Rhodope-Pontide (RP) unit and the EAAC.

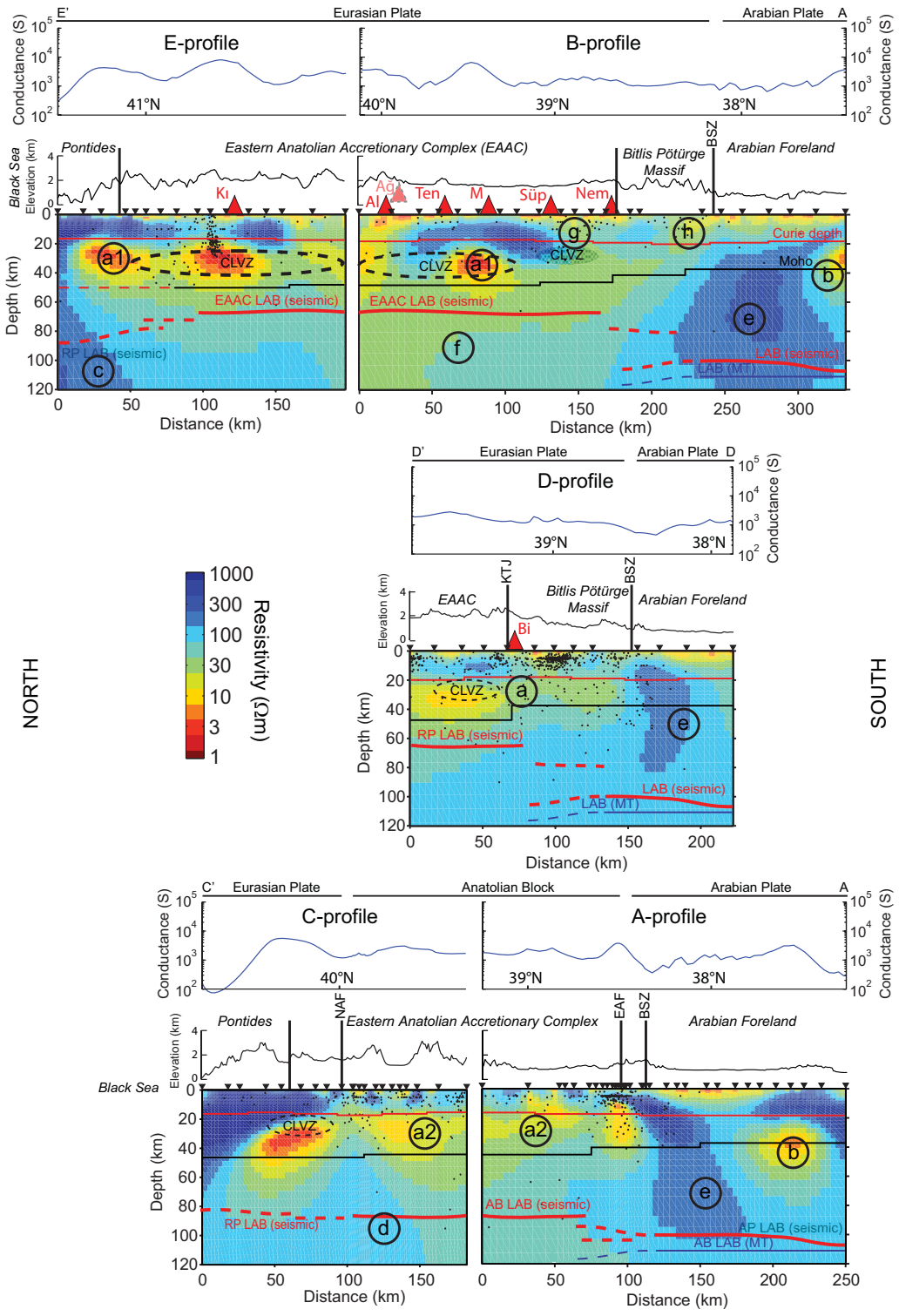

See next page for figure caption.

Figure 7-3. 2-D resistivity models obtained by inversion of MT data. Small dots show earthquake hypocenters between 1960 and 2004 KOERI, Turkelli et al. (2003) and Kaypak and Eyidoğan (2005). Black line represents the approximate Moho depth from receiver functions (Zor et al., 2003). Thin red line shows the Curie depth (Bektaş et al., 2007). Thick dashed and solid red lines show the approximate depth to the base of the lithosphere from teleseismic (Gök et al., 2007). Blue line shows LAB obtained from constrained 2-D MT inversion. The main geoelectric features are shown as letters and explained in the text. Volcanic centers are shown by red triangles as follows: Nem: Nemrut, Süp: Süphan, M: Meydandağ, Ten: Tendürek, Ağ: Ağrı, Al: Aladağ, Ki: Kısırdağ, Bi: Bingöl.

7.3.1 Arabian Plate

Three profiles (A, D, and B) cross the BSZ and show similar resistivity structures within the Arabian Plate. The sedimentary basin on the Arabian foreland produces the low resistivity from the surface to a depth of 5 km. South of the BSZ, the lower crust exhibits a high electrical resistivity on all three profiles. A low resistivity feature ("b" in Figure 7-3) may be related to intraplate volcanism at Karacadağ volcano, whose 1.9-0.1 Ma old lavas exhibit a mantle origin (Pearce et al., 1990, Notsu et al., 1995). The lateral east-west extent of this anomaly could not be determined from the MT data due to limited station coverage. A low resistivity feature is required to fit the MT data on the A-profile but may not be needed on the B-profile (see chapter 5 for discussion). The top of this feature is at a depth of 30 km but the depth of its base cannot be determined from the MT data alone. This feature could extend down to base of the lithosphere and is not necessarily confined in the lower crust.

The lithosphere of the Arabian Plate is characterized by a resistive zone (100-300 Ωm) that terminates close to the BSZ ("e" in Figure 7-3). All three profiles crossing the BSZ show that the resistive Arabian lithosphere extends ~30 km north of the BSZ. This boundary is marked on Figure 7-6C and also indicated by the 3-D inversion resistivity-depth slices (Figure 5-18) This could be a result of the limited resolution of the MT data, but the presence of this feature on all three profiles suggests it is real. Additional support for the extension of Arabian lithosphere north of the BSZ comes from the S-wave receiver functions in this area that map the lithosphere-asthenosphere boundary of the Arabian Plate. According to these studies a deep (~100 km) LAB was traced as far north as 39° N at 41°-42° E longitude (Angus et al., 2006). North of this region the LAB becomes shallower

60-65 km, and more typical for the Anatolian Plateau, and also for recent and active backarcs (Hyndman et al., 2005).

7.3.1.1 Lithospheric thickness of the Arabian Foreland derived from MT data

The lithospheric mantle typically has a resistivity of 10^2-10^4 Ωm (Xu et al., 2000). The lithosphere-asthenosphere boundary (LAB) is associated with a decrease in electrical resistivity that is caused by two factors (Partzsch et al., 2000). The first effect occurs as increasing temperatures permit thermal activation of charge carriers (electrons and ions) to move more easily through the mineral lattice just below the melting point. The second effect occurs as partial melting provides an alternate route for ions to move through the rock. This second effect will dominate the electrical conduction at melt fractions above 3% (Partzsch et al. 2000). The depth of the LAB can be determined from very long period (>10^4 s) magnetotelluric data. However, imaging to the LAB can be inhibited by the presence of conductors in the crust and upper mantle. In eastern Anatolia conductors include the sedimentary basin on the Arabian Plate, upper mantle conductors (A and B-profiles), and zones of lower crustal low resistivity (C, D and E-profiles)

Two-dimensional inversion of the MT data on the Arabian Plate on the A and B-profiles indicated the LAB to be at a depth of around 110 km. To exclude the complicating effects of MT stations outside of the Arabian Plate, only MT stations on the Arabian plate on the A-profile were used in constrained 2-D inversions. The data were inverted with the LAB fixed in the inversion model. The resistivity of the asthenosphere was assumed to be 30 Ωm as determined from the sensitivity analysis in chapter 5. This is comparable with the 10 Ωm used for the resistivity of the asthenosphere at northern Canada (Jones and Craven, 2004).

Various LAB depths were investigated and the minimum r.m.s misfit was obtained when the LAB was fixed at around 110 ±10 km (Figure 7-4). This depth is comparable to estimates from the S-wave receiver function analysis of Angus et al., (2006). The LAB was determined to be at 100 km depth along an east-west transect at 37° N longitude in the study area while this boundary was hardly visible at 38° N longitude (Angus et al., 2006).

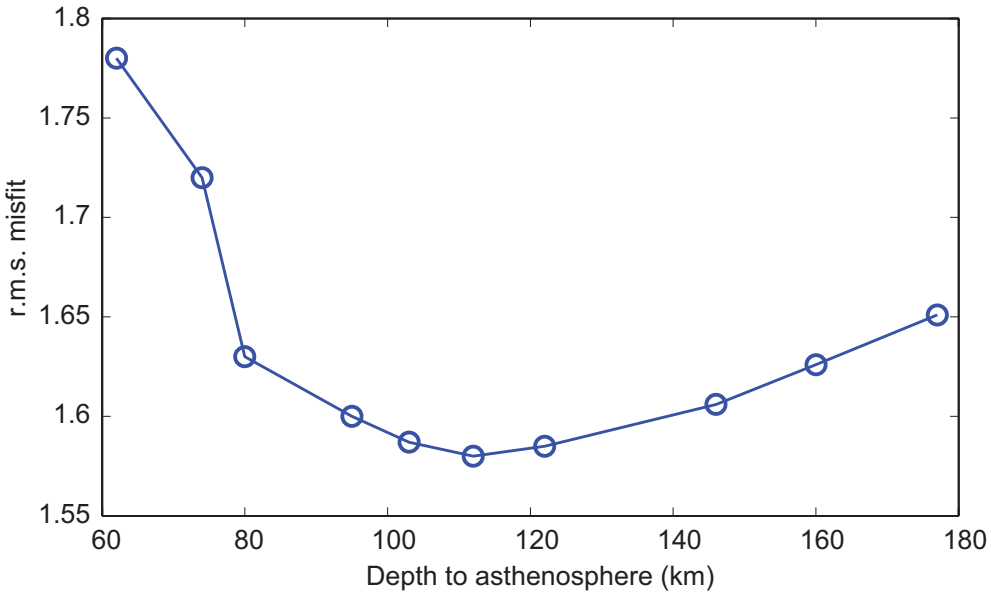

Figure 7-4. Experimental determination of the LAB depth beneath the Arabian plate using the MT stations south of the BSZ on the A-profile. The resistivity of the asthenosphere was fixed at 30 Ωm at various depths. The final r.m.s misfit of the 2-D inversion is shown as a function of depth of the LAB.

7.3.2 Eastern Anatolia

Eastern Anatolia can be divided into the Anatolian Block (AB) and the eastern Anatolian Plateau (EAP) in terms of the geoelectric characteristics derived in this study. The Karlıova Triple Junction (KTJ) defines a north-south boundary that separates regions with differing upper mantle structure in the Anatolian Block (west of the KTJ) and the eastern Anatolian Plateau (east of the KTJ).

7.3.2.1 Anatolian Block

Profiles A and C traverse the region where the Anatolian Block is moving to the west relative to Eurasia. A zone of lower crustal low resistivity (10-20 Ωm) is localized beneath the Anatolian block, bounded by the NAF on the north and the EAF on the south ("a2" in Figure 7-3). The geoelectric structure of the upper crust beneath the Anatolian block is significantly different from that of the adjacent Arabian Plate. Vertical zones of low resistivity extending from the surface to the lower crust are observed which are coincident with the North Anatolian and East Anatolian Faults.

Resolution of upper mantle resistivity structure beneath the Anatolian Block is hindered due to the presence of crustal conductors ("a2" in Figure 7-3) that limit the penetration of electromagnetic signals. However, it is clear that upper mantle resistivity is lower than beneath the Arabian Plate.

Seismic studies have shown that the mantle lid beneath the EAAC is only 15-20 km thick while it is approximately 50 km thick beneath the Anatolian Block (Gök et al., 2007). This supports the idea that the high resistivities imaged beneath the Anatolian Block imply a strong rheology compared to EAAC (Figure 7-3). However, the Anatolian Block is also characterized by the strong attenuation of Sn waves and slow Pn propagation in general (Pn <7.7 km/s) with an exception along a roughly N-S aligned band of relatively normal Pn (7.9-8.0 km/s) velocities just west of where the C and A-profiles join. These values are low compared to global average of 8.2 km/s observed in stable continental regions (Mooney et al., 1998). The widespread lower Pn velocities within the MT stations coverage on the Anatolian Block can be associated with the widespread lower crustal conductor in the region (Figure 7-6).

There is no zone of lower crustal low seismic velocity beneath the Anatolian Block while there are several located on the Anatolian Plateau (Angus et al., 2006). In the following sections it is shown that ~2% of partial melting is expected for the lower crust in this region. Therefore, this relatively low fraction may not be readily detected by crustal seismic velocity studies. However, both methods indicate higher fractions of partial melting explained in the next section.

7.3.2.2 Anatolian Plateau

Profiles B and E are located where direct convergence occurs between the Arabian and Eurasian plates. The upper crust consists of low resistivity sedimentary rocks (10-30 Ωm) that are underlain by highly resistive (100-300 Ωm) crystalline basement rocks of the EAAC unit. EAAC upper crust is separated from the Bitlis Pötürge Massif (BPM) by a vertical zone of low resistivity which is spatially coincident with Nemrut and Süphan volcanoes ("g" in Figure 7-3). The BPM appears to be separated from the Arabian

Foreland with a similar low resistivity zone that extends down to the lower crust ("h" in Figure 7-3).

The lower crustal resistivity in this region is lower than that of the Anatolian Block to the west of the KTJ and shows significant horizontal variability ("a1" in Figure 7-3). Localized pockets in the lower crust have resistivities around 2-5 Ωm ("a1" in Figure 7-3) and the crustal resistivity between these pockets is 10-30 Ωm. Underneath the crust, the upper mantle is imaged as a region with low resistivity 10-30 Ωm ("f" in Figure 7-3).

The next stage in interpretation is to relate the bulk resistivity values to melt fraction and crustal rheology. This stage has two steps (1) using the observed resistivity values to infer fluid fraction, and (2) using the fluid fraction to infer rheology.

Observations of subsurface resistivity are routinely converted into estimates of porosity/fluid fraction (see Bedrosian, 2007 for a recent review). Schilling et al. (1997) used MBLM and estimated 14-27% partial melting in the crust beneath the magmatic arc in Northern Chile. Unsworth et al. (2005) used MBLM for Southern Tibet and estimated 5-14% partial melting was required to account for the observed low resistivity. Soyer and Unsworth (2004) explained the enhanced conductivity in the backarc of the Cascadia subduction zone on the basis of partial melting and estimated a melt fraction <4% .

As already discussed earlier in this chapter (7.3.2), the cause of the anomalous conductivity is likely due to fluids particularly partial melting. The three methods to calculate the porosity were described in section 7.1.2. These methods are used to determine possible melt fractions in eastern Anatolia. Figure 7-5 relates the low bulk resistivities beneath eastern Anatolia to melt fraction. Two values were used for the melt resistivity to define upper and lower limits of the melt fraction. The resistivity of the rock grains was assumed to be 300 Ωm but this value has a minimal effect on the bulk resistivity as the melt is inter-connected. The scaling factor C=1.47 is used in Archie's Law and results were very similar to those obtained from MBLM. The only exception to this agreement was observed at lower melt fractions (0.01% and 0.1%) since MBLM takes into account the thermal reduction of the resistivity (Schilling et al., 1997).

Figure 7-5 shows that a minimum of 5% (solid lines in Figure 7-5) and maximum of 14% (dashed lines in Figure 7-5) partial melt is needed to explain the 2-5 Ωm bulk resistivity observed beneath the EAAC. Furthermore, the 10-30 Ωm resistivity observed in the upper mantle beneath the EAAC and at lower crustal depths throughout most of eastern Anatolia requires a melt fraction <2%. It is likely that water-unsaturated partial melting at temperatures higher than 650° C increases the resistivity due to dilution of the water into the melt phase (Wannamaker, 1986) at upper mantle depths beneath the EAAC.

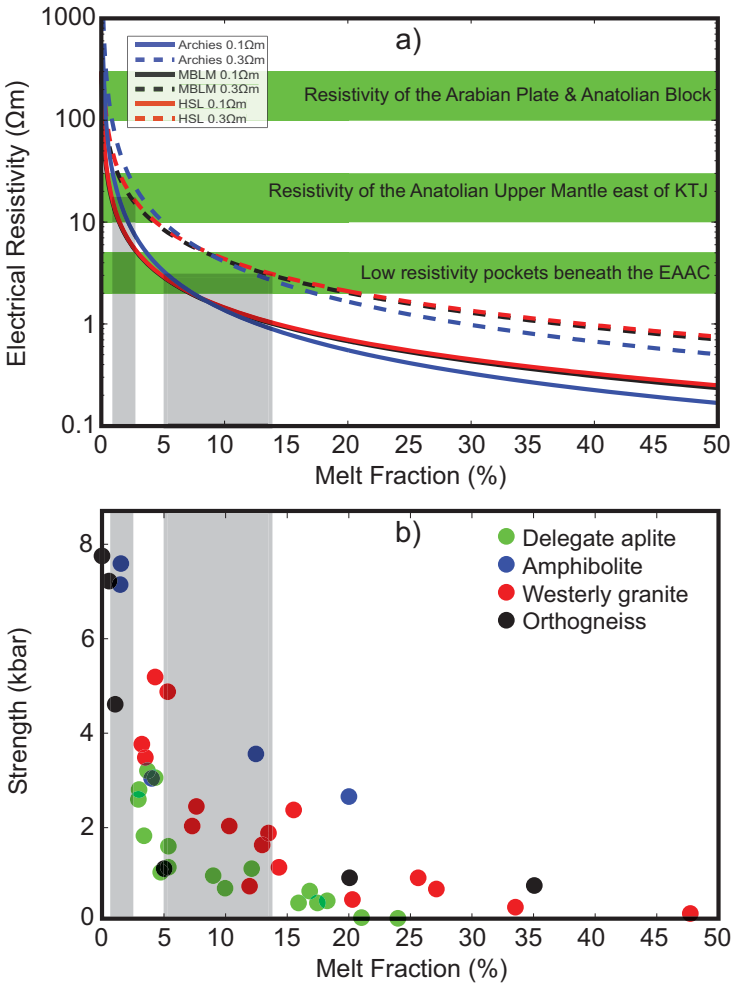

Figure 7-5. Experimental results showing the electrical resistivity (a) and strength of crustal rocks as a function of melt fraction (b). Blue, black and red curves on the upper panel (a) show the bulk electrical resistivity of a rock sample as a function of melt fraction calculated using Archie's Law, MBLM and HSL respectively. The melt resistivity is 0.1 Ωm for solid lines and 0.3 Ωm for dashed lines. This figure allows the resistivity to be related to the melt fraction and strength (b is modified from Rosenberg and Handy, 2005).

A recent review of experimental studies on the strength of partially molten crustal rocks showed that strength is a nonlinear function of melt fraction (Rosenberg and Handy, 2005). It was previously thought that the most significant change in strength occurred at the rheological critical melt percentage (typically between 10-30%) where the rock essentially looses all its strength (Arzi, 1978). However, it can be seen in Figure 7-5 that a factor of ten strength reduction occurs between 0 and 7% melt fractions (Rosenberg and Handy, 2005). Therefore, the 5-14% melt fraction required to account for the low resistivity pockets beneath the EAAC, can reduce the strength of the crust by a factor of ten. This reduction in strength at lower crustal depths may be sufficient to allow crustal flow to occur beneath the eastern Anatolian Plateau, in a similar style to that proposed for Tibet (Beaumont et al., 2001). Even if crustal flow does not occur, this may permit upper crust to be detached from the lower crust. Note that melt fractions in excess of 10% are considered unrealistic to certain petrologists.

7.3.3 Pontides

The Pontides record the geological and tectonic signatures of the southward subduction and consumption of the Paleo-Tethyan Ocean floor and northward subduction of the Neo-Tethyan Ocean floor in the late Cretaceous (Yılmaz et al., 1997). The closure of the Neo-Tethys resulted in the collision between the Pontides arc and the Tauride-Anatolide platform. The present Pontide Mountains were uplifted as a horst block during the late Miocene (Yılmaz et al., 1997). Six MT stations on the C and E-profiles were located in the Pontide mountains. The crustal resistivity is ~1000 Ωm in this region and this is almost an order of magnitude higher than that observed anywhere else in the study area. Limited variations in the crustal resistivity structure were observed between the Black Sea and the NAF on the C-profile (Figure 7-3). The upper mantle resistivity beneath the Pontides is $\geq$ 300 Ωm which is comparable to the upper mantle resistivity of the Arabian Plate ("c" in Figure 7-2). Combined with the fast Pn velocities (Al-Lazki et al., 2004) and efficient Sn propagation around the Black Sea (Gök et al., 2003), high resistivity values could be interpreted as indicating the presence of rheologically strong lithosphere. Complementary evidence comes from the receiver function analysis of Gök et al., (2007) where the existence of a mantle lid was observed. This evidence is also consistent with the GPS measurements that show this region acts as a rigid block (McClusky et al., 2003).

McClusky et al., (2000) noted that deformation in this area is characterized by motion of continental lithosphere around the Black Sea. This motion is expressed as a rapid velocity change across the NAF as the Anatolian block moves westward at a velocity of 21mm/yr south of the NAF and the Pontides move northward at 1-3 mm/yr to the north of the NAF. McClusky et al., (2000) suggested that the oceanic lithosphere underlying the Black Sea is stronger than the continental lithosphere to the south and hence represents a backstop that resists deformation and deflects the continental lithosphere. However, findings from this thesis, and recent seismic observations (Turkelli et al., 2003) indicate that the continental mantle lid beneath the EAAC, south of the Pontide mountains is either very thin or completely absent and may be replaced by hot asthenospheric material. Therefore, the oceanic lithosphere beneath the Black Sea may deflect the motion of the rheologically weak upper mantle and crust of Anatolia.

The relative motion of the tectonic blocks changes from west to east at the KTJ which is also observed as a resistivity boundary between the Anatolian Block and the Anatolian Plateau. In contrast to the GPS and resistivity observations, Sn efficiency and Pn velocity maps obtained from the ETSE passive seismic array experiment show that a gradual transition from weak to strong rheology occurs within the Pontides rather than a sharp change (Gök et al., 2003; Al-Lazki et al., 2003). Joint inversion of the teleseismic receiver functions and surface wave group velocities showed that the lithosphere beneath the EAAC is 60-65 km thick while it is 85-90 km thick beneath the Pontides (Gök et al., 2007).

7.4 Comparison of resistivity models with other geophysical observations

MT data can be used to generate models of the electrical resistivity distribution within the Earth. Electrical resistivity models can be interpreted with greater confidence when compared to other independent data from other geophysical and geological methods. This integrated approach is described in the following section.

7.4.1 Seismic velocity

7.4.1.1 Crust

Passive seismic data have shown that a crustal low velocity zone is not observed across the entire Anatolian plateau (Zor et al., 2003). The dashed white lines in panels A and B in Figure 7-6 show the lower crustal low velocity zones inferred from receiver function studies (Zor et al., 2003; Angus et al., 2006; Gök et al., 2007). Low velocities are locally observed in a series of discrete pockets that are inferred to represent accumulations of magma (Angus et al., 2006). The low resistivity values in these regions can be accounted for with 5-14% partial melting as described above.

7.4.1.2 Upper mantle

Sn is a shear wave which propagates within the mantle lid of the lithosphere and is observed at frequencies of 0.5 -20 Hz. Due to the high frequency content of Sn, this phase is quite sensitive to the temperature and presence of partial melt in the upper mantle. The efficiency of Sn propagation can be quantified by comparing the amplitude of the Sn wave to other regional waves (Pg and Lg). Most of the Anatolian Plateau is characterized by the absence of Sn or inefficient Sn propagation (Figure 3-8) (Gök et al., 2000 and 2003; Sandvol et al., 2001; Damegh et al., 2004). Gök et al. (2007) used the laboratory results of Hammond and Humphreys (2000) and estimated that 2-3% partial melting was required in the upper mantle and lower crust beneath the eastern Anatolian Plateau to account for the 15% reduction in S-wave velocities. This result is in good agreement with the 1-2% partial melting estimated from MT data for the upper mantle (Figure 7-5).

Pn is a P-wave that is analogous to Sn and is often used to infer the rheology and fabric of the mantle lithosphere. Higher Pn velocities (>8 km/s) imply the presence of a tectonically stable mantle lid. The presence of partial melt can reduce the Pn velocity (Figure 7-7). However, partial melt causes a 2-3 larger reduction in the velocity of Sn compared to Pn (Figure 7-7) even at low melt fractions (Mavko, 1980) because shear wave velocity is

proportional to the square root of the shear modulus[1]. Assuming 8 km/s to be a normal Pn velocity, Figure 7-6D shows that a 5-6% velocity reduction is observed for the region around the Lesser Caucasus and northeast of the KTJ. Both seismic and MT images clearly identify the Arabian Plate with cold (blue) colors which represents fast Pn velocities and high resistivity values. The Anatolian Block and the Anatolian Plateau are characterized by low Pn velocities and low resistivity values. Both these parameters imply a weak rheology and require the presence of shallow asthenosphere to account for the observed values. This effect is discussed in detail below and illustrated in Figure 7-7.

The seismic and electrical properties of the upper mantle are mutually consistent since zones of elevated fluid content are expected to exhibit a reduction in both electrical resistivity and seismic velocity. Very low Pn velocities (~7.6 km/s) are observed beneath the Lesser Caucasus and north of the KTJ, the same regions with the lowest resistivities (A, B and D in Figure 7-6). According to Figure 7-7, a 5% reduction in Pn velocity can be explained by ~2% partial melt in the upper mantle. In addition, a 15% reduction in the shear wave velocity (Gök et al., 2007) can be accounted for by 2-3% partial melt when using the tubes and films model (Mavko, 1980).

Figure 7-6. Depth slices of electrical resistivity at (A) 30 km, (B) 45 km, (C) 60 km from 2-D inversion of MT data. (D) Pn seismic velocity in the upper mantle from Al-Lazki et al., (2004), (E) Bouguer gravity from Ates et al. (1999), (F) Moho depth from Gök et al. (2007) and shear wave splitting directions from Sandvol et al., (2003). The MT data have been interpolated between the profiles to a distance that reflects the region sampled by each MT station. The dashed white lines on (A) and (B) indicates the crustal low velocity zones described by Angus et al., (2006), Zor et al., (2003) and Gök et al., (2007). The dashed white line on (E) show the very low Bouguer anomaly zone (<-130mgal). The dashed black line on (C) shows the northernmost extremity of the Arabian plate defined from 2-D and 3-D inversions.

See next page for Figure 7-6.

[1] Shear modulus is the ratio of shear stress to shear strain. Shear wave velocities are proportional to the square root of the shear modulus.

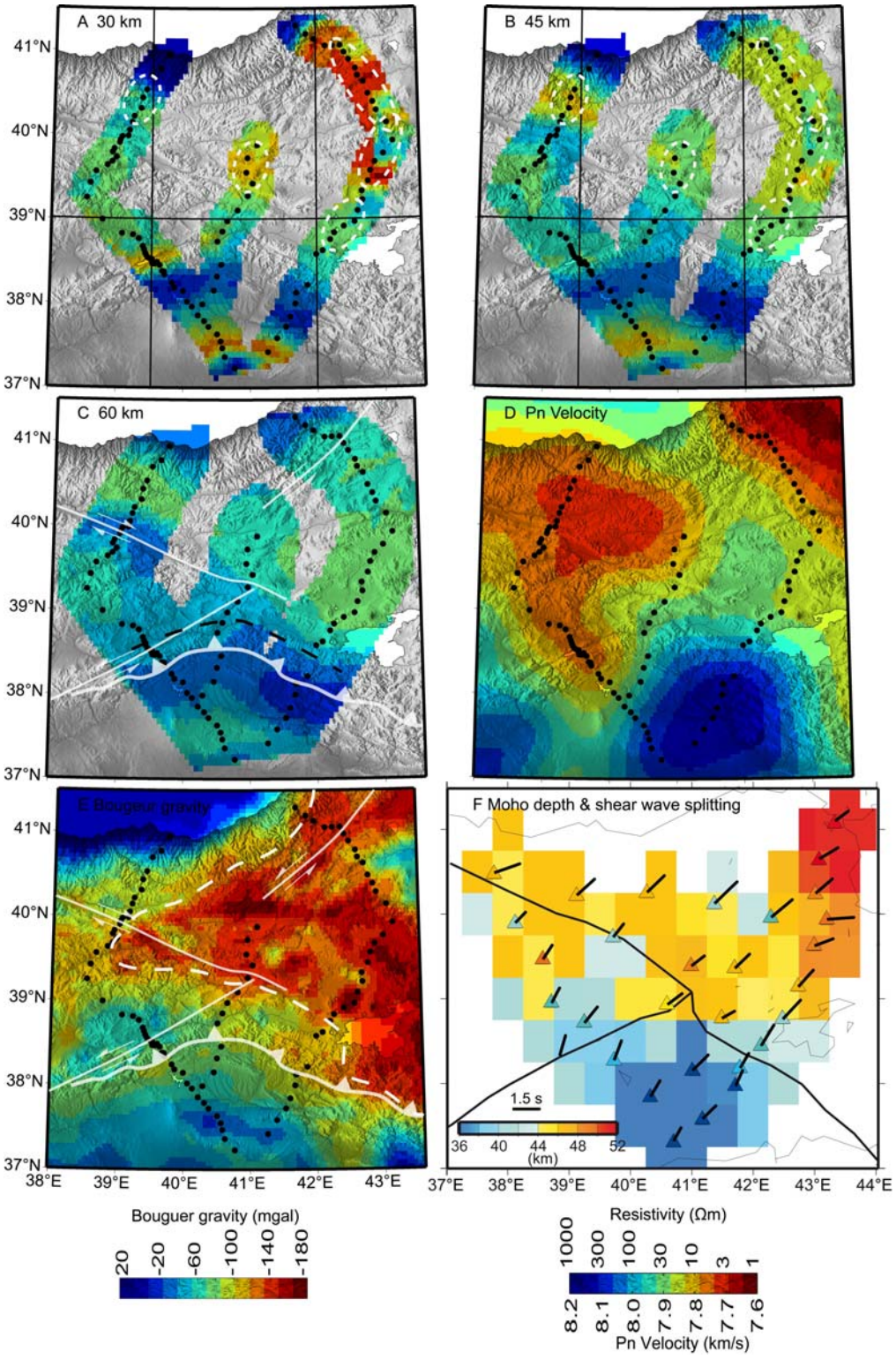

See previous page for figure caption.

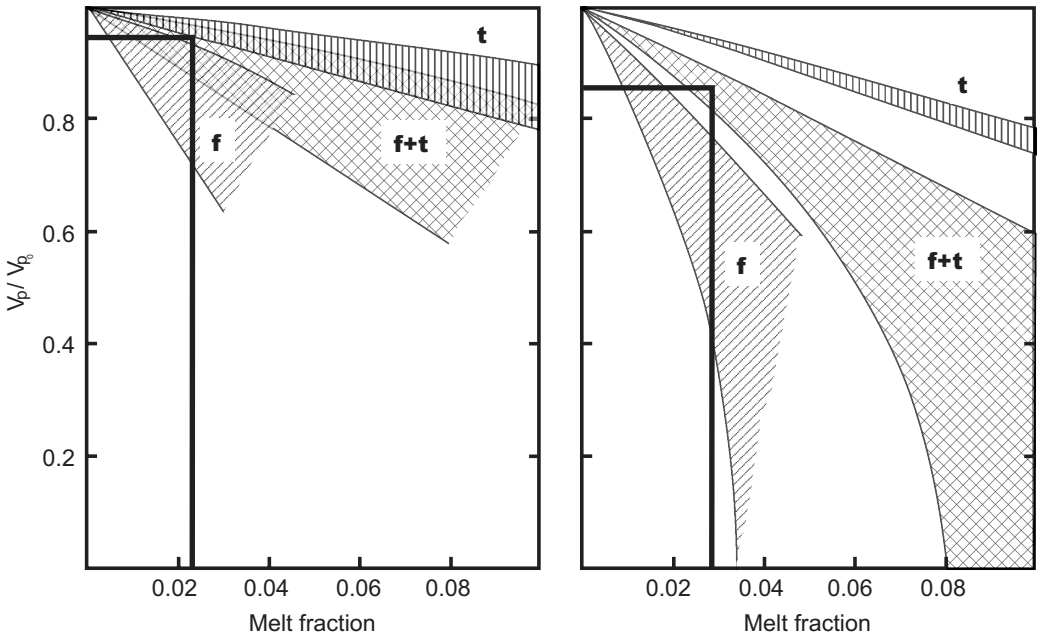

Figure 7-7. Computed P and S wave velocity of olivine as a function of melt fraction. V_P and V_S are velocities of partially molten rock and V_{Po} and V_{So} are velocities of solid rock. Curves are for three different melt geometries, tubes (t), films (f), tubes (t+f) and films (Mavko, 1980).

7.4.2 Shear wave splitting

Lattice preferred orientation of mantle minerals can cause significant seismic anisotropy (Sandvol et al., 2003b). Determination of the fast and slow directions as well as the amount of anisotropy is widely used to infer the shear direction (deformation direction) in the upper mantle. However, anisotropy can be generated in both the asthenosphere and the lithosphere, thus additional data are needed to define the origin of the anisotropy.

The shear wave splitting directions shown in Figure 7-6F show a consistent alignment of 35° ±15° NE (Sandvol et al., 2003b). This direction is distinct from the east-northeast plate motions derived from GPS data. The orientation of the splitting direction was explained by Sandvol et al., (2003) as being due to the development of upper mantle fabric (and not due to crustal strain). This explanation requires a decoupling of the crust from the underlying upper mantle in order for both to move in different directions. However, a simpler explanation can be proposed if absolute plate motions are considered. Kreemer and Holt (2001) showed that the absolute motion of the Arabian Plate is around 47° NE which is

roughly parallel to the observed shear wave splitting directions in eastern Anatolia (Sandvol et al., 2003b).

7.4.3 Earthquake distribution

Additional evidence for a shallow asthenosphere comes from the absence of subcrustal earthquakes (Turkelli et al., 2003) and regional seismic velocity models (Piromallo and Morelli, 2003; Maggi and Priestley, 2005). Therefore, the absence of both subcrustal earthquakes and high resistivity slab beneath the Anatolian Plateau invalidates models that proposed the ongoing subduction of the Arabian Plate. The base of the seismogenic zones throughout eastern Anatolia corresponds the top of the lower crustal low resistivity layer. The only exception to this occurs around the EAF on the A and D-profiles where some earthquake activity occurs at the base of the crust (Figure 7-3). Moderate to large earthquake epicenters are concentrated around the strike slip faults rather than being widespread distribution in the Anatolian Plateau or concentrated along the Bitlis Suture Zone (Figure 3-6). This distribution may also imply that northward movement of the Arabian plate is mostly accommodated by continental escape rather than underthrusting or subduction of the Arabian Plate underneath eastern Anatolia.

7.4.4 Gravity

A negative Bouguer gravity anomaly is observed throughout eastern Anatolia. The lowest values (<-130 mGal) occur on the eastern Anatolian Plateau (Figure 7-6E) in a triangular zone bounded by the NAF in the west and southwest, the Bitlis Pötürge Massif in the south and southeast and the Pontides in the north. This triangular zone roughly coincides with the EAAC, a region of low resistivity crust and mantle, low Pn velocity and deeper Moho depth (Figure 7-6F). Recent surface wave studies also detected a triangle shaped low velocity zone east of the KTJ and north-northeast of the NAF (Gök et al., 2007). Therefore, as mentioned earlier in this chapter, the KTJ represents an east-west boundary between a weak upper mantle and relatively normal upper mantle. This observation is supported by the observation of a low resistivity pocket between the NAF and the Pontides around the C-profile. 3-D MT modeling showed that this conductor may stop just before reaching the C-profile and possibly is the westernmost extension of the low resistivity pockets

underneath the B and E-profiles. However, there are no MT data north of 40° N between C and E-profiles to constrain the continuation of this anomaly.

7.5 Geodynamic implications

The magnetotelluric data collected in this project provide the first deep electrical resistivity images of the Arabia – Eurasia continent-continent collision zone in eastern Anatolia. The resistivity models can be related to the tectonic units and interpreted accordingly. Three first order results have been obtained in this study.

(1) A widespread low resistivity layer at lower crustal depths was observed throughout eastern Anatolia.

(2) The NAF and BSZ are not just surface features, but are lithospheric scale boundaries between regions of low and high upper mantle resistivity.

(3) Significant upper mantle resistivity variations occur between the Arabian Plate and Anatolian Plateau. These observations are consistent with some of the previously suggested geodynamic models for the study area and inconsistent with others.

In the following sections possible geodynamic models are evaluated with the deep MT resistivity models constructed in this thesis.

7.5.1 Active subduction

The P-wave tomography results of Piromallo and Morelli (2003) show that the subducting slab beneath the eastern Anatolian Plateau has detached and sunk into the mantle. A north-south section around 42° E in Piromallo and Morelli (2003) shows that the broken slab can be imaged as a high velocity feature at a depth of 500 km. The break point of the slab occurred around 38° N at this longitude. Furthermore, as explained in section 7.4.3, the absence of subcrustal earthquakes and thrust faults throughout the Plateau also invalidates active subduction.

The absence of the Arabian plate (i.e. high resistivity) at depth north of the BSZ invalidates models that invoke active subduction (Rotstein and Kafka, 1982). However, the penetration of MT signals is strongly attenuated in the mid-lower crustal conductors in this region. In addition, MT data are sensitive to the depth to the top of the conductive layers and not to the depth extent of these layers, which may be affected by smearing in the inversion. Therefore, the absence of a resistive block beneath this region in the MT resistivity sections con not be directly linked to the absence of a resistive slab.

Seismic receiver functions (Angus et al., 2006) and MT data indicate that the northern extension of the Arabian plate is approximately 30 km north of the surface trace of the BSZ. A region with low Bouguer gravity anomalies also starts approximately 30 km north of the BSZ east of 41° E (Figure 7-6E). Therefore, the boundary between the Arabian and Eurasian lithosphere could be located north of the BSZ, around Lake Van.

7.5.2 Tectonic escape and crustal thickening

Tectonic escape of the Anatolian Block as proposed by McKenzie, (1972) is clearly occurring as observed in the GPS data. The resistivity structure across the NAF does not seem to change rapidly from east to west and resistivity models at 60 km depth (Figure 7-6C) show a boundary roughly following the NAF from the E-profile in the north, D and B-profiles in the southeast. Therefore, this observation supports the idea that the mantle lid of the Anatolian Block may remain intact with the overlying crust and is extruded as a relatively non-deforming block towards the west.

The lithospheric thickening model (Dewey et al., 1986) proposes that the northward motion of the Arabian Plate is accommodated by thickening of the lithosphere and forms a plateau. Recent P-wave tomography results of Piromallo and Morelli (2003) and receiver function (Zor et al., 2003; Angus et al., 2006; Gök et al., 2007) indicate that the region has a thick crust. However, the crust is not thick enough to isostasically support the plateau and there is a thin mantle lid beneath the crust (Şengör et al., 2003; Gök et al., 2007).

This study did not provide information on the thickness of the crust due to enhanced conductivity at lower crust. However, the observed upper mantle resistivities (10-30 Ωm)

are much lower than the values expected (10^2-10^4 Ωm) for the lithospheric mantle (Xu et al., 2000) therefore may indicate partially molten hot material of the asthenosphere.

7.5.3 Northward moving slab

Models that proposed the detachment and northward movement of the Tethyan slab (Innocenti et al., 1982a,b) were invalidated by geochemistry results that indicated volcanism started earlier (~11 Ma) in the north and migrated southward (Keskin, 2003). As mentioned above, the MT resistivity models indicate relatively low resistivity values in the upper mantle beneath the Anatolian Plateau. Therefore MT data are likely not able to detect a resistive slab at depth in a low resistivity mantle (partially molten) asthenosphere. Therefore MT resistivity models are not capable of determining if this model is applicable.

7.5.4 Delamination and slab break-off

Lithospheric delamination results in local convection of the upper mantle and the development of a shallow asthenosphere (Pearce and et al., 1990). A range of models including delamination and slab break-off have been proposed (Gögüş and Pysklywec, 2008; Şengör et al., 2003; Keskin, 2003). A modified scenario requires two subduction zones along the Pontides and BSZ (Barazangi et al., 2006) to account for the southward motion of the magmatic front from the Pontides (~11 Ma) to the Bitlis-Pötürge Massif (~2 Ma). However, numerical geodynamic modeling (Gögüş and Pysklywec, 2008) showed that plateau uplift, variation in crustal thickness and high volcanic activity in eastern Anatolia can be generated by lithospheric delamination and subsequent extension.

These models are typified by the cartoon of Keskin (2007) in Figure 7-8A. The geological sections and MT models are not exactly coincident. MT models are obtained from the B and E-profiles while the tectonic section is constructed as two segments, (1) from south of Karacadağ to north of the Van Lake, and (2) from Van Lake to southeast Georgia (thick black line in Figure 7-8C).

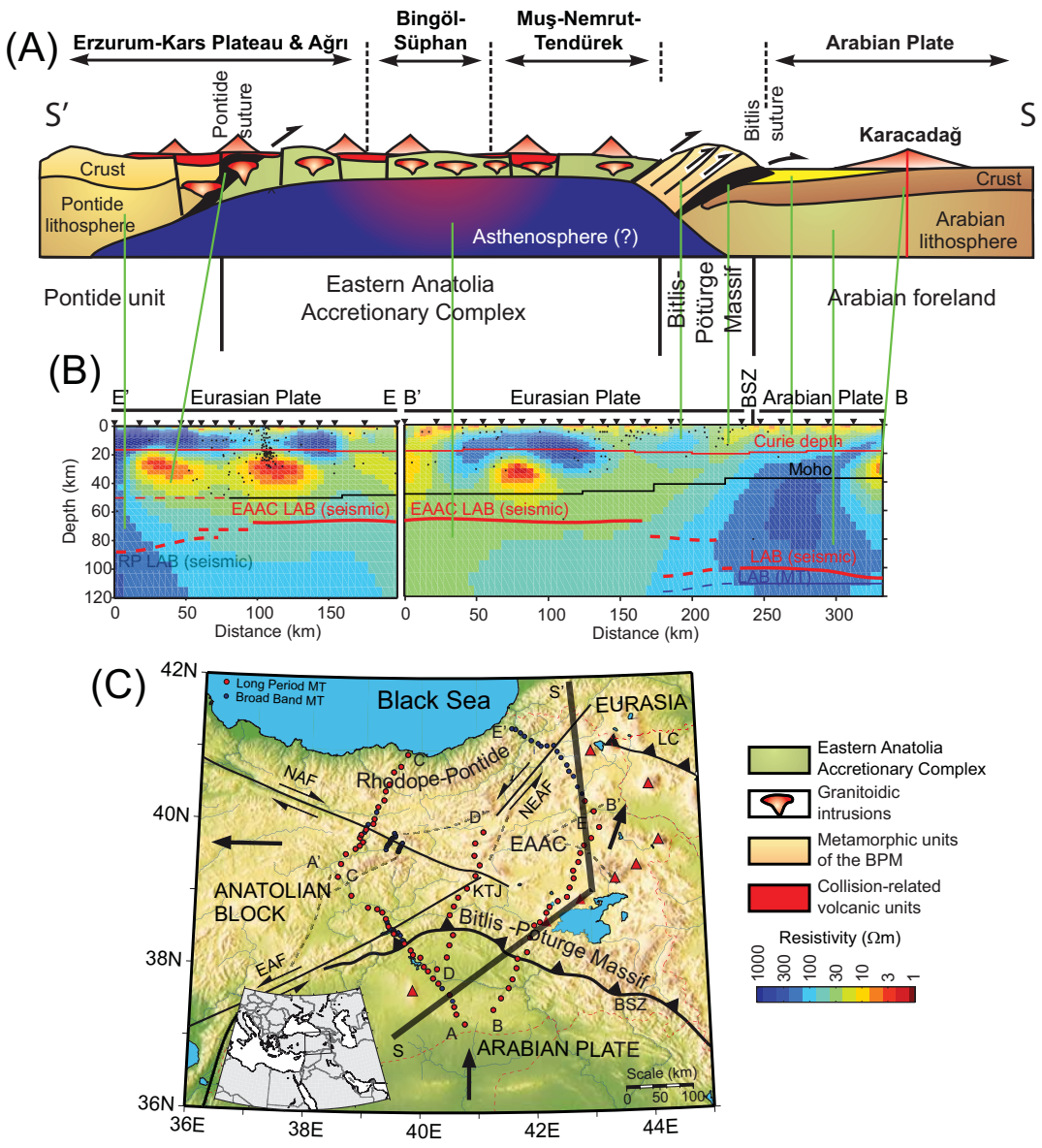

Figure 7-8. (A) Cross section summarizing the crustal and upper mantle structure of the eastern Anatolian Plateau by Keskin (2007). (B) resistivity model for the B and E-profiles. (C) Location map.

According to the tectonic section (Figure 7-8A), the crust of the Anatolian Plateau is thicker in the north and highly deformed by faults and granitoidic volcanic intrusions. However, the crust of the Arabian Plate and Pontides is relatively undeformed and uniform in thickness. The MT sections shown in Figure 7-8B show the Pontide upper crust as highly resistive from 0 km to 20 km distance on the E-profile. In addition, these sections

include a very low resistivity pocket at mid to lower crustal depths. The C-profile in Figure 7-3 also shows that the Pontide upper crust is highly resistive and uniform, and similar to the E-profile area includes a very low resistivity pocket. This very low resistivity anomaly on the C and E-profiles may be related to the Pontide Suture Zone (Figure 7-8). The upper crust of the Anatolian Plateau is described by resistive blocks with conductive vertical channels extending from the surface to the lower crustal low resistivity layer. These channels are spatially correlated with known faults and volcanic centers. Therefore, MT data also indicate highly deformed upper crust for the region.

The upper mantle in the MT model is resistive beneath the Arabian Plate and Pontides (see also Figure 7-3). This feature is in good agreement with the tectonic section above and the numerical modeling results of Gögüş and Pysklywec (2008). The Bitlis Pötürge Massif was also imaged as a resistive block north of the BSZ on the B-profile (Figure 7-3B).

Geodynamic models that predict the presence of a shallow asthenosphere beneath the eastern Anatolian Plateau are supported by the resistivity models presented in this thesis. Particularly, the highly conductive lower crust could be rich in fluids (partial melt) and hot due to direct contact with the convecting asthenosphere. Furthermore, the 10-30 Ωm resistivity determined for the upper mantle beneath the Anatolian Plateau is too low for lithospheric upper mantle. However, highly deformed and laterally discontinuous upper crust and conductive lower crust does not allow MT measurements to confirm the variation of the crustal thickness predicted by the numerical models of delamination in eastern Anatolia (Gögüş and Pysklywec, 2008).

7.6 Comparison with India – Asia collision

7.6.1 Geological and geophysical studies of the India – Asia collision

To fully understand the tectonic processes that occur during continent-continent collisions, it is important to study several collisions to investigate the range of conditions and scenarios that can occur. This approach can also give some insight into the temporal evolution of continent-continent collisions. The Arabia – Eurasia collision in eastern Anatolia is relatively young, and can be compared with a more mature collision such as the

India – Asia collision. This is the best developed modern collision and has created the Himalaya and the Tibetan Plateau, the largest and highest plateau on Earth (Dewey and Burke, 1973; Molnar and Tapponnier, 1975). The India – Asia collision was preceded by subduction of the neo-Tethyan lithosphere in the early Tertiary (60-65 Ma) (Gansser, 1980). The date of the terminal continent-continent collision between India and Asia is thought to have occurred at 40-50 Ma when the northward velocity of India decreased from 10-15 cm/yr to 5 cm/yr (Molnar and Tapponnier, 1975). Despite the ongoing debate about the age of the collision (Aitchison et al., 2007), it is clear that the India – Asia continent-continent collision is at least 35-40 Ma older than the Arabia – Eurasia collision in eastern Anatolia, which started 11-13 Ma (Şengör and Kidd, 1979; Dewey et al., 1986; Keskin et al., 1998).

The pre-collision geology of the Tibetan Plateau is composed of a series of accreted terranes separated by east-west trending sutures (Figure 7-9). The late Jurassic Indus-Tsangpo Suture (ITS) defines the southern edge of the Lhasa block where closure of the Tethyan Ocean occurred.

Geophysical studies have made a major contribution to understanding the India – Asia collision. The 5 km high Tibetan Plateau is characterized by an average crustal thickness of 70-75 km that is 90-110% compensated with an Airy isostasic model (Braitenberg et al., 2000). INDEPTH seismic reflection showed that the Indian plate underthrusts Southern Tibet as far north as the ITS (Zhao et al, 1993). Evidence for partial melting in the mid-crust comes from heat flow (Francheteau et al., 1984), seismic reflection bright spots (Brown et al., 1996) and high conductivity at mid to lower crustal levels from magnetotelluric studies (Chen et al., 1996; Li et al., 2003; Unsworth et al., 2004 and 2005). Teleseismic studies showed that Southern Tibet is characterized by a seismically fast Indian lithosphere that extends as far north as the Banggong – Nuijang Suture (BNS) in Central Tibet (Barazangi and Ni, 1982). To the north the lithosphere is thinner and an anomalous upper mantle is present that does not permit S-wave propagation (Barazangi and Ni, 1982). This implies underthrusting of the Indian lithosphere and a major change from rheologically strong lithosphere to weakened lithosphere.

A northward dipping slab was not visible and this was interpreted as supportive evidence for subhorizontal underthrusting of India under the Tibetan crust (Barazangi and Ni, 1982; Owens and Zandt, 1997). However, seismic tomography imaged a subvertical high velocity zone (Tilmann et al., 2003) just south of the BNS which could be the subducting Indian lithosphere. This can explain the rheologically weak upper mantle and strong attenuation of S waves north of the BNS as water is released from the subduction. In addition, mantle convection due to subduction can reduce the strength of the lithosphere.

Numerous geodynamic models have been suggested to explain the formation of the Tibetan Plateau, and are very similar to those proposed for the Arabia – Eurasia collision. These models include underthrusting of the Indian Plate (Argand, 1924), eastward extrusion of the lithosphere (Tapponnier et al., 1982) and southward subduction of the Asian Lithosphere (Willett and Beaumont, 1994). Recent models invoke large-scale crustal flow as a key component of the deformation (Clark and Royden, 2000; Beaumont et al., 2001; Klemperer, 2006).

The first flow model suggests that the inherently weak Tibetan lower crust flows eastward out of the collision zone causing uplift of the plateau. The Tarim Basin, Qaidam Basin and the Sichuan Basins have stronger lithosphere; therefore, the crustal flow is diverted around these stable regions (Clark and Royden, 2000). This model is supported by the eastward extension of the plateau where uplift is observed without crustal shortening (Wang et al., 1998).

The second flow model suggests that surface denudation at high Himalayan ranges promotes southward crustal flow and ductile extrusion of the metamorphic units (Beaumont et al., 2001). In the absence of the surface denudation the only crustal flow is eastward (Beaumont et al., 2001). Eastward flow could also be the cause of the relatively uniform elevation of the plateau. This model strongly depends on the viscosity of the lower crust and the thickness of the flowing layer. Unsworth et al. (2005) calculated that a melt fraction of 5-14% would reduce the overall viscosity by one order of magnitude required for flow to occur.

7.6.2 Comparison of resistivity models for Tibet and eastern Anatolia

MT data were collected in Tibet from 1995 to 2001 as part of the INDEPTH (International Deep Profiling of Tibet and Himalaya) project. Figure 7-9 shows a comparison of resistivity models from these two continent-continent collision zones. This includes the E and B-profiles from eastern Anatolia and the 100 and 600 lines from Tibet (Unsworth et al., 2004 and 2005) respectively.

The mid crust between the Indus – Tsangpo Suture (ITS) in the south and the Kunlun Fault in the north is highly conductive (Figure 7-9). This includes the entire north-south extent of the Tibetan Plateau. However, south of the ITS, the lithosphere below a depth of 40 km can be identified as the underthrusting Indian Plate from resistivity and seismic reflection data (Unsworth et al., 2005; Nelson et al., 1996). The eastern Anatolian Plateau was also found to have anomalously conductive lower crust between the Pontides in the north and BSZ in the south. However, the conductivity of this layer is higher in Tibet than in Anatolia

Despite the significant difference in crustal thickness, the top of the highly conductive layer is roughly at 20 km depth in both regions (Figure 7-9). However, the conductive crustal layer is laterally continuous in Tibet while conductivity variations are observed within this layer towards northeastern part of the Anatolian Plateau. To quantify the visual differences in MT models, conductance required to satisfy observed MT data for both regions is compared in the following paragraphs.

MT data cannot distinguish between a thick layer with high resistivity and a thin layer with low resistivity. However, they can give a reliable estimate of the conductance which is the product of conductivity and thickness. For example, a 20 km thick layer with 5 Ωm resistivity (0.2 S/m conductivity) and 40 km thick 10 Ωm resistivity (0.1 S/m conductivity) layer have the same conductance (4000 S). Computation of the conductance allows comparison of different models without concern about the geometry of the final model.

The conductance beneath the Tibetan plateau is in the range 6000-10,000 S and is lower along the northern and southern margins. High crustal conductance values have been reported in subduction zones such as the Altiplano with values in excess of 20,000 S (Brasse et al., 2002). This requires 10-30% of fluids according to Archie's Law. In each

case the high conductivity has been interpreted as a result of partial melting. In eastern Anatolia the highest conductance values are localized conductive pockets (Figure 7-9), and the conductance does not exceed 10,000 S. Over the rest of the Anatolian Plateau, the conductance has an average value of 2000 S. The conductance over the low resistivity pockets in eastern Anatolia is comparable to the Tibetan Plateau and the Andes.

Assuming the bulk resistivity for the low resistivity pockets is 2-5 Ωm and the layer conductance is 10,000 S, this requires that the partially molten layer in the crust is 30 km thick. It was shown above that the melt fraction is at least 5-14% within the pockets. Conductance and topography curves are spatially smooth across the Tibetan Plateau. However, they show significant variations across eastern Anatolia. This difference could be due to the fact that the partial melting beneath eastern Anatolia is localized in discrete channels, rather than in a continuous layer as in Tibet. This observation is supported by the fact that in Anatolia the crustal low velocity zones are spatially localized and not observed across the whole plateau (Zor et al., 2003; Angus et al., 2006; Gök et al., 2007).

Both eastern Anatolia and the Tibetan Plateau have experienced the northward subduction of the Tethys Ocean. The subduction of the Tethyan Lithosphere took place at the northern margin of the eastern Anatolian Plateau (EAP) until 11 Ma and at the southern margin along the Bitlis arc until the Oligocene (Keskin, 2007). However, the subduction of the Tethyan lithosphere was in the south and much earlier (Mesozoic) in Tibet. Therefore, Asian crust and mantle was weakened due to northward subduction. However, there might be no continental crust and upper mantle prior to subduction in eastern Anatolia. Crust was accumulated as a huge subduction accretionary prism (Şengör et al., 2003; Keskin, 2003). Therefore, EAP was once underlain by the subducting slab and continental collision-related crustal thickening started at least 40 Ma later than Tibet. Furthermore, various geophysical data show that India is underthrusting Tibet but Arabian Plate is not underthrusting eastern Anatolia because the slab is already broken off. This difference could be one of the main reasons for the larger amount of volcanism in eastern Anatolian compared to Tibet as the crust is in direct contact with hot asthenospheric material. Another difference is that the subducting slab beneath the Tibetan plateau is of continental origin while oceanic lithosphere of the Tethyan Ocean was underthrusting and subducting beneath the Anatolian Plateau.

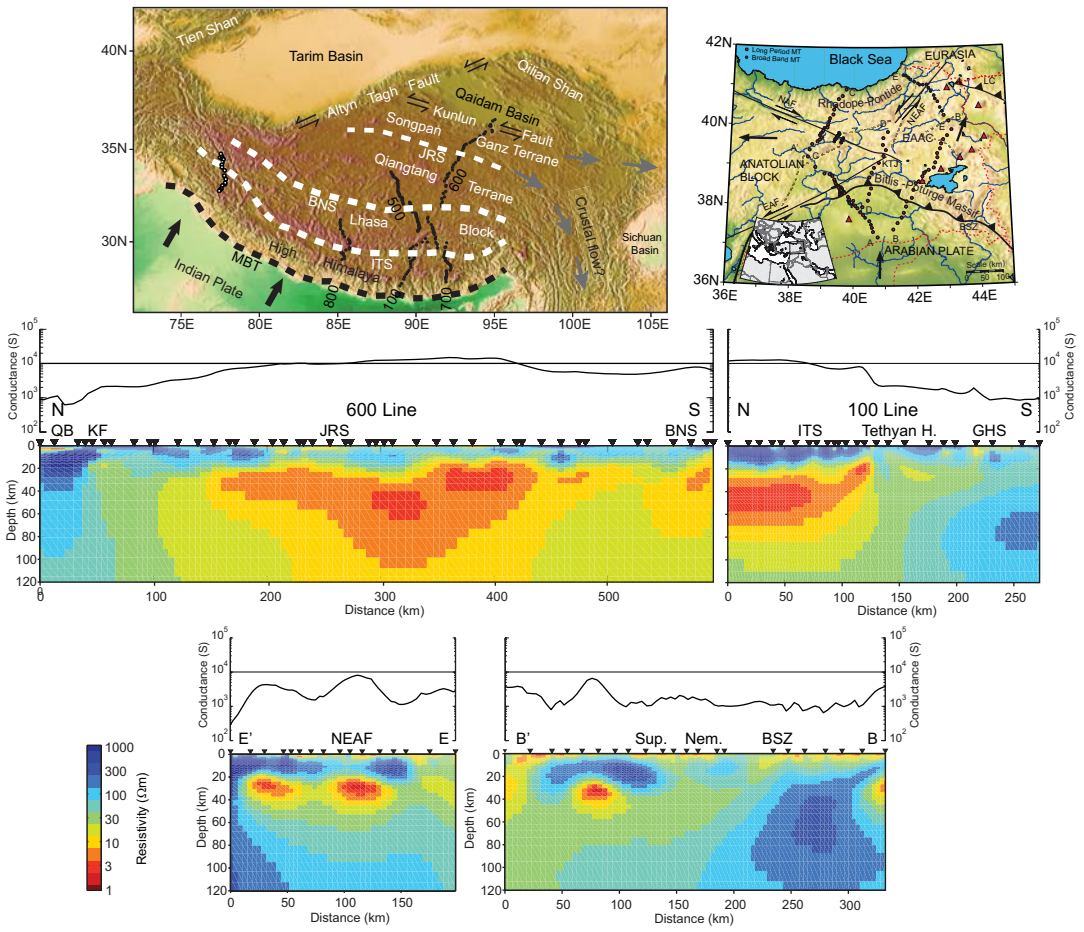

Figure 7-9. Comparison of MT resistivity models of the Tibetan Plateau (100 and 600 lines) and eastern Anatolian Plateau (E and B-profiles). The 600 line model is from Unsworth et al. (2004), and 100 line model from Unsworth et al. (2005). Simplified tectonic map of Tibet is from Unsworth et al. (2005). BNS, Banggong – Nuijang Suture; GHS= Great Himalaya Suture; ITS= Indus – Tsangpo Suture; JRS= Jinsha River Suture; KF= Kunlun Fault; QB= Qaidam Basin; BSZ= Bitlis Suture Zone; NEAF= North East Anatolian Fault; Süp= Süphan; Nem= Nemrut.

In summary, both regions exhibit unusually low resistivities for the lower crust and upper mantle. These observations require 5-14% percent wet partial melting in the lower crust and 1-2% melting in the upper mantle. Partial melting at lower crustal levels seem to be widespread in Tibet while it could be limited to narrow channels in eastern Anatolian Plateau. Despite similar geoelectric features both regions may have evolved differently. The source of the low resistivity is attributed to partial melting in both regions. The mechanism that causes the partial melting is possibly shallow asthenosphere throughout eastern Anatolia, and doubled crustal thickness due to underthrusting of Indian Plate in

southern Tibet, and upwelling of the asthenosphere in the central Tibet. Therefore, eastern Anatolia is more analogous to central and northern Tibet rather than southern Tibet. The biggest differences between the two regions are vast amount of volcanism and relatively normal thickness of the crust in eastern Anatolia. This difference is inferred to underthrusting of the oceanic lithosphere of the Tethyan Ocean underneath eastern Anatolia compared to underthrusting of the continental lithosphere of the Indian Plate underneath Tibet.

8 CONCLUSIONS

The first long-period MT data from eastern Anatolia have been described and interpreted in this thesis. The most significant findings are summarized below.

8.1 Structures imaged with MT

- Erzincan Basin: The thickness of the Erzincan basin was found to be 3 ±0.25 km from the MT data. This is in a good agreement with recent estimates from seismic tomography (Aktar et al., 2004; Kaypak and Eyidoğan, 2005). MT provides an independent estimate of the basin thickness which has an important effect on the amplification of the earthquake waves.

- Strike-slip fault zones: A well defined fault-zone conductor was imaged beneath the East Anatolian Fault (EAF) at Hazar Lake and requires at least 4-7% interconnected fluids to account for the observed conductivity. The location of the EAF conductor spatially correlates with a band of low seismic activity along the fault and provides new example for the idea that high conductivity in fault zones is due to increased fluid content and these fault segments are weak. So the fluids are allowing the fault to slip without earthquakes (creep). A high conductivity was not observed within the NAF around Refahiye. Therefore, this segment of the NAF could be rheologically a strong fault.

- Structure of Arabian Plate: Upper mantle of the Arabian plate has a high resistivity (100-300 Ωm). The depth of the lithosphere-asthenosphere boundary (LAB) on the Arabian plate was found to be around 110 km from the MT data. This is an independent estimate of the LAB thickness for this region and comparable to 100

km from S-wave receiver function analysis (Angus et al., 2006). Karacadağ volcano on the Arabian foreland may be located above an isolated conductivity anomaly as imaged on A-profile. A continuation of this anomaly towards east was also observed on the B-profile and this suggests an east-west trend rather than a localized anomaly related only to Karacadağ intraplate volcano. This conductor could be a region of upper mantle melting that supplies magma to the volcano.

- Structure of Pontides: Pontides upper crust is a uniform highly resistive layer that has the highest resistivity observed in this survey, ~1000 Ωm. The southern part of the Pontide lower crust includes very low resistivity pockets (2-5 Ωm). The upper mantle beneath the Pontides is also more resistive (100-300 Ωm) than the Anatolian Plateau and similar to the Arabian Plate upper mantle resistivity values.

- Structure of Anatolian Plateau - Crust: The resistivity structure of the upper crust is variable horizontally. Generally, high resistivity upper crust has been divided by vertical channels of broad low resistivity zones. These broad low resistivity zones correlate with the known fault zones and volcanic centres. The lower crust is more homogenous and imaged as a widespread low resistivity layer (10-30 Ωm) beneath the Anatolian Plateau. This may indicate the presence of a fluid-rich lower crust. The lower crust towards the northeast of the Anatolian Plateau has very low resistivity pockets (2-5 Ωm). These regions could indicate zones of weakness that may represent the locations of the most active deformation as defined by geodetic data (Reilinger et al., 2006).

- Structure of Anatolian Plateau – Upper mantle: The Bitlis Suture Zone in the south and the Pontide mountains in the north are the boundaries of the low resistivity (10-30 Ωm) upper mantle beneath the Anatolian Plateau. Observed resistivities are one order of magnitude smaller than expected for lithospheric upper mantle and could be an indication of shallow asthenosphere.

8.2 Tectonic implications

A low resistivity layer is observed in the mid and lower crust of both the Tibetan Plateau and eastern Anatolia. This layer in Tibet can be explained with the presence of a few percent (5-14%) partial melt (Unsworth et al., 2005). The mid-crustal low resistivity layer in Tibet appears to be spatially continuous, while it exhibits significant lateral variation beneath eastern Anatolia. The very low resistivities observed at mid and lower crustal levels throughout the Tibetan Plateau are only matched by localized pockets of very low resistivity beneath the eastern Anatolian Plateau. In both locations, these regions of low crustal resistivity could represent zones of deformation. It should be noted that in Southern Tibet the MT profiles are parallel to the inferred flow direction, while in eastern Anatolia, the profiles are orthogonal to crustal flow in an east-west direction.

Eastern Anatolia and the Northern Tibetan Plateau both exhibit unusually low resistivities in the upper mantle. This may indicate the presence of a shallow asthenosphere with a melt fraction around 2%.

Despite different tectonic histories, both continent-continent collisions have developed a similar structure. The Altiplano in South America has also developed a similar structure despite not being a continent-continent collision.

The low resistivity lower crustal layer detected by the MT data could represent a weak layer that decouples the crust and upper mantle. It is possible that (a) fluids are controlling the observed deformation through weakening the lithosphere or (b) that the deformation produces zones of enhanced fluid content through maintaining a network of interconnected cracks (Türkoğlu et al., 2008). Both scenarios are possible in different tectonic settings. In terms of the widespread lower crustal low resistivity beneath the Anatolian Block and Plateau, either scenario could be possible. The vertical low resistivity zone associated with the EAF on the A-profile could be an example of (b). The zone of low resistivity in the asthenosphere beneath the Anatolian Plateau could be an example of (a) with the melt produced by delamination (Pearce et al., 1990) and localized upper mantle convection which allows deformation to occur (Türkoğlu et al., 2008).

8.3 Future research

This study has provided the first images of deep resistivity structure beneath eastern Anatolia. Additional MT data collection is required to fully understand the geoelectric structure of the region and its tectonic significance. Future MT data collection should be focused on developing 3-D models and address the following questions.

- Examine the fault-zone conductors on the EAF and NAF and determine their along-strike extent. This would allow a fuller investigation of the relationship between seismicity and fault zone resistivity structure.

- Investigate the low resistivity anomaly observed close to Karacadağ volcano on A-profile. This coincides with a rapid topographic change close to Syrian border that may be caused by upwelling of the hot material from asthenosphere. A closely spaced grid of broad band MT stations covering an area between 40° E to 42° E longitudes and 37° N to 38° N longitudes could provide enough information to model this anomaly in 3-D.

- An extension of the D-profile to the Black Sea coast would be valuable because it would provide information about the 3-D low resistivity anomaly beneath the Pontides on the C-profile. 3-D inversion and modeling suggest that this feature does not necessarily exist beneath the C-profile but may exist east of the profile and could be continuation of low resistivity pockets beneath the B and E-profiles.

- The low resistivity pockets on the B and E-profiles could represent zones of crustal flow. Additional stations and profiles to both the east and west are needed to see if these features are channels or localized anomalies.

- MT profiles across the Zagros mountains between Iran and Iraq have significant importance for understanding the evolution of the continental convergence and for imaging the continuation of the conductivity anomalies observed in eastern Anatolia.

9 REFERENCES

Argand, E., La tectonique de l' Asie, Intl. Geol. Cong. Rep. Sess. 13, 170-372, 1924.

Aitchison, J. C., Ali, J. R., Davis, A. M., When and where did India and Asia collide? J. Geophys. Res., 112, doi:10.1029/2006JB004706, 2007.

Aktar, M., Dorbath, C. and Arpat, E., Seismic Velocity and Fault Structure of Erzincan Basin (Turkey) using local earthquake tomography, Geophysical Journal International, 156, 497-505, 2004.

Al-Damegh, K., Sandvol, E., Al-Lazki, A., and Barazangi, M., Regional seismic wave propagation (Lg and Sn) and Pn attenuation in the Arabian plate and surrounding regions, Geophysical Journal International, 157, 775-795, 2004

Al-Lazki, A., Sandvol, E., Seber, D., Barazangi, M., Turkelli, N. and Mohamad, R., Pn tomographic imaging of mantle lid velocity and anisotropy at the junction of the Arabian, Eurasian and African plates, Geophysical Journal International, 158, 1024-1040, 2004.

Al-Lazki, A., Seber, D., Sandvol, E., Turkelli, N., Mohamad, R. and Barazangi, M., Tomographic Pn velocity and anisotropy structure beneath the Anatolian plateau (eastern Turkey) and the surrounding regions, Geophysical Research Letters, 30, 24, 8043, 2003.

Allen, C. R., Active faulting in northern Turkey, Contrib. No. 1577, Div. Geol. Sci., Calif. Inst. Technol., pp. 32, 1969.

Altınok, Y., Alpar, B. and Yaltırak, C., Şarköy-Mürefte 1912 earthquake's tsunami, extension of the associated faulting in the Marmara Sea, Turkey. J. Seismol., 7, 329-346, 2003.

Ambraseys, N. N., and Jackson J., Faulting associated with historical and recent earthquakes in the Eastern Mediterranean region, Geophysical Journal International, 133, 390-406, 1998.

Ambraseys, N. N., Some characteristic features of the North Anatolian fault zone, Tectonophysics, 9, 143-165, 1970.

Angus, D. A., Wilson, D. C., Sandvol, E. and Ni, J. F., Lithospheric structure of the Arabian and Eurasian collision zone in Eastern Turkey from S-wave receiver functions: Geophysical Journal International, 166, 3, 1335-1346, 2006.

Archie, G. E., Electrical Resistivity Log as an Aid in Determining Some Reservoir Characteristics, Trans., AIME, 146, 54-62, 1942.

Armijo, R., Meyer, B., Hubert-Ferrari, A. and Barka, A., Westward propagation of North Anatolian Fault into the Northern Aegean: timing and kinematics, Geology, 27, 267-270, 1999.

Armijo, R., Meyer, B., King, G. C. P., Rigo, A. and Papanastassiou, D., Quaternary evolution of the Gulf of Corinth rift and its implications for the Late Cenozoic evolution of the Aegean, Geophys. J. R. Astron. Soc., 126, 11-53, 1996.

Arpat, E. and Şaroğlu, F., The east Anatolian fault system: thoughts on its development, Bull. Miner. Res. Explor. Ins. Turk., No. 78, 33-39, 1972.

Arzi, A., Critical phenomena in the rheology of partially melted rocks, Tectonophysics, 44, 173-184, 1978.

Ateş, A., 1999. Possibility of deep gabbroic rocks, east of Tuz Lake, central Turkey, interpreted from aeromagnetic data. J. Balkan geophys. Soc., 2, 15–29.

Aydın, I., Karat, H. I. and Koçak, A., Curie point depth map of Turkey, Geophys. J. Int., 162, 633-640, 2005.

Aytun, A., Creep measurements in the İsmetpaşa region of the North Anatolian fault zone, in: Multidisciplinary approach to earthquake prediction 2, edited by: Isikara, A. M., Vogel, A., Friedrich Vieweg and Sohn, Braunschweig-Wiesbaden, 279-292, 1980.

Bahr, K., Geological noise in magnetotelluric data: a classification of distortion types, Physics of the Earth and Planetary Interiors, 66, 24-38, 1991.

Bahr, K., Interpretation of the magnetotelluric impedance tensor: regional induction and local telluric distortion. J. Geophys., 62, 119-127, 1988.

Barazangi, M. and Ni, J., Velocities and propagation characteristics of Pn and Sn beneath the Himalayan arc and Tibetan Plateau: possible evidence for underthrusting of Indian continental lithosphere beneath Tibet, Geology, 10, 179-185, 1982.

Barazangi, M., Continental collision zones: Seismotectonics and crustal structure, in Encyclopedia of Solid Earth Geophysics, edited by D. James, 58-75, Van Nostrand Reinhold Company, New York, 1989.

Barazangi, M., Sandvol, E., and Seber, D., Structure and tectonic evolution of the Anatolian plateau in eastern Turkey, in Dilek, Y., and Pavlides, S., eds., Postcollisional tectonics and magmatism in the Mediterranean region and Asia: Boulder, Colorado, Geological Society of America Special Paper, 409, 463-474, 2006.

Barazangi, M., Seber, D., Chaimov, T., Best, J., Litak, R., Al-Saad, D., and Sawaf, T., Tectonic evolution of the northern rabian plate in western Syria, in Recent evolution and seismicity of the Mediterranean region, Amsterdam, Kluwer, 117-140, 1993.

Barka, A. A., and Eyidogan, H., The Erzincan earthquake of 13 March 1992 in eastern Turkey, Terra Nova, 5, 190-194, 1993.

Barka, A. A., Cohen, H., Akyüz, S., and Watchorn, F., Tectonic evolution of the Niksar and Tasova-Erbaa pull-apart basins, North Anatolian Fault Zone: Their significance for the motion of the Anatolian Block, Tectonophysics, 322, 3-4,243-264, 2000.

Barka, A. A., Slip distribution along the North Anatolian fault associated with the large earthquakes of the period 1939 to 1967. BSSA, 86, 5, 1238-1254, 1996.

Barka, A. and Gülen, L., Complex evolution of the Erzincan Basin (eastern Turkey). J. Struct. Geol., 11, 275-283, 1989.

Barka, A. and Reilinger, R., Active tectonics of the Eastern Mediterranean region: deduced from GPS, neotectonic and seismicity data, Annali di Geofisica, 40-43, 1997.

Barka, A., and Kadinsky-Cade, K., Strike-slip fault geometry in Turkey and its influence on earthquake activity, Tectonics, 7, 663-684, 1988

Barka, A., The 17 August 1999 İzmit earthquake, Science, 285, 1858-1859, 1999.

Barka, A., The North Anatolian Fault Zone, Annales Tectonicae, 6, 164-195, 1992.

Beaumont, C., Jamieson, R. A., Nguyen, M. N. and Lee, B., Himalayan tectonics explained by extrusion of a low-viscosity crustal channel coupled to focused surface denudation, Nature, 414, 738-742, 2001.

Becken, M., Ritter, O., Park, S. K., Bedrosian, P. A., Weckmann, U., Weber, M., A deep crustal fluid channel into the San Andreas fault system near Parkfield, California, Geophysical Journal International, 173, 2, 718-732, 2008.

Bedrosian, P. A., MT+, Integrating Magnetotellurics to Determine Earth Structure, Physical State, and Processes, Surveys of Geophysics, 28, 121-167, 2007.

Bedrosian, P. A., Unsworth, M. J., and Egbert, G.,Magnetotelluric imaging of the creeping segment of the San Andreas Fault near Hollister, Geophysical Research Letters, 29, 1-4, 2002.

Bedrosian, P. A., Unsworth, M. J., and Fei, W., Structure of the Altyn Tagh Fault and Daxue Shan from magnetotelluric surveys: implications for faulting associated with the rise of the Tibetan Plateau, Tectonics 20, 474–486, 2001.

Bedrosian, P., Unsworth, M., Egbert, G., and Thurber, C., Geophysical images of the creeping San Andreas Fault: implications for the role of crustal fluids in the earthquake process, Tectonophysics 358, 137-158, 2004.

Beekmans, N. M., and Heyne, L., Correlation between impedance, microstructure and composition of calcia-stabilized zirconia, Journal: Electrochimica Acta,21, 303-310, 1976.

Bektaş, Ö., Ravat, D., Büyüksaraç, A., Bilim, F. and Ateş, A., Regional Geothermal Characterisation of East Anatolia from Aeromagnetic, Heat Flow and Gravity Data, Pure and Applied Geophysics, 164, 975-998, 2007.

Berdichevsky, M. N., and M. S. Zhdanov, Advanced theory of deep geomagnetic sounding, Elsevier, Amsterdam, 1984.

Beydoun, Z. R., Arabian Plate Hydrocarbon Geology and Potential–A Plate Tectonic Approach, AAPG Studies in Geology, 33, 77p, 1991.

Bhattacharyya, B. K., and Leu, L. K., Spectral Analysis of gravity and magnetic anomalies due to two-dimensional structures: Geophysics, 40, 993-1013, 1975.

Boerner, D. E., Kurtz, R. D., Craven, J. A., Ross, G. M. and Jones, F. W., A synthesis of EM studies in the LITHOPROBE Alberta Basement Transect: constraints on Paleoproterozoic indentation tectonics. Canadian Journal of Earth Sciences, 37, 1509-1534, 2000.

Boguslavsky, S. G., Zhorov, V. A. and Ivashchenko, I. K., Formation of the vertical salinity profile in the Black Sea, Phys. Oceanogr., 5, 443-449, 1994.

Borevsky, L., Milanovsky, S., and Yakovlev, L., 'Fluid-thermal regime in the crust-super deep drilling data', in: E. Barbier, G. Frye, E. Iglesias, and G. Palmason (eds.), Proc. World Geotherm. Congress, Int. Geotherm. Assoc., Auckland, New Zealand, 975-981, 1995.

Bostock, M. and Kennett, B. L. N., The effect of 3-D structure on Lg propagation patterns, Geophys. J. Int., 101, 355-365, 1990.

Bozkurt, E., Neotectonics of Turkey—a synthesis, Geodynamica Acta, 14, 3-30, 2001.

Braitenberg, C., Zadro, M., Fang, J.,Wang, Y. and Hsu, H. T., The gravity and isostatic Moho undulations in Qinghai-Tibet Plateau, J. Geodyn., 30, 489-505, 2000.

Brasse, H., Lazaeta, P., Rath, V., Schwalenburg, K., Soyer, W., and Haak, V., The Bolivian Altiplano Conductivity Anomaly, J. geophys. Res. 107,10.1029/2001JB000391, 2002.

Brown, C., Tectonic interpretation of regional conductivity anomalies, Surveys in Geophysics, 15, 123-157, 1994.

Brune, J. N., Henyey, T. L., and Roy, R. F., Heat flow, stress, and rate of slip along the San Andreas fault, California, Journal of Geophysical Research, 74, 3821-3827, 1969.

Burford, R. O., and Harsh, P. W., Slip on the San Andreas Fault in central California from alignment array surveys, Seismological Society of America Bulletin, 70, 1233- 1261, 1980.

Burke, K. and Şengör, C., Tectonic escape in the evolution of the continental crust. In Barazangi M. and Brown L. (eds.). Reflection Seismology: the continental crust. AGU Geodyn. Ser., 14, 41-53, 1986.

Byerlee, J. D., Friction of rocks, Pure and Applied Geophysics, 116, 615-626, 1978.

Byerlee, J., Model for episodic flow of high pressure water in fault zones before earthquakes, Geology, 21, 303-306, 1993.

Cagniard, L., Basic theory of the magnetotelluric method of geophysical prospecting, Geophysics, 18, 605-635, 1953.

Çakır, Z., Akoglu, A., Belabbes, S., Ergintav, S., and Meghraoui, M., Creeping along the Ismetpasa section of the North Anatolian Fault (western Turkey): Rate and extent from InSAR, Earth and Planetary Science Letters, 238, 225-234, 2005.

Camfield, P. A., and Gough, D. I., A possible Proterozoic plate boundary in North America, Canadian Journal of Earth Sciences, 14, 1229-1238, 1977.

Canıtez, N., and Üçer, S. B., A Catalogue of Focal Mechanism Diagrams for Turkey and Adjoining Areas, İTÜ Maden Fak., Arz Fiziği Enst. Yayın No. 25. 111 pp., 1967.

Chapman, D. S., and Furlong, K. P., Thermal state of the continental crust, in Fountain, D.M., Arculus, R.J., and Kay, R.W., eds., Continental lower crust: Developments in Geotectonics: Elsevier, Amsterdam, 23, 179-199, 1992.

Chave, A. D. and Smith, J. T., On electric and magnetic galvanic distortion tensor decompositions, Journal of Geophysical Research, 99, 4669-4682, 1994.

Chave, A. D. and Thomson, D. J., Some comments on magnetotelluric response function estimation, J. Geophys. Res., 94, 14215-14225, 1989.

Chave, A. D., Thomson, D. J. and Ander, M. E., On the robust estimation of power spectra, coherences, and transfer functions, J. Geophys. Res., 92, 633-648, 1987.

Chen, L., Booker, J. R., Jones, A. G., Wu, N., Unsworth, M. J., Wei, W., Tan, H., Electrically Conductivity Crust in Southern Tibet from INDEPTH Magnetotelluric Surveying, Science, 274, 1694-1696,1996.

Clark, M. K. and Royden, L. H., Topographic ooze: Building the Eastern margin of Tibet by lower crustal flow, Geology, 28, 703-706, 2000.

Connard, G., Couch, R. and Gemperle, M., Analysis of aeromagnetic measurements from the cascade range in central Oregon, Geophysics, 48, 376-390, 1983.

Conrad, C. P. and Lithgow-Bertelloni, C., The temporal evolution of plate driving forces: Importance of ‘‘slab suction’’ versus ‘‘slab pull’’ during the Cenozoic, J. Geophys. Res., 109, 2004.

Constable, S. C., Parker, R. L. and Constable, C. G., Occam's inversion: a practical algorithm for generating smooth models from EM sounding data, Geophysics, 52 , 289-300, 1987.

Constable, S., and Heinson, G., In defence of a resistive oceanic upper mantle: reply to a Comment by Tarits, Chave and Schultz, Geophysical Journal International, 114, 717-723, 1993.

de Groot-Hedlin, C. and Constable, S., Occam's inversion to generate smooth, two-dimensional models for magnetotelluric data, Geophysics, 55 , 1613-1624, 1990.

de Groot-Hedlin, C. D., Removal of the static shift in two dimensions by regularized inversion, Geophysics, 56, 2102-2106, 1991.

Dewey, J. E. and Burke, K. C. A., Tibetan, Variscan and Precambrian basement reactivation: products of continental collision. J. Geol., 81, 683-692, 1973.

Dewey, J. F. and Şengör A. M. C., Aegean and surrounding regions: complex multiplate and continuum tectonics in a convergent zone, Geol. Soc. Am. Bull., 90, 84-92, 1979.

Dewey, J. F., Hempton, M. R., Kidd, W. S. F., Şaroğlu, F. and Şengor, A. M. C., Shortening of continental lithosphere: the neotectonics of eastern Anatolia-a young collision zone, in Collision Tectonics (Coward, M.P., and Ries, A.C., editors), Geological Society Special Publication, 19, 3-36, 1986.

Dolmaz, M. N., Elitok, Ö., and Kalyoncuoglu, Y., Interpretation of seismicity in the eastern Anatolian collision zone using geophysical (seismicity and aeromagnetic) and geological data, Pure and Applied Geophysics, 165, 311-330, 2008.

Dosso, H. W. and Meng, Z. W., The coast effect response in geomagnetic field measurements, Phys. Earth Planet. Inter., 70, 39-56, 1992.

Duba, A. G. and Shankland, T. J., Free carbon and electrical conductivity in the Earth's mantle, Geophysical Research Letters, 9, 1171-1174, 1982.

Ducea, M. N., and Park, S., Enhanced mantle conductivity from sulfide minerals, Geophysical Research Letters, 27, 2405-2408, 2000.

Egbert, G. D. and Booker, J. R., Robust estimation of geomagnetic transfer functions, Geophys. J. R. Astron. Soc., 87, 173-194, 1986.

Egbert, G. D., Robust multiple-station magnetotelluric data processing, Geophys. J. Int., 130, 475-496, 1997.

Egeran, N. and Lahn, E., Note sur la carte sismique de la Turquie au 1:2.400.000. Maden Tetk. Arama Enst. Mecmuası, year 9, No. 2/32, pp. 279–289+one foldout map, 1944.

Elkins-Tanton, L. T., Continental magmatism caused by lithospheric delamination, http://www.mantleplumes.org/LithDelam.html, 2004.

Ercan, T., Fujitani, T., Madsuda, J-I., Notsu, K., Tokel, S. and Tadahide, U. I., Dogu ve guneydogu Anadolu Neojen-Kuvaterner volkanitlerine iliskin yeni jeokimyasal, radyometrik ve izotopik verilerin yorumu, M.T.A. Dergisi, 110, 143-164, 1990.

Ershov, A.V. and Nikishin, A.M., Recent Geodynamics of the Caucasus–Arabia–East Africa Region, Geotectonics, 38 (2), 123-136, 2004.

Evans, K. F., Burford, R. O., and King, G. C. P., Propagating episodic creep and aseismic behavior of the Calaveras Fault north of Hollister, California, Journal of Geophysical Research, 86, 3721– 3735, 1981.

Farquharson, C.G., Oldenburg, D.W. and Haber, E., An algorithm for the three-dimensional inversion of magnetotelluric data: 72nd Ann. Internat. Mtg. Soc. Expl. Geophys., 649-652, 2002.

Fielding, E., Wright, T. J., Parsons, B., England, P., Rosen, P., Hensley, S., and Bilham, R., Topography of northwest Turkey from SAR interferometry: Applications to the 1999 Izmit earthquake geomorphology and co-seismic strain (abstract), Eos Trans. AGU, 80, 663, 1999.

Fischer, G., Szarka, L., Adam, A. and Weaver, J. T., The magnetotelluric phase over 2-D structures, Geophys, J. Int., 108, 778- 786, 1992.

Fournier, R. O. and Rowe, J. J., The solubility of amorphous silica in water at high temperatures and high pressures, American Mineralogist, 62, 1052-1056, 1977.

Francheteau, J., Jaupart, C., Xian, J. S., Wen-Hua, K., De-Lu, L., Jia-Cha, B., Hun-Pin, W., and Hsia-Yeu, D., High heat flow in southern Tibet, Nature, 307, 32-36, 1984

Frost, B. R., Fyfe, W. S., Tazaki, K., and Chan, T., Grain boundary graphite in rocks and implications for high electrical conductivity in the lower crust, Nature, 340, 134-136, 1989.

Fuenzalida, H., Dorbath, L., Cisternas, A., Eyidoğan, H., Barka, A.A., Rivera, L., Haessler, H., Philip, H., Lyberis, N., Mechanism of the 1992 Erzincan earthquake and its aftershocks, tectonics of the Erzincan Basin and decoupling of the North Anatolian Fault, Geophysical Journal International 129, 1-28, 1997.

Gamble, T. D., Goubau, W. M., and Clarke, J., Magnetotellurics with a remote reference, Geophysics, 44, 53-68, 1979.

Gansser, A., The significance of the Himalayan suture zone, Tectonophysics, 62, 181-191, 1980.

Garcia, X. and Jones, A. G., Robust processing of magnetotelluric data in the AMT dead band using the continuous wavelet transform, Geophysis, 73, 223-234, 2008.

Gaucher, E., Modele en profondeur et en vitesse du basin d'Erzincan, M.Sc. Report. University of Paris, Paris, 1993.

Gelati, R., Miocene marine sequence from Lake Van, Eastern Turkey, Rivista Italiana di Paleontologia e Stratigrafia, 81, 477-490, 1975.

Gögüş, O. H., and Pysklywec, R. N., Mantle lithosphere delamination driving plateauuplift and synconvergent extension in eastern Anatolia, Geology, 9, 723-726, 2008.

Gök, R., Pasyanos, M. and Zor, E., Lithospheric structure of the continent-continent collision zone: eastern Turkey, Geophys. J. Int., 169(3), 1079-1088, 2007.

Gök, R., Turkelli, N., Sandvol, E., Seber, D. and Barazangi, M., Regional wave propagation in Turkey and surrounding regions, Geophys. Res. Lett., 27(3), 429-432, 2000.

Gök, R., Turkelli, N., Sandvol, E., Seber, D. and Barazangi, M., Sn attenuation in the Anatolia and Iranian plateau and surrounding regions, Geophys. Res. Lett., 30(24), 8042, 2003.

Görür, N., Oktay F. Y, Seymen İ. and Şengör, A. M. C., Palaeotectonic evolution of the Tuzgölü basin complex, central Turkey: sedimentary record of a Neo-Tethys closure, In Geological Evolution of the Eastern Mediterranean, ed. JE Dixon, AHF Robertson, Geol. Soc. London Spec. Publ., 17, 467-482, 1984.

Grant, F. S., and West, G. F., Introduction to the electrical methods, in Interpretation Theory in Applied Geophysics, edited by R. R. Shrock, 385– 401, McGraw-Hill, New York, 1965.

Groom, R. W. and Bailey, R. C., Decomposition of magnetotelluric impedance tensors in presence of local three-dimensional galvanic distortion, Journal of Geophysical Research, 94 , 1913-1925, 1989.

Grosser, H., Baumbach, M., Berckhemer, H., Baier, B., Karahan, A., Schelle, H., Kruger, F., Paulat, A., Michel, G., Demirtas¸, R., Gençoğlu, S., Yılmaz, R., The Erzincan (Turkey) earthquake (M_s = 6. 8) of March 13, 1992 and its aftershock sequence, Pure and Applied Geophysics, 152, 465-505, 1998.

Gupta, S., Rai, S. S., Prakasam, K. S., Srinagesh, D., Chadha, R. K., Priestley, K. and Gaur, V. K., First evidence for anomalous thick crust beneath mid-Archean western Dharwar craton Current Science, 84, 9, 2003.

Hammond, C.W. & Humphreys, E.D., Upper mantle seismic wave velocity: Effects of realistic partial melt geometries, J. Geophys. Res,, 105, 10975-10986, 2000.

Hashin, Z. and Shtrikman, S., A variational approach to the theory of the effective magnetic permeability of multiphase materials, Journal of Applied. Physics, 33, 3125-3131, 1962.

Heise, W. and Pous, J., Anomalous phases exceeding 90° in magnetotellurics: anisotropic model studies and a field example, 155, 308-318, 2003.

Hempton, M. R., and Dune, L., Sedimentation in pull-apart basins: active examples in eastern Turkey, J. Geol., 92, 513-530, 1984.

Hempton, M. R., Constraints on Arabian plate motions; an extensional history of the Red sea, Tectonics, 6, 668-705, 1987.

Hempton, M. R., Structure and morphology of the East Anatolian Transform fault zone near Lake Hazar, southeastern Turkey, Geol. Soc. of Amer. Bull., 96, 233-243, 1985.

Hirono, T., Fujimoto, K., Yokoyama, T., Hamada, Y., Tanikawa, W., Tadai, O., Mishima, T., Tanimizu, M., Lin, W., Soh, W., and Song, S.-R., Clay mineral reactions caused by frictional heating during an earthquake: An example from the Taiwan Chelungpu fault, Geophysical Research Letters, 35, L16303, 2008.

Houseman, G. A. and England, P. C., Finite strain calculations of continental deformation. 1, Method and general results for convergent zones. J. Geophys. Res., 86, 6115-6132, 1986.

Housman, G. A., McKenzie, D. P. and Molnar, P., Convective instability of a thickened boundary layer and its relevance for the thermal evolution of continental collision belts, J. Geophys. Res., 86, 6115-6132, 1981.

Huber, P., Robust Statistics, John Wiley & Sons, New York, 153-199, 1981.

Hunt, C. P, Moskowitz, B. M. and Banerjee, S. K., Magnetic properties of rocks and minerals, A Hand book of physical constants, AGU reference Shelf 3,189-203, 1995.

Hyndman, R. D., and Lewis, T. S., Geophysical consequences of the Cordillera-Craton thermal transition in S.W. Canada, Tectonophysics, 306, 397-422, 1999.

Hyndman, R. D., Currie, C. A. and Mazzotti, S., Subduction zone backarcs, continental mobile belts, and orogenic heat, GSA Today, 15(2), 4-10, 2005.

İlkışık, O. M., Öztürk, S., Şener, C. and Tokgöz, T., Geothermic investigations in Turkey, Jeofizik, 9/1-2, 117-122, 1995 (in Turkish).

Innocenti, F., Manetti, P., Mazzuoli, R., Pasquaré, G. and Villari, L., Anatolia and northwestern Iran, in Andesites, Ed. R.S. Thorpe, John Wiley & Sons, 1982a.

Innocenti, F., Mazzuoli, R., Pasquaré, G., Radicati di Brozolo, F. and Villari, L., Tertiary and Quaternary volcanism of the Erzurum-Kars area (Eastern Turkey): Geochronological data and geodynamic evolution, J. Volc. Geotherm. Res., 13, 223-240, 1982b.

Irwin, W. P., and Barnes, I., Effect of geologic structure and metamorphic fluids on seismic behavior of the San Andreas fault system in central and northern California, Geology, 3, 713–716, 1975.

Jackson, J. and McKenzie, D. P., Active tectonics of Alpine-Himalayan Belt between western Turkey and Pakistan, Geophys. J. R. Astron. Soc., 77, 185-264, 1984.

Jackson, J., and McKenzie, D., The relationship between plate motions and seismic moment tensors and the rate of active deformation in the Mediterranean and Middle East, Geophysical Journal of Royal Astronomical Society, 93, 45-73, 1988.

Janssen, C., Michel, G. W., Bau, M., Luders, V., and Muhle, K., The North Anatolian Fault Zone and the role of fluids in seismogenic deformation, Journal of Geology, 105, 387-403, 1997.

Jiracek, G., Near-surface and topographic distortions in electromagnetic induction, Survey in Geophysics, 11, 163-203, 1990.

Jones, A. G., Chave, A. D., Egbert, G., Auld, D. and Bahr, K., A comparison of techniques for magnetotelluric response function estimation, J. Geophys. Res., 94, 14201-14213, 1989.

Jones, A. G., Geomagnetic induction studies in southern Scotland, Ph.D. Thesis, University of Edinburgh, 1977.

Jones, A. G., Lazaeta, P., Ferguson, I. J., Chave, A. D., Evans, R. L., Garcia, X., Spratt, J., The electrical structure of the Slave craton, Lithos, 71, 505-527, 2003.

Jones, A. G., Ledo, J. and Ferguson, I., Electromagnetic images of the Trans-Hudson Oregon: the North American Central Plains anomaly revealed, Canadian Journal of Earth Sciences, 42: 457-478, 2005.

Jones, A. G., Static shift of magnetotelluric data and its removal in a sedimentary basin environment, Geophysics, 53, 967-978, 1988.

Jones, A.G., Kurtz, R.D., Boerner, D.E., Craven, J.A., McNeice, G.W., Gough, D.I., DeLaurier, J.M. and Ellis, R.G., Electromagnetic constraints on strike-slip fault geometry - the Fraser River Fault system. Geology, 20, 561-564 1992.

Jones, F. W. and Price, A. T., The perturbations of alternating geomagnetic fields by conductivity anomalies, Geophys. J. Roy. Astron. Soc., 20, 317-334, 1970.

Juli`a, J., Ammon, C. J., Herrmann, R. B. and Correig, A. M., Joint inversion of receiver function and surface wave dispersion observations, Geophys. J. Int., 143(1), 99-112, 2000.

Jupp, D. L. and Vozoff, K., Stable iterative methods for the inversion of geophysical data, Geophys. J. Roy. Astr. Soc., 42, 67-72, 1975.

Karapetian, S. G., Jrbashian, R. T. and Mnatsakanian, A. K., Late collision rhyolitic volcanism in the north-eastern part of the Armenian Highland: Journal of Volcanology and Geothermal Research, 112, 189-220, 2001.

Karat, H. İ. and Aydın, İ., Report on Preparation of the Curie Isotherm Depth Map of Turkey, Unpublished Report no. 10638, MTA, Ankara, 2004 (in Turkish).

Karato, S., -I., Seismic anisotropy in the deep mantle, boundary layers and the geometry of mantle convection, Pure and Applied Geophysics, 151, 565-587, 1998.

Kaufman, A. A., and Keller, G. V., The Magnetotelluric Sounding Method, Amsterdam, Elsevier, 595 pp, 1981.

Kaypak, B. and Eyidoğan, H.,One dimensional crustal structure of the Erzincan basin, eastern Turkey and relocations of the 1992 Erzincan earthquake (M_s=6.8) aftershock sequence. Phys. Earth Planet. Sci., 151, 1-20, 2005.

Keskin, M., eastern Anatolia: A Hot Spot in a Collision Zone Without a Mantle Plume, in Foulger, G. R., and Jurdy, D. eds., The Origins of Melting Anomalies: Plumes, Plates,

and Planetary Processes (P^4 book): Geological Society of America Special Paper, 430, 2007.

Keskin, M., Magma generation by slab steepening and breakoff beneath a subduction-accretion complex: An alternative model for collision-related volcanism in eastern Anatolia, Turkey, Geophysical Research Letters, 30(24), 8046, 2003.

Keskin, M., Pearce, J. A. and Mitchell, J. G., Volcano-stratigraphy and geochemistry of collision-related volcanism on the Erzurum-Kars Plateau, North Eastern Turkey, Journal of Volcanology and Geothermal Research, 85, 355-404, 1998.

Keskin, M., Pearce, J. A., Kempton, P. D. and Greenwood, P., Magma-crust interactions and magma plumbing in a post-collision setting: Geochemical evidence from the Erzurum-Kars Volcanic Plateau, Eastern Turkey, in Dilek, Y., and Pavlides, S., eds., Postcollisional tectonics and magmatism in the Mediterranean region and Asia, Boulder, Colorado, Geological Society of America Special Paper 409, 475-505, 2006.

Ketin, İ. and Rösli, F., Makroseismische Untersuchungen über das nordwest-anatolische Beben vom 18 März 1953, Eclogae Geol. Helv., 46, 187-208, 1953.

Ketin, İ., Über die tektonisch-mechanischen Folgerungen aus den grossen anatolischen Erdbeben des letzten Dezenniums., Geol. Rund., 36, 77-83, 1948.

Kharaka, Y. K., Thordsen, J. J., Evans, W. C., and Kennedy, B. M., Geochemistry and hydromechanical interactions of fluids associated with the San Andreas fault system, California, in faults and subsurface fluid flow in the shallow crust, edited by: Haneberg, W. C., Mosely, P. S., Moore, J. C., and Goodwin, L. B., Geophysical Monograph, 113, 129-148, 1999.

King, G. C. P., Hubert-Ferrari, A., Nalbant, S. S., Meyer, B., Armijo, R. and Bowman, D., Coulomb interactions and the 17 August 1999 İzmit, Turkey earthquake. C.R. Acad. Sci. II Ser. A 333, 557-569, 2001.

Klemperer, S. L., Crustal flow in Tibet: geophysical evidence for the physical state of Tibetan lithosphere, and inferred patterns of active flow. In: Law, R. D., Searle, M. P. & Godin, L. (eds.) Channel Flow, Ductile Extrusion and Exhumation in Continental Collision Zones, Geological Society, London, Special Publications, 268, 39-70, 2006.

Koçak, A., Convective heat discharge map of Turkey prepared by using hot springs temperature, in Seminar on New Developments in Geothermal Energy, MTA, Ankara, 1989.

Koçyiğit, A., Yılmaz, A., Adamia, S. and Kuloshvili, S., Neotectonics of East Anatolian Plateau (Turkey) and Lesser Caucasus: implications for transition from thrusting to strike-slip faulting, Geodin. Acta, 14, 177-195, 2001.

Kozlovsky, E. A., Kola Super-deep: interim results and prospects, Episodes, 4, 9-11, 1982.

Kreemer, C., H., and Holt, W. E., A no-net-rotation model of present day surface motions, Geophys. Res. Lett., in press, 2003.

Lazaeta, P. and Haak, V., Beyond magnetotelluric decomposition: Induction, current channeling, and magnetotelluric phases over 90°, J. Geophys. Res., 108(B6), 2305, 2003.

Le Pichon, X., Chamot-Rooke, N., Huchon, P. and Luxey P., Implications des nouvelles mesures de g´eod´esie spatiale en Gr`ece et en Turquie sur l'extrusion lat´erale de l'Anatolie et de l'Eg´ee, C.R. Acad. Sci. Ser. II, 316, 983-990, 1993.

Le Pichon, X., Chamot-Rooke, N., Rangin, C. and Şengör, A. M. C., The North Anatolian Fault in the Sea of Marmara. J. Geophys. Res., 108, 2179, 2003.

Le Pichon, X., Şengör, A. M. C., Demirbağ, E., Rangin, C., İmren, C., et al., The active Main Marmara Fault, Earth Planet. Sci. Lett., 192, 595-616, 2001.

Lebedev, E. B. and Khitarov, N. I., Dependence on the beginning of melting of granite and the electrical conductivity of its melt on high water vapor pressure, Geochem. Int., 1, 193-197, 1964.

Ledo, J., 2-D versus 3-D magnetotelluric data interpretation, Surveys in Geophysics, 26, 671-806, 2005.

Leech, M. L., Singh, S., Jain, A. K., Klemperer, S. L. and Manickavasagam, R.M., The onset of India – Asia continental collision: Early steep subduction required by the timing of UHP metamorphism in the western Himalaya, Earth and Planetary Science Letters, 234, 83-97, 2005.

Li, S., Unsworth, M., Booker, J. R., Wei, W., Tan, H, and Jones, A. G., Partial melt or aqueous fluid in the mid-crust of southern Tibet? Constraints from INDEPTH magnetotelluric data, Geophysical Journal International, 153, 289-304, 2003.

Li, X., Kind, R., Yuan, X.,Wölbern, I. and Hanka,W., Rejuvenation of the lithosphere by the Hawaiian plume, Nature, 427, 827-829, 2004.

Mackie R. L., Madden T. R. and Wannamaker P. E., Three-dimensional magnetotelluric modeling using difference equations-Theory and comparisons to integral equation solutions, Geophysics, 58, 215-226, 1993.

Mackie, R. L. and Madden, T. R., Three-dimensional magnetotelluric inversion using conjugate gradients: Geophys. J. Internat., 115, 215-229, 1993.

Mackie, R. L., Livelybrooks, D. W., Madden, T. R., and Larsen, J. C., A magnetotelluric investigation of the San Andreas fault at Carrizo Plain, California, Geophysical Research Letters, 24, 1847-1850, 1997.

Madden, T. and Nelson, P., A defense of Cagniard's magnetotelluric Method: ONR Report, MIT Geophysics Lab, 1964.

Maggi A. and Priestley, K., Surface waveform tomography of the Turkish-Iranian plateau, Geophys. J. Int., 160 (3), 1068-1080, 2005.

Mareschal, M., Kellett, R. L., Kurtz, R. D., Ludden, J. N., Ji, S., and Bailey, R. C., Archean cratonic roots, mantle shear zones and deep electrical anisotropy, Nature, 375, 134-137, 1995.

Marquis, G., Hyndman, R. D., Geophysical support for aqueous fluids in the deep crust: seismic and electrical relationships, Geophysical Journal International, 110, 91-105, 1992.

Marti, A., Queralt, Q., Jones, A. G., and Ledo, J., Improving Bahr's invariant parameters using the WAL approach, Geophysical Journal International, 163, 38-41, 2005.

Mavko, G. M., Velocity and attenuation in partially molten rocks, Journal of Geophysical Research, 85, 5173-5189, 2005.

McClusky, S., Balassanian. S., Barka, A., Demir, C. and Ergintav, S., Georgiev, I., Gurkan, O., Hamburger, M., Hurst, K., Hans-Gert, H. -G., Karstens, K., Kekelidze, G., King, R., Kotzev, V., Lenk, O., Mahmoud, S., Mishin, A., Nadariya, M., Ouzounis, A., Paradissis, D., Peter, Y., Prilepin, M., Reilinger, R., Sanli, I., Seeger, H., Tealeb, A., Toksöz, M. N. and Veis, G., Global positioning system constraints on plate kinematics and dynamics in the eastern Mediterranean and Caucasus, Journal of Geophysical Research, 105, 5695-5719, 2000.

McClusky, S., Reilinger, R., Mahmoud, S., Ben Sari, D. and Tealeb, A., GPS constraints on Africa (Nubia) and Arabia plate motions, Geophys. J. Int., 155, 126-138, 2003.

McKenzie, D. and Jackson, J., The relationship between strain rates, crustal thickening, palaeomagnetism, finite strain and fault moments within a deforming zone, Earth Planet. Sci. Lett., 65, 182-202, 1983.

McKenzie, D. P., Active tectonics of the Mediterranean region, Geophys. J. R. Astron. Soc., 30, 109-185, 1972.

McKenzie, D., East Anatolian Fault: A major structure in Eastern Turkey, Earth and Planetary Science Letters, 29, 189-193, 1976.

McNeice, G. M. and Jones, A. G., Multisite, multifrequency tensor decomposition of magnetotelluric data: Geophysics, 66, 158-173, 2001.

Menke, W., Geophysical data analysis: discrete inverse theory, Int. Geophys. Ser., vol. 45, 1989.

Mitchell, J. and Westaway, R., Chronology of Neogene and Quaternary uplift and magmatism in the Caucasus: constraints from K - Ar dating of volcanism in Armenia, Tectonophysics, 304, 157-186, 1999.

Molnar, P and Tapponnier, P., Active tectonics of Tibet, J. Geophys. Re,. 83, 5361-5375, 1978.

Mount, V. S., and Suppe, J., State of stress near the San Andreas fault: Implications for wrench tectonics, Geology, 15, 1143-1146, 1987.

Mooney, W.D., Laske, G. and Masters, G., CRUST 5.1: A global crustal model at 5°x5°, J. Geophys. Res., 103, 727-747, 1998.

Nalbant, S. S., McCloskey, J., Steacy, S., and Barka, A. A., Stress accumulation and increased seismic risk in eastern Turkey: Earth and Planetary Science Letters, 195, 291-298, 2002.

Negi, J. G., Agrawal, P. K. and Pandey, O. P., Large variation of Curie depth and lithospheric thickness beneath the Indian subcontinent and a case for magnetothermometry, Geophysical Journal International, 88, 763-775, 1987.

Nelson, K. D., et al., Partially molten middle crust beneath southern Tibet: synthesis of project INDEPTH results, Science 274, 1684-1687, 1996.

Newman,G. A. and Alumbaugh, D. L., Three-dimensional massively parallel electromagnetic inversion-I. Theory, Geophys. J. Internat., 128, 345-354, 1997.

Notsu, K., Fujitani, T., Ui, T., Matsuda, J., and Ercan, T., Geochemical features of collision-related volcanic rocks in central and eastern Anatolia, Turkey: Journal of Volcanology and Geothermal Research, 64, 171-192, 1995.

Ogawa, Y. and Uchida, T., A two-dimensional magnetotelluric inversion assuming Gaussian static shift, Geophys. J. Int., 126, 69-76, 1996.

Oldenburg, D. W., McGillivray, P. R. and Ellis, R. G., Generalized subspace methods for large scale inverse problems, Geophys. J. Internat., 114, 12-20, 1993.

Olsen, K. B., Site amplification in the Los Angeles Basin from three-dimensional modeling of ground motion, Bulletin of the Seismological Society of America, 90, 6B, 77-94, 2000.

Örgülü, G., Aktar, M., Turkelli, N., Sandvol, E. and Barazangi, M., Contribution to the seismotectonics of Eastern Turkey from moderate and small size events, Geophysical Research Letters, 30, 24, 8040, 2003.

Örgülü, G., and Aktar, M., Regional Moment Tensor Inversion for Strong Aftershocks of the August 17, 1999 Izmit Earthquake (Mw=7.4), Geophsical Research Letters, Vol.28, 371-374, 2001.

Owens, T. J. and Zandt, G., Implications of crustal property variations for models of Tibetan plateau evolution, Nature 387, 37-43, 1997.

Ozacar, A. A., Gilbert, H. and Zandt, G., Upper mantle discontinuity structure beneath East Anatolian Plateau (Turkey) from receiver functions, Earth and Planetary Science Letters, 269, 426-434, 2008.

Pamukçu, O. A., Akçığ, Z., Demirbaş, Ş. and Zor, E., Investigation of Crustal Thickness in eastern Anatolia Using Gravity, Magnetic and Topographic Data, Pure and Applied Geophysics, 164, 2345-2358, 2007.

Park, S. K. and Mackie, R. L., Resistive (Dry?) lower crust in an active orogen, Nanga Parbat, northern Pakistan, Tectonophysics, 316, 359-380, 2000.

Parker, R. L, The inverse problem of electromagnetic induction: existence and construction of solutions based on incomplete data, Journal of Geophysical Research, 85, 4421-4428, 1980.

Parker, R. L. and Booker, J. B., Optimal one-dimensional inversion and bounding of magnetotelluric apparent resistivity and phase measurements, Phys. Earth Planet. Inter., 98, 269-282, 1996.

Parkinson, W. D., Directions of rapid geomagnetic variations, Geophys. J. R. Astr. Soc., 2, 1-14, 1959.

Parkinson, W. D., The influence of continents and oceans on geomagnetic variations, Geophysical Journal of the Royal Astronomical Society, 6, 441-449, 1962.

Parsons, T., Toda, S., Stein, R. S., Barka, A., and Dietrich, J. H., Heightened odds of large earthquakes near İstanbul: An interaction based probability calculation, Science, 288, 661-665, 2000.

Partzsch, G. M., Schilling, F. R. and Arndt, J., The influence of partial melting on the electrical behaviour of crustal rocks: laboratory examinations, model calculations and geological interpretations, Tectonophysics, 317, 189-203, 2000.

Pearce, J. A., Bender, J. F., De Long, S. E., Kidd, W. S. F., Low, P. J., Guner, Y., Şaroğ lu, F., Yılmaz, Y., Moorbath, S., and Mitchell, J. G., Genesis of collision volcanism in eastern Anatolia, Turkey: Journal of Volcanology and Geothermal Research, 44, 189-229, 1990.

Pek, J. and Verner, T., Finite difference modelling of magnetotelluric fields in 2-D anisotropic media, Geophysical Journal International, 128, 505-521, 1997.

Philip, H., Cisternas, A., Gvishiani, A. and Gorshkov, A., The Caucasus: an actual example of the initial stages of continental collision, Tectonophysics, 161, 1-21, 1989.

Piromallo, A. and Morelli, P., P wave tomography of the mantle under the Alpine-Mediterranean area, J. Geophys. Res., 108, 2003.

Price, A. T.,The theory of magnetotelluric methods when the source field is considered, J. Geophys. Res., 67, 1907-1918, 1962.

Priestley, K. and McKenzie, D., The thermal structure of the lithosphere from shear wave velocities, Earth. Planet. Sci. Lett., 244, 285-301, 2006.

Provost, A.-S., Chery, J., and Hassani, R., 3-D mechanical modeling of the GPS velocity field along the north Anatolian fault, Earth and Planetary Science Letters, 209, 361-377, 2003.

Rao, C. K., Jones, A. G. and Moorkamp, M., The geometry of the Iapetus suture in Central Ireland deduced from a magnetotelluric survey, Geophysical Journal International, 161: 134-141, 2007.

Rasmussen, T. M., Roberts, R. G. and Pedersen, L. B., Magnetotellurics along the Fennoscandian Long Range profile, Geophysical Journal International, 89: 799-820, 1987.

Reilinger, R. E., Ergintav, S., Bürgmann, R., McClusky, S., Lenk, O., Barka, A., Gurkan, O., Hearn, L., Feigl, K. L., Cakmak, R., Aktug, B., Ozener, H., and Töksoz, M. N., Coseismic and postseismic fault slip for the 17 August, M = 7.5, Izmit, Turkey earthquake, Science, 289, 1519-1524, 2000.

Reilinger, R., McClusky, S., Vernant, P., Lawrence, S., Ergintav, S., Cakmak, R., Ozener, H., Kadirov, F., Guliev, I., Ruben, S., Nadariya, M., Hahubia, G., Mahmoud, S., Sakr, K., ArRajehi, A., Paradissis, D., Al-Aydrus, A., Prilepin, M., Guseva, T., Evren, E., Dmitrotsa, A., Filikov, S.V., Gomez, F., Al-Ghazzi, R., and Karam, G., GPS constraints on continental deformation in the Africa-Arabia-Eurasia continental collision zone and implications for the dynamics of plate interactions: Journal of Geophysical Research, 111, 2006.

Ritter, O., Hoffmann-Rothe, A., Bedrosian, P. A., Weckmann, U. and Haak, V., Electrical conductivity images of active and fossil fault zones, *Geological Society, London, Special Publications*, 245: 165-186, 2005.

Rodi, W. and Mackie, R. L., Nonlinear conjugate gradients algorithm for 2-D magnetotelluric inversions, Geophysics, 66 , 174-187, 2001.

Rotstein, Y. and Kafka, A. L., Seismotectonics of the southern boundary of Anatolia, eastern Mediterranean region, subduction, collision and arc jumping, J. Geophys. Res., 87, 7694-7706, 1982.

Russell, R. D. and Narod, B. B., Fluxgate sensors for Geophysical applications, in Current Topics in Magnetics Research, J. Menon General Editor, 1, 59-70, 1994.

Sandvol, E., Al-Damegh, K., Calvert, A., Seber, D., Barazangi, M., Mohamad, R., Gok, R., Turkelli, N. and Gurbuz, C., Tomographic imaging of Lg and Sn Propagation in the Middle East, Pure App. Geophys., 158, 1121-1163, 2001.

Sandvol, E., Turkelli, N., and Barazangi, M., 2003a, The eastern Turkey seismic experiment: The study of a young continent-continent collision, Geophysical Research Letters, 30, 24, 8038, 2003a.

Sandvol, E., Turkelli, N., Zor, E., Gok, R., Bekler, T., Gurbuz, C., Seber, D. and Barazangi, M., Shear wave splitting in a young continent-continent collision, An example from eastern Turkey: Geophysical Research Letters, 30, 24, 8041, 2003b.

Şaroğlu, F., Emre, Ö. and Kuşçu, İ., Türkiye Diri Fay Haritası (Active Fault Map of Turkey), scale 1:2,000,000, one sheet. Maden Tetk. Arama Genel Müdürlüğü, Ankara, 1992.

Sasaki, Y., Full 3-D Inversion of electromagnetic data on PC, J. Appl. Geophys., 46, 45-54, 2001.

Schilling, F. R., Partzsch, G. M., Brasse, H. and Schwarz, G., Partial melting below the magmatic arc in the central Andes deduced from geoelectromagnetic field experiments and laboratory data, Physics of the Earth and Planetary Interiors, 103, 17-31, 1997.

Schmeling, H., Numerical models on the influence of partial melt on elastic, anelastic and electric properties of rocks. part II: Electrical conductivity, Phys. Earth Planet. Inter., 43, 123- 136, 1986.

Schmucker, U., Regional induction studies: a review of methods and results. Phys. Earth Planet. Inter., 7, 365-378, 1973.

Şengör A. M. C., A new model for the late Palaeozoic-Mesozoic tectonic evolution of Iran and implications for Oman, Geol. Soc. London Spec. Publ., 49, 797-831, 1990.

Şengör, A. M. C. and Kidd, W. S. F., Post-collisional tectonics of the Turkish-Iranian Plateau and a comparison with Tibet, Tectonophysics, 55, 361-376, 1979.

Şengör, A. M. C. and Yilmaz, Y., Tethyan evolution of Turkey: a plate tectonic approach, Tectonophysics, 75, 181-241, 1981.

Şengör, A. M. C., Görür, N. and Şaroğlu, F., Strikeslip faulting and related basin formation in zones of tectonic escape: Turkey as a case study. In Strike-slip Deformation, Basin Formation, and Sedimentation, Soc. Econ. Paleontol. Miner. Spec. Publ. 37 (in honor of J.C. Crowell), ed. Biddle, K. T. and Christie-Blick, K., 227-264, 1985.

Şengör, A. M. C., Özeren, S., Genç, T. and Zor, E., East Anatolian high plateau as a mantle-supported, N-S shortened domal structure, Geophysical Research Letters, 30(24), 8045, 2003.

Şengör, A. M. C., Tüysüz, O., İmren, C., Sakınç, M., Eyidoğan, H., Görür, N., Le Pichon, X. and Rangin, C., The North Anatolian Fault: A New Look Annu. Rev. Earth Planet. Sci., 33, 37-112, 2005.

Seymen, İ. and Aydın, A., The Bingöl earthquake fault and its relation to the North Anatolian Fault Zone, Bull. Miner. Res. Explor. Inst., No. 79, 1-8, 1972.

Seymen, İ., Kelkit Vadisi Kesiminde Kuzey Anadolu Fay Zonunun Tektonik Özelliği: Dr. Eng., İstanbul Tek. Üniv., Maden Fak., XIX+192 pp.+2 foldout maps, 1975.

Shin, Y. H., Xu H., Braitenberg, C., Fang, J. and Wang, Y., Moho undulations beneath Tibet from GRACE-integrated gravity data. In review process at Geophysical Journal International, 170, 971-985, 2007.

Sibson, R. H., Frictional constraints on thrust, wrench and normal faults, Nature, 249, 542-544, 1974.

Simpson, F. and Bahr, K., Practical Magnetotellurics, Cambridge University Press, 254 pp, 2005.

Simpson, F. and Warner, M., Coincident magnetotelluric, P-wave and S-wave images of the deep continental crust beneath the Weardale granite, NE England: seismic layering, low conductance and implications against the fluids paradigm, Geophys. J. Int., 133, 419-434, 1998.

Simpson, F., A comparison of electromagnetic distortion and resolution of upper mantle conductivities beneath continental Europe and the Mediterranean using islands as windows, Phys. Earth. Planet. Inter., 129, 117-130, 2002.

Sims, W. E., Bostick, F. X. and Smith, H. W., The estimation of magnetotelluric impedance tensor elements from measured data, Geophysics, 36, 938-942, 1971.

Siripunvaraporn, W. and Egbert, G., An effient data-subspace inversion for two-dimensional magnetotelluric data, Geophysics, 65, 791-803, 2000.

Siripunvaraporn, W., Egbert, G. and Uyeshima, M., Interpretation of two-dimensional magnetotelluric profile data with three-dimensional inversion: synthetic examples, *Geophys. J. Int., 160,* 804-814, 2005a.

Siripunvaraporn, W., Egbert, G., Lenbury, Y. and Uyeshima, M., Three-dimensional magnetotelluric inversion: data-space method, Physics of the Earth and Planetary Interiors, 150, 3-14, 2005b.

Sleep, N. H., and M. L. Blanpied, Creep, compaction and the weak rheology of major faults, Nature, 359, 687-692, 1992.

Smith, J. T. and Booker, J. R., Rapid inversion of two- and three-dimensional magnetotelluric data, Journal of Geophysical Research, 96 , 3905-3922, 1991.

Smith, J. T., Estimating galvanic-distortion magnetic fields in magnetotellurics, Geophysical Journal International, 130 , 65-72, 1997.

Stein, R. S., Barka, A. and Dieterich, J. H., Progressive failure on the North Anatolian fault since 1939 by earthquake stress triggering, Geophys. J. Int., 128, 594-604, 1997.

Stenberg, B. K., Washburn, J. C. and Pellerin, L., Correction for the static shift in magnetotellurics using transient electromagnetic soundings, Geophysics 53, 1459-1468, 1988.

Stoeser, D. and Camp, V., Pan-African microplate accretion of the Arabian Shield, Geol. Soc. Am. Bull., 96, 817-826, 1985.

Swift, C. M., A magnetotelluric investigation of an electrical conductivity anomaly in the southwestern United States, Ph.D. Thesis, Mass. Inst. of Tech, 1967.

Talebian, M. and Jackson, J., Offset on the main recent fault of NW Iran and implications for the late Cenozoic tectonics of the Arabia-Eurasia collision zone, Geophys. Journ. Int., 150, 422-439, 2002.

Tanaka, A., Okubo, Y. and Matsubayashi, O., Curie point depth based on spectrum analysis of the magnetic anomaly data in East and Southeast Asia, Tectonophysics, 306, 461-470, 1999.

Tank, S. B., Honkura, Y., Ogawa, Y., Matsushima, M., Oshiman, N., Tuncer, M. K., Celik, C., Tolak, E., and Isikara, A. M., Magnetotelluric imaging of the fault rupture area of the 1999 Izmit (Turkey) earthquake, Phys. Earth Planet. Inter., 150, 213-225, 2005.

Tapponnier, P., Peltzer, G., Le Dain, A. Y., Armijo, R., Propating extrusion tectonics in Asia : New insights from simple experiments with plasticine, Geology, 10, 610-616, 1982.

Tapponnier, P**.,** Zhiqin, X., Roger, F., Meyer, B., Arnaud, N., Wittlinger, G., and Jingsui Y., Oblique stepwise rise and growth of the Tibetan Plateau, Science 294, 1671-1677 2001.

Tatar, Y., Kuzey Anadolu Fay Zonunun Erzincan-Refahiye arasindaki bölümü üzerinde tektonik incelemeler. Yerbilimleri, 4, 201-236, 1978.

Tauber, S., Banks, R., Ritter, O. and Weckmann, U., A high-resolution magnetotelluric survey of the Iapetus Suture Zone in southwest Scotland, Geophysical Journal International, 153: 548-568, 2003.

ten Grotenhuis, S. M., Drury, M. R., Spiers, J., and Peach, C. J, Melt distribution in olivine rocks based on electrical conductivity measurements, Journal of Geophysical Research, 110, doi:10.1029/2004JB003462, 2005.

Tesha, A. L., A. A. Nyblade, G. R. Keller, and D. I. Doser (1997), Rift localization in suture-thickened crust: Evidence from Bouguer gravity anomalies in northeastern Tanzania, East Africa, Tectonophysics, 278, 315-328, 1997.

Tezcan, A. K., and Turgay, M. I., Heat Flow Density Distribution in Turkey, Publication of the Mineral Research and Exploration (MTA), Ankara, 1987.

Tezcan, A. K., Geothermal explorations and heat flow in Turkey, in Terrestrial Heat Flow and Geothermal Energy in Asia, pp. 23-42, eds. Gupta, M.L. & Yamano, M., Oxford and IBH publishing Co. Pvt. Ltd., New Delhi, 1995.

Tezcan, A. K., Geothermal studies, their present status and contribution to heat flow contouring in Turkey, in Terrestrial Heat Flow in Europe, 283-291, eds. Cermak, V. & Rybach, L., Springer Verlag, Berlin, 1979.

Tikhonov, A. N. and Arsenin, V. Y., Solutions of Ill-Posed Problems, V.H. Winston and Sons: Washington, D.C., 1977.

Tikhonov, A. N., Determination of the electrical properties of deep layers of the Earth's crust. Dokl. Acad. Nauk. SSR, 73, 295-297, 1950 (in Russian).

Tilmann, F., Ni, J., INDEPTH III Seismic Team, Seismic Imaging of the Downwelling Indian Lithosphere Beneath Central Tibet, Science, 300, 1424-1427, 2003.

Topuz, G., Altherr, R., Kalt, A., Satır, M., Werner, O. and Schwarz, W. H., Aluminous granulites from the Pulur complex, NE Turkey: A case of partial melting, efficient melt extraction and crystallization, Lithos, 72, 183-207, 2004

Torres-Verdin, C. and Bostick, F. X., Principles of spatial surface electric field filtering in magnetotellurics: Electromagnetic array profiling (EMAP), Geophysics, 57, 603-622, 1992.

Turkelli, N., Sandvol, E., Zor, E., Gök, R., Bekler, T., Al-Lazki, A., Karabulut, H., Kuleli, S., Eken, T., Gürbüz, C., Bayraktutan, S., Seber, D., and Barazangi, M., Seismogenic zones in Eastern Turkey, Geophysical Research Letters, 30(24), 8039, 2003.

Türkoğlu, E., Unsworth, M. and Pana, D., Deep electrical structure of Northern Alberta (Canada): Implications for diamond exploration, accepted for publication in CJES January 2009.

Türkoğlu, E., Unsworth, M., Çağlar, İ., Tuncer, V. and Avşar, Ü., Lithospheric structure of the Arabia-Eurasia collision zone in eastern Anatolia: Magnetotelluric evidence for widespread weakening by fluids? Geology, 36, 619-622, 2008.

Tyburczy, J. A. and Waff, H. S., Electrical conductivity of molten basalt and andesite to 25 kbar pressure: geophysical significance and implications for charge transport and melt structure, J. geophys. Res., 88, 2413-2430, 1983.

Uchida, T., Smooth 2-D inversion for magnetotelluric data based on statistical criterion ABIC, Journal of Geomagnetism and Geoelectricity, 45, 841-858, 1993.

Unsworth, M. J., Egbert, G. D., and Booker, J. R., High Resolution electromagnetic imaging of the San Andreas Fault in Central California, J. Geophys. Res., 104, 1131-1150, 1999.

Unsworth, M. J., Jones, A. G., Wei, W., Marquis, G., Gokarn, S. G. and Spratt, J. E., Crustal rheology of the Himalaya and Southern Tibet inferred from magnetotelluric data, Nature, 438, 78-81, 2005.

Unsworth, M. J., Malin, P. E., Egbert, G. D., Booker, J. R. Internal structure of the San Andreas fault zone at Parkfield, California, Geology 25:359-362, 1997.

Unsworth, M. J., Wei, W., Jones, A. G., Li, S., Bedrosian, P. A., Booker, J. R., Jin, S., and Deng, M., Crustal and upper mantle structure of Northern Tibet imaged with magnetotelluric data, J. Geophys. Res., 109, 2004.

Utada, H. and Munekane, H., On galvanic distortion of regional 3-D MT impedances On galvanic distortion of regional three-dimensional magnetotelluric impedances, Geophys. J. Int., 140, 385-398, 2000.

Vanyan, L., and Gliko, A. O., Seismic and electromagnetic evidence of dehydration as a free water source in the reactivated crust, Geophysical Journal International, 137, 159-162, 1999.

Vanyan, L., Tezkan, B., and Palshin, N., Low electrical resistivity and seismic velocity at the base of the upper crust as indicator of rheologically weak layer, Surveys in Geophysics, 22, 131-154, 2001.

Vernant, P., Nilforoushan, F., Hatzfeld, D., Abbassi, M. R., Vigny, C., Masson, F., Nankali, H., Martinod, J., Asttiani, A., Bayer, R., Tavakoli, F. and Chery, J., Present-day crustal deformation and plate kinematics in the Middle East constrained by GPS measurements in Iran and northern Oman, Geophys. J. Int., 157, 381-398, 2004.

Vozoff, K., The magnetotelluric method, in Misac N. Nabighian ed., Electromagnetic methods in applied geophysics, vol.2: SEG, 641-711, 1991.

Waff, H. S., Theoretical considerations of electrical conductivity in a partially molten mantle and implications for geothermometry, J. Geophys, Res., 79, 4003-4010, 1974.

Wait, J. R., Electromagnetic Waves in Stratified Media. Golem Press, Boulder, 1970.

Wait, J. R., On the relation between telluric currents and the earth's magnetic field, Geophysics, 19, 281-289, 1954.

Wang, E., Burchfiel, B. C., Royden, L. H., Liangzhong, C., Jishen, C., Wenxin, L., and Zhiliang, C., Late cenozoic xianshuihe-xiaojiang, red river, and dali fault systems of southwestern sichuan and central yunnan, China, Special Paper - Geological Society of America, 327, 108, 1998.

Wannamaker, P. E., Affordable magnetotellurics: interpretation in natural environments, in Three-dimensional electromagnetics, ed. By M. Oristaglio and B. Spies, Geophys. Devel. Ser., no. 7, Soc. Explor. Geophys., Tulsa, 349-374, 1999.

Wannamaker, P., Stodt, J. and Rijo, L., A stable finite element solution for two-dimensional magnetotelluric modelling, Geophys. J. R. Astr. Soc., 88 , 277-296, 1987.

Weidelt, P., The inverse problem of geomagnetic induction, Zeitschrift für Geophysik, 38, 257-289, 1972.

Westaway, R. and Arger, J., Kinematics of the Malatya-Ovacık fault zone, Geodin. Acta, 14, 103-131, 2001.

Westaway, R. and Arger, J., The Gölbaşı basin, southeastern Turkey: A complex discontinuity in a major strike-slip fault zone, J. Geol. Soc. London, 153, 729-743, 1996.

Westaway, R., Present-day kinematics of the Middle East and eastern Mediterranean, J. Geophys. Res., 99, 12071-12090, 1994.

Whittall, K. P. and Oldenburg, D. W., Inversion of Magnetotelluric Data for a One Dimensional Conductivity, Society of Exploration Geophysics monograph, vol. 5, 1992.

Wiese, H., Geomagnetische Tiefentellurik Teil II: Die Streichrichtung der Untergrundstrukturen des elektrischen Widerstandes, erschlossen aus geomagnetischen Variationen, Geofis. Pura et Appl., 52, 83-103, 1962.

Willet, S. D., and Beaumont, C., Subduction of Asian mantle beneath Tibet inferred from models of continental collision, Nature, 369, 642–645, 1994.

Williams, C. F., Grubb, F.V. and Galanis Jr., S.P., Heat flow in the SAFOD pilot hole and implications for the strength of the San Andreas Fault, Geophys. Res. Lett., 31, 2004.

Xu, Y., Shankland, T. J. and Poe, B. T., Laboratory-based electrical conductivity of the Earth's mantle. Journal of Geophysical Research, 105, 27865-27875, 2000.

Yardley, B. W. D., and Valley, J. W., The petrologic case for a dry lower crust, Journal of Geophysical Research, 102, 12173-12185, 1997.

Yılmaz, H. and Özel, S., Crustal Structure of the Eastern Part of Central Anatolia (Turkey), Turkish J. Earth Sci., 18, 169-185, 2008.

Yilmaz, H., Over, S. and Ozden, S., Kinematics of the East Anatolian Fault Zone between Turkoglu (Kahramanmaras) and Celikhan (Adiyaman), eastern Turkey, Earth Planets Space, 58, 1463-1473, 2006.

Yilmaz, Y., New evidence and model on the evolution of the Southeast Anatolia Orogen, Geol. Soc. America Bull., 105, 251-271, 1993.

Yilmaz, Y., Tüysüz, O., Yigitbaş, E., Genç, Ş. C. and Şengör, A. M. C., Geology and tectonic evolution of the Pontides, in Regional and Petroleum geology of the Black Sea and Surrounding Region, edited by A. G. Robinson, AAPG Memoir, 68, 183-226, 1997.

Zhao, W., Nelson, K. D., and INDEPTH team, Deep seismic reflection evidence for continental underthrusting beneath southern Tibet, Nature, 366, 557-559, 1993.

Zhdanov, M. S. and Hursan, G., 3-D electromagnetic inversion based on quasi-analytical approximation, Inverse Problems, 16, 1297-1322, 2000.

Zhdanov, M. S., and Keller, G. V., Electrical Methods in Geophysical Exploration: Amsterdam, Elsevier, 929 pp, 1994.

Zhu, B., Kidd, W. S. F., Rowley, D. B., Currie, B. S., and Shafique, N., Age of Initiation of the India-Asia Collision in the East-Central Himalaya, The Journal of Geology, 113, 265–285, 2005.

Zoback, M. D., Zoback, M. L., Mount, V. S., Suppe, J., Eaton, J. P., Healy, J. H., Oppenheimer, D., Reasenberg, P., Jones, L. M., Raleigh, C. B., Wong, I. G., Scotti, O., and Wentworth, C., New evidence on the state of stress of the San Andreas fault system, Science, 238, 1105-1111, 1987.

Zor, E., Gürbüz, C., Türkelli, N., Sandvol, E., Seber, D. and Barazangi, M., The crustal structure of the East Anatolian Plateau from receiver functions: Geophysical Research Letters, 30(24), 8044, 2003.

APPENDIX-A

MT DATA, 2-D INVERSION RESPONSES AND STATISTICS

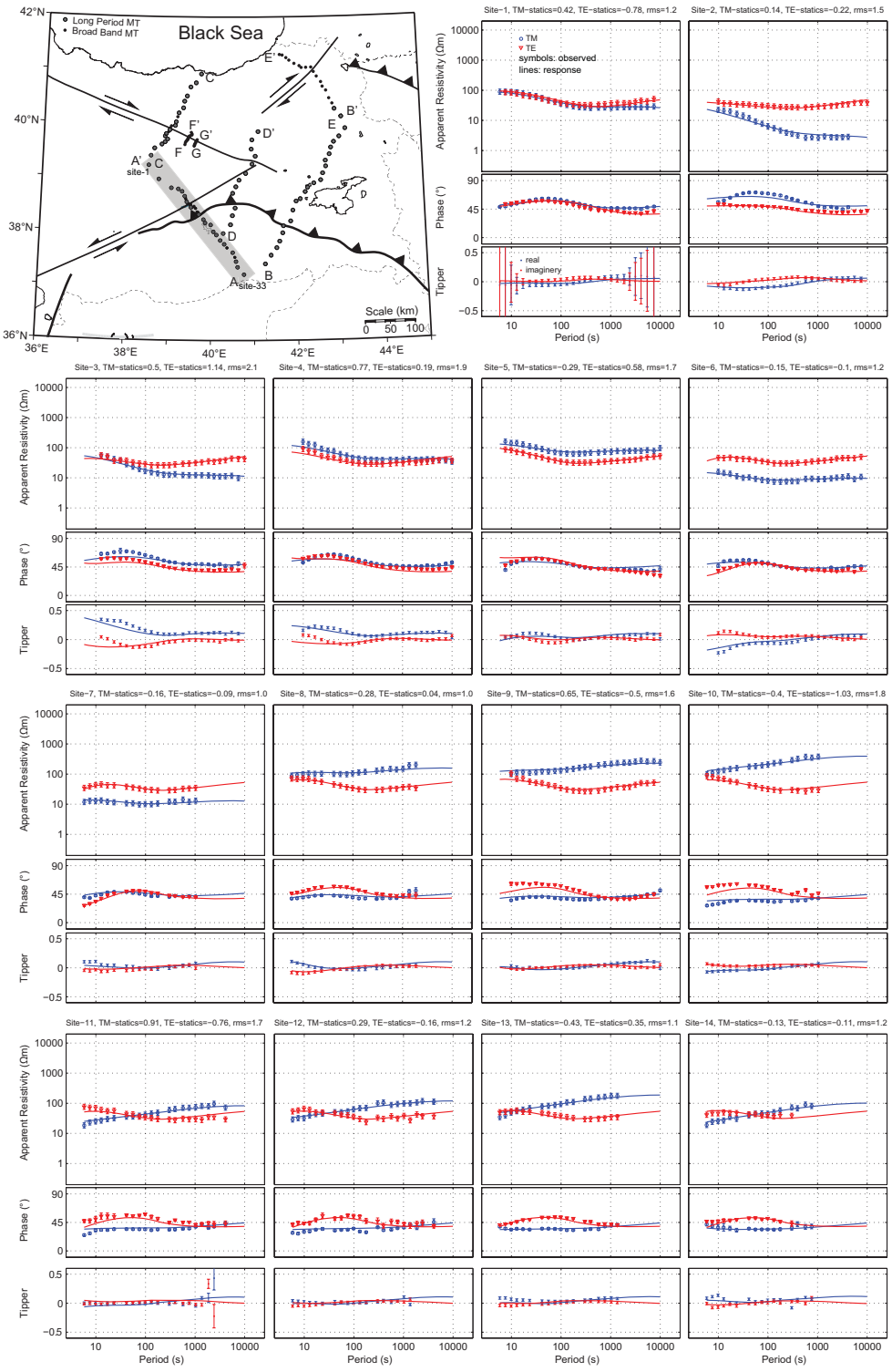

Figure A-1. A-profile MT data and 2-D inversion results with statistics for each station. Station names are modified to follow the locations from the map easily.

Figure A-1 continued…

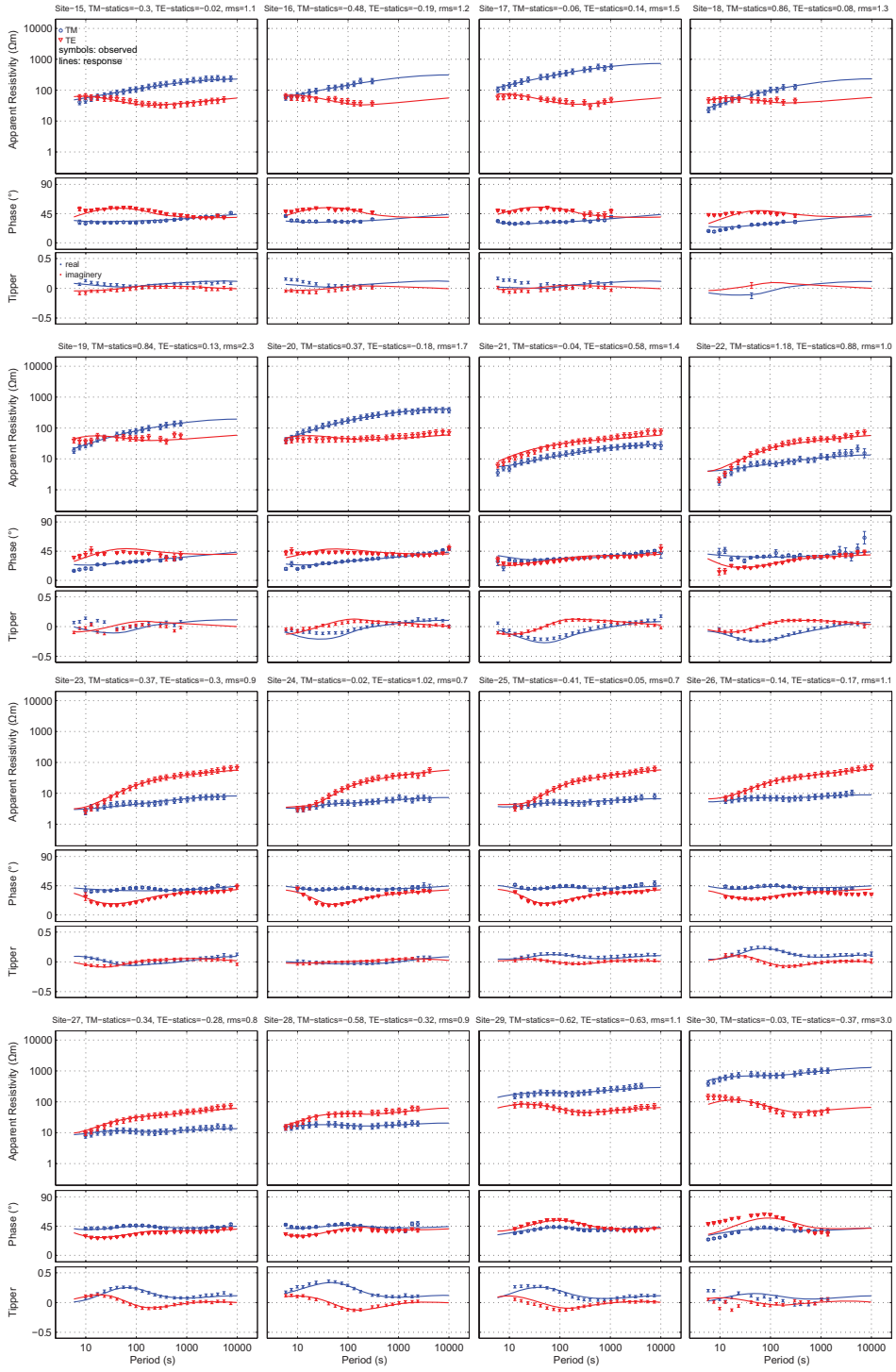

Figure A-1 continued…

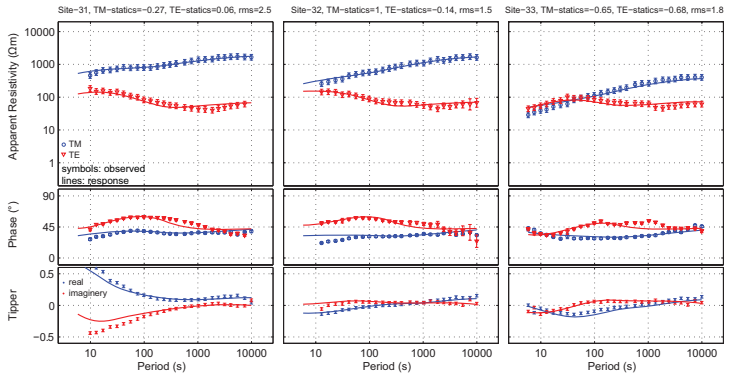

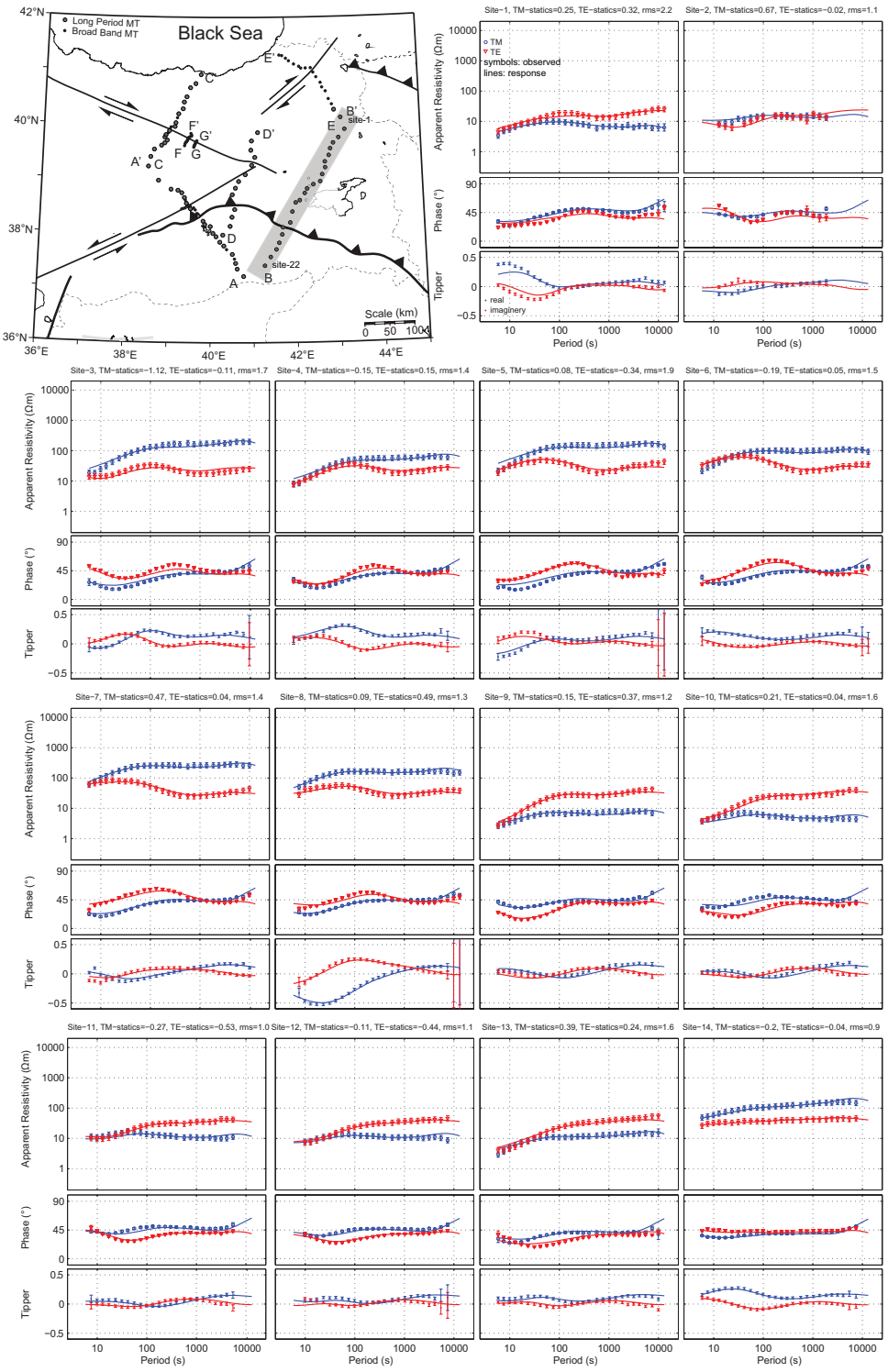

Figure A-2. B-profile MT data and 2-D inversionresults with statistics for each station. Station names are modified to follow the locations from the map easily.

Figure A-2 continued…

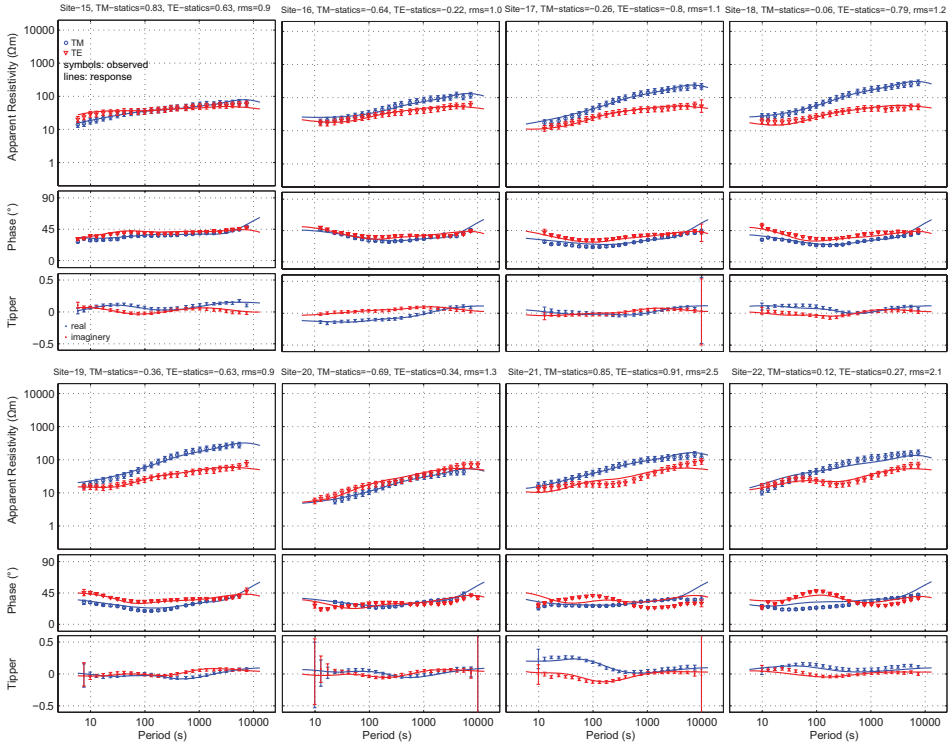

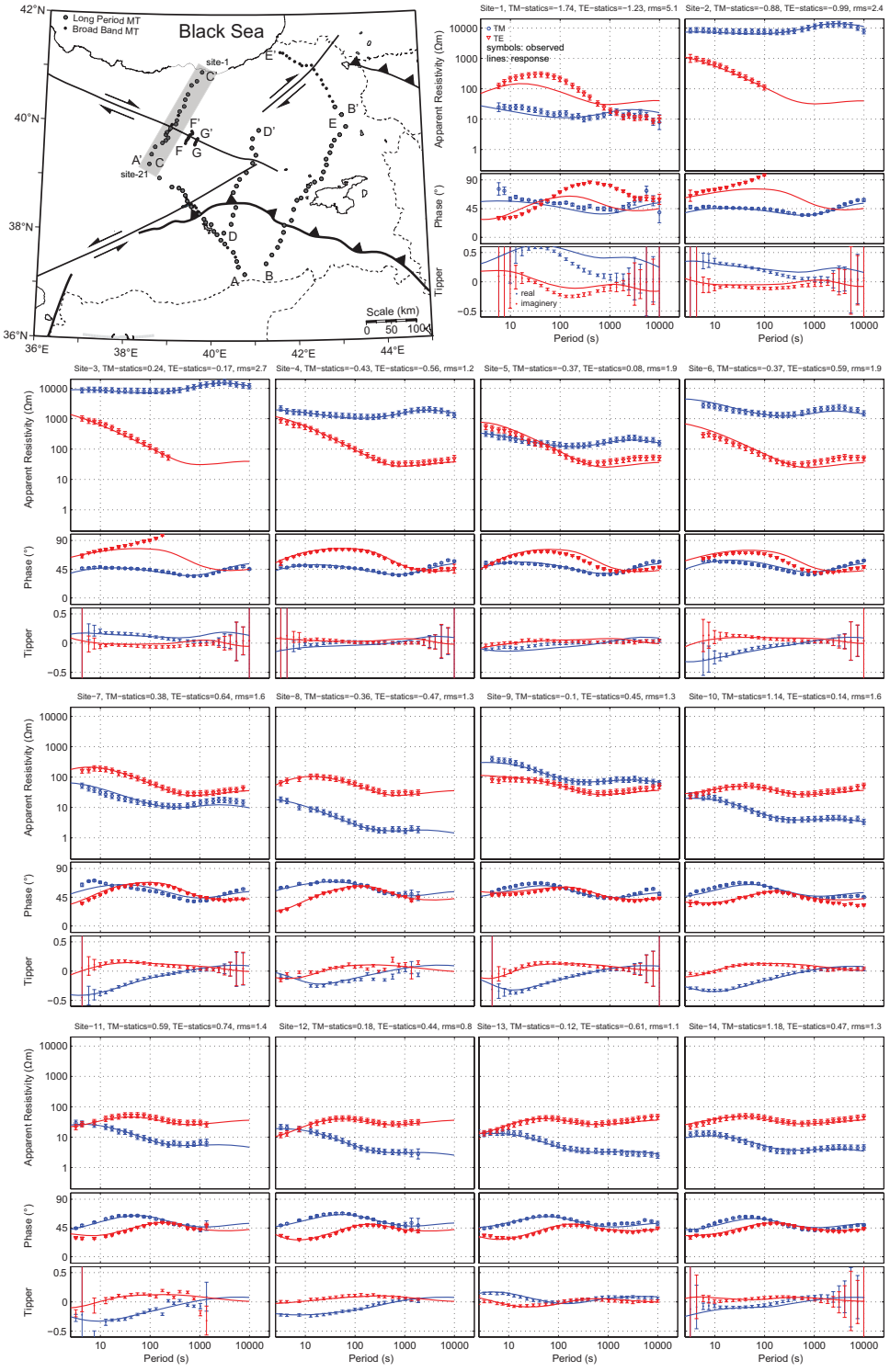

Figure A-3. C-profile MT data and 2-D inversion results with statistics for each station. Station names are modified to follow the locations from the map easily.

Figure A-3 continued…

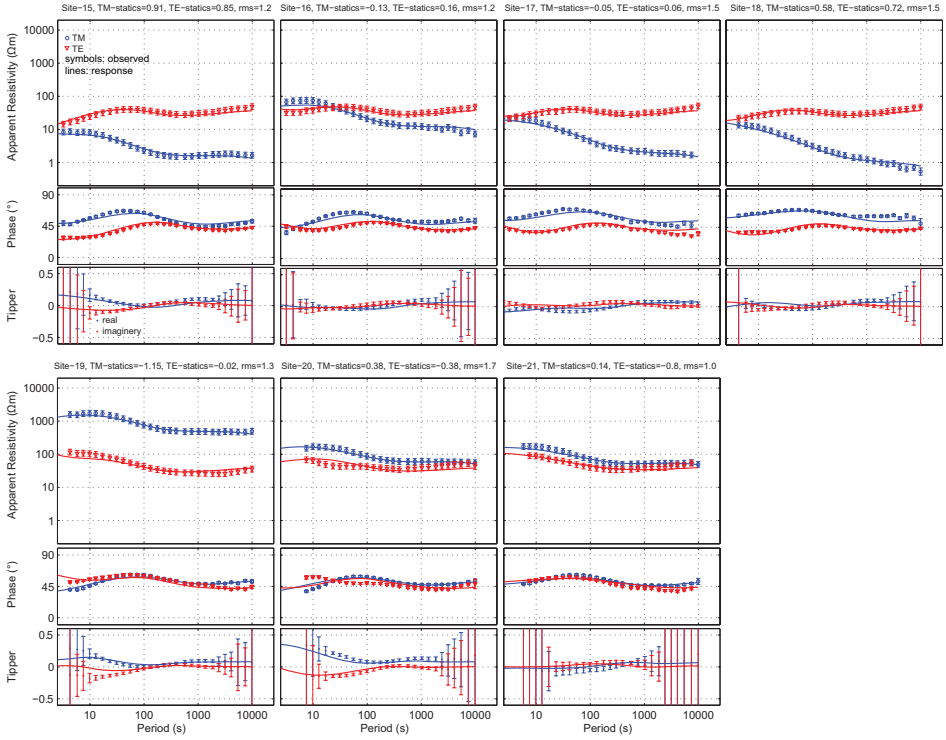

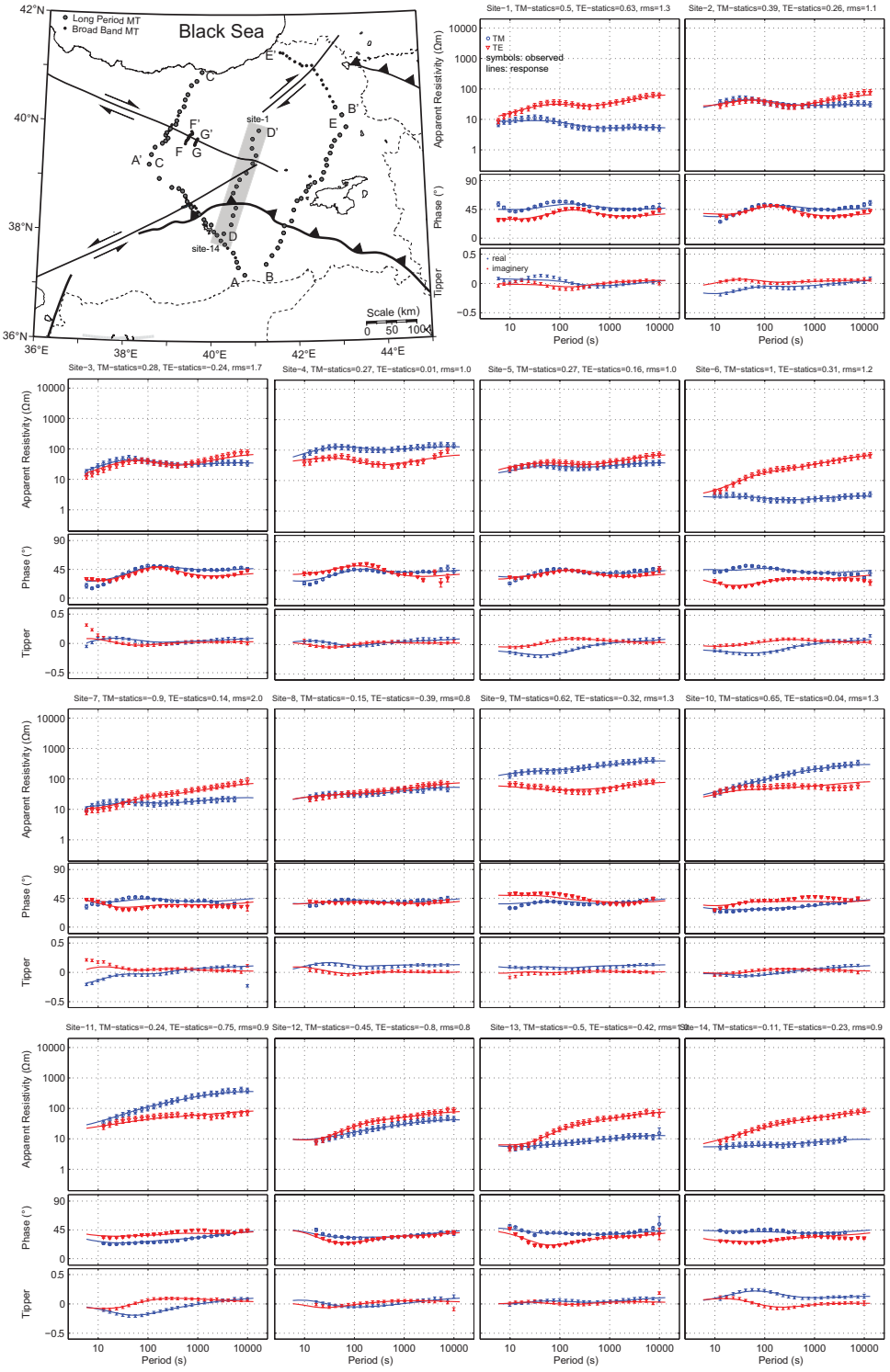

Figure A-4. D-profile MT data and 2-D inversion results with statistics for each station. Station names are modified to follow the locations from the map easily.

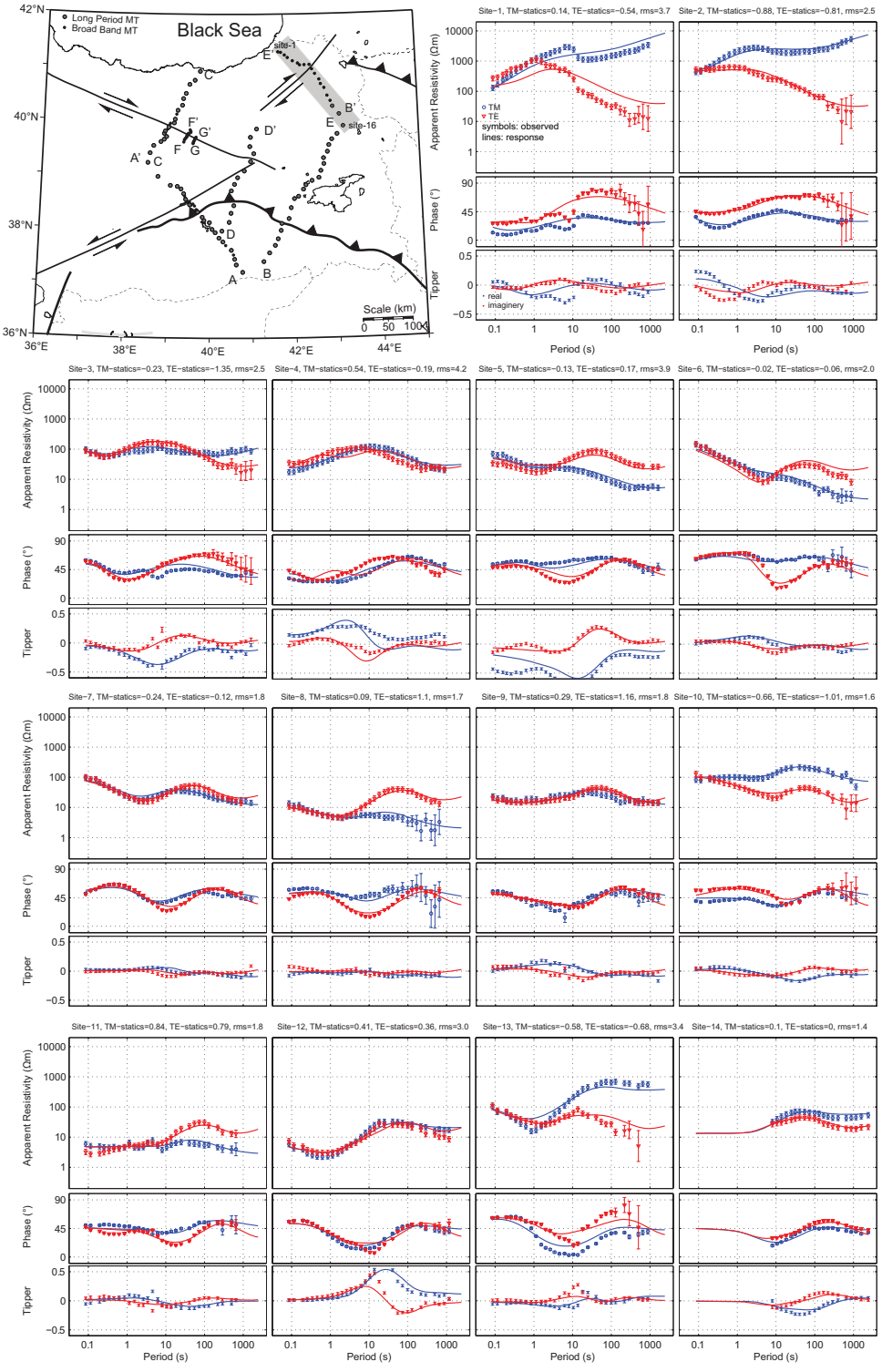

Figure A-5. E-profile MT data and 2-D inversion results with statistics for each station. Station names are modified to follow the locations from the map easily.

Figure A-5 continued…

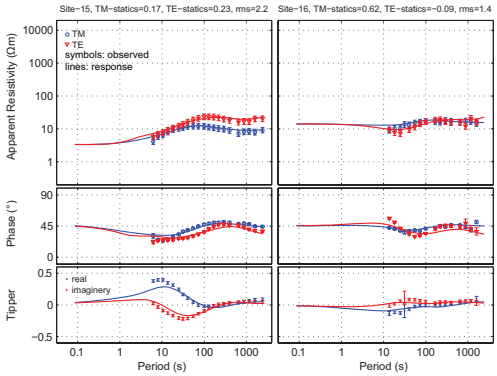

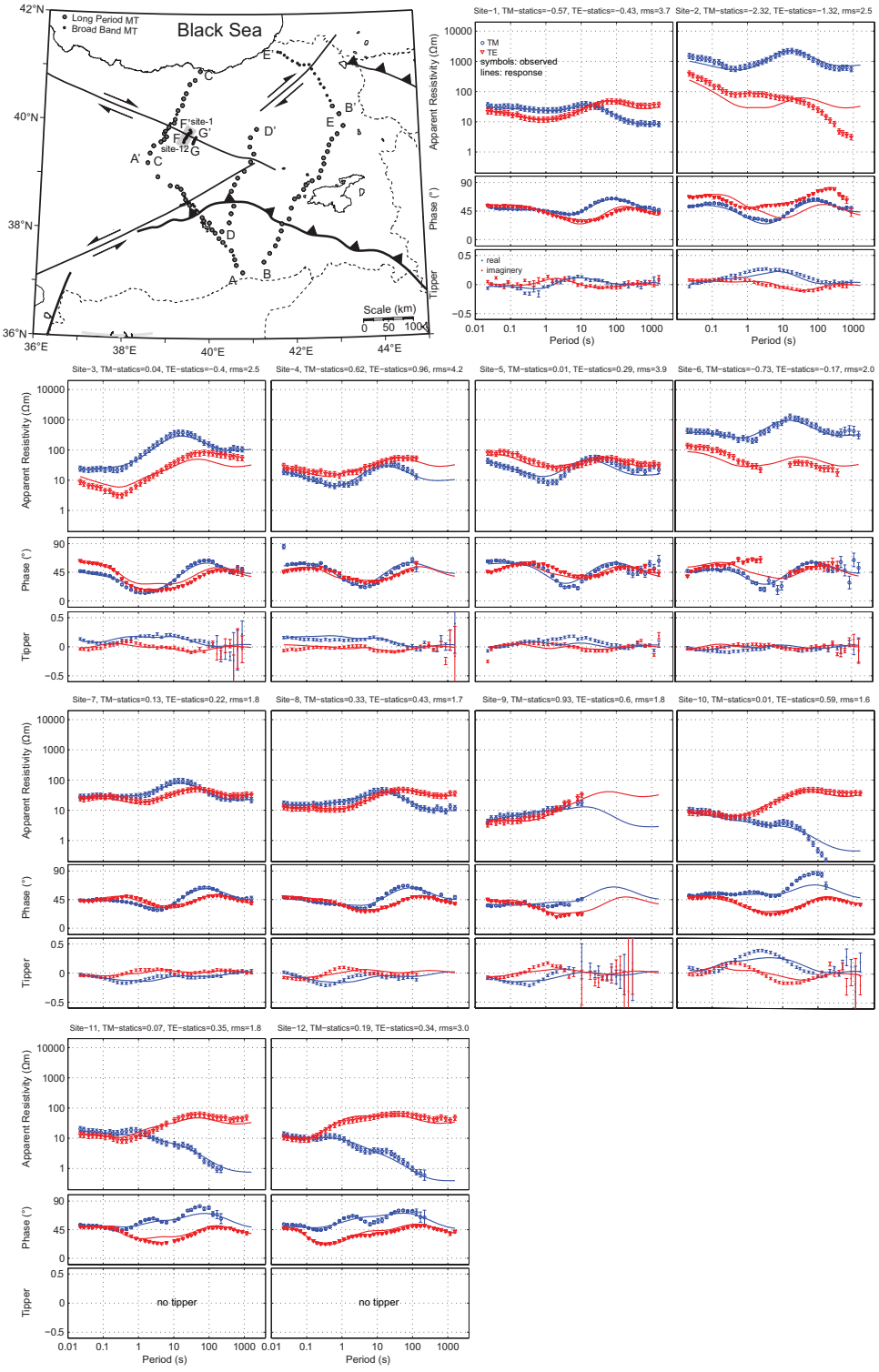

Figure A-6. F-profile MT data and 2-D inversion results with statistics for each station. Station names are modified to follow the locations from the map easily.

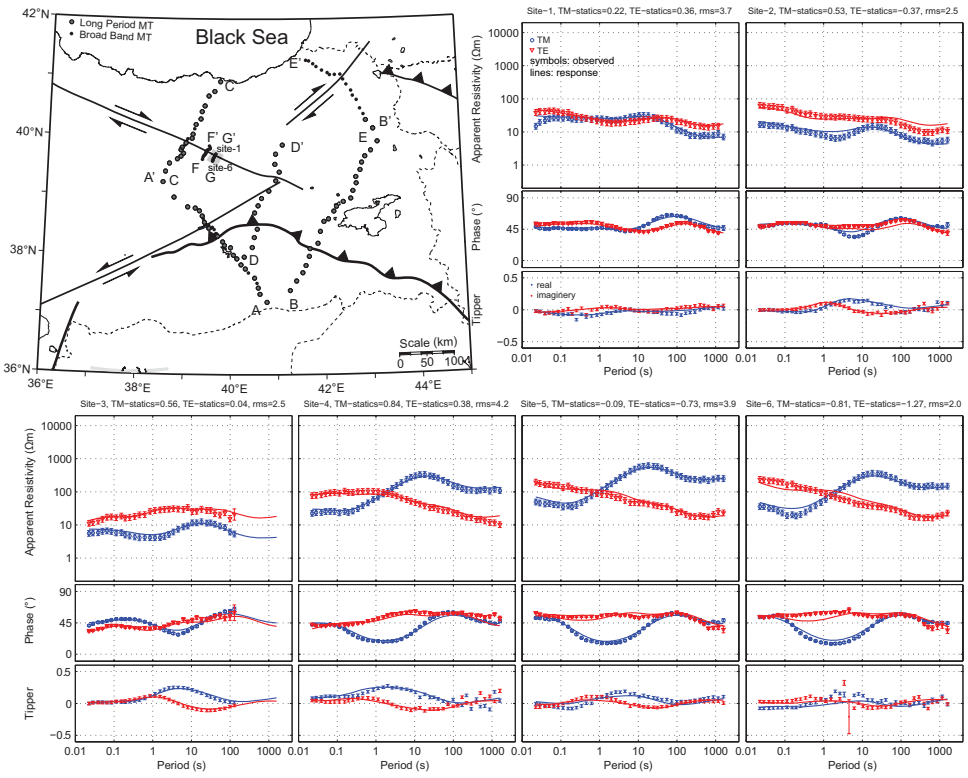

Figure A-7. G-profile MT data and 2-D inversion results with statistics for each station. Station names are modified to follow the locations from the map easily.